



**HAL**  
open science

# Multiscale modeling of the seismic response of buildings: Coupling between Homogenization Method and Multifiber Element Method

Graciela Franco Ariza

► **To cite this version:**

Graciela Franco Ariza. Multiscale modeling of the seismic response of buildings: Coupling between Homogenization Method and Multifiber Element Method. Materials. Université Gustave Eiffel, 2021. English. NNT: 2021UEFL2044 . tel-04606980

**HAL Id: tel-04606980**

**<https://theses.hal.science/tel-04606980v1>**

Submitted on 10 Jun 2024

**HAL** is a multi-disciplinary open access archive for the deposit and dissemination of scientific research documents, whether they are published or not. The documents may come from teaching and research institutions in France or abroad, or from public or private research centers.

L'archive ouverte pluridisciplinaire **HAL**, est destinée au dépôt et à la diffusion de documents scientifiques de niveau recherche, publiés ou non, émanant des établissements d'enseignement et de recherche français ou étrangers, des laboratoires publics ou privés.



École doctorale 531 : Sciences, ingénierie et environnement

Doctorat UGE

THÈSE

Pour obtenir le grade de docteur délivré par

**Université Gustave Eiffel**

**Spécialité : structures et matériaux**

*présentée par*

Carolina FRANCO ARIZA

25 octobre 2021

**Modélisation multi-échelle de la réponse sismique des  
bâtiments : couplage homogénéisation et éléments multifibres**

Directeur de thèse: **Jean-François SEMBLAT**  
Encadrants de thèse: **Céline CHESNAIS**  
**Cédric DESPREZ**  
**Cédric GIRY**

**Composition du jury**

Ioannis STEFANO	École Centrale de Nantes	Président
Claude BOUTIN	École Nationale des Travaux Publics de l'État	Rapporteur
Katrin BEYER	École Polytechnique Fédérale de Lausanne	Rapporteur
Filip FILIPPOU	University of California Berkeley	Examineur
Hélène DUMONTET	Université Pierre et Marie Curie	Examineur
Pierre-Alain NAZÉ	Géodynamique et Structure	Examineur
Jean-François SEMBLAT	École Nationale Supérieure de Techniques Avancées	Directeur de thèse
Céline CHESNAIS	Université Gustave Eiffel	Encadrant de thèse

Thèse préparée au sein des départements GERS et MAST

Laboratoires: **Sols, Roches et Ouvrages géotechniques (GERS/SRO)**

**Expérimentation et Modélisation pour le Génie Civil et Urbain (MAST/EMGCU)**



Doctoral school 531 : Sciences, engineering and environment

**Doctorat UGE**

DOCTORAL THESIS

To obtain the degree of Doctor of Philosophy

**Université Gustave Eiffel**

**Speciality: structures and materials**

*by*

Carolina FRANCO ARIZA

25th October 2021

**Multiscale modeling of the seismic response of buildings:  
Coupling between Homogenization Method and Multifiber  
Element Method**

Thesis director: **Jean-François SEMBLAT**  
Thesis supervisors: **Céline CHESNAIS**  
**Cédric DESPREZ**  
**Cédric GIRY**

**Jury composition**

Ioannis STEFANO	École Centrale de Nantes	President
Claude BOUTIN	École Nationale des Travaux Publics de l'État	Reporter
Katrin BEYER	École Polytechnique Fédérale de Lausanne	Reporter
Filip FILIPPOU	University of California Berkeley	Examiner
Hélène DUMONTET	Université Pierre et Marie Curie	Examiner
Pierre-Alain NAZÉ	Géodynamique et Structure	Examiner
Jean-François SEMBLAT	École Nationale Supérieure de Techniques Avancées	Thesis director .
Céline CHESNAIS	Univeristé Gustave Eiffel	Thesis supervisor

Ph.D. Thesis prepared in the GERS and MAST departments  
Laboratories: **Soils, Rocks and Geotechnical Structures (GERS/SRO)**  
**Urban and Civil Engineering Testing and Modeling (MAST/EMGCU)**

## Declaration of Authorship

I, Carolina FRANCO ARIZA, declare that this thesis titled, “Multiscale modeling of the seismic response of buildings: Coupling between Homogenization Method and Multifiber Element Method” and the work presented in it are my own. I confirm that:

- This work was done wholly or mainly while in candidature for a research degree at this University.
- Where any part of this thesis has previously been submitted for a degree or any other qualification at this University or any other institution, this has been clearly stated.
- Where I have consulted the published work of others, this is always clearly attributed.
- Where I have quoted from the work of others, the source is always given. With the exception of such quotations, this thesis is entirely my own work.
- I have acknowledged all main sources of help.
- Where the thesis is based on work done by myself jointly with others, I have made clear exactly what was done by others and what I have contributed myself.

Signed:

---

Date:

---



*“Success isn’t permanent and failure isn’t fatal; it’s the courage to continue that counts.”*

Mike Ditka

UNIVERSITÉ GUSTAVE EIFFEL

*Abstract*

École doctorale 531 : Sciences, ingénierie et environnement  
GERS/SRO and MAST/EMGCU laboratories

Doctor of Philosophy

**Multi-scale modeling of the seismic response of buildings:  
coupling homogenization and multifiber elements**

by Carolina FRANCO ARIZA

Thesis Director: Jean-François SEMBLAT

Thesis Supervisors: Céline CHESNAIS Cédric DESPREZ Cédric GIRY

In earthquake engineering, the assessment of the dynamic response of structures is a major challenge for predicting and reducing their vulnerability. Two approaches are commonly used for the design and diagnosis of the seismic vulnerability of buildings. The first one is based on the evaluation of global parameters, i.e., at the scale of the structure, such as inter-story or top-story displacements whose main advantage consists in being easily read and compared with seismic measurements. This approach often implements simplified models that do not include important mechanical properties of the structure (e.g., retrofitting with composite materials). The second one, more accurate but also more expensive, consists in performing detailed nonlinear numerical simulations to obtain damage indicators at the local scale, i.e., the scale of the materials, such as strains, stresses or damage variables.

Research studies based on multifiber finite elements have confirmed that the contrast between global and local indicators could lead to discrepancies and hinders the consistency of the evaluation of vulnerability, especially for retrofitted buildings. Therefore, the main purpose of this project is to propose a strategy based on simplified and advanced methods to improve the integration of the local and global scales in the definition of the damage indicators. A double scale change is performed by coupling the homogenization method (HM) and the multifiber finite element method (MEM). The first method links, on the one hand, the description at the scale of the structure (global scale) thanks to an equivalent "beam" model and, on the other hand, an intermediate scale corresponding to a single story of the structure. The equivalent beam properties are determined from a static analysis of a typical story, which is here modeled with multifiber finite elements. This second method allows analyzing the nonlinear effects at the material scale (local scale) controlling the global seismic response of the structure. The chosen modeling strategy keeps the link between the different scales while limiting the computation costs.

This research is divided into three parts. The first part presents the implementation of HM on complex multi-frame structures (with more than two frames per story). The analytical solution of this method has been developed and verified in earlier works for simpler cases (i.e., single and double frame structures). An enriched formulation of the finite element method is also developed to evaluate the dynamic response outside the harmonic framework and improve numerical applications. A second part describes the MEM numerical modeling of a single story based on the information obtained at the global scale, and the identification of the damage level in the materials as well as in the structural elements. Finally, the third and last part proposes a strategy which could be used in the future for the definition of damage criteria which better capture the effects at all scales.

**Keywords:** seismic vulnerability, homogenization, multifiber elements, enriched finite elements, damage indicators.

UNIVERSITÉ GUSTAVE EIFFEL

*Résumé*

École doctorale 531 : Sciences, ingénierie et environnement  
Laboratoires GERS/SRO et MAST/EMGCU

pour l'obtention du titre de Docteur

**Modélisation multi-échelle de la réponse sismique des bâtiments :  
couplage homogénéisation et éléments multifibres**

par Carolina FRANCO ARIZA

Directeur: Jean-François SEMBLAT

Encadrants: Céline CHESNAIS Cédric DESPREZ Cédric GIRY

Cette thèse cherche à modéliser la réponse dynamique des bâtiments à l'aide de méthodes robustes et simplifiées. En génie parasismique, l'évaluation de la réponse dynamique des structures est un enjeu majeur pour la prévision et la réduction de leur vulnérabilité. Deux approches sont couramment utilisées pour la conception et le diagnostic de vulnérabilité sismique des bâtiments. La première est basée sur l'évaluation de paramètres globaux, c'est-à-dire à l'échelle de la structure, tels que le déplacement en tête ou le déplacement inter-étages. Ces indicateurs de dommages globaux présentent l'avantage de pouvoir être estimés simplement et comparés à des mesures sous séisme. Par contre, ces méthodes mettent souvent en œuvre des modèles simplifiés qui ne prennent pas en compte certaines spécificités de la structure étudiée (e.g. un renforcement par matériaux composites). La deuxième approche, plus précise mais aussi plus coûteuse, consiste à réaliser des simulations numériques non linéaires détaillées pour accéder à des indicateurs de dommages à l'échelle locale, c'est-à-dire à l'échelle des matériaux, tels que les déformations, les contraintes, les variables d'endommagement.

La comparaison de ces deux approches ayant montré des incohérences, cette thèse propose une stratégie d'analyse originale pour développer de nouveaux indicateurs de dommages. L'objectif est d'améliorer la corrélation entre les indices de dommages locaux et globaux en utilisant des méthodes simplifiées et avancées. Pour cela, un double changement d'échelles est réalisé en couplant la méthode d'homogénéisation (MH) et la méthode des éléments finis multifibres (MEM). La première méthode fait le lien entre, d'une part, la description à l'échelle de la structure (échelle globale) grâce à un modèle de «poutre» équivalente et, d'autre part, une échelle appelée intermédiaire correspondant à un étage du bâtiment. La nature du modèle de poutre ainsi que ses paramètres sont déterminés à partir d'une analyse statique d'un étage type, qui est ici modélisé avec des éléments finis multi-fibres. Cette deuxième méthode permet l'analyse à l'échelle des matériaux (échelle locale) des effets non linéaires contrôlant la réponse sismique globale de la structure. La stratégie de modélisation retenue conserve le lien entre les différentes échelles tout en limitant les coûts de calculs.

Cette recherche est divisée en trois parties. La première présente l'implémentation de MH sur des structures réticulées complexes (structures comprenant plusieurs portiques par étage). La solution analytique de cette méthode a été développée et vérifiée dans des travaux antérieurs pour des cas plus simples (i.e. structures avec un ou deux portiques par étage). Une formulation enrichie de la méthode des éléments finis est également élaborée pour évaluer la réponse dynamique en dehors du régime harmonique en vue d'une meilleure implémentation numérique. Une deuxième partie propose, à partir de l'information obtenue au niveau global, la mise en œuvre de MEM sur le modèle numérique d'un étage et l'identification du niveau de dommage dans les matériaux ainsi que dans les éléments structuraux. Finalement, la troisième et dernière partie propose une stratégie qui pourra servir à l'avenir à définir des indicateurs d'endommagement capturant les effets à toutes les échelles décrites.

**Mots clés :** vulnérabilité sismique, homogénéisation, éléments multifibre, éléments finis enrichis, indicateurs d'endommagement.



## *Acknowledgements*

This Ph.D. work was prepared at the GERS/SRO and MAST/EMGCU laboratories of the French Institute of Science and Technology for Transport, Development and Networks (IFSTTAR), now the University Gustave Eiffel.

I would like to sincerely thank all those who helped me, directly or indirectly, to successfully achieve this work.

First of all, I want to express my gratitude to my thesis director Jean-François SEMBLAT and my supervisors, Céline Chesnais, Cédric Giry and Cédric Desprez who gave me their wise advice, encouragement and patience throughout the last three years of my research work. Thank you for putting your trust in me.

My sincere thanks go to the members of my thesis committee, Prof. Claude Boutin, Prof. Katrin Beyer, Prof. Filip Filippou, Prof. Ioannis Stefanou, Mr. Pierre-Alain Nazé and Prof. Hélène Dumontet. My special thanks go to Claude Boutin and Katrin Beyer for the time devoted to the critical evaluation of my Ph.D. manuscript. I wish to thank Prof. Ioannis Stefanou for his leadership during my research presentation.

I also want to say thanks to Prof. Fabian Bonilla and Prof. Fernando Lopez-Caballero for their pertinent advice. I well appreciated our fruitful discussions.

Je souhaiterais témoigner ma profonde gratitude aux membres du laboratoire SRO/GERS. Je vous remercie de m'avoir accueillie, de vos sourires en permanence et votre gentillesse. Merci bien. Grâce à vous et nos réunions conviviales, j'ai pu améliorer mon niveau de français.

Je tiens à remercier profondément Benoît qui m'a aidée dans la phase avec la plus grande quantité de calculs de ma thèse. Je sais qu'il y avait des téraoctets d'information pas très facile à gérer. Merci Benoît pour ta disponibilité et ton aide inconditionnelle.

I just want to say thanks to my colleagues and friends, Stefania, Hiba, Loren, Margot, Wassim, Roberto, Danilo, Chiara, Gisela, Rym and Quang-Huy who shared daily with me at the office, at coffee breaks and at the numerous "pots". There were many memorable moments of everything...happiness, confusion and incertitude. I learned a lot from you all.

My deep thanks to my dear friend Andrea Chaparro who was always with me through my ups and downs. My special thanks also to my friends in Colombia and Turkey for their friendship over the years.

Gracias madre mia y hermano mio por su apoyo constante, por creer siempre en mi. Ustedes han dado a mi vida una gran motivación. Los amo. Padre, tu que estás en el cielo, gracias. Las ganas con las que me enseñaste matemáticas me gustó tanto que resulté apasionada por los números y la ingeniería. Estos estudios son tu legado.

El final de esta página está dedicado a las personas que más amo en el mundo, mi compañero de vida, Ricardo, y mi maravillosa hija, Sofía. A ustedes dedico todo mi esfuerzo y este gran trabajo que sin su apoyo no hubiera podido llevar a cabo. Gracias por su paciencia durante las largas noches de trabajo y durante mi ausencia en ciertos fines de semana. Los amo profundamente.

Thanks to all of you, merci à tous et à toutes, gracias a todos.

# Contents

<b>Declaration of Authorship</b>	<b>ii</b>
<b>Abstract</b>	<b>v</b>
<b>Acknowledgements</b>	<b>ix</b>
<b>Introduction</b>	<b>1</b>
General context . . . . .	1
Motivations and goals . . . . .	3
Adopted methodology . . . . .	4
Thesis outline . . . . .	6
<b>1 Homogenized beam models for the dynamic analysis of buildings</b>	<b>7</b>
1.1 Abstract . . . . .	7
1.2 Continuous models for reticulated structures . . . . .	7
1.3 Homogenization method of Periodic Discrete Media (HPDM) . . . . .	10
1.4 Main results on single frame structures . . . . .	11
1.4.1 Framework of previous studies . . . . .	11
1.4.2 Governing mechanisms and associated kinematic variables . . . . .	11
1.4.3 Equivalent Beam Model: construction and equation of motion . . . . .	13
1.4.4 Specific homogenized beam models . . . . .	17
Identification criterion . . . . .	18
Shear beam model . . . . .	19
Euler-Bernoulli or global bending beam model . . . . .	19
Slender Timoshenko beam model . . . . .	20
Inner bending and shear beam model . . . . .	20
1.4.5 Additional homogenized beam models . . . . .	22
1.5 Homogenized beam models for multiple frame structures . . . . .	24
1.5.1 Results of the HPDM implementation on double and triple frame structures . . . . .	24
1.5.2 Hybrid analysis . . . . .	26
Kinematic variables . . . . .	26
Macroscopic parameters . . . . .	27
Computation of the shear stiffness of the cell $K_s$ . . . . .	28
Application to triple frame structures . . . . .	30



1.5.3	Influence of the number of frames . . . . .	37
1.5.4	Influence of the governing mechanism(s) on the modal properties . . .	40
1.6	Conclusion and perspectives . . . . .	45
<b>2</b>	<b>Finite element formulation of the homogenized beam</b>	<b>47</b>
2.1	EBM Weak formulation . . . . .	47
2.2	Enriched finite element formulation for reticulated structures . . . . .	50
2.2.1	Finite element of the EBM . . . . .	50
2.2.2	Choice criterion of the interpolation functions . . . . .	52
2.2.3	Derivation of the interpolation functions . . . . .	53
2.2.4	Elementary matrices . . . . .	56
2.3	Validation of the homogenized finite beam element . . . . .	60
2.3.1	A realistic steel structure . . . . .	60
2.3.2	Free vibration analysis . . . . .	63
	Eigenfrequencies and eigenmodes . . . . .	63
2.3.3	A parametric study: principles of the analysis . . . . .	65
	Description of the studied structures . . . . .	66
	Eigenfrequency assessment . . . . .	67
	Analysis of the divergence . . . . .	70
	Eigenmode assessment . . . . .	72
2.4	Conclusion and perspectives . . . . .	73
<b>3</b>	<b>Application to real structures</b>	<b>75</b>
3.1	Homogenized finite beam element model for a time history analysis using a real seismic record . . . . .	76
3.1.1	Newmark's method for linear systems . . . . .	76
	Equation of motion . . . . .	76
	Time discretization of the equation of motion . . . . .	77
	Step by step procedure . . . . .	78
	Stability and accuracy . . . . .	78
	Selection of damping properties . . . . .	78
3.1.2	A steel frame structure subjected to a moderate ground motion . . . .	80
3.2	Homogenized beam models of structures with various typical stories . . . .	82
3.2.1	Integration of different unit cell properties in the HBFEM model . . . .	82
3.2.2	Case study: the Grenoble City Hall (GCH) . . . . .	85
	Description of the structure . . . . .	85
	Previous works . . . . .	86
	Scope of this study . . . . .	87
	Numerical model of the GCH building . . . . .	89
	Construction of 1D models for the GCH building . . . . .	93
	Scheme 1: Analysis of the GCH building quasi-periodic section . . . .	94
	The GCH building dynamic behavior . . . . .	100

	Scheme 2: Analysis of the entire GCH building (non-periodic + quasi-periodic sections) . . . . .	107
3.2.3	Discussion about the results and the implemented methodology . . . . .	109
3.3	Conclusion and perspectives . . . . .	110
3.3.1	Main results . . . . .	110
3.3.2	Limitations and future works . . . . .	111
	Soil-structure interaction . . . . .	111
	Maximum stiffness contrast between two periodic substructures . . . . .	112
	Encountered types of behavior in regular concrete structures . . . . .	112
<b>4</b>	<b>Towards a new damage indicator using the Equivalent Beam Model and multifiber beam elements</b>	<b>113</b>
4.1	Continuation of the hybrid analysis: story and element scales . . . . .	114
4.1.1	Computation of the nodal rotation . . . . .	115
4.1.2	Hybrid analysis : Part II . . . . .	115
4.1.3	Computation of the internal forces . . . . .	116
4.1.4	Verification of the hybrid procedure . . . . .	118
4.1.5	Conclusions of the return to the element scale . . . . .	126
4.2	Introducing non-linear behavior into the Equivalent Beam Model . . . . .	127
4.2.1	Coupling of the HBFEM and multifiber beam element method (MFEM) Multifiber beam element principles . . . . .	127
4.2.2	Local scale: Constitutive laws for concrete and reinforcing steel . . . . .	128
	Concrete behavior: La Borderie's model . . . . .	128
	Reinforcing steel behavior: modified Giuffrè-Menegotto-Pinto . . . . .	130
4.2.3	Intermediate scale: Prescribing the macrodeformation to a single story Shear stiffness evolution . . . . .	131
	Inner bending stiffness evolution . . . . .	133
	Global bending stiffness evolution . . . . .	135
4.2.4	Global scale: Implementation of the Newmark method for non-linear analysis . . . . .	136
4.3	About the need for a new damage indicator . . . . .	140
4.3.1	Main characteristics of damage indicators . . . . .	141
4.3.2	Discrepancies between damage indicators . . . . .	142
	Example of the Grenoble City Hall . . . . .	142
4.3.3	Strategy for the definition of a new damage indicator . . . . .	143
	Form of the Behavior Response based Damage Indicator (BRDI) . . . . .	143
4.4	Conclusions and perspectives . . . . .	144
	<b>General conclusions</b>	<b>145</b>

# List of Figures

1	Building-type structures studied in this work . . . . .	1
2	Main topics investigated in this work for the modeling of the seismic response of buildings . . . . .	3
3	The different scales considered in the present work . . . . .	5
1.1	Idealized single frame structures studied in [Boutin and Hans, 2003, Hans and Boutin, 2008]	11
1.2	Mechanisms that govern the transverse behavior of the single frame structures: shear of the cells (stiffness $K_s$ ), inner bending (stiffness $\mathcal{K}_i$ ) and global bending (stiffness $\mathcal{K}_g$ ). In this schematic, fixed-free ends are considered as boundary conditions.[Chesnais, 2010] . . . . .	12
1.3	Schematic representation of the mechanisms included in the EBM [Chesnais, 2010].	12
1.4	Global (left) and intermediate (right) kinematics of the physical problem . . .	13
1.5	Notation and sign convention for the Equivalent Beam Model. . . . .	14
1.6	The two mechanisms contributing to the total shear force $\mathcal{T} = T - \mathcal{M}'$ . $T$ comes from the shear deformation of the cell generated by the local bending of all the elements (left) and $-\mathcal{M}'$ comes from the shear deformation of the cell generated by the synchronized bending of the vertical elements (right). . . . .	15
1.7	Map of the transverse macroscopic behaviors as a function of $C$ and $\gamma$ . [Hans and Boutin, 2008]	19
1.8	Schematic representation of the mechanisms included in the upgraded EBM [Chesnais, 2010]. . . . .	23
1.9	Global (left) and intermediate (right) kinematics of the physical problem . . .	27
1.10	Boundary conditions A (Left) and B (Right) associated with the shear deformation of the story model . . . . .	29
1.11	Studied triple frame structures. The thicknesses of the elements are given in Table 1.6. . . . .	31
1.12	Studied triple frame structures. Cell deformation under the boundary conditions A (orange line) and B (blue dashed line) . . . . .	32
1.13	Behavior identification for the ten studied structures. The orange squares correspond to the values of $K_s$ calculated with the boundary conditions A and the blue circles correspond to the values of $K_s$ calculated with the boundary conditions B. . . . .	35
1.14	Relative error on the first vibration frequency obtained with the full finite element model (reference) and the hybrid analysis using the EBM with the boundary conditions A and B, and the specific beam model with the value of $K_s$ calculated using the boundary conditions B. . . . .	36

1.15	Unit frames of the studied structures and governing mechanism(s) when $N = 10$ and $N_f = 3$ . <b>Case 1 (blue frame)</b> : identical thin walls and floors ( $a_m/l_m = a_p/l_m = O(\varepsilon^2)$ ) $\rightarrow$ shear; <b>Case 2 (purple frame)</b> : walls thicker than the floors with a high contrast ( $a_m/l_m = O(\varepsilon^1)$ and $a_p/l_m = O(\varepsilon^2)$ ) $\rightarrow$ inner bending and shear; <b>Case 3 (red frame)</b> : walls thicker than the floors with a smaller contrast ( $a_m/l_m = O(\varepsilon^1)$ and $a_p/l_m = O(\varepsilon^{5/3})$ ) $\rightarrow$ inner bending and shear; <b>Case 4 (green frame)</b> : identical thick walls and floors ( $a_m/l_m = a_p/l_m = O(\varepsilon^1)$ ) $\rightarrow$ slender Timoshenko (global bending and shear) . . . . .	38
1.16	Identified macroscopic behavior for each case as the number of cells $N$ increases.	38
1.17	Identified macroscopic behavior for each case as the number of frames per story $N_f$ increases. . . . .	39
1.18	Evolution of the fundamental frequency with respect to the number of frames per story $N_f$ . Blue circled line: numerical model. Red starred line: hybrid analysis with the EBM. Cyan starred line: classical Timoshenko beam model;	40
1.19	Frequency ratios as functions of the dimensionless parameter $C$ for (A) a continuous Timoshenko beam [Hans, 2002] and (B) the EBM of the studied triple frame structures. . . . .	41
1.20	3-D representation of the frequency ratios as functions of the macroscopic constants $C$ and $\gamma$ . . . . .	42
1.21	Domain behavior variation according to the vibration mode of a set of ten structures. Each line represents a specific structure. . . . .	43
1.22	Relationship between the natural frequency ratios and the governing mechanism(s) of the first vibration mode. . . . .	44
1.23	Evolution of (Top) the transverse displacement and (Bottom) the macroscopic rotation for the studied structures. . . . .	45
2.1	Finite element discretization for reticulated structures based on the EBM.(a) Physical problem, EBM, boundary conditions. (b) Definition of finite elements.	51
2.2	Nodal displacements and their derivatives in the discrete element with the notation defined in Equation (2.21). . . . .	53
2.3	Hermite cubic interpolation functions (top) and their derivatives (bottom) for $u^e$ . . . . .	54
2.4	Nodal macroscopic rotation in the discrete element . . . . .	55
2.5	Lagrange quadratic interpolation functions (left) and their derivatives (right) for $\alpha^e$ . . . . .	56
2.6	Elevation (left) and plan view (right) of the studied steel structure (all dimensions are in m). . . . .	61
2.7	Comparison of the first three mode shapes of the structure shown in Figure 2.6. The diamond-dotted dashed black lines corresponds to the <i>EBM</i> . The square-dotted full black lines refer to the detailed FEM model ( <i>DFEM</i> ). The round-dotted dashed grey lines are associated with the <i>HBFEM</i> model. The triangle-dotted dashed black lines are for the Timoshenko beam model ( <i>TFEM</i> ). 65	65

2.8 Domain behavior identification graph for the studied structures. Circle blue, square red, and triangle green dots correspond to the set of the four hundred structures with  $N = 10$ ,  $N = 20$  and  $N = 30$ , respectively. . . . . 67

2.9 Variation of the relative error between the first natural frequency obtained with the HBFEM model and the first natural frequency obtained with the EBM as a function of the number of finite elements  $N_e$ . Each dot represents the result of a single structure evaluated with a fixed  $N_e$ . The 400 structures' properties are:  $E = 30\text{GPa}$ ,  $\nu = 0.3$ ,  $\rho = 2300\text{ kg/m}^3$ ,  $N = 10$ , the unit cell is a single frame (two vertical elements and one horizontal of length 3000 mm), thicknesses vary from 50 mm to 1950 mm with a step of 100 mm, all the structures are clamped at the base and free at the top. For (b) the case corresponds to a structure with 50 mm thick vertical elements and a 250 mm thick horizontal element. The predominant mechanism is the shear of the cell generated by the local bending of the vertical elements. . . . . 68

2.10 Variation of the relative error between the first natural frequency obtained with the HBFEM model and the first natural frequency obtained with the EBM as a function of the number of finite elements  $N_e$ . Each dot represents the result of a single structure evaluated with a fixed  $N_e$ . The structures' properties are:  $E = 30\text{ GPa}$ ,  $\nu = 0.3$ ,  $\rho = 2300\text{ kg/m}^3$ , a)  $N = 20$ , and b)  $N = 30$ , the unit cell is a single frame (two vertical elements and one horizontal), the thicknesses vary from 50 mm to 1950 mm with a step of 100 mm, all the structures are clamped at the base and free at the top. . . . . 69

2.11 Variation of the relative error  $\epsilon^{f_{\text{HBFEM}}}$  for the first three natural frequencies as a function of the number of finite elements  $N_e$ . Each dot represents the result of a single structure evaluated with a fixed  $N_e$ . The structures' properties are:  $E = 30\text{ GPa}$ ,  $\nu = 0.3$ ,  $\rho = 2300\text{ kg/m}^3$ ,  $N = 10$ , a)  $a_m = 150\text{ mm}$  and  $a_p = 50\text{ mm}$  (shear behavior), b)  $a_m = 500\text{ mm}$  and  $a_p = 100\text{ mm}$  (inner bending behavior), c)  $a_m = 500\text{ mm}$  and  $a_p = 150\text{ mm}$  (shear behavior), and d)  $a_m = 500\text{ mm}$  and  $a_p = 500\text{ mm}$  (slender Timoshenko behavior). The unit cell is a single frame (two vertical elements and one horizontal). All the structures are clamped at the base and free at the top. . . . . 70

2.12 Relative error  $\epsilon^{f_x}$  as a function of the ratio  $C$  between the global bending stiffness and the shear stiffness for the set of four hundred structures with  $N = 10$ . (a) Assessment of the EBM with the detailed numerical model used as reference, (b) assessment of the HBFEM model (for  $N_e = 1 : 1 : 100$ ) with the EBM used as a reference. . . . . 71

2.13 Relative error  $\epsilon^{f_{\text{HBFEM}}}$  as (a) a function of  $C$  and as (b) a function of the thickness contrast between the horizontal elements (thickness  $a_p$ ) and the vertical elements (thickness  $a_m$ ) for the set of four hundred structures with  $N = 10$  when  $N_e = 10$ . . . . . 72

2.14	Comparison of the first three mode shapes provided by the HBFEM model with three different numbers of finite elements: $N_e = 3$ , $N_e = N$ and $N_e = 100$ . The diamond-dotted dashed black lines correspond to the EBM. The square-dotted full grey lines refer to the full FEM model. The triangle-dotted dashed blue lines are for the HBFEM model with $h_e = Nl_m/3 > l_m$ . The star-dotted dashed green lines are for the HBFEM model with $h_e = l_m$ . The round-dotted red lines are for the HBFEM model with $h_e = Nl_m/100 < l_m$ . . . . .	73
3.1	Ground acceleration record (a) and amplitude spectrum (b) of the north-south component of the earthquake event recorded on August 2, 2017 in Ibaraki, Japan. The magnitude is 5.5 and the peak acceleration is 0.13 g. . . . .	81
3.2	Top roof displacements (a) and their amplitude spectra (b) obtained with the detailed finite element model (grey) and the HBFEM model (black) . . . . .	82
3.3	Structure composed of two periodic substructures (Left). HBFEM model parameters and nodal definition at the boundary between the two substructures (Right) . . . . .	83
3.4	Nodal kinematic variables of the finite beam elements located at the boundary node $n + 1$ between the two substructures . . . . .	83
3.5	The Grenoble City Hall tower block. Top left: General view [Jacques Mossot, 2007]. Top right: Front side view of the tower block [Michel et al., 2010b]. Bottom: typical story and ground story plan views . . . . .	87
3.6	Hybrid strategy for free vibration analysis with the HBFEM model . . . . .	88
3.7	Quasi-periodic and non-periodic sections of the GCH tower block. . . . .	89
3.8	Sections considered in the numerical model (the stories are numbered from the transfer slab). Top left: column and beam sections for the two typical stories. The cross-section of the columns slightly decrease from the 6th story. Top right: pillar sections. Bottom: plan view of the distribution considered in the numerical model . . . . .	90
3.9	Full detailed numerical model (12275 nodes and 21278 elements) of the Grenoble City Hall tower block [Desprez, 2010]. . . . .	91
3.10	Full detailed numerical model DFEM-1 of the 11th-story quasi-periodic section of the Grenoble City Hall tower block. (9864 nodes and 17080 elements.) . . .	95
3.11	Full detailed multifiber beam model of a single story in Cast3M . . . . .	97
3.12	Boundary conditions in the Cast3M story model (Transverse direction) . . . .	98
3.13	Boundary conditions in the ETABS story model (Transverse direction) . . . .	98
3.14	Shear deformation of the unit cell in Cast3M. Top: Longitudinal direction. Bottom: Transverse direction. The colors represent the vertical displacements	99
3.15	Shear deformation of the unit cell in ETABS. Top: Longitudinal direction. Bottom: Transverse direction. The colors represent the vertical displacements.	99

3.16	On the left, comparison between the mode shapes obtained using the EB-1 (diamonds), EB-2 (triangles), HBFEM-1 model with the two unit cell properties (gray circles) and the detailed numerical model DFEM-1 of Figure 3.10 (squares) for the longitudinal (top) and transverse (bottom) directions. The mode shapes are normalized with respect to the maximum displacement. On the right, correlation (MAC values) for the first vibration mode (red) and the second vibration mode (blue). . . . .	102
3.17	On the left, comparison of the first two mode shapes obtained with the HBFEM-2 model with the four unit cell properties (gray circles) and the detailed numerical model DFEM-2 of Figure 3.9 (squares) for the longitudinal (top) and transverse (bottom) directions. The mode shapes are normalized with respect to the maximum displacement. On the right, correlation (MAC value) for the first vibration mode (red) and the second vibration mode (blue). . . . .	109
4.1	Stages of the proposed hybrid analysis . . . . .	115
4.2	Boundary conditions associated with global bending deformation of the story model . . . . .	116
4.3	Notation at the element scale: nodal description of the kinematics and the internal forces: axial force $\mathbf{N}$ , shear force $\mathbf{T}$ and bending moment $\mathbf{M}$ . . . . .	117
4.4	Shear force (top) and bending moment (bottom) of the walls for the first two eigenmodes. Single frame structure (Case 0). . . . .	123
4.5	Shear force (top) and bending moment (bottom) of the external and internal walls for the first two eigenmodes. Triple frame structure (Case 12). . . . .	124
4.6	Principle of the multifiber beam element [CAPDEVIELLE, 2016] . . . . .	128
4.7	Stress-strain relationship for concrete- La Borderie damage model [Ile et al., 2008]	129
4.8	Stress-strain relationship for steel- Giuffrè-Menegotto-Pinto including buckling stiffness softening . . . . .	130
4.9	Boundary conditions associated with shear deformed model . . . . .	132
4.10	Comparison of shear stiffness evolution obtained with the numerical model and the analytical equation for $K_s$ (Equation(1.2)) . . . . .	132
4.11	Shear deformation on a single frame story using boundary conditions of Figure 4.9 . . . . .	133
4.12	Boundary conditions associated with inner bending deformed model . . . . .	133
4.13	Total bending moment of the vertical elements as a function of the imposed nodal rotation difference . . . . .	134
4.14	Inner bending deformation on a single frame story using boundary conditions of Figure 4.12 . . . . .	134
4.15	Boundary conditions associated with global bending deformed model . . . . .	135
4.16	Global bending moment - macroscopic rotation distortion relationship . . . . .	136
4.17	Global bending deformation on a single frame story using boundary conditions of Figure 4.15 . . . . .	136
4.18	Non-linear analysis procedure . . . . .	138

4.19 Elevation of the studied RC frame structure (all dimensions are in m). . . . .	139
4.20 HBFEM model validation, roof displacement time-history. . . . .	140
4.21 Numerical simulation results before and after the proposed reinforcement strategy of the Grenoble City Hall building [Desprez, 2010]. . . . .	143



# List of Tables

1.1	Kinematic variables associated with each mechanism . . . . .	13
1.2	Beam models issued from the HPDM implementation on single frame structures. The macroscopic kinematic variables of the transverse steady-state motion are the transverse displacement $\hat{u}$ and the global rotation $\hat{\alpha}$ . The boundary conditions are given for a beam of length $H$ clamped at the base and free at the top. . . . .	21
1.3	Case study in [Chesnais, 2010]. Comparison of the frequencies of the first three modes in the longitudinal direction. . . . .	22
1.4	Analytical expressions of the shear stiffness of the cell $K_s$ for single, double and triple frame structures . . . . .	25
1.5	Case study in [Chesnais, 2010]. Comparison of the eigen frequencies of the first three vibration modes obtained with a finite element model of the whole structure and a shear beam model where the shear stiffness $K_s$ is calculated with the boundary conditions A and B . . . . .	30
1.6	Element thicknesses of the studied triple frame structures in mm. . . . .	31
1.7	Shear stiffness of the cell $K_s$ computed with the analytical expression issued from the homogenization of triple frame structures (Equation (1.18) of Table 1.4) and the numerical model of a story using the boundary conditions A and B. . . . .	32
1.8	Boundary conditions A applied on the numerical model of a story: Macroscopic properties. . . . .	34
1.9	Boundary conditions B applied on the numerical model of a story: Macroscopic properties. . . . .	34
1.10	Comparison of the first vibration frequency obtained with the full finite element model and the hybrid analysis using the EBM. . . . .	35
1.11	Comparison of the first vibration frequency obtained with the full finite element model and the hybrid analysis using the specific beam model and the value of $K_s$ calculated with the boundary conditions B. . . . .	36
2.1	Geometric and material properties of the structural members . . . . .	61
2.2	Macroscopic parameters of the studied structure . . . . .	62
2.3	Geometric and material properties of the Timoshenko beam model . . . . .	62
2.4	Eigenfrequencies of the first three transverse vibration modes in Hz. . . . .	64

2.5	Differences (%) between the eigenfrequencies of each of the analyzed models and those of the detailed numerical model according to Equation (3.12) and Table 2.4. . . . .	64
2.6	Eigenfrequencies of the first three transverse vibration modes in Hz computed with the detailed numerical model (subscript DFEM), the EBM (subscript EBM), the HBFEM model with three different mesh sizes: $N_e = 3$ , $N_e = N$ and $N_e = 100$ . . . . .	73
3.1	Classical proportional damping models . . . . .	80
3.2	Geometrical properties extracted from the detailed numerical model. (a) Average of the two basement story heights = $0.5 \times (3.47 + 4.68)$ m. (b) 4 beams in the longitudinal direction. (c) 3 beams in the transverse direction. . . . .	91
3.3	First vibration modes of the Grenoble City Hall from the full detailed numerical model [Desprez, 2010] . . . . .	92
3.4	Comparison of the first modal frequencies of the Grenoble City Hall building obtained with the ambient vibrations and the numerical model. . . . .	93
3.5	Analyzed models in the schemes 1 and 2 . . . . .	94
3.6	First vibration modes of the upper tower section of the Grenoble City Hall building (full detailed numerical model DFEM-1) . . . . .	96
3.7	Comparison of the shear stiffness $K_s$ obtained with the story model in Cast3M and in ETABS (897 nodes and 1320 elements). . . . .	99
3.8	Variation of the shear stiffness with respect to the mesh density used to model the floor in Cast3M. . . . .	99
3.9	Macroscopic parameters for the typical stories 1 and 2 in the longitudinal (L) and transverse (T) directions. . . . .	100
3.10	Identified behaviors in the longitudinal direction. . . . .	100
3.11	Identified behaviors in the transverse direction. . . . .	100
3.12	Comparison of the first two modal frequencies in Hz for the <b>longitudinal</b> direction with the quasi-periodic section numerical model (Figure 3.10). . . . .	101
3.13	Comparison of the first two modal frequencies in Hz for the <b>transverse</b> direction with the quasi-periodic section numerical model (Figure 3.10). . . . .	102
3.14	Macroscopic parameters for the inner Timoshenko model with $N = 11$ stories. . . . .	105
3.15	Comparison of the first two modal frequencies in Hz for the <b>longitudinal</b> direction obtained with the HBFEM-1 model (mode 1), the inner Timoshenko model (mode 2) and with the quasi-periodic section numerical model (Figure 3.10). . . . .	105
3.16	Comparison of the first two modal frequencies in Hz for the <b>transverse</b> direction obtained with the HBFEM-1 model (mode 1), the inner Timoshenko model (mode 2) and with the quasi-periodic section numerical model (Figure 3.10). . . . .	105
3.17	Comparison of the first two modal frequencies in Hz for the <b>longitudinal</b> direction obtained with the HBFEM-1 model (mode 1), the modified HBFEM model (mode 2) and with the quasi-periodic section numerical model (Figure 3.10). . . . .	106

3.18	Comparison of the first two modal frequencies in Hz for the <b>transverse</b> direction obtained with the HBFEM-1 model (mode 1), the modified HBFEM model (mode 2) and with the quasi-periodic section numerical model (Figure 3.10). .	106
3.19	Ground and basement story macroscopic parameters in the longitudinal (L) and transverse directions (T). . . . .	107
3.20	Comparison of the first two modal frequencies in Hz for the <b>longitudinal</b> direction with the detailed numerical model (Figure 3.9). . . . .	108
3.21	Comparison of the first two modal frequencies in Hz for the <b>transverse</b> direction with the detailed numerical model (Figure 3.9). . . . .	108
4.1	List of the studied cases with different thicknesses for external and internal walls $a_{me}$ and $ami$ , respectively. $n_w$ are the number of walls, and $a_p$ the thickness of the floors. $a_p$ and $a_m$ are given in mm . . . . .	119
4.2	List of the computed kinematic variables mm-rad, shear forces in KN, and bending moment in KN mm . . . . .	120
4.3	Macroscopic properties and identified mechanism(s) of the studied structures. Case 9 and 15 are not reported. . . . .	121
4.4	Comparison of the results obtained with the full finite element model and the HBFEM. Case 9 and 15 are not reported. . . . .	122
4.5	R/C elements: material parameters for concrete . . . . .	129
4.6	R/C elements: material parameters for steel . . . . .	131
4.7	Geometry and material properties of the 10-story reinforced concrete structure taken as case study. . . . .	139
4.8	Non-cumulative damage indices . . . . .	142

# List of Abbreviations

<b>DOF</b>	<b>D</b> egree <b>O</b> f <b>F</b> reedom
<b>EBM</b>	<b>E</b> quivalent <b>B</b> eam <b>M</b> odel
<b>FEM</b>	<b>F</b> inite <b>E</b> lement <b>M</b> ethod
<b>FFT</b>	<b>F</b> ast <b>F</b> ourier <b>T</b> ransform
<b>HBFEM</b>	<b>H</b> omogenized <b>B</b> eam <b>F</b> inite <b>E</b> lement
<b>HPDM</b>	<b>H</b> omogenization of <b>P</b> eriodic <b>D</b> iscrete <b>M</b> edia
<b>IFSTTAR</b>	<b>I</b> nstitut <b>F</b> rançais des <b>S</b> ciences et <b>T</b> echnologies des <b>T</b> ransports, de l' <b>A</b> ménagement et des <b>R</b> éseaux
<b>MDOF</b>	<b>M</b> ulti <b>D</b> egree <b>O</b> f <b>F</b> reedom
<b>ME</b>	<b>M</b> ultifiber <b>B</b> eam <b>E</b> lement
<b>PSD</b>	<b>P</b> ower <b>S</b> pectral <b>D</b> ensity
<b>RHA</b>	<b>R</b> esponse <b>H</b> istory <b>A</b> nalysis
<b>SDOF</b>	<b>S</b> ingle <b>D</b> egree <b>O</b> f <b>F</b> reedom

# Nomenclature

$K_s$	Shear stiffness
$\mathcal{K}_g$	Global bending stiffness
$\mathcal{K}_i$	Inner bending stiffness
$E$	Elastic Modulus
$G$	Shear modulus
$A$	Area of the cross section of each element
$I_w$	Area moment of inertia of each wall
$I_M$	Global inertia or area moment of inertia defined by $Ad^2$ . Where $d$ corresponds to the distance between the vertical symmetric axis of the unit cell and the centroidal axis of the element section
$I_{\mathcal{M}}$	Inner bending inertia or area moment of inertia .
$\Lambda$	Linear mass or mass per length
$\omega$	Circular vibration frequency
$L$	Characteristic size of the vibrations of the structure
$\lambda$	Macroscopic wavelength
$x$	Longitudinal axe (along the equivalent beam)
$y$	Transverse axe
$H$	Building height from soil surface
$u$	Transverse displacement at global scale
$v$	Longitudinal displacement at global scale
$\alpha$	Macroscopic rotation or rotation at global scale
$\theta$	Nodal rotation
$t$	Time

$\mathcal{T}$	Total shear force
$T$	Shear force
$\mathcal{M}$	Inner bending moment
$M$	Global bending moment
$N$	Axial force acting on the element
$\mathbf{M}$	Moment acting on the element
$\mathbf{T}$	Shear force acting on the element

*Dedicated to my daughter, Sofia.*

# Introduction

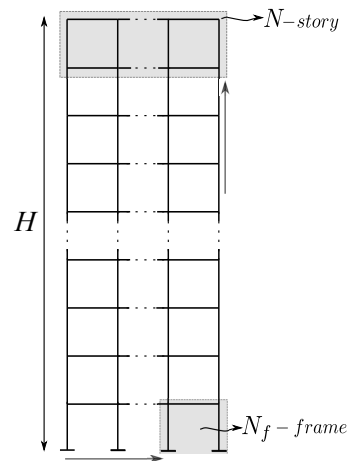
## General context

*Keywords: multiscale / simplified, robust, continuous models / regular buildings / seismic vulnerability assessment*

This Ph.D. thesis consists in modeling the seismic response of regular and periodic buildings using simplified but efficient and robust techniques. Regular buildings account for buildings whose typical story is plane-symmetrical and repeats all along the height of the structure. This is the case of existing ordinary mid-rise, and high-rise reinforced concrete buildings commonly found in high-density urban areas (Figure 1a). More specifically, in this work, the buildings are considered as periodic discrete, or reticulated, media. Periodic, because their story -or unit cell- repeats itself all along the building height  $H$  and discrete, because the story is constituted by the assembly of  $N_f$  frames made by the arrangement of vertical and horizontal elements as presented in Figure 1b.



(A) Example of periodic buildings



(B) 2D structure of a periodic building

FIGURE 1: Building-type structures studied in this work

In earthquake engineering, the seismic vulnerability assessment of infrastructures involves data analysis, numerical modeling, dynamic characterization and damage detection. This work focuses on the last three: numerical modeling, dynamic characterization and estimation of damage. Firstly, numerical modeling becomes absolutely necessary for the evaluation of the structural response. With the ongoing advances in technology and increase



of computational resources, fully detailed numerical models based on finite element methods have been used to simulate the structure mechanical functioning. However, special interest has always been devoted to developing simplified modeling techniques to perform quick but realistic analysis in both linear and nonlinear frameworks. Various strategies have been proposed for the construction of global simple models for buildings. Buildings have been idealized, as common use, as one dimensional (1D) lumped-mass systems (e.g., [Michel and Gueguen, 2006]) or more recently as coupled shear-flexural continuous models (e.g., [Cruz and Miranda, 2017b], [Cruz and Miranda, 2017a]). On the one hand, a lumped-mass system consists of a discretized model where each story is represented by its mass lumped at the floor level. These masses are connected by massless rods characterized by the story stiffness. In this idealization, the floor system is assumed rigid in bending, and relevant effects such as the deformation of the structural elements are neglected. This model is widely used in earthquake engineering to describe the seismic response of "shear" buildings. In this type of model, the assumption of infinitely rigid floors does not permit any joint rotation, and no axial deformation in the columns takes place. Such a situation is not valid for "slender" buildings whose axial deformation is not negligible. On the other hand, a couple shear wall model consists in connecting an Euler-Bernoulli beam to a shear beam with high axial stiffness elements (with rigid links)[Meza Fajardo and Papageorgiou, 2019]. This model has been used recently to estimate floor accelerations and interstory drift ratio demands [Cruz and Miranda, 2017b, Cruz and Miranda, 2017a]. Much more refined techniques, such as homogenization, can represent buildings as enriched continuous models (e.g., [Boutin et al., 2005, Chesnais et al., 2011a]). In the homogenization of buildings, the structure is usually considered as periodic reticulated. The main advantage of homogenization is that there is no assumption about the nature of the equivalent beam model. The only assumption is the scale separation. Moreover, the formulation is completely analytical, and it is always possible to find the forces on the elements. We can easily identify the key parameters that govern the dynamics of the building from the static analysis of a single story reducing significantly the computational cost.

Secondly, dynamic characterization is an essential step for the system identification. Modal identification techniques provide the structure eigenfrequencies and mode shapes. Time history analysis can provide other dynamic parameters such as the shear base forces, displacements or accelerations due to seismic excitation. The last two are particularly useful for determining the damage level of a structure based on global indicators such as the top roof displacement and inter-story drift.

In this context, this Ph.D. project challenges three main topics as presented in Figure 2: construction of continuous models for building-type structures, simplified and robust modeling techniques in structural dynamics, and the definition of damage indicators for the seismic vulnerability assessment of buildings. Our interest lies in developing a 1D model capable of capturing the seismic force effects for the structural elements at the local scale and the structure response at the global scale. Configurations where this 1-D model can be useful include the study of the seismic vulnerability of existing structures and the design of new ones. The

construction of this 1-D model relies on advanced modeling techniques used at different scales: homogenization and multifiber finite element formulations.

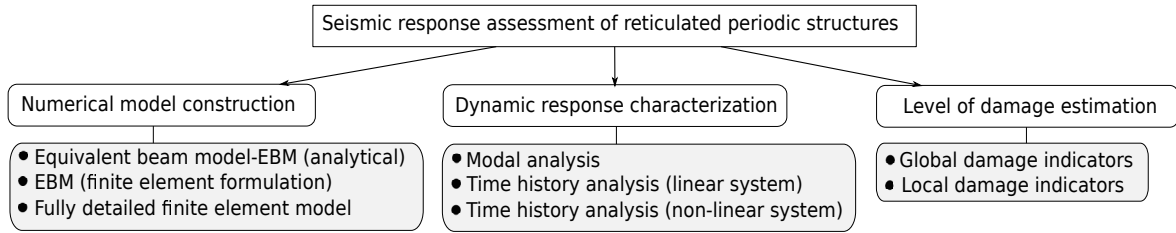


FIGURE 2: Main topics investigated in this work for the modeling of the seismic response of buildings

## Motivations and goals

The initial motivation of this work is earthquake engineering. On the one hand, different structural characteristics should be defined to achieve the desired performance level in the early stages of the seismic design. However, in the urgency of initial stage decisions, engineers commonly opt for complex 3D models that could be impractical. On the other hand, most of the existing buildings do not fulfill the requirements of current seismic design codes. Therefore, their performance evaluation and diagnosis are primary steps to reduce their seismic vulnerability. However, full finite models aiming at a realistic representation can quickly make the objective difficult. For this reason, a simplified model that can evaluate with acceptable accuracy the expected seismic response of these configurations is necessary. Homogenized equivalent beam models have shown outstanding results for the dynamic characterization of single and double frame structures. However, many questions need still to be answered:

Can we extend the implementation of the equivalent beams to model complex multi-frame structures? If so, how to go back to the local scale and determine the forces on the elements? How to improve the implementation of the EBM in numerical simulations? Is it possible to obtain good results out of the harmonic regime? How can we model the non-linear response using the EBM? This thesis searches to answer these questions and, for that, proposes to utilize simplified and robust numerical modeling strategies based on a double scaling between structure scale(global analysis), story scale (intermediate analysis), and element scale (local analysis).

Herein, we also want to demonstrate that the classification of the building behavior in terms of the typology ("slender" or tall buildings versus short or low rise buildings) widely adopted in current seismic codes is not entirely appropriate, and a classification depending on the behavior governing mechanism or mechanisms could be adopted.

## **Adopted methodology**

Three modeling techniques are used simultaneously to describe the system response: homogenized beam models, enriched finite element models, and multi-fiber beam elements. The generalized beam model, derived from a homogenization technique, is a 1-D model used to estimate the global response of the building (e.g., natural frequencies and mode shapes). This model is implemented in the enriched finite element formulation. The multi-fiber beam elements are used to compute the story properties required to feed the generalized beam model. They can capture non-linear effects at the material scale. Figure 3 presents the analyzed scales in this work : global scale (or structure scale), intermediate scale (or story scale), and local scale (material or element scale).

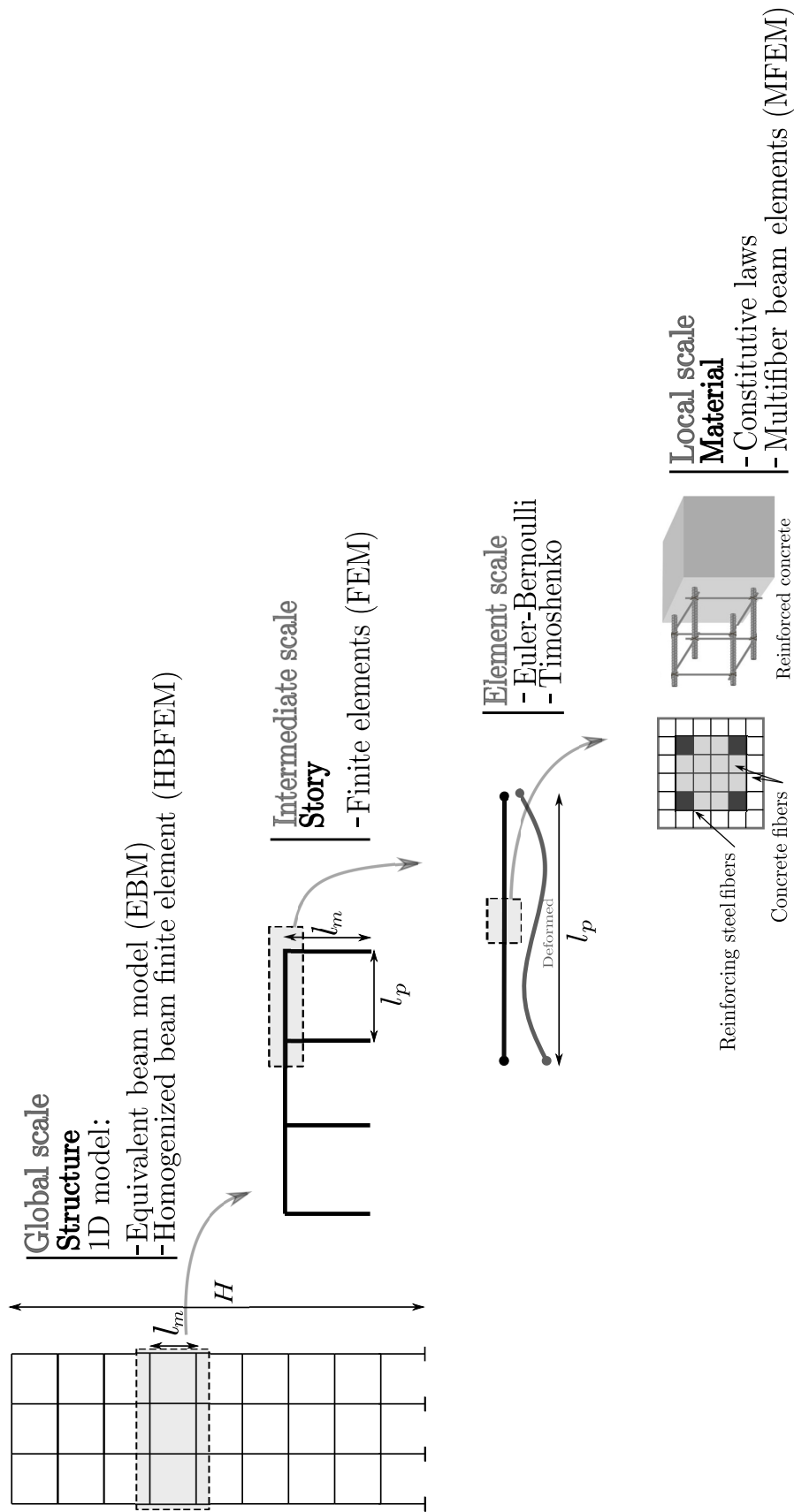


FIGURE 3: The different scales considered in the present work

## Thesis outline

This thesis consists of four parts.

### **Construction of the Equivalent Beam Model (EBM)**

After the definition of the problem and the objective of this work in Chapter 1 focuses on the dynamic description of reticulated structures at the global scale through the equivalent beam models issued from the Homogenization method of Periodic Discrete Media (HPDM). First, a summary of previous works on single and double frame structures is presented, and the contribution of this thesis is introduced. Next, we deal with the linear elastic behavior within the harmonic regime of several multiple frame structures. Finally, the strategy used to treat more complex structures is detailed.

### **Finite element formulation of the EBM**

A new enriched finite element formulation is proposed in Chapter 2 to facilitate the numerical implementation of the equivalent beam model. First, the weak form of the EBM is derived. Then, the construction of approximation functions for the solution fields is discussed. Finally, new elementary stiffness and mass matrices are given. The eigenmodes and the transient response of the enriched model are then assessed.

### **Application to real structures**

Chapter 3 presents the implementation of the generalized beam model on realistic structures and the use of the HBFEM model on actual structures. Even if we work within the linear elastic framework, the analyses are not limited to free vibrations, and time history analyses are also realized.

### **Return to Intermediate scale**

After focusing on the global dynamic description of structures, the local description is considered. Chapter 4 investigates how the forces on the elements can be recovered. Finally, a modeling strategy is proposed. The challenge here lies in the definition of the most appropriate boundary conditions to apply on a unit cell.

### **Towards a new damage indicator**

Now, within the framework of non-elasticity, the multifiber beam element method is required. The construction of the story model is then realized with beams discretized with multifiber beam elements. The constitutive laws selected for the concrete and steel rebars are based on existing models appropriate for cycling loads. Finally, the modeling strategy using the HBFEM model in the non-linear range is presented. A strategy for the construction of a novel damage indicator is also proposed.

## Chapter 1

# Homogenized beam models for the dynamic analysis of buildings

### 1.1 Abstract

This chapter aims to present a dynamic characterization of periodic and reticulated structures (periodic assemblies of beams and plates such as common reinforced concrete buildings made of identical stories) by means of homogenized beam models. Two different scales are involved in this analysis: global and intermediate scales. The “global scale” corresponds to the scale of the structure and the “intermediate scale” corresponds to the scale of a story. The proposed approach consists in describing the global behavior of the structure with an Equivalent Beam Model (*EBM*) according to the following process: (i) static analysis of only one story for the determination of the mechanical properties of the global model, (ii) dynamic analysis of the EBM, which is a 1D analytical model.

The analytical formulation of the EBM, focus of this work, was rigorously developed in previous studies considering idealized buildings made of the repetition of a single frame. This formulation is a generalized form of the classical Euler-Bernoulli and Timoshenko descriptions adding a new mechanism: the inner bending of vertical elements. This chapter begins with a summary of the previous studies on frame structures and their main conclusions. Then, we investigate how these results can be extended to more complex structures through the analysis of various multiple frame structures. All the analytical results derived from the EBM are verified using numerical simulations with full finite element models.

### 1.2 Continuous models for reticulated structures

For a wide range of applications, simplified models for the assessment of structural dynamics of periodic media can be as relevant as many sophisticated models while reducing computational costs. In the last decades, the search for global scale modeling of heterogeneous materials and structural systems such as reticulated structures (i.e, arrangement of beam or plate elements) has been of concern in many fields of engineering: aeronautics [Bennet et al., 1986, Abrate and Sun, 1983], bio-mechanics [Aoubiza et al., 1996], aerospace [Heki, 1968, Heki, 1972, Noor and Mikulas, 1988], structural and earthquake engineering [Hans et al., 2000,

Boutin et al., 2005, Chesnais et al., 2011a]. Most modeling approaches take advantage of the periodicity, the repetition of an elementary cell, which is the main morphological feature of these structures. In order to obtain an equivalent homogeneous model that represents the mechanical behavior, various approaches have been widely used: generalized continuum approaches [Noor and Mikulas, 1988], variational approaches [Kerr and Accorsi, 1985], finite difference operator [Noor, 1988], energy balance [McCallen and Romstad, 1988] and homogenization techniques. The latter technique is now well-founded and differs from the others because it does not state *a priori* hypotheses about the nature of the equivalent medium. Conversely, the nature of the medium is an inherent result of the method implementation [Chesnais, 2010]. It represents a crucial advantage because it ensures a deep understanding of the structural system functioning and the related continuum theory.

Homogenization methods have been implemented, for instance, in the description of massive periodic media [Bensoussan et al., 1978, Sanchez-Palencia, 1983, Allaire et al., 2016], perforated media [Cioranescu and Paulin, 1999] and then extended to periodic discrete media [Caillerie et al., 1989, Tollenaere and Caillerie, 1998, Moreau and Caillerie, 1998, Yi et al., 2015]. An extension of homogenization to higher frequencies can be found in the work of [Boutin et al., 2014, Rallu et al., 2018] about wave propagation in different periodic systems. The scale separation concept of homogenization is used by considering the amplitude of periodic eigenmodes instead of the amplitude of the mean displacement of a unit cell to analyze the structure behavior beyond the diffraction frequency (when the wavelength becomes of the same order as the unit cell size and the classical homogenization is not possible). Under this approach, high-frequency modes can still be homogenized and [Rallu et al., 2018] derives analytical expressions of the wave dispersion curves. Common conclusions of these studies recognize that reticulated structures are characterized by enriched kinematics that cannot be completely described by conventional continuum mechanics approaches.

According to Germain terminology [Germain, 1973], reticulated structures have been modeled as second gradient (of the displacement) models [Abdoul-Anziz and Seppecher, 2018] or Cosserat media [Pradel and Sab, 1998, Forest et al., 2001]. On one side, a Cosserat medium is a continuum with rigid particles with independent rotational and translational degrees of freedom (e.g., granular structures such as superplastic and acoustic materials). In a complete Cosserat medium, the strain energy depends on the particle relative displacement and rotation. For example, the Timoshenko beam theory can be considered as a 1D Cosserat medium formulation [Battista et al., 2018]. On the other side, in a second gradient material, the particles are assumed to be deformable. In this case, an additional term depending on the second gradient of displacement appears in the strain energy. Boutin et al. in [Boutin et al., 2010] state that four behaviors may arise in frame structures according to the stiffness contrast between the cell elements and the number of cells: Cauchy continuum behavior when the macroscopic kinematics is only governed by the cell translation, micromorphic medium behavior when the cell translation and inner deformation have to be taken into account, Cosserat like behavior when the cells experience translation and rotation and complex

micromorphic medium behavior when the three effects (translation, rotation, and inner deformation of the cells) have to be included. Dos Reis et al [Dos Reis and Ganghoffer, 2012] develop a discrete asymptotic homogenization technique of lattices assuming a medium of Cosserat type. Abdoul-Anziz et al. [Abdoul-Anziz and Seppecher, 2018] analyze 1D, 2D, and 3D structures with various cell geometry. They recover classical models (e.g., Euler-Bernoulli and Timoshenko for beams, Cosserat for membranes, or Kirchhoff-Love and Mindlin-Reissner for plates). In other terms, depending on the properties of the structural elements and the considered scale, Cauchy, Cosserat [Pradel and Sab, 1998] or second gradient models [Abdoul-Anziz and Seppecher, 2018, Boutin et al., 2017] can be relevant to describe the mechanical behavior of reticulated structures.

This work finds special interest in the results on reticulated structure dynamics provided by the implementation of the Homogenization method of Periodic Discrete Media (HPDM) and the models presented in [Boutin and Hans, 2003, Hans and Boutin, 2008, Chesnais, 2010] form the basis of this study. The HPDM is an analytical technique developed by Caillerie in [Caillerie et al., 1989]. As for all homogenization methods, its main assumption is scale separation. This means that the size of the unit cell of the periodic structure must be much smaller than the characteristic size of the deformation of the structure. The unit cell usually defines the local or microscopic scale while the deformation of the structure defines the global or macroscopic scale. But, because of the double change of scale in this thesis, *the unit cell size corresponds to the intermediate scale* and the local scale refers to the material scale. The HPDM has been applied systematically to investigate the harmonic vibration of structures periodic in one direction whose unit cell is a single frame [Hans and Boutin, 2008] or a double frame [Chesnais, 2010]. These studies reveal that the stiffness contrast between bending and tension-compression in the beams constituting the frames leads to enriched local kinematics, and the choice of different beam thicknesses gives rise to various types of macroscopic behaviors. The transverse dynamics is then described by an enriched beam model, called hereafter Equivalent Beam Model (EBM), which is a 1D continuous model that integrates the local kinematics in the periodic unit cell and can recover all the identified behaviors. The EBM describes the behavior of the structure at the global scale. For example, the EBM can be used to determine the structure natural frequencies and the associated mode shapes. Besides, a method has been proposed to estimate the internal forces and the deformations in the structural elements once the global deformation of the structure is known. The equation of motion of the EBM is a sixth-order differential equation that corresponds to a generalized form of the fourth-order Timoshenko beam equation. The difference in the ordinary differential equation order is attributed to a new internal mechanism that may appear under large stiffness contrasts between the cell components. One limitation of the EBM is that the analytical expressions of its parameters become very large and complex when the number of unit cell elements increases. Thus, a numerical extension to study more complex structures has been proposed in [Chesnais, 2010] still within the framework of free vibration analyses, and the development has been widened during this thesis [Franco et al., 2019].

In this chapter, we present the continuous models issued from the implementation of



the homogenization method of periodic discrete media (HPDM). The transverse dynamic characterization of multiframe structures is performed through a multiple scale analysis to estimate fundamental vibration frequencies and mode shapes (free vibration analysis). Our main objectives are listed below for the various scales.

At the global scale:

- Introduce the beam models at the basis of this work
- Present a strategy to analyze multiple frame structures
- Verify the proposed strategy by comparing the results with those of fully detailed numerical models
- Understand the mechanical functioning of regular buildings by the study of reticulated multiframe structures

At the intermediate scale:

- Solve the kinematics of the multiframe structures by performing the static analysis of a single unit cell
- Estimate the parameters that governs the structural behavior

### 1.3 Homogenization method of Periodic Discrete Media (HPDM)

The HPDM implementation on reticulated structures consists of two main steps: discretization and homogenization. In the first step, the structure is considered as a periodic lattice of interconnected beams. The local dynamic equilibrium equations of the beams are integrated over their length to derive the forces and moments at their extremities (nodes) rigorously. Thus, the equilibrium of the entire structure is equivalent to the equilibrium of the set of nodes and the discrete kinematic variables are the unknown motions of the nodes. The second step is the homogenization process based on the existence of a small parameter called the scale ratio  $\varepsilon = l_m/L$ . This parameter relates the size of the unit cell  $l_m$  to the characteristic macroscopic length  $L$  which depends on the vibration wavelength  $\lambda$ :  $L = \lambda/2\pi$ . Thus, the homogenization of the physics is possible when the cell size is very small compared to  $\lambda$ . This condition of scale separation implies that the HPDM is limited to the first modes of each vibration type. Hereafter, the unknown kinematic variables are searched as continuous functions of the space variable(s) in the direction(s) of periodicity and as asymptotic expansions in powers of the scale ratio  $\varepsilon$ . Each physical parameter is also scaled in terms of the powers of the scale ratio through a normalization process. As a result, the same physics is kept in the homogenized model, which corresponds to the limit behavior obtained when  $\varepsilon$  tends to 0.

## 1.4 Main results on single frame structures

### 1.4.1 Framework of previous studies

[Boutin and Hans, 2003, Hans and Boutin, 2008] applied the HPDM on building-type structures (interconnected walls and floors) as shown in Figure 1.1. These idealized single frame structures have a total height  $H = N l_m$ , where  $N$  is the number of unit cell,  $l_m$  the height of the cells and  $l_p$  their width. The homogenization is performed in the framework of linear elasticity and small deformations. The interconnected elements are considered as Euler-Bernoulli beams with massless and rigid connections. A systematic study is conducted to assess the evolution of the overall structural behavior with respect to the stiffness contrast between the walls and floors. This contrast is introduced by varying the element thicknesses  $a_m$  and  $a_p$ . Besides, a change of variables is performed to uncouple the longitudinal and transverse kinematics and distinguish between the rigid body motion of the unit cell and its internal deformation.

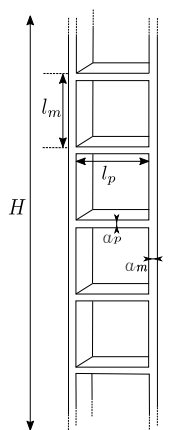


FIGURE 1.1: Idealized single frame structures studied in [Boutin and Hans, 2003, Hans and Boutin, 2008]

### 1.4.2 Governing mechanisms and associated kinematic variables

The previous studies on single frame structures reveal that three mechanisms govern the structural behavior in the transverse direction: shear of the cells (stiffness  $K_s$ ), inner bending (stiffness  $\mathcal{K}_i$ ), and global bending (stiffness  $\mathcal{K}_g$ ) (Figure 1.2). The cell shear deformation is generated by the local bending (i.e. between neighboring nodes) of the vertical and/or horizontal elements. For the inner bending mechanism, the vertical elements behave as cantilever bending beams at the structure scale and are synchronized by the horizontal ones. These horizontal elements have a large axial stiffness and bend locally. The global bending mechanism occurs because of the out-of-phase tension-compression of the vertical elements.

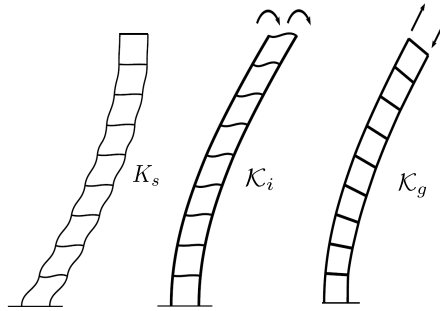


FIGURE 1.2: Mechanisms that govern the transverse behavior of the single frame structures: shear of the cells (stiffness  $K_s$ ), inner bending (stiffness  $K_i$ ) and global bending (stiffness  $K_g$ ). In this schematic, fixed-free ends are considered as boundary conditions.[Chesnais, 2010]

The relative importance of the mechanisms depends on the stiffness contrast between the vertical and horizontal elements, and various macroscopic behaviors described by different beam models can be generated. For example, inner bending can only appear if the horizontal elements are much more flexible than the vertical ones. Specific beam-like models such as the classical Euler-Bernoulli and Timoshenko beams can be retrieved. More original models with inner bending can also be derived. The latter corresponds well to the sandwich beam model used to represent stratified plates [Boutin and Viverge, 2016, Viverge et al., 2016]. These three mechanisms are included in the generalized beam model called generic in [Boutin and Hans, 2003, Hans and Boutin, 2008, Chesnais, 2010] and called hereafter Equivalent Beam Model (EBM). The association of the three mechanisms included in the EBM is represented by the schematic in Figure 1.3. The shear stiffness  $K_s$  works in series with the global bending stiffness  $K_g$ , and the inner bending stiffness  $K_i$  is connected in parallel. The homogenization method provides the analytical expressions of the three stiffnesses, which only depend on the elasto-static properties of the unit cell.

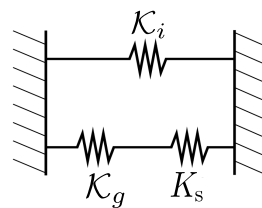


FIGURE 1.3: Schematic representation of the mechanisms included in the EBM [Chesnais, 2010].

The transverse motion of single frame structures is parametrized by three kinematic variables: the mean transverse displacement,  $u$ , the cell rotation,  $\alpha$ , and the mean nodal rotation,  $\theta$ . The first two, representing the unit cell rigid body motion, appear explicitly in the global dynamic description of the structure (global scale). Conversely,  $\theta$ , associated with the unit cell deformation (intermediate scale), is a hidden variable obtained from the rigid body motion thanks to the internal equilibrium of the unit cell. Figure 1.4 illustrates a deformed reticulated system made of interconnected beam elements. The macroscale deformation of the structure

at level  $n$  is given by the horizontal displacement  $u_n$ , and the rotation  $\alpha_n$ . The bending of each beam element, implicitly linked to  $\theta$ , corresponds to the deformation at the intermediate scale.

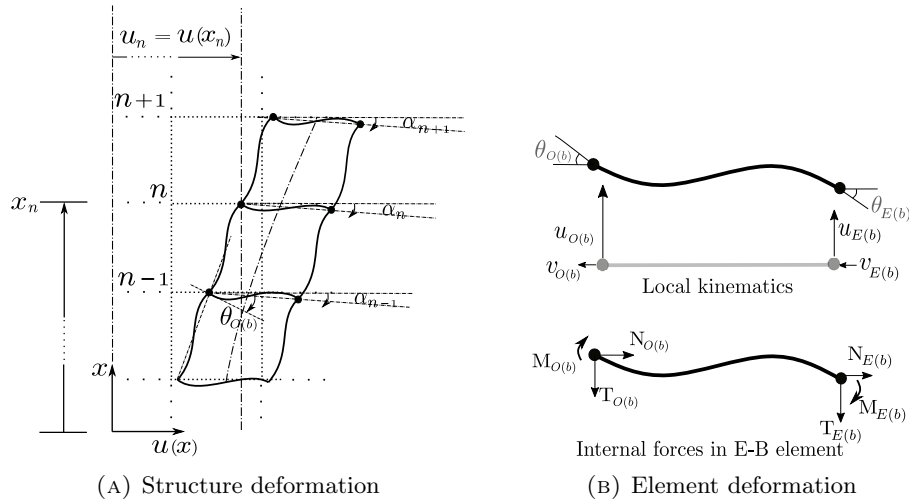


FIGURE 1.4: Global (left) and intermediate (right) kinematics of the physical problem

Table 1.1 presents, for each mechanism or combination of mechanisms, the associated kinematic variables and an example of a structure described by the orders ( $O(\varepsilon^k)$ ) of the element thicknesses.

Mechanism	Kinematic variables	Example of structure
Shear	$u$	$\frac{a_m}{l_m}, \frac{a_p}{l_m} = O(\varepsilon^2)$
Shear and global bending	$u, \alpha$	$\frac{a_m}{l_m}, \frac{a_p}{l_m} = O(\varepsilon)$
Inner bending	$u, u'$	$\frac{a_m}{l_m} = O(\varepsilon), \frac{a_p}{l_m} = O(\varepsilon^2)$

TABLE 1.1: Kinematic variables associated with each mechanism

### 1.4.3 Equivalent Beam Model: construction and equation of motion

The equations of the Equivalent Beam Model are written using the Cartesian coordinate system presented in Figure 1.5. *By convention, the displacements are positive if they have the same direction as the frame vectors and the forces are positive if they have the opposite direction.* The internal loads are exerted by the left-hand side on the right-hand side of the sections.

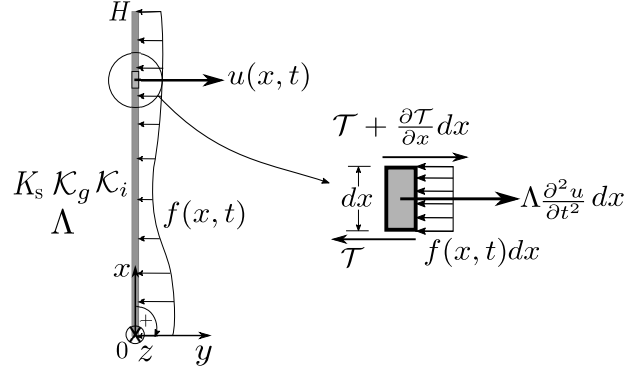


FIGURE 1.5: Notation and sign convention for the Equivalent Beam Model.

The three mechanisms governing the elastic response in transverse vibrations of the EBM are associated with three force and moments defined by the constitutive laws given in Equation (2.1). *Constitutive laws:*

$$\begin{aligned}
 \text{Shear Force} \quad T(x, t) &= K_s \left( \frac{\partial u(x, t)}{\partial x} - \alpha(x, t) \right) \\
 \text{Inner bending moment} \quad \mathcal{M}(x, t) &= K_i \frac{\partial^2 u(x, t)}{\partial x^2} \\
 \text{Global bending moment} \quad M(x, t) &= K_g \frac{\partial \alpha(x, t)}{\partial x}
 \end{aligned} \tag{1.1}$$

where  $u(x, t)$  and  $\alpha(x, t)$  are the transverse displacement and the cell rotation, respectively.  $T(x, t)$  is the shear force generated by the shear of the cells (local bending of the elements),  $\mathcal{M}(x, t)$  is the inner bending moment (generated by the bending of the vertical elements at the global scale) and  $M(x, t)$  is the global bending moment (generated by the out-of-phase tension-compression of the vertical elements). The parameters  $K_s$ ,  $K_i$  and  $K_g$  are the shear stiffness of the cell, the inner bending stiffness and the global bending stiffness respectively<sup>1</sup>. These parameters and the linear mass  $\Lambda$  of the EBM are also called the macroscopic parameters and can be determined from the static properties of the unit cell.

The macroscopic parameters of a single frame structure, whose unit cell is made of two vertical elements and one horizontal element of densities  $\rho_m$  and  $\rho_p$ , Young modulus  $E_m$  and  $E_p$ , lengths  $l_m$  and  $l_p$ , transverse area  $A_m$  and  $A_p$ , and second area moment  $I_m$  and  $I_p$  respectively, are defined as:

$$\begin{aligned}
 K_s &= \frac{k_p 2 k_m}{k_p + 2 k_m}, \quad k_m = 12 \frac{E_m I_m}{l_m l_m}, \quad k_p = 12 \frac{E_p I_p}{l_m l_p} \\
 K_i &= 2 E_m I_m, \quad K_g = E_m A_m \frac{l_p^2}{2}, \quad \Lambda = 2 A_m \rho_m + \frac{A_p l_p \rho_p}{l_m}
 \end{aligned} \tag{1.2}$$

<sup>1</sup>Take stiffness in the large sense: resistance of an elastic body to deformation in response to an applied force. The shear stiffness is given in units of [force] (e.g., Newtons, pounds). The dimension of the global and inner bending stiffnesses is [force][length]<sup>2</sup> (e.g., Newton-meter<sup>2</sup>, pounds-feet<sup>2</sup>)

where  $k_p$  and  $k_m$  correspond to the static bending stiffness of the horizontal and vertical elements respectively. The inner bending stiffness  $\mathcal{K}_i$  corresponds to the sum of the flexural stiffnesses of all the walls. The global bending stiffness  $\mathcal{K}_g$  is the sum of the traction-compression stiffnesses of the walls times the square of the distance from the axis of symmetry. The parameters  $\Lambda$ ,  $\mathcal{K}_i$  and  $\mathcal{K}_g$  are easily computed no matter the number of walls in the unit cell. However, the analytical formulation of the shear stiffness  $K_s$  becomes very complex as soon as new elements are added in the cell (e.g., walls, floors, braces). Consequently, a numerical procedure based on a finite element model of the unit cell has been proposed in [Chesnais, 2010] for the computation of the shear stiffness  $K_s$  associated with other geometries. It will be presented in Section 1.5.2 and validated through the analysis of various multiple frame structures.

The equilibrium at time  $t$  of an elementary part at location  $x$  of the EBM is described by Equations (2.2) on the domain  $\Omega = [0, H]$  and the time window  $[0, t_D]$ .

*Equilibrium equations:*

$$\forall x \in \Omega, \forall t \in [0, t_D], \left\{ \begin{array}{l} \mathcal{T}(x, t) = T(x, t) - \frac{\partial \mathcal{M}(x, t)}{\partial x} \\ \frac{\partial \mathcal{T}(x, t)}{\partial x} = \Lambda \frac{\partial^2 u(x, t)}{\partial t^2} + f(x, t) \\ \frac{\partial \mathcal{M}(x, t)}{\partial x} = -T(x, t) \end{array} \right. \quad (1.3)$$

where  $\mathcal{T}$  corresponds to the total shear force applied on the elementary part and  $f(x, t)$  is the linear density of the external transverse load.

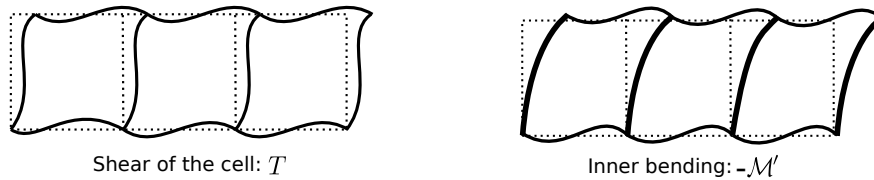


FIGURE 1.6: The two mechanisms contributing to the total shear force  $\mathcal{T} = T - \mathcal{M}'$ .  $T$  comes from the shear deformation of the cell generated by the local bending of all the elements (left) and  $-\mathcal{M}'$  comes from the shear deformation of the cell generated by the synchronized bending of the vertical elements (right).

Note that the EBM exhibits two differences compared with the classical Timoshenko beam model used to describe thick beams with a solid cross-section. First, the existence of an inner bending mechanism leads to the introduction of an additional inner bending moment  $\mathcal{M}(x, t)$  associated with a new constitutive law and a new term  $\frac{\partial \mathcal{M}(x, t)}{\partial x}$  in the force balance equation. The shear of the cells and the global bending are connected in series as in the Timoshenko beam model whereas the inner bending is connected in parallel to the two other mechanisms. Therefore, the total shear force  $\mathcal{T}$  results from two contributions: a shear force  $T$  caused by the shear deformation of the cells and a shear force  $-\mathcal{M}'$  caused by the inner bending of the

vertical elements (Figure 1.6). The second difference is that the rotational inertia does not appear in the moment balance equation. This is due to the fact that the stiffness of the shear of the cells is much smaller than in solid cross-section beams. Consequently, the shear effect and the rotational inertia effect do not appear in the same frequency range. The rotational inertia in frame structures is associated with non classical vibration modes at much higher frequencies. We can refer to [Chesnais, 2010, Chesnais et al., 2011b] to treat such cases. We recall that this study focuses on the description of the transverse dynamics of the first vibration modes which involves the analysis in the lowest frequency range.

*Virtual work formulation:* From the equilibrium equations (Equations (2.2)), we develop the weak formulation of the EBM using the virtual work principle. Let us define two virtual fields  $u^*$  and  $\alpha^*$  homogeneous respectively to a transverse displacement and a cell rotation. The second equation of equilibrium (Equation (2.2)) is multiplied by  $u^*$  and the third one by  $\alpha^*$ . They are summed and integrated over the domain  $\Omega$  to obtain<sup>2</sup>,

$$\int_{\Omega} \left\{ \left[ \frac{\partial \mathcal{T}}{\partial x} - \Lambda \frac{\partial^2 u}{\partial t^2} - f \right] u^* + \left[ \frac{\partial \mathcal{M}}{\partial x} + T \right] \alpha^* \right\} dx = 0 \quad (1.4)$$

Thanks to a first integration by parts and the use of the first equation of equilibrium (Equation (2.2)) to replace  $\mathcal{T}$ , one can get,

$$[\mathcal{T}u^* + M\alpha^*]_O^H + \int_{\Omega} \left\{ \left[ -T + \frac{\partial \mathcal{M}}{\partial x} \right] \frac{du^*}{dx} - M \frac{d\alpha^*}{dx} + \left[ -\Lambda \frac{\partial^2 u}{\partial t^2} - f \right] u^* + T\alpha^* \right\} dx = 0 \quad (1.5)$$

A second integration by parts is performed, and we finally obtain,

$$\begin{aligned} & \left[ \mathcal{T}u^* + M\alpha^* + \mathcal{M} \frac{du^*}{dx} \right]_O^H - \int_{\Omega} \left\{ T \left( \frac{du^*}{dx} - \alpha^* \right) + \mathcal{M} \frac{d^2 u^*}{dx^2} + M \frac{d\alpha^*}{dx} \right\} dx \\ & - \int_{\Omega} \left\{ \left[ \Lambda \frac{\partial^2 u}{\partial t^2} + f \right] u^* \right\} dx = 0 \end{aligned} \quad (1.6)$$

Equation (1.6) can be summarized,

$$\begin{aligned} \mathcal{W}_{acc}^* &= \mathcal{W}_{int}^* + \mathcal{W}_{ext}^* \\ \mathcal{W}_{acc}^* &= \int_{\Omega} \Lambda \frac{\partial^2 u}{\partial t^2} u^* dx \\ \mathcal{W}_{ext}^* &= - \int_{\Omega} f u^* dx \\ \mathcal{W}_{int}^* &= \left[ \mathcal{T}u^* + M\alpha^* + \mathcal{M} \frac{du^*}{dx} \right]_O^H - \int_{\Omega} \left\{ T \left( \frac{du^*}{dx} - \alpha^* \right) + \mathcal{M} \frac{d^2 u^*}{dx^2} + M \frac{d\alpha^*}{dx} \right\} dx \end{aligned} \quad (1.7)$$

$\mathcal{W}_{acc}^*$ ,  $\mathcal{W}_{ext}^*$  and  $\mathcal{W}_{int}^*$  are the virtual works associated with the inertia forces, the external forces and the internal forces, respectively. Through this virtual work formulation, the

<sup>2</sup>For the sake of conciseness, the dependency on  $x$  and  $t$  is omitted on purpose later on.

boundary conditions of the EBM can be identified correctly. The force boundary conditions (defined on  $\partial\Omega_F$ ) concern the total shear force  $\mathcal{T}$ , the global bending moment  $M$  and the inner bending moment  $\mathcal{M}$ . The displacement boundary conditions (defined on  $\partial\Omega_u$ ) concern the transverse displacement  $u$ , its first derivative  $\partial u/\partial x$  and the cell rotation  $\alpha$ . As usual, the domains associated with the two types of boundary conditions verify:  $\partial\Omega_u \cap \partial\Omega_F = \emptyset$  and  $\partial\Omega_u \cup \partial\Omega_F = \partial\Omega$  where  $\partial\Omega$  is the boundary of the domain  $\Omega$ . It is important to note that the boundary conditions depend on the total shear force  $\mathcal{T}$  whereas the virtual work  $\mathcal{W}_{int}^*$  depends, in the bulk, on the shear force  $T$  generated only by the shear of the cell.

The weak form of the EBM will be recalled later in Chapter 2.

#### *The EBM Equation of motion*

We now consider the harmonic vibration of the EBM at the circular frequency  $\omega$ . In this case, each variable  $V$  can be written in the following form:  $V(x, t) = \hat{V}(x) \cos(\omega t)$ . The space and time dependencies are uncoupled and  $\cos(\omega t)$  is simplified afterwards. For a structure of height  $H$ , stiffnesses  $K_s$ ,  $\mathcal{K}_g$ ,  $\mathcal{K}_i$  and linear mass  $\Lambda$ , the transverse free vibration of the EBM is described by a sixth order differential equation (ODE) resulting of the combination of the equilibrium equations (2.2) (with no external force  $f(x, t) = 0$ ) and the constitutive laws (Equations (2.1)) [Hans and Boutin, 2008]:

$$\frac{\mathcal{K}_i \mathcal{K}_g}{K_s} \frac{d^6 \hat{u}(x)}{dx^6} - (\mathcal{K}_i + \mathcal{K}_g) \frac{d^4 \hat{u}(x)}{dx^4} - \frac{\mathcal{K}_g \Lambda \omega^2}{K_s} \frac{d^2 \hat{u}(x)}{dx^2} + \Lambda \omega^2 \hat{u}(x) = 0 \quad (1.8)$$

for  $0 < x < H$

For a structure clamped at the bottom and free at the top, the boundary conditions are  $\hat{u} = 0$ ,  $\frac{d\hat{u}}{dx} = 0$  and  $\hat{\alpha} = 0$  at  $x = 0$  and  $\hat{\mathcal{T}} = 0$ ,  $\hat{\mathcal{M}} = 0$  and  $\hat{M} = 0$  at  $x = H$ .

The modal properties (i.e. eigenfrequencies and mode shapes) can be determined analytically by looking for the non-zero solutions of this set of equations. The complete resolution is presented in the appendix of [Chesnais, 2010]. The general solution of Equation (1.8) can be written:

$$\hat{u}(x) = o \cos\left(b_1 \frac{x}{L}\right) + p \sin\left(b_1 \frac{x}{L}\right) + q \operatorname{ch}\left(b_2 \frac{x}{L}\right) + r \operatorname{sh}\left(b_2 \frac{x}{L}\right) + s \operatorname{ch}\left(b_3 \frac{x}{L}\right) + t \operatorname{sh}\left(b_3 \frac{x}{L}\right) \quad (1.9)$$

where  $o$ ,  $p$ ,  $q$ ,  $r$ ,  $s$ , and  $t$  are constants that depend on the boundary conditions.

#### 1.4.4 Specific homogenized beam models

As the EBM includes the three possible mechanisms in single frame structures, it can always be used to describe their behavior. But, when the effects of one or two mechanisms are negligible, the EBM can degenerate into simpler beam models (for example, the Euler-Bernoulli and Timoshenko beams). The governing mechanism(s) evolve as a function of the properties of the frame elements conditioned to the scale ratio. Hence, a specific stiffness contrast between the vertical and horizontal elements can lead to a simplified version of the generalized equation of motion (Equation 1.8).



In previous studies and this work, the variation of the element stiffnesses is done by increasing or decreasing their thickness. In a systematic study [Hans and Boutin, 2008], the HPDM was implemented on single frame structures with different element thicknesses. This generated classical and non-classical beam models associated with different controlling mechanisms. In this section, we illustrate how the EBM can degenerate into simpler beam models. We start by introducing the identification criterion proposed by [Hans and Boutin, 2008]. This criterion provides an *a priori* knowledge of the structure behavior and, as a consequence, the related specific beam model can be determined from the static analysis of a single unit cell without re-implementing the homogenization method.

### Identification criterion

As the implementation of the HPDM on each specific structure can be tedious, Boutin and Hans [Hans and Boutin, 2008] proposed an identification criterion that provides the predominant mechanism(s) of a given structure. The criterion is derived from a dimensional analysis performed on the Equivalent Beam Model formulation given in Equation (1.8). The latter is written in terms of the displacement function  $\bar{u}$  resulting of the variable change  $\bar{x} = \frac{x}{L}$  (Equation (2.39)).

$$C\gamma \frac{d^6 \bar{u}(\bar{x})}{d\bar{x}^6} - (1 + \gamma) \frac{d^4 \bar{u}(\bar{x})}{d\bar{x}^4} - \Omega^2 \frac{d^2 \bar{u}(\bar{x})}{d\bar{x}^2} + \frac{\Omega^2}{C} \bar{u}(\bar{x}) = 0 \quad \text{for } 0 < \bar{x} < H/L \quad (1.10)$$

The contrast between the global bending and shear stiffnesses,  $C = \frac{\mathcal{K}_g}{\mathcal{K}_s L^2} = \varepsilon^{\mathbf{x}}$  and the contrast between the inner bending and global bending stiffnesses  $\gamma = \frac{\mathcal{K}_i}{\mathcal{K}_g} = \varepsilon^{\mathbf{y}}$ , represented by their order of magnitude  $\mathbf{x}$  and  $\mathbf{y}$  with respect to the scale ratio  $\varepsilon$  constitute the base of the identification criterion. The parameters  $C$  and  $\gamma$  are called macroscopic constants. The constant  $\Omega^2 = \frac{\Lambda \omega^2 L^2}{\mathcal{K}_s}$ , which compares the translation inertia and the shear stiffness, does not participate in the criterion.

According to the relative importance of the mechanisms, the orders of magnitude  $\mathbf{x}$  and  $\mathbf{y}$  vary and the equation of motion (2.39) can degenerate into simpler models. This information is summarized in the graph of Figure 1.7 depending on  $\mathbf{x}$  and  $\mathbf{y}$ . This is a quick tool, which avoids the implementation of the HPDM to identify the specific beam model that describes the structure behavior correctly with the least calculations. Moreover, this criterion enables to analyze structures too complex to be modelled analytically with the HPDM.

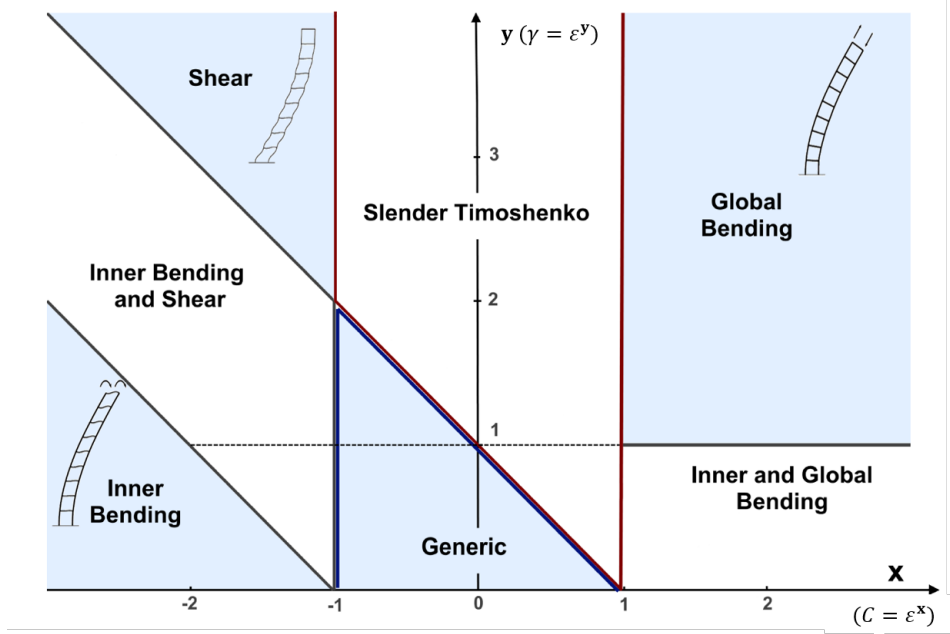


FIGURE 1.7: Map of the transverse macroscopic behaviors as a function of  $C$  and  $\gamma$ . [Hans and Boutin, 2008]

### Shear beam model

The EBM degenerates into a shear beam model (Equation (1.11)) when the shear of the cell is more flexible than the global bending but stiffer than the inner bending, which corresponds to  $C > O(\varepsilon^{-1})$  and  $C\gamma < O(\varepsilon)$ . This occurs, for example, when the structural elements are very thin:  $a_m/l_m = O(\varepsilon^2)$  and  $a_p/l_m = O(\varepsilon^2)$ .

$$\frac{d^2\hat{u}(x)}{dx^2} + \frac{\Lambda\omega^2}{K_s}\hat{u} = 0 \quad \text{for } 0 < x < H \quad (1.11)$$

### Euler-Bernoulli or global bending beam model

When the thickness of the elements is increased, for example  $a_m/l_m = O(\varepsilon^{1/2})$  and  $a_p/l_m = O(\varepsilon^{1/2})$ , the shear of the cell  $K_s$  becomes much stiffer than the global bending  $K_g$ . So the macroscopic constants  $C < O(\varepsilon)$  and  $\gamma < O(\varepsilon)$  are negligible in Equation (2.39) and the EBM turns into the global bending beam model with the following equation of motion:

$$K_g \frac{d^4\hat{u}(x)}{dx^4} - \Lambda\omega^2\hat{u} = 0 \quad \text{for } 0 < x < H \quad (1.12)$$

This equation has the form of the motion equation of the usual Euler-Bernoulli beam used to describe the bending of "massive" beams characterized by an out-of-phase traction compression of each side. In a single frame structure, the bending of the structure is led by this out-of-phase traction compression in the vertical elements.

### Slender Timoshenko beam model

The slender Timoshenko beam model is encountered from the analysis of structures where the shear stiffness of the cell  $K_s$  is of the same order as the global bending stiffness  $\mathcal{K}_g$ . For example, structures with equally thick elements with the following slenderness:  $a_m/l_m = a_p/l_m = O(\varepsilon)$ , lead to this model. Accordingly, considering the macroscopic constants  $C = O(1)$  and  $\gamma \leq O(\varepsilon)$  causes that the terms associated with  $C\gamma$  and  $\gamma$  disappear in Equation (2.39) and the equation of motion becomes:

$$\mathcal{K}_g \left( \frac{d^4 \hat{u}(x)}{dx^4} + \frac{\Lambda \omega^2}{K_s} \frac{d^2 \hat{u}(x)}{dx^2} \right) - \Lambda \omega^2 \hat{u} = 0 \quad \text{for } 0 < x < H$$

This model includes the shear of the cell  $K_s$  and the global bending of the vertical elements  $\mathcal{K}_g$ . The difference with the classical Timoshenko beam model of massive beams is that the shear effect comes from the bending of the elements at the cell scale and not from the internal shear of the elements (given by  $GA_s$  where  $G$  is the shear modulus and  $A_s$  the reduced cross-section area). Moreover, only the translation inertia  $\Lambda \omega^2$  appears at the leading order, whereas the rotational inertia linked to the macroscopic rotation  $\alpha$  is negligible. That means that the transverse and rotational dynamics are uncoupled and occur within different frequency ranges [Chesnais et al., 2011a]. The participation of the rotational inertia occurs at higher frequencies and is associated with gyration modes, investigated in [Chesnais et al., 2011b].

### Inner bending and shear beam model

Consider that the shear stiffness  $K_s$  is smaller than the global bending stiffness  $\mathcal{K}_g$  and of the same order as the inner bending stiffness  $\mathcal{K}_i$ , which is consistent with the condition  $\mathcal{K}_i \ll \mathcal{K}_g$  in single frame structures. Thus,  $C > O(\varepsilon^{-1})$ ,  $\gamma \leq O(\varepsilon)$ , and  $C\gamma = O(1)$ . The EBM equation of motion degenerates into the form:

$$\mathcal{K}_i \frac{d^4 \hat{u}(x)}{dx^4} - K_s \frac{d^2 \hat{u}(x)}{dx^2} - \Lambda \omega^2 \hat{u} = 0 \quad \text{for } 0 < x < H \quad (1.13)$$

Structures described by this model have vertical elements thicker than the horizontal elements, for example:  $a_m/l_m = O(\varepsilon)$  and  $a_p/l_m = O(\varepsilon^{5/3})$ . The vertical elements bend at the structure scale similarly to cantilever beams and their motion is synchronized by the horizontal elements which have a high axial stiffness.

In Table 1.2, we provide the motion equations of the described specific models together with their analytical solution according to [Boutin and Hans, 2003].

Model	Macroscopic Kinematic Variables	Constitutive Laws Balance Equations	Equation of motion Boundary conditions	Analytical solution
Shear beam	$\hat{u}$	$T = K_s \hat{u}'$ $\mathcal{T}' = \mathcal{T}' = -\Lambda \omega^2 \hat{u}$	$\hat{u}'' + \frac{\Lambda \omega^2}{K_s} \hat{u} = 0$ at $x = 0, \hat{u} = 0$ at $x = H, \mathcal{T} = 0 \Rightarrow \hat{u}' = 0$	$\hat{u}(x) = o \cos(bx) + p \sin(bx)$ $o = 0$ $p \cos(bH) = 0$ $\hat{u}(x) = p \sin(bx), \omega_k^2 = \frac{K_s}{\Lambda} * \left( \frac{(2k-1)\pi}{2H} \right)^2$
Slender Timoshenko beam	$\hat{u}, \hat{\alpha}$	$T = K_s(\hat{u}' - \hat{\alpha})$ $M = K_g \hat{\alpha}'$ $M' = -T$ $\mathcal{T}' = -\Lambda \omega^2 \hat{u}$	$K_g \hat{u}^{(4)} + \frac{K_s \Lambda \omega^2}{K_s} \hat{u}'' - \Lambda \omega^2 \hat{u} = 0$ at $x = 0, \hat{u} = 0, \hat{\alpha} = 0$ at $x = H, M = 0 \Rightarrow \hat{\alpha}' = 0, \mathcal{T} = 0 \Rightarrow \hat{\alpha}'' = 0$	$\hat{u}(x) = o \cos(b_1 x) + p \sin(b_1 x) + t \cosh(b_2 x) + r \sinh(b_2 x)$ $\hat{\alpha}(x) = \left( 1 + \frac{\Lambda \omega^2}{K_g^2} K_g \right) \hat{u}' + \frac{K_g}{K_s} \hat{u}^{(3)}$
Inner bending and shear beam	$\hat{u}$	$T = K_s \hat{u}'$ $\mathcal{M} = K_i \hat{u}''$ $\mathcal{T} = T - \mathcal{M}'$ $\mathcal{T}' = -\Lambda \omega^2 \hat{u}$	$K_i \hat{u}^{(4)} - K_s \hat{u}'' - \Lambda \omega^2 \hat{u} = 0$ at $x = 0, \hat{u} = 0, \hat{u}' = 0$ at $x = H, \mathcal{M} = 0 \Rightarrow \hat{u}'' = 0, \mathcal{T} = 0 \Rightarrow \hat{\alpha}'' = 0$	$\hat{u}(x) = o \cos(b_1 x) + p \sin(b_1 x) + t \cosh(b_2 x) + w \sinh(b_2 x)$
Global bending beam	$\hat{\alpha} = \hat{u}'$	$M = K_g \hat{u}''$ $\mathcal{T}' = -\Lambda \omega^2 \hat{u}$ $M' = -T$	$K_g \hat{u}^{(4)} - \Lambda \omega^2 \hat{u} = 0$ at $x = 0, \hat{u} = 0, \hat{u}' = 0$ at $x = H, M = 0 \Rightarrow \hat{u}'' = 0, \mathcal{T} = 0 \Rightarrow \hat{u}^{(3)} = 0$	$\hat{u}(x) = o \cos(bx) + p \sin(bx) + q \cosh(bx) + r \sinh(bx)$ $\cos(bH) \cosh(bH) + 1 = 0$
Generic beam of [Hans and Bontin, 2008] called here EBM	$\hat{u}, \hat{\alpha}$	$T = K_s(\hat{u}' - \hat{\alpha})$ $M = K_g \hat{\alpha}'$ $\mathcal{M} = K_i \hat{u}''$ $(T - \mathcal{M}')' = -\Lambda \omega^2 \hat{u}$ $M' = -T$	$\frac{K_i K_g \hat{u}^{(6)}}{K_s} - (K_i + K_g) \hat{u}^{(4)} - K_g \frac{\Lambda \omega^2}{K_s} \hat{u}'' + \Lambda \omega^2 \hat{u} = 0$ at $x = 0, \hat{u} = 0, \hat{u}' = 0, \hat{\alpha} = 0$ at $x = H, \mathcal{M} = 0 \Rightarrow \hat{u}'' = 0, M = 0 \Rightarrow \hat{\alpha}' = 0, \mathcal{T} = 0 \Rightarrow K_s(\hat{u}' - \hat{\alpha}) - K_i \hat{u}^{(3)} = 0$	$\hat{u}(x) = o \cos(b_1 x) + p \sin(b_1 x) + q \cosh(b_2 x) + r \sinh(b_2 x) + s \cosh(b_3 x) + t \sinh(b_3 x)$ $\hat{\alpha}(x) = \left( 1 + \frac{\Lambda \omega^2}{K_g^2} K_g \right) \hat{u}' + \frac{K_i K_g \hat{u}^{(3)}}{K_s} - \frac{K_i K_g \hat{u}^{(5)}}{K_s}$

TABLE 1.2: Beam models issued from the HPDM implementation on single frame structures. The macroscopic kinematic variables of the transverse steady-state motion are the transverse displacement  $\hat{u}$  and the global rotation  $\hat{\alpha}$ . The boundary conditions are given for a beam of length  $H$  clamped at the base and free at the top.

### 1.4.5 Additional homogenized beam models

In [Chesnais, 2010], the study of a real 16-story reinforced concrete shear wall building (see the figure in Table 1.3) reveals that the shear stiffness of the very thick vertical elements (i.e.,  $GA_s$  where  $G$  is the shear modulus and  $A_s$  the reduced cross-section area) can emerge at the leading order and needs to be taken into account both at the element and structural scales. As the structural elements were modelled by Euler-Bernoulli beams during the HPDM implementation, the effects of the shear of the walls are neglected in the EBM. The comparison of the frequencies of the first three modes in the longitudinal direction obtained with the EBM of the building with those obtained with its full finite element model shows that the minimum difference is 11% (Table 1.3). Thus, to account for the inner shear of the walls, Chesnais proposes the integration of the shear effect as a new mechanism in the global description of the EBM. The results obtained with this upgraded EBM match much better the full finite element model results with errors of 2%, 5% and 9% for the first, second and third eigenfrequencies, respectively.



Mode	Full FEM	EBM		Upgraded EBM	
	$f_i$ (Hz)	$f_i$ (Hz)	error (%)	$f_i$ (Hz)	error (%)
1	2.08	2.31	11	2.13	2.2
2	7.26	9.53	31	7.63	5.1
3	14.30	23.33	63	15.61	9.2

TABLE 1.3: Case study in [Chesnais, 2010]. Comparison of the frequencies of the first three modes in the longitudinal direction.

The upgraded EBM includes in total four mechanisms: the three already known of the EBM (shear of the cell  $K_s$ , global bending  $K_g$  and inner bending  $K_i$ ) and the new mechanism given by the shear of the walls  $K_m$ . The latter is associated in series to the rest of the mechanisms and emerges at the structure scale when the thickness of the vertical elements is very important (See Figure 1.8).

The motion equation for the transverse vibration of the upgraded EBM including the shear of the vertical elements  $K_m$  is:

$$\begin{aligned}
 \mathcal{K}_i \mathcal{K}_g \left( \frac{1}{K_s} - \frac{1}{K_m} \right) \frac{d^6 \hat{u}(x)}{dx^6} - \left( \mathcal{K}_i + \mathcal{K}_g - \Lambda \omega^2 \frac{\mathcal{K}_i \mathcal{K}_g}{K_m} \left( \frac{1}{K_s} - \frac{1}{K_m} \right) \right) \frac{d^4 \hat{u}(x)}{dx^4} \\
 - \left( \frac{\mathcal{K}_i}{K_m} + \frac{\mathcal{K}_g}{K_s} \right) \Lambda \omega^2 \frac{d^2 \hat{u}(x)}{dx^2} + \Lambda \omega^2 \hat{u}(x) = 0
 \end{aligned} \tag{1.14}$$

Details on the construction of the constitutive laws and equilibrium equations that lead to Equation (1.14) are presented in [Chesnais, 2010, Chesnais et al., 2011a].

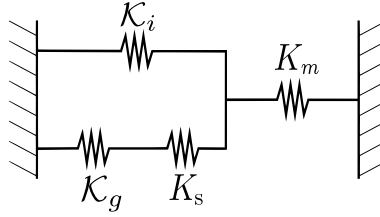


FIGURE 1.8: Schematic representation of the mechanisms included in the upgraded EBM [Chesnais, 2010].

[Chesnais et al., 2011a] analyzes the importance of the shear of the walls according to the order of magnitude of their slenderness:

- *Vertical elements with  $a_m/l_m \leq O(\varepsilon)$ .* The vertical structural components are thin enough to be modeled as Euler-Bernoulli beams at the story and structure scales. Here, the shear deformation of the elements can be neglected, and the original EBM is valid to model ordinary frame buildings.
- *Vertical elements with  $O(\varepsilon) < a_m/l_m < O(\varepsilon^{-1})$ .* The vertical elements are sufficiently thick to need to be modeled as Timoshenko beams at the story scale and the analytical expression of the stiffness of the shear of the cell  $K_s$  has to be adapted. Nevertheless, at the structure scale, the elements still behave as Euler-Bernoulli beams. Under this condition, the EBM is still valid. Applications concern the first vibration modes of frame buildings with shear walls.
- *Vertical elements with  $a_m/l_m \geq O(\varepsilon^{-1})$ .* The vertical elements are very thick for the modeling at the story and the structure scales. Thus, the shear of the walls appears at the leading order and highly influences the structure's global behavior. A new mechanism, accounting for the shear of the walls, needs to be included in the EBM. The upgraded EBM by [Chesnais, 2010] is then recommended to model shear wall buildings, especially for the higher modes.

For the higher modes, the shear of the cell  $K_s$  and the global bending  $K_g$  can frequently be neglected and, in this case, the upgraded EBM degenerates into a specific model that Chesnais calls the inner Timoshenko model. Even if this model is mathematically similar to the slender Timoshenko model of Section 1.4.4 with the same type of equations, it describes a completely different physics. In the slender Timoshenko model, the governing mechanisms are the global bending  $K_g$  corresponding to the out-of-phase tension-compression of the walls and the shear of the cells  $K_s$  resulting from the local bending of the structural elements. The inner Timoshenko model is used when the very thick vertical elements behave as cantilever beams at the structure scale. It includes therefore the inner bending  $K_i$  and the shear of the walls  $K_m$ . So, the macro parameters of the inner Timoshenko model are given by the inner bending stiffness  $K_i$  instead of

the global bending stiffness  $\mathcal{K}_g$  and the shear stiffness of the walls  $K_m$  instead of the shear stiffness of the unit cell  $K_s$ . The transverse steady-state motion equation is then given by:

*Inner Timoshenko beam*

$$\mathcal{K}_i \left( \hat{u}^{(4)} + \frac{\Lambda \omega^2}{K_m} \hat{u}'' \right) - \Lambda \omega^2 \hat{u} = 0 \quad (1.15)$$

The importance of the inner bending stiffness  $\mathcal{K}_i$  can be weighted with respect to  $K_m$  through the parameter  $C^m = \frac{\mathcal{K}_i}{K_m L^2}$  where  $L$  depends on the mode number  $k$  and is defined as  $L = 2H / (\pi(2k - 1))$ . So, the conditions mentioned above can be complemented with:

- $C^m = O(1)$ . The inner bending  $\mathcal{K}_i$  and the shear of the walls  $K_m$  have the same importance.
- $C^m \leq O(\varepsilon)$ . The inner bending governs the behavior.
- $C^m \geq O(\varepsilon^{-1})$ . The shear of the walls controls the behavior.

*Note.* Although this upgraded version of the EBM provided better results for the real case study presented in Chesnais' works, the original EBM (with three mechanisms) constitutes the departure point of this thesis. The implementation of the upgraded EBM could be part of future works once the limitations of the two models are identified thanks to the study of multiple frame structures.

## 1.5 Homogenized beam models for multiple frame structures

### 1.5.1 Results of the HPDM implementation on double and triple frame structures

The extensive implementation of the HPDM on single frame structures [Hans and Boutin, 2008] provides two main results: a family of beam models to describe their global structural behavior and an identification criterion. However, the behavior evolution becomes a matter of concern when the complexity of the structure geometry increases because of the enrichment of the unit cell kinematics. Chesnais thus applied the HPDM to double frame structures [Chesnais, 2010] and triple frame structures (see figures in Table 1.4). For the double frame structures, the macro models and the identification criterion remain valid, but the expressions of the macroscopic parameters and the internal equilibrium of the cell are modified. For the triple frame structures, a new mode of inner deformation of the unit cell appears when the inner floor  $pi$  is flexible. As this mechanism is not included in the EBM, it cannot describe such structures correctly. Nevertheless, the effect of the new mechanism is predominant only in a minority of structures with particular contrasts between the structural elements. When the inner deformation of the unit cell is negligible, the framework defined from the previous

results on simpler structures remains valid: the EBM and the identification criterion still apply provided that the expressions of the macroscopic parameters are adapted. In particular, the expression of the shear stiffness  $K_s$  becomes more complex and differs from the expressions given in the literature. The analytical expressions of the shear stiffness of the cell  $K_s$  given by the HPDM are presented in Table 1.4. They are functions of the local bending stiffness of the walls and floors. The material and geometric properties (i.e., Young's modulus  $E$ , second moment of area  $I$  and length  $l$ ) of both walls and floors can be different and respectively identified with the subscripts  $m$  and  $p$ . The inner and outer elements are also differentiated with the subscript  $i$  and  $e$ , respectively.

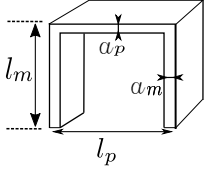
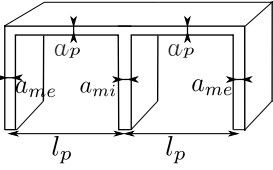
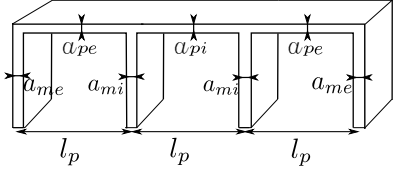
Single frame	Double frame	Triple frame
		
$\frac{2k_p k_m}{k_p + 2k_m}$	$\frac{k_p(k_p(2k_{me} + k_{mi}) + 12k_{me}k_{mi})}{k_p^2 + 2k_p(2k_{me} + k_{mi}) + 6k_{me}k_{mi}}$	$\frac{(2k_{mi} + 2k_{me})k_{pe}(k_{pe} + 2k_{pi}) + 3(2k_{mi} + 2k_{me})(k_{pi} + 2k_{pe})}{k_{pe}^2 + 3(2k_{me}(k_{pi} + 2k_{mi})) + 2k_{pe}(k_{pi} + 2k_{me} + 2k_{mi})}$
(1.16)	with $k_j = \frac{12E_j I_j}{l_m l_j}$	and $j = m, me, mi, p, pe$ or $pi$
	(1.17)	(1.18)

TABLE 1.4: Analytical expressions of the shear stiffness of the cell  $K_s$  for single, double and triple frame structures

The equations in Table 1.4 show that the shear stiffness  $K_s$  quickly becomes complex and is strongly dependent on the number of elements in the cell.

Thus, in the present study, we search for the validation of a numerical procedure that allows us to solve the internal kinematics of the unit cell whatever the number of frames  $N_f$ . We rely on the numerical validation of the analytical results for single frame structures to extend its implementation to multiple frame structures. We will see that the results of the proposed numerical analysis on triple frame structures validate the previous analytical results for most of the treated cases. Moreover, only for some highly contrasted structures, whose behavior is governed by the deformation of a small part, it is required to adapt the models. The overall conclusion of these studies is that the homogenized models derived from the study of single frame structures can be generalized to many periodic reticulated structures where the unit cell components are slender enough to be described by Euler-Bernoulli beams at the structure scale. However, the application of the HPDM quickly becomes tedious, and the shear stiffness and the internal equilibrium become too complex. Thus, a procedure that substitutes part of those analytical expressions by a numerical analysis has been proposed [Chesnais, 2010,



Chesnais et al., 2011a]. This procedure enables equally and much more simply:

1. to compute the macroscopic parameters by imposing the macro deformation of the unit cell (this step is called the intermediate scale analysis (I))
2. to build the equivalent beam model that describes the global behavior (this is called here the global scale analysis (G))

The numerical simulation and the analytical integration process that implies both intermediate and global scales will be called *hybrid analysis* from now on.

### 1.5.2 Hybrid analysis

The hybrid analysis consists of a numerical substitution of the evolving analytical expressions (i.e.,  $K_s$ ) to complete the EBM. In other words, this method looks to reconstruct the parameters that depend strongly on the structure geometry based on a finite element (FE) model of a single story subjected to a static analysis. This type of modeling is applicable to any structure that

- respects the conditions of periodicity and scale separation,
- is not too highly contrasted to avoid the global behavior to be governed by the deformation of a small part,
- has structural elements slender enough to be modelled as Euler-Bernoulli beams at the structure scale.

In this section, the implemented procedure for the different static analyses on the story is detailed. Our case studies correspond to triple frame structures with different properties for the inner and outer vertical and horizontal elements. First, we focus on finding the most relevant modeling technique for a single story. The main difficulty relies on the selection of pertinent boundary conditions for the element ends so that the single modeled story is deformed as if it was inside the entire structure. We compare the shear stiffness of the cell  $K_s$  obtained from the numerical simulations with the analytical formula of Equation (1.18). Besides, we perform the modal analysis using the EBM and specific models to validate the hybrid analysis by comparing the results with those of a fully detailed finite element (FE) model.

#### Kinematic variables

In the HPDM, the kinematic variables represent the node movements. As the number of elements or frames per story increases, the number of kinematic variables increases. Many of the new variables are "hidden" variables that describe the deformation of the cells and only appear in the internal equilibrium equations. But, if a new mechanism appears in the structure, then there is also a new driving variable, i.e., a new variable in the beam model that describes the global behavior of the structure. Within the framework of this thesis, we only

consider "low contrast" structures (which are very numerous) to remain within the domain of validity of the EBM. Hence, only two governing variables describe the global structure behavior:  $u$  and  $\alpha$ .

Figure 1.9 illustrates a deformed reticulated system of three frames. At a level  $n$ , the global deformation is described by the transverse displacement  $u_n$  and the macroscopic rotation  $\alpha_n$ . This transverse displacement and macroscopic rotation correspond to the "average" solutions of the story deformation, which are classically obtained in homogenization procedures. The description of the internal kinematics of the unit cell requires more variables that do not appear in the global description as found by [Chesnais, 2010] for double frame structures. At the element scale, as in single frame structures, the local bending can be described with a nodal rotation  $\theta$ , and nodal horizontal and vertical displacements  $u$  and  $v$ , respectively. This real nodal motion is the sum of the average motion given by the two governing variables and the local fluctuations given by the hidden kinematics variables, which are obtained by solving the internal equilibrium equations.

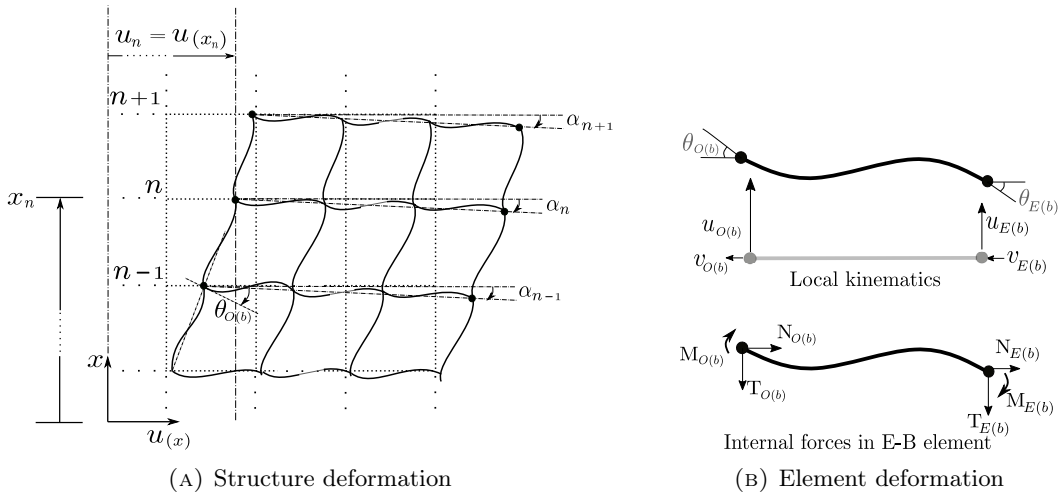


FIGURE 1.9: Global (left) and intermediate (right) kinematics of the physical problem

### Macroscopic parameters

The transverse dynamics of reticulated structures is described by the EBM whose macroscopic parameters, namely the global bending stiffness  $\mathcal{K}_g$ , inner bending stiffness  $\mathcal{K}_i$ , linear mass  $\Lambda$  and shear stiffness of the cell  $K_s$  are estimated from the static analysis of a unique story (unit cell). On the one hand, for the first three macroscopic parameters ( $\mathcal{K}_g$ ,  $\mathcal{K}_i$ , and  $\Lambda$ ) their analytical expression does not change with the number of elements in the unit cell. The global bending stiffness  $\mathcal{K}_g$  corresponds to the sum of the tension-compression stiffnesses of the vertical elements multiplied by the square of the lever arms  $d_i$  and the inner bending stiffness  $\mathcal{K}_i$  is the sum of the bending stiffnesses of the vertical elements, expressed as, respectively:

$$\mathcal{K}_g = \sum_{j=1}^{N_f+1} E_{c_j} A_j d_j^2$$

and

$$\mathcal{K}_i = \sum_{j=1}^{N_f+1} E_{c_j} I_j$$

where  $N_f$  is the number of frames per story,  $N_f + 1$  is the number of vertical elements,  $E_{c_j}$  is the elastic modulus and  $I_j$  is the second moment of area. If all the vertical elements have the same elastic modulus, it is possible to define the global inertia of the structure  $I_g = \sum_{j=1}^{N_f+1} A_j d_j^2$ .

The linear mass  $\Lambda$  is the total mass of the unit cell divided by its size.

$$\Lambda = \frac{1}{l_m} \left( \sum_{j=1}^{N_f+1} \rho_j A_j l_j \right)$$

On the other hand, we have seen that the analytical formulation for  $K_s$  becomes complex as new elements are added in the cell (e.g., walls, floors, braces). Therefore, this parameter is determined through a numerical procedure detailed in the following paragraph.

### Computation of the shear stiffness of the cell $K_s$

In transverse motions, unbraced reticulated structures are characterized by a high deformability in shear generated by the local bending of the arranged elements. In this section, we aim to reproduce this macro deformation on a single unit cell of the structure through an elastostatic analysis. As evidenced analytically by the HPDM (expressions given in Table 1.4), the bending stiffnesses of both vertical and horizontal elements are relevant in the calculation of the shear stiffness in the unit cell. The unit cell deforms in shear and all the elements bend individually according to their geometric and elastic properties. The unit cell can be modelled numerically as the arrangement of Euler-Bernoulli beam elements with nodal connections. The shear deformation can be imposed to this Finite Element (FE) model guided by the expression of the shear stiffness given in Equation 1.19. One method to impose the shear distortion of the unit cell FE model is by applying a differential displacement  $\Delta U$  between the top and the bottom nodes. It is also possible by imposing a force  $T$  at the top nodes. However, the expected shear deformation is only obtained under specific boundary conditions. In the HMPD, the kinematic variables are the movements of the nodes therefore the boundary conditions only concern the degrees of freedom of these points. We search for boundary conditions that allow the bending of each vertical and horizontal element and recover their fully resistance to the applied distortion. Once the FE model of the single story with appropriate boundary conditions is subjected to the distortion  $\Delta U$ , the shear stiffness of the cell  $K_s$  can be obtained from the computation of the sum of the shear force  $T_j$  in each vertical element  $j$ .

$$\sum_{j=1}^{N_f+1} T_j = K_s \frac{\Delta U}{l_m} \quad (1.19)$$

The selection of the appropriate boundary conditions for the single cell FE model challenges two main objectives:

- Impose the macro deformation of the unit cell, in this case, the shear deformation of the cell where the vertical and horizontal elements deform in bending. And,
- Approximate the deformation of the unit cell as if it was within the whole structure. In the numerical homogenization procedures, it is usually realized by imposing periodic boundary conditions.

[Chesnais, 2010, Chesnais et al., 2011a] propose a solution to generate the distortion of the cell by imposing the differential horizontal displacement  $\Delta U$  between the bottom and top of each vertical element. For the treated cases, the rigid body movement is prevented by blocking in addition the vertical displacement of the nodes located at the ends of the floor. Periodic boundary conditions are set for the rotation and vertical degrees of freedom. Two different conditions are tried to evaluate the shear of the cell. Figure 1.10 presents the story or unit cell FE model under both boundary conditions A and B. For both cases, the conditions on the nodal rotations are identical: for each vertical element, the rotations of the top and bottom ends are set to be equal. Their difference mainly concerns the vertical degree of freedom. On the one hand, condition A restricts the vertical displacement of the outer vertical elements and lets free ends on the inner vertical elements (see Figure 1.10(Left)). According to the case study in [Chesnais, 2010] (see figures in Table 1.5), one concludes that the vertical displacements of the internal nodes do not allow the complete shear of the cell. The deformed shape of the story shows the rotation of the stiffest parts and the shear stiffness value only takes into account the stiffness of the flexible elements.

On the other hand, condition B blocks the vertical displacements of every vertical element (see Figure 1.10(Right)). Compared to condition A and the FE model of the entire structure, condition B gives better results.

In this thesis, we perform an extended numerical study to confirm Chesnais analytical and numerical results. We start by treating triple frame structures and we widen the study to large multiple frame structures.

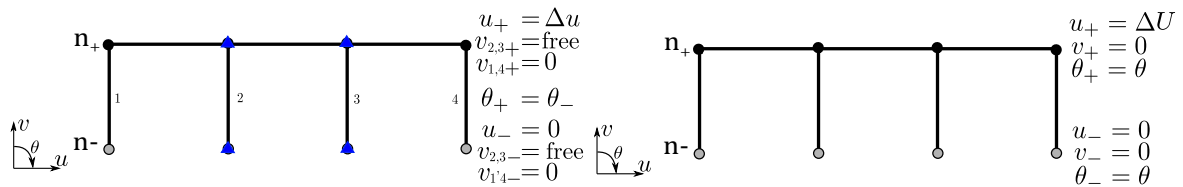


FIGURE 1.10: Boundary conditions A (Left) and B (Right) associated with the shear deformation of the story model

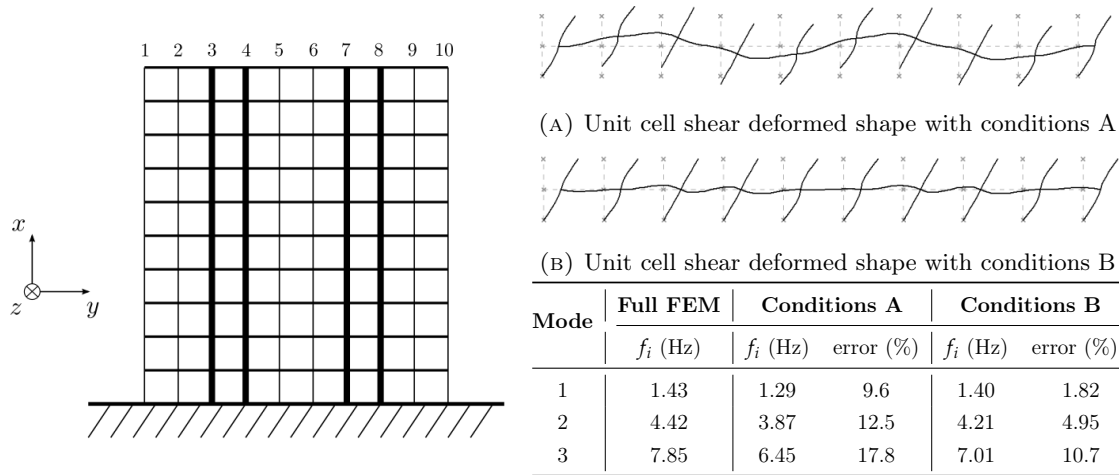


TABLE 1.5: Case study in [Chesnais, 2010]. Comparison of the eigen frequencies of the first three vibration modes obtained with a finite element model of the whole structure and a shear beam model where the shear stiffness  $K_s$  is calculated with the boundary conditions A and B

### Application to triple frame structures

We now apply the hybrid analysis to ten triple frame structures to verify the analytical results obtained by Chesnais with the HPDM. In the present work, we consider structures with  $N = 15$  stories, which corresponds to a scale ratio  $\varepsilon = \pi/2N \approx 0.105$  for the first vibration mode. The unit cells are constituted of a symmetric arrangement of four vertical and three horizontal elements which can have different thicknesses (see Figure 1.11 and Table 1.6). The thicknesses are noted  $a_{mi}$  and  $a_{me}$  for the external and internal vertical elements (or walls) respectively,  $a_{pi}$  and  $a_{pe}$  for the external and internal horizontal elements (or floors) respectively. For all the structures, the vertical and horizontal elements are 3 m long. The material properties are: elastic modulus  $E = 30$  GPa, Poisson's ratio  $\nu = 0.2$  and mass density  $\rho = 2300$  kg/m<sup>3</sup>. We are interested in: (i) Testing the two types of boundary conditions, A and B, in order to determine the best boundary conditions for the calculation of  $K_s$ , (ii) Comparing the numerical value of  $K_s$  with the result of the analytical formula given in Equation (1.18), (iii) Identifying the governing mechanism(s) associated with each structure. (iv) Evaluating the accuracy of the EBM for complex structures.

The FE model of the single story is built in the FEM-based code Cast3M [CEA, 2017] using the two different boundary conditions A and B. We use Euler-Bernoulli beams for the vertical and horizontal elements with nodal connections. The analytical equations of the EBM are entirely coded in MatLab [MATLAB, 2015] as well as its finite element formulation which will be presented in Chapter 2. The code is written to enter all the geometric and material information of the structure as inputs. When the macroscopic parameters are evaluated, the Cast3M outputs are imported automatically by the code to be post-processed in the MatLab environment. The unit cell shear deformation under both boundary conditions is illustrated in Figure 1.12 for all the treated cases. In black lines, we present the undeformed story and in orange and blue the deformed shapes of the story using the condition A and B, respectively.

One can notice that minor differences exist for the cases 1-4 and 9 where there is no much stiffness contrast between the inner vertical and horizontal elements. On the contrary, where the inner part is strongly contrasted with respect to the outer part like in cases 6 and 8, the deformed shape highly differs under both boundary conditions.

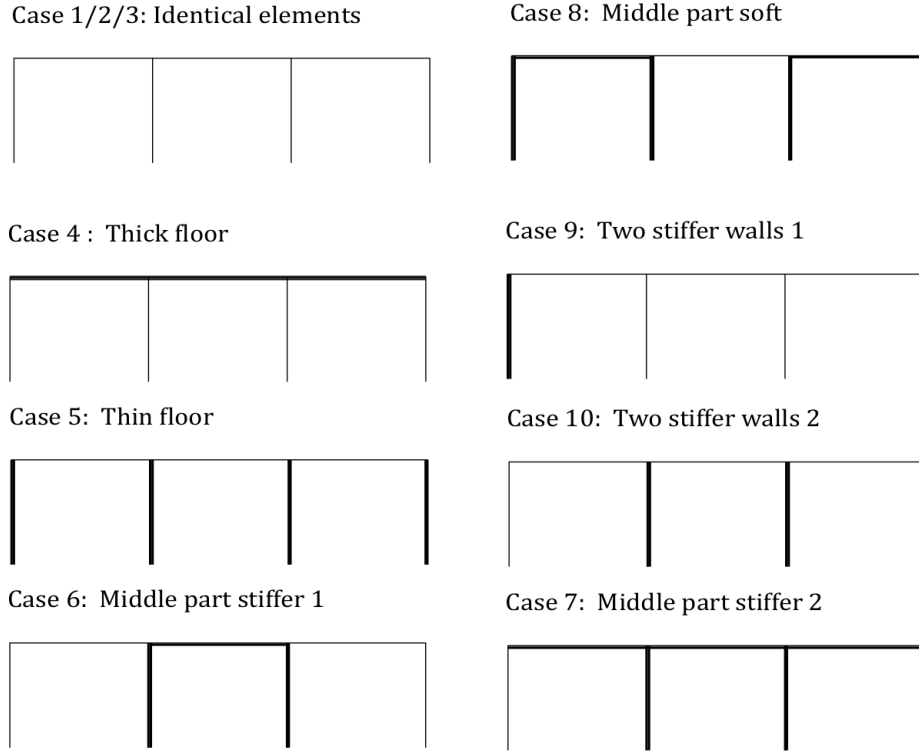


FIGURE 1.11: Studied triple frame structures. The thicknesses of the elements are given in Table 1.6.

Case Study		$a_{mi}$	$a_{me}$	$a_{pi}$	$a_{pe}$
1	Identical elements $O(\varepsilon^2)$	32.90	32.90	32.90	32.90
2	Identical elements $O(\varepsilon^{1/2})$	970.81	970.81	970.81	970.81
3	Identical elements $O(\varepsilon)$	314.16	314.16	314.16	314.16
4	Thick floor	32.90	32.90	314.16	314.16
5	Thin floor	314.16	314.16	32.90	32.90
6	Middle part stiffer 1	314.16	69.80	314.16	69.80
7	Middle part stiffer 2	314.16	69.80	314.16	314.16
8	Middle part soft	314.16	314.16	69.80	314.16
9	Two stiffer walls 1 (External)	69.80	314.16	69.80	69.80
10	Two stiffer walls 2 (Internal)	314.16	69.80	69.80	69.80

TABLE 1.6: Element thicknesses of the studied triple frame structures in mm.

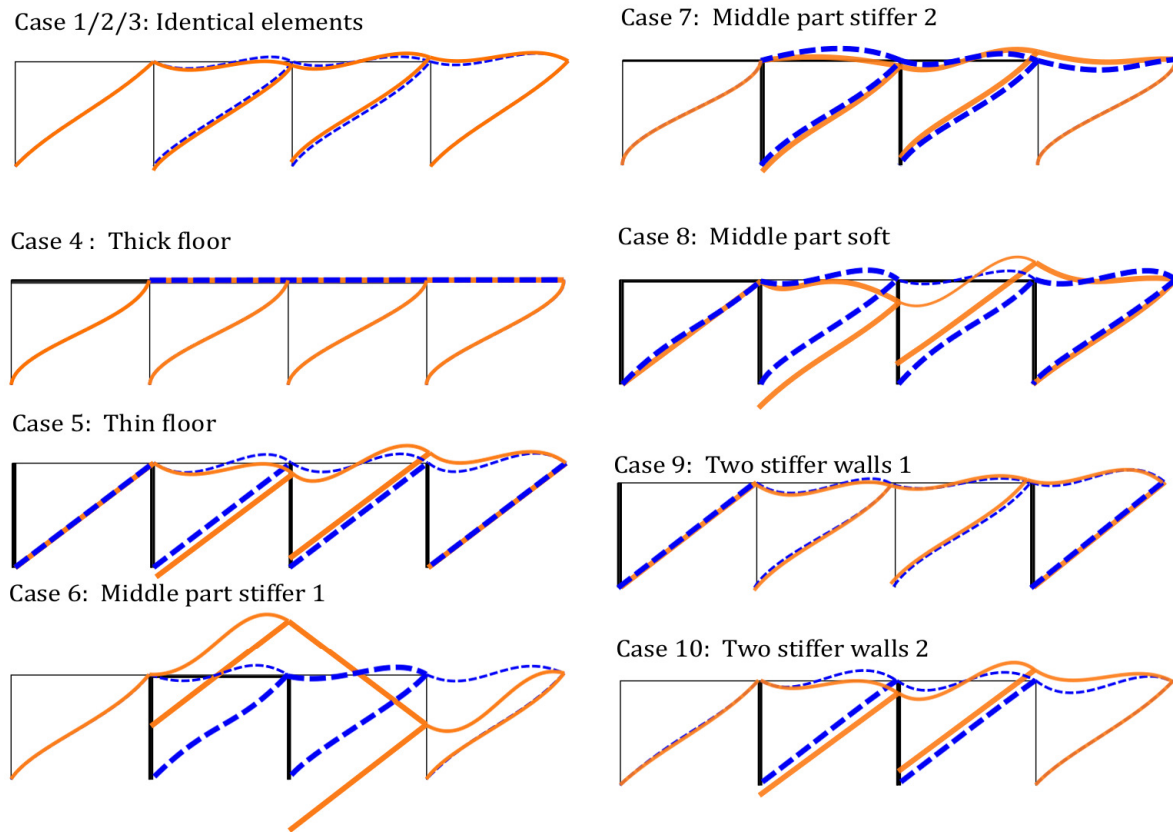


FIGURE 1.12: Studied triple frame structures. Cell deformation under the boundary conditions A (orange line) and B (blue dashed line)

Case	Shear Stiffness [MN]					
	Analytical	Story CA	error %	Story CB	error %	
1	Identical Elements 1	0.20	0.20	-0.51	0.20	0.00
2	Identical Elements 2	5048.11	5023.30	-0.49	5048.10	0.00
3	Identical Elements 3	171.07	170.23	-0.49	171.07	0.00
4	Thick floor	0.47	0.47	-0.04	0.47	-0.83
5	Thin floor	0.36	0.36	-0.06	0.36	-0.06
6	Middle part stiffer 1	70.16	4.09	-1616.65	70.16	0.00
7	Middle part stiffer 2	92.21	74.89	-23.12	92.21	0.00
8	Middle part soft	138.31	9.73	-1322.06	138.30	-0.01
9	Two stiffer walls 1 (External)	2.16	2.10	-2.71	2.16	0.04
10	Two stiffer walls 2 (Internal)	2.95	2.93	-0.91	2.95	0.00

TABLE 1.7: Shear stiffness of the cell  $K_s$  computed with the analytical expression issued from the homogenization of triple frame structures (Equation (1.18) of Table 1.4) and the numerical model of a story using the boundary conditions A and B.

The type of boundary conditions used in the one-story model can strongly influence the coherence of the results. Herein, numerical calculations with the conditions B give the same shear stiffness as the analytical formula (see Table 1.7). Tables 1.8 and 1.9 present the macroscopic constants  $C$  and  $\gamma$  that allow the behavior identification of each of the studied cases on the domain map of Figure 1.13.

This numerical study verifies that in the construction of the finite element model of a single story, the vertical degree of freedom must be restrained in each node (boundary conditions B) to obtain the correct value of  $K_s$ . The results show a very good precision of the hybrid analysis with a reduced computational cost compared to an explicit finite element model of the complete structure, except when the behavior is governed by the new mechanism due to the deformation of a localized section of the structure as for cases 6 and 8. When the homogenization indicates that the new mechanism is associated with others as for cases 3 and 7, the EBM and therefore the hybrid analysis should not be used, but good results are nevertheless obtained using the condition B. Another important point is that, once the governing mechanism(s) is(are) identified, the use of the specific model (Table 1.2) may give results even closer to those of the full finite element model as presented in Table 1.11 and in the bar chart of Figure 1.14).



Case study	Conditions	$\Lambda$ ton mm <sup>-1</sup>	$\mathcal{K}_i$ MN mm <sup>2</sup>	$\mathcal{K}_g$ MN mm <sup>2</sup>	$\mathcal{K}_s$ MN	C	x	$\gamma$	y
1	Identical Elements 1	5.3 E-4	3.56E+05	4.44E+10	0.196	276.802	-2.490	8.018E-06	5.2
2	Identical Elements 2	1.56E-2	9.15E+09	1.31E+12	5023.300	0.318	0.508	7.000E-03	2.2
3	Identical Elements 3	5.06E-3	3.10E+08	4.24E+11	170.230	3.036	-0.492	7.310E-04	3.2
4	Thick floor	2.47E-3	3.56E+05	4.44E+10	0.474	114.238	-2.100	8.018E-06	5.2
5	Thin floor	3.12E-3	3.10E+08	4.24E+11	0.356	1452.500	-3.227	7.310E-04	3.2
6	Middle part stiffer 1	2.81E-3	1.57E+08	1.27E+11	4.087	37.927	-1.611	1.200E-03	2.9689
7	Middle part stiffer 2	3.93E-3	1.57E+08	1.27E+11	74.894	2.070	-0.322	1.200E-03	2.9689
8	Middle part soft	4.50E-3	3.10E+08	4.24E+11	9.726	53.134	-1.761	7.311E-04	3.2001
9	Two stiffer walls 1 (External)	2.25E-3	1.57E+08	3.91E+11	2.102	226.723	-2.404	4.007E-04	3.4666
10	Two stiffer walls 2 (Internal)	2.25E-3	1.57E+08	1.27E+11	2.927	52.954	-1.957	1.200E-03	2.9689

TABLE 1.8: Boundary conditions A applied on the numerical model of a story: Macroscopic properties.

Case study	Conditions	$\Lambda$ ton mm <sup>-1</sup>	$\mathcal{K}_i$ MN mm <sup>2</sup>	$\mathcal{K}_g$ MN mm <sup>2</sup>	$\mathcal{K}_s$ MN	C	x	$\gamma$	y
1	Identical Elements 1	5.3 E-4	3.56E+05	4.44E+10	0.197	275.445	-2.490	8.018E-06	5.2
2	Identical Elements 2	1.56E-2	9.15E+09	1.31E+12	5048.100	0.316	0.510	7.000E-03	2.2
3	Identical Elements 3	5.06E-3	3.10E+08	4.24E+11	171.069	3.021	-0.490	7.310E-04	3.2
4	Thick floor	2.47E-3	3.56E+05	4.44E+10	0.470	114.195	-2.100	8.018E-06	5.2
5	Thin floor	3.12E-3	3.10E+08	4.24E+11	0.356	1452.500	-3.227	7.310E-04	3.2
6	Middle part stiffer 1	2.81E-3	1.57E+08	1.27E+11	70.161	2.209	-0.351	1.200E-03	2.9689
7	Middle part stiffer 2	3.93E-3	1.57E+08	1.27E+11	92.213	1.681	-0.230	1.200E-03	2.9689
8	Middle part soft	4.50E-3	3.10E+08	4.24E+11	138.300	3.736	-0.584	7.310E-04	3.2001
9	Two stiffer walls 1 (External)	2.25E-3	1.57E+08	3.91E+11	2.160	220.645	-2.392	4.007E-04	3.4666
10	Two stiffer walls 2 (Internal)	2.25E-3	1.57E+08	1.27E+11	2.954	52.476	-1.755	1.200E-03	2.9689

TABLE 1.9: Boundary conditions B applied on the numerical model of a story: Macroscopic properties.

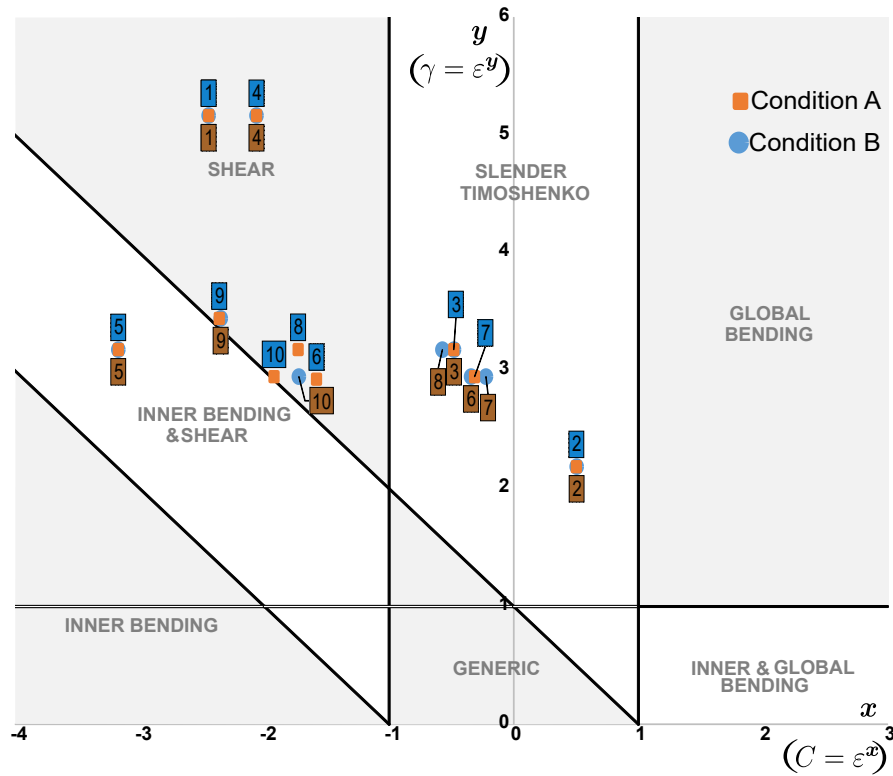


FIGURE 1.13: Behavior identification for the ten studied structures. The orange squares correspond to the values of  $K_s$  calculated with the boundary conditions A and the blue circles correspond to the values of  $K_s$  calculated with the boundary conditions B.

Case	Frequency [Hz]				
	Full FEM	Hybrid Analysis			
		Condition A	error %	Condition B	error %
1	0.11	0.11	-2.0	0.11	-2.2
2	1.95	2.02	-3.5	2.02	-3.6
3	0.95	0.98	-2.7	0.98	-2.9
4	0.07	0.08	-5.0	0.07	-5.0
5	0.12	0.12	0.4	0.12	0.4
6	0.71	0.25	64.7	0.82	-16.6
7	0.75	0.71	4.7	0.77	-3.2
8	0.78	0.30	61.6	0.95	-22.4
9	0.21	0.21	0.1	0.21	-1.0
10	0.24	0.24	-0.5	0.24	-0.9

TABLE 1.10: Comparison of the first vibration frequency obtained with the full finite element model and the hybrid analysis using the EBM.

Case	Frequency [Hz]		
	Full FEM	Specific	error%
1 Identical Elements 1 $O(\epsilon^2)$	0.11	0.11	0.86
2 Identical Elements 2 $O(\epsilon^{1/2})$	1.95	1.99	-1.99
3 Identical Elements 3 $O(\epsilon)$	0.95	0.95	-0.18
4 Thick floor	0.07	0.08	-3.19
5 Thin floor	0.12	0.12	0.45
6 Middle part stiffer 1	0.71	0.80	-13.25
7 Middle part stiffer 2	0.75	0.75	-0.78
8 Middle part soft	0.77	0.92	-18.74
9 Two stiffer walls 1 (External)	0.21	0.22	-1.27
10 Two stiffer walls 2 (Internal)	0.24	0.24	0.00

TABLE 1.11: Comparison of the first vibration frequency obtained with the full finite element model and the hybrid analysis using the specific beam model and the value of  $K_s$  calculated with the boundary conditions B.

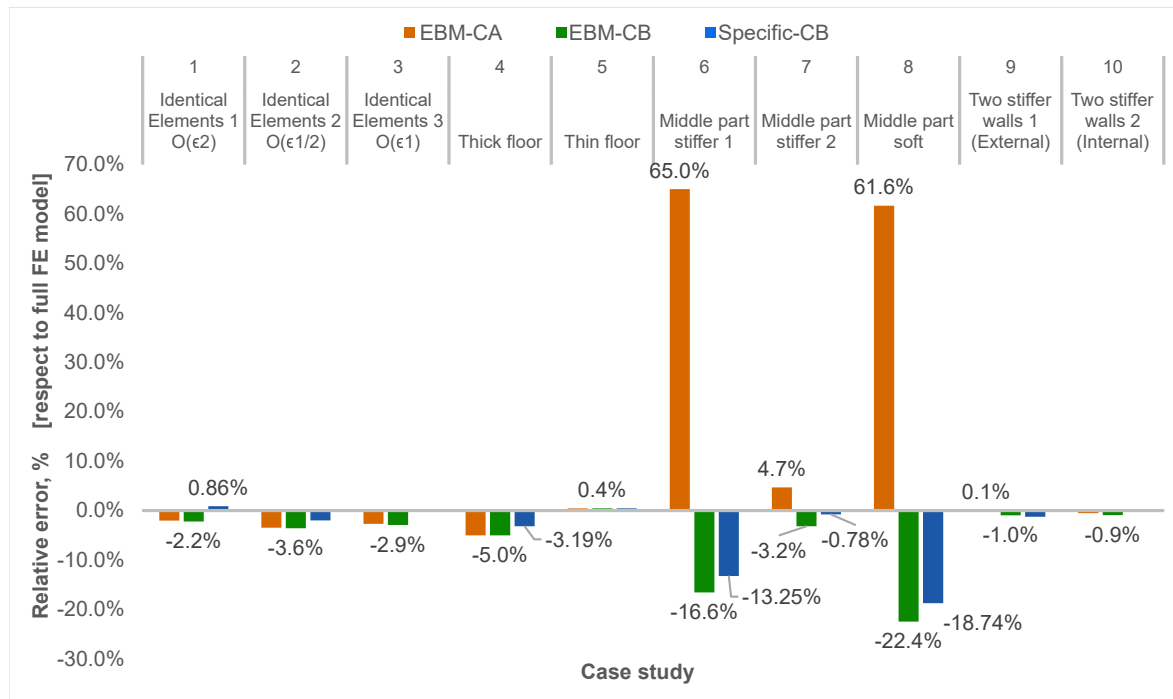


FIGURE 1.14: Relative error on the first vibration frequency obtained with the full finite element model (reference) and the hybrid analysis using the EBM with the boundary conditions A and B, and the specific beam model with the value of  $K_s$  calculated using the boundary conditions B.

### 1.5.3 Influence of the number of frames

In this section, we continue to evaluate the efficiency of the proposed hybrid procedure by analyzing more complex structures. We are also interested in the evolution of the global behavior when the number of cells and the number of frames per story vary. The verification consists in comparing the results obtained from two different methods.

1. Hybrid analysis: the analytical formulation of the Equivalent Beam Model is used to study the dynamic behavior of the structure at the global scale while the local information is obtained thanks to a static numerical model of a single story,
2. Fully numerical analysis with a FEM model of the entire structure. This model is built through the Cast3M FEM software [CEA, 2017] and consists of a 2D model, where the elements are Euler-Bernoulli beams discretized with a fine mesh density.

For all the treated structures, the material properties are: elastic modulus  $E = 30$  GPa, Poisson's ratio  $\nu = 0.2$  and mass density  $\rho = 2300$  kg/m<sup>3</sup>. The frame span and wall length are 3 m. The stiffness contrasts between the floors and the walls are chosen to obtain a different type of behavior for each case. Figure 1.15 presents the unit frames of the studied structures. The parametric study is performed by varying (i) the number of cells  $N$  from 10 to 100 ( $N_f$  set to 3) and (ii) the number of frames per story  $N_f$  from 1 to 20 ( $N$  set to 10). These values are selected to represent possible configurations of real structures. The number of cells  $N$  could have been set to 5 that is the minimum to respect the scale separation condition. The comparison is limited to the first eigenfrequency values and the macroscopic behavior is identified thanks to the criterion based on  $C$  and  $\gamma$ .

For each unit frame, the variations of  $N$  (Figure 1.16) and  $N_f$  (Figure 1.17) generate two different straight lines on the map of the possible beam models. [Hans and Boutin, 2008] predicted, analytically, the same tendency. When the number of cells  $N$  increases, each structure tends to behave as a combination of the inner and global bending mechanisms (Figure 1.16). On the opposite side, the increase of the number of frames per story causes the decrease of the importance of the global bending, and the structure behavior moves to the left at each iteration. The bubble's size represents the magnitude of the relative error between the numerical and hybrid first frequency values. It is noted that the error decreases when increasing  $N$ , but it remains almost constant by the  $N_f$  increment. For both studies, the errors are very low, less than 5% for all the treated cases.

The evolution of the first vibration frequency according to the number of frames  $N_f$  for the different unit frames is illustrated in Figure 1.18. As the number of the same unit frame increases, the frequency gradually increases. This is explained by the increment of the cell stiffness. In addition to the hybrid analysis (red starred line) and the completely numerical analysis (blue circled line), the classical Timoshenko beam model for solid-cross section beams (cyan starred line) is also considered. The purpose is to highlight the influence of the new mechanism, the inner bending, which is not included in the Timoshenko beam model. On each graph, the relative error between the reference (numerical) and the beam model with the largest discrepancy is presented. For example, in Figure 1.18 for the unit frame 1, only a

relative error of 4.5% exists between all the models (that includes the EBM and the classical Timoshenko model). However, for the unit frame 2, a difference of 47% is obtained between the reference and the Timoshenko model. The EBM results are very close to the reference in all the studied cases.

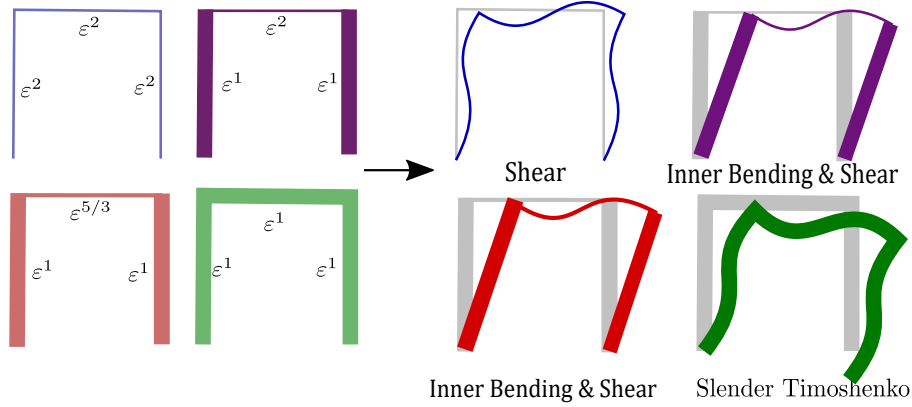


FIGURE 1.15: Unit frames of the studied structures and governing mechanism(s) when  $N = 10$  and  $N_f = 3$ . **Case 1 (blue frame)**: identical thin walls and floors ( $a_m/l_m = a_p/l_m = O(\varepsilon^2)$ )  $\rightarrow$  shear; **Case 2 (purple frame)**: walls thicker than the floors with a high contrast ( $a_m/l_m = O(\varepsilon^1)$  and  $a_p/l_m = O(\varepsilon^2)$ )  $\rightarrow$  inner bending and shear; **Case 3 (red frame)**: walls thicker than the floors with a smaller contrast ( $a_m/l_m = O(\varepsilon^1)$  and  $a_p/l_m = O(\varepsilon^{5/3})$ )  $\rightarrow$  inner bending and shear; **Case 4 (green frame)**: identical thick walls and floors ( $a_m/l_m = a_p/l_m = O(\varepsilon^1)$ )  $\rightarrow$  slender Timoshenko (global bending and shear)

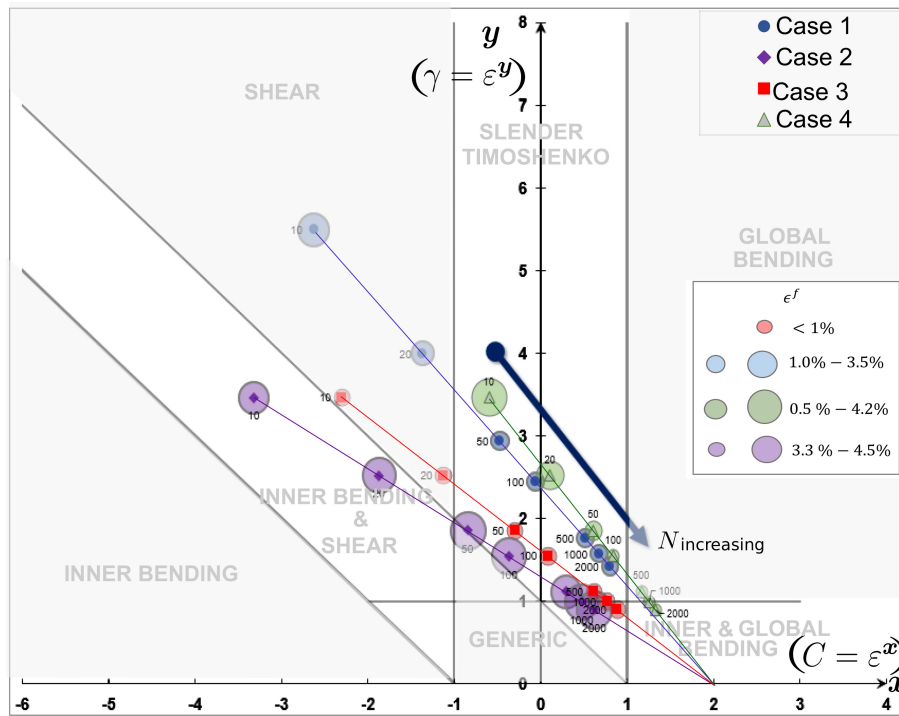


FIGURE 1.16: Identified macroscopic behavior for each case as the number of cells  $N$  increases.

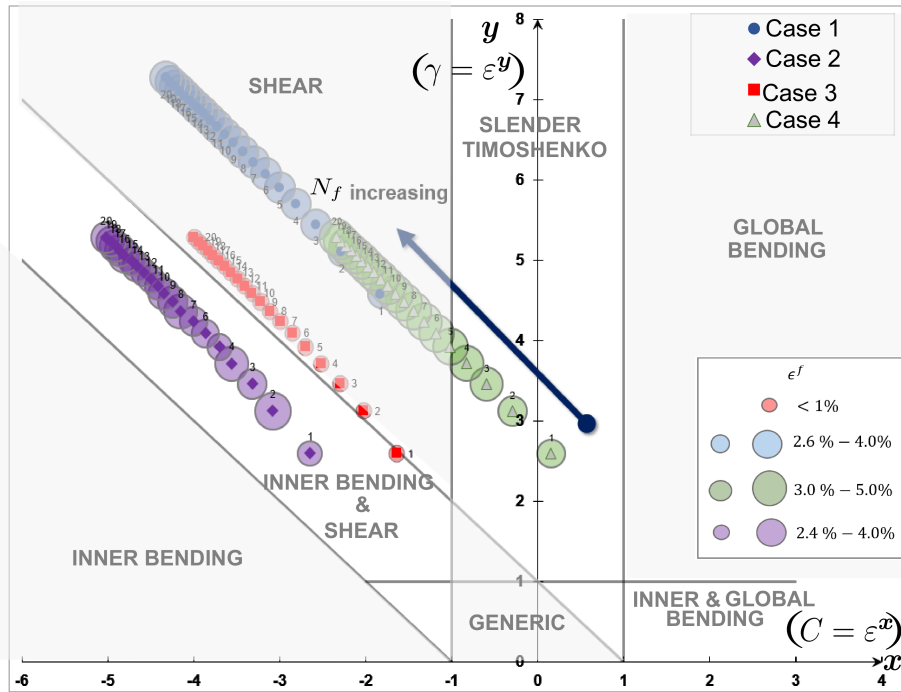


FIGURE 1.17: Identified macroscopic behavior for each case as the number of frames per story  $N_f$  increases.

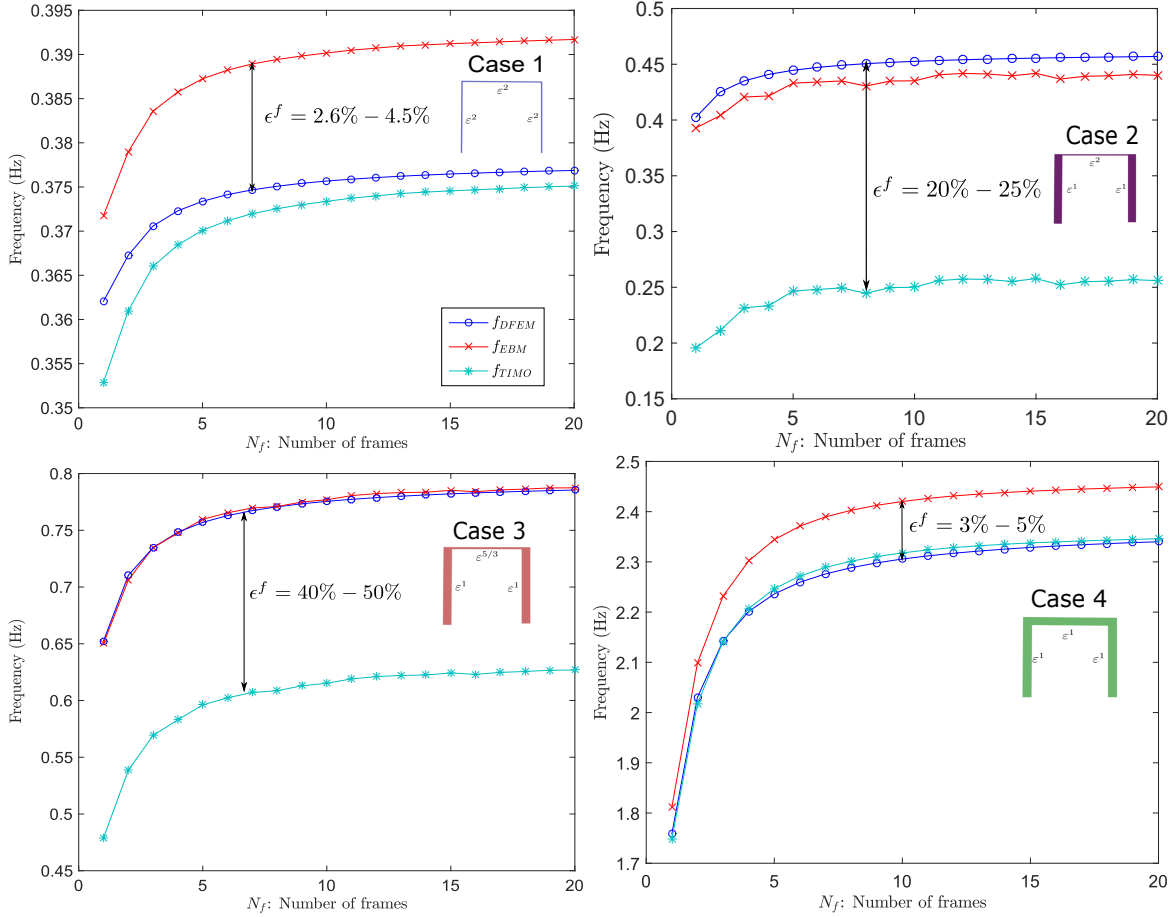


FIGURE 1.18: Evolution of the fundamental frequency with respect to the number of frames per story  $N_f$ . Blue circled line: numerical model. Red starred line: hybrid analysis with the EBM. Cyan starred line: classical Timoshenko beam model;

#### 1.5.4 Influence of the governing mechanism(s) on the modal properties

We decide to enlarge the numerical studies to retrieve numerically analytical relationships for the eigenfrequencies and observe the evolution of the vibration mode shapes when the geometric features of the structures vary. Four hundred triple frame structures clamped at the base and free at the top are tested. The number of cells  $N$  is fixed at 10. Each cell is a triple frame composed of four identical vertical elements and three identical horizontal elements of length  $l_m = l_p = 3$  m. Only two parameters vary from one structure to another: the thicknesses of the vertical and horizontal elements which can have different values (from 50 mm to 1950 mm with a step of 100 mm).

The estimation of the macroscopic parameters  $\Lambda$ ,  $\mathcal{K}_i$ ,  $K_s$  and  $\mathcal{K}_g$  is performed from the static analysis of a single unit cell as described in the hybrid analysis section (Section 1.5.2). The governing mechanism(s) of each of the structures is(are) identified utilizing the identification criterion based on the macroscopic constants  $C$  and  $\gamma$ . The relationship between the eigenfrequencies and the stiffness contrast for the Timoshenko model presented by [Hans, 2002]

(Figure 1.19(A)) is reproduced numerically with the EBM and the hybrid analysis (Figure 1.19(B)). The ratio between the various eigenfrequencies and the first frequency for each structure is computed and plotted as a function of the macroscopic constant  $C$  (i.e., the ratio between the global bending stiffness and the shear of the cell stiffness). In the numerical graph (Figure 1.19(B)) each studied structure is represented with three dots: the blue, orange and green colors represent the second, third and fourth vibration modes, respectively. Firstly, we can see in both graphs, the analytical and numerical ones, that the frequency ratios are also a characteristic of the beam model. The values of the frequency ratios decrease as the shear mechanism starts governing the dynamic behavior. Thus, for the structures governed by the shear mechanism, the eigenfrequencies follow the sequence of the odd numbers (1; 3; 5;...). For the structures governed by the global bending mechanism, the sequence follows (1; 6.25; 17.36;...). However, notice that there are structures that form an extended region because of the inner bending and shear mechanisms interaction. For these structures the frequency ratios can have values in between. Structures located within this region could not be modelled with the Timoshenko model.

The frequency ratios are also presented as functions of the macroscopic constants  $C$  and  $\gamma$  in Figure 1.21. This graph is the three-dimensional representation of the numerical graph of Figure 1.19(B) with  $\gamma$  included. We see that the structures with a high contrast between the inner bending and global bending mechanisms have frequency ratios that follow the sequence (1; 6.25; 17.36;...), characteristic of bending.

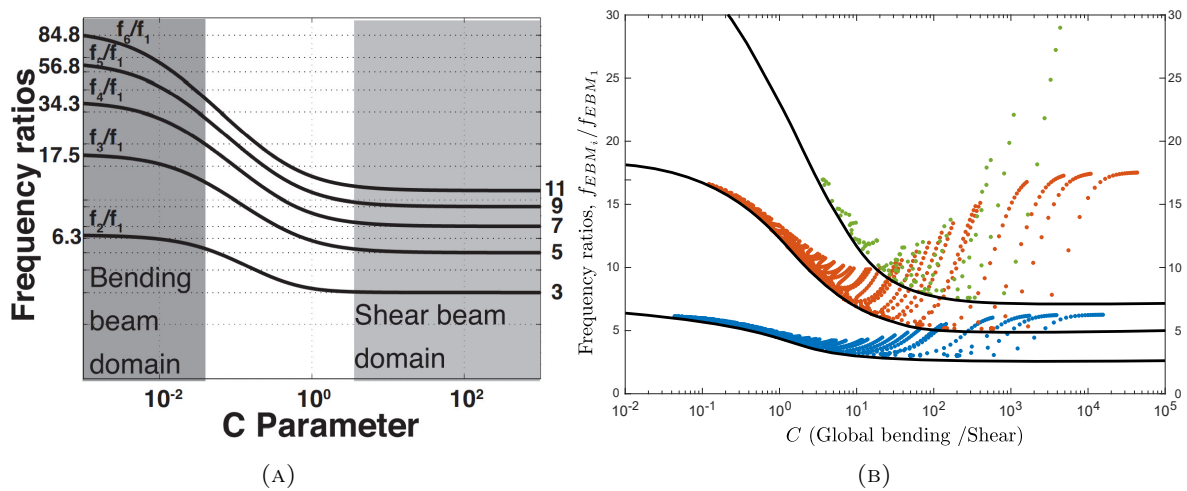


FIGURE 1.19: Frequency ratios as functions of the dimensionless parameter  $C$  for (A) a continuous Timoshenko beam [Hans, 2002] and (B) the EBM of the studied triple frame structures.



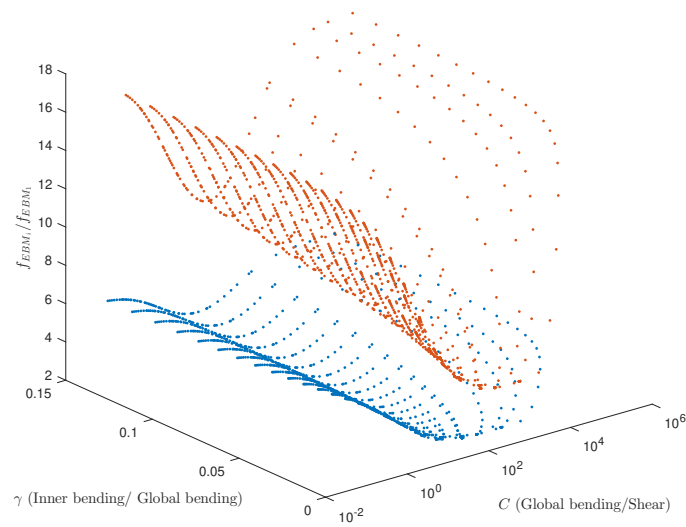


FIGURE 1.20: 3-D representation of the frequency ratios as functions of the macroscopic constants  $C$  and  $\gamma$

Ten structures are now selected from the total to illustrate that the mechanism(s) governing the dynamic behavior depend(s) on the vibration mode. Figure 1.21 shows the identified governing mechanism(s) on the domain behavior map for the first three vibration modes. One colored line represents a single structure and each dot corresponds to a vibration mode. Let's notice that every line converges to the point 2 of the horizontal axes  $\mathbf{x}$ . The properties of the cell define the slope of the line which crosses necessarily the point  $(\mathbf{x}=2, \mathbf{y}=0)$  [Hans and Boutin, 2008].

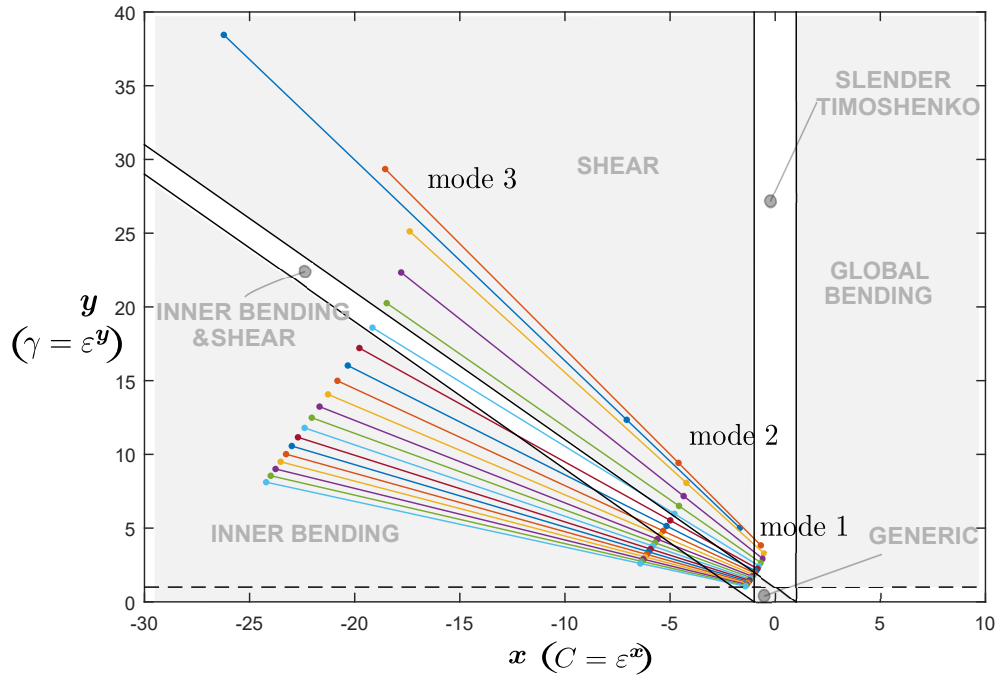


FIGURE 1.21: Domain behavior variation according to the vibration mode of a set of ten structures. Each line represents a specific structure.

Another way to see how the mechanisms are associated with the frequency ratios is by considering Figure 1.22. The horizontal axis corresponds to the macroscopic constant  $C$  and the vertical axis is the ratio between the frequency  $f_{EBM_i}$  of the mode  $i$  and the first frequency  $f_{EBM_1}$ . This graph is the same as in Figure 1.19(B) but with a differentiation of the governing mechanism(s). In this figure, the identification criterion is performed only by considering the first vibration mode. Each dot corresponds to a different structure, and each color represents its identified structural behavior. For example, the black starred dots are the structures whose behavior, in the first vibration mode, is governed by the inner bending mechanism. The magenta starred dots belong to the inner bending combined with the shear of the cell. The blue dots refer to the structures purely behaving as shear beams. The green squared dots represent the structures governed by all three mechanisms. The red dots are the structures controlled by the shear and global bending mechanisms (Slender Timoshenko beam). Finally, the structures behaving as Euler Bernoulli beams (global bending mechanism) are illustrated by yellow dots.

Each curve made by the dots trend represents a specific thickness of the horizontal elements  $a_p$ . Over this line, the structures with the thickest walls are located at the top end of the curve, and the structures with the thinnest walls at the bottom end. So, the thickness of the walls  $a_m$  decreases as we move up-down on a curve given by  $a_p$ . When we start moving from the right to the left of the graph, we find structures with much thicker floors. Thus, the structures with stiff horizontal and vertical elements are those on the yellow region (i.e., global bending mechanism). We may think that only structures with very stiff vertical and horizontal elements are linked to very high frequency ratios, but in fact, the stiffness contrast between both elements can reproduce large ratios (inner bending mechanism) as well

as minimal frequency ratios (shear mechanism).

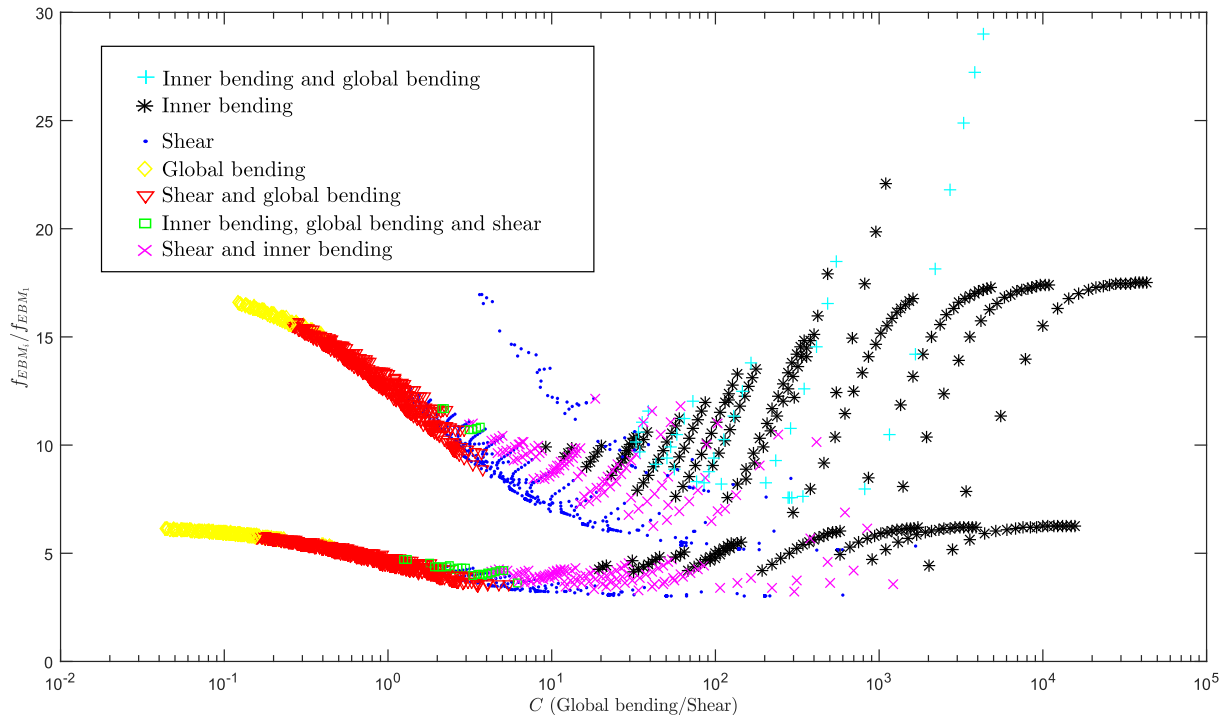


FIGURE 1.22: Relationship between the natural frequency ratios and the governing mechanism(s) of the first vibration mode.

During this parametric study, we have also investigate the evolution of the transverse motion of the structures by comparing the form of the first mode shape. Figure 1.23(Top) presents the normalized transverse displacement  $\hat{u}$  with respect to the top-story displacement  $\hat{u}_{max}$  obtained for each structure. In this graph, the horizontal axis represents the position of each story of the analyzed structures. The two thick black lines enclose the mode shapes of the studied structures. The line on the top border corresponds to the deformed shape of a shear beam (a quarter a cosine form) which can be associated with the structures governed by the shear mechanism. The line in the opposite side represents the deformed shape of an Euler-Bernoulli beam (a quarter of a sine form), which corresponds to the structures governed by the global bending or inner bending mechanism. The structures combining these mechanisms, e.g., Slender Timoshenko behavior, have an intermediate mode shape. Figure 1.23(Bottom) shows the normalized macroscopic rotation  $\hat{\alpha}$  with respect to  $\hat{u}_{max}$ . The maximum values of  $\hat{\alpha}$  are linked to the structures with a high importance of the global bending mechanism. On the contrary, the very low values of  $\hat{\alpha}$  are associated with mainly shear or inner bending type structures where the deformation is lead by the transverse displacement  $\hat{u}$ .

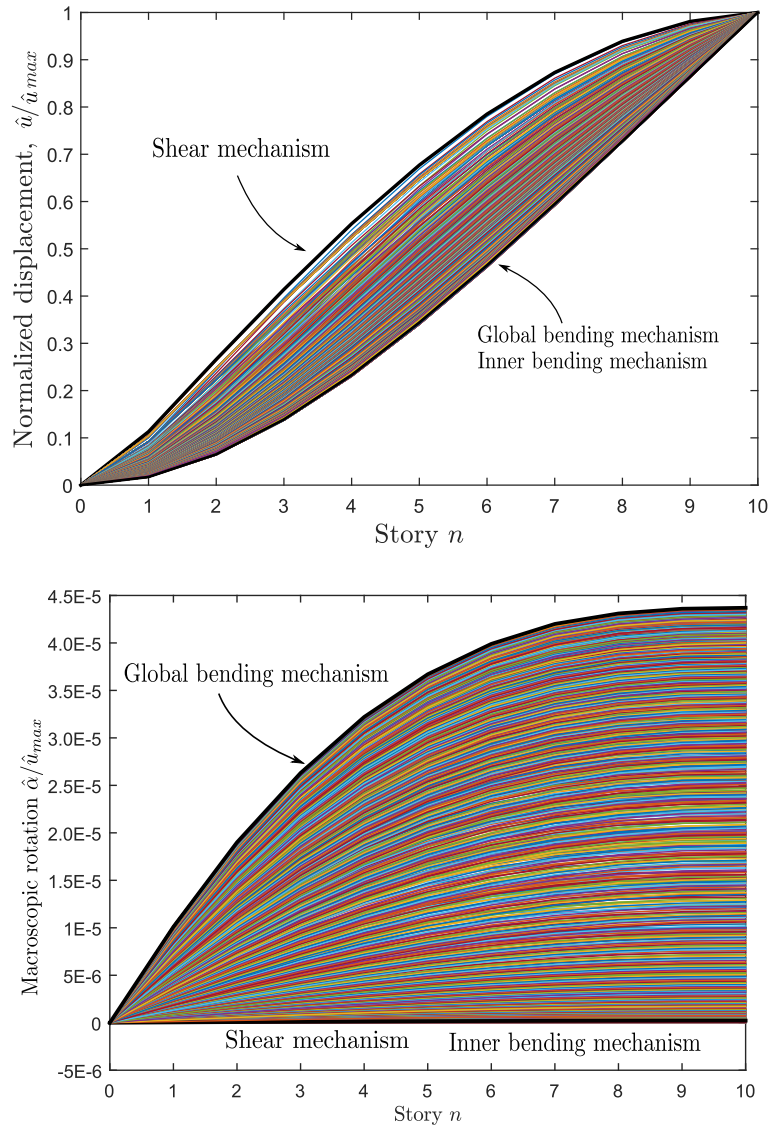


FIGURE 1.23: Evolution of (Top) the transverse displacement and (Bottom) the macroscopic rotation for the studied structures.

## 1.6 Conclusion and perspectives

The interest of this chapter is threefold:

- introduce the beam models issued from the homogenization method of periodic discrete media (HPDM) implemented on single frame structures, especially the generic beam model of [Boutin and Hans, 2003, Hans and Boutin, 2008], here called Equivalent Beam Model (EBM), which constitutes the basis of this study,
- provide a numerical procedure, here called *hybrid analysis*, that solves the kinematics within the unit cell and allows the calculations of the macroscopic parameters from the static analysis of a unique cell (or story),

- and understand the mechanical functioning of a reticulated structure and the effect of the variation of its characteristics.

We implemented the hybrid analysis on several fictitious structures and reproduced the analytical results given in the literature. These previous results were restricted to very simple cases: single and double frame structures. In this work, the EBM was applied to a great variety of multiple frame structures. The comparisons with numerical models built in the Cast3M FEM software conclude that the analytical results are encouraging, and more complex structures could be modeled.

We have seen that the type of boundary conditions used in the one-story model can strongly influence the coherence of the results. It was verified that the estimation of the shear stiffness of the cell closest to the analytical formula is obtained when adopting the boundary conditions B: differential horizontal motion between the bottom and the top of each vertical element, periodic nodal rotation and blocking of the vertical displacement of every node. Likewise, in the present study, the analysis of triple frame structures validates the previous results (beam models, identification criterion, procedure of the hybrid analysis) for most of the treated cases. Only for some highly contrasted structures, whose behavior is governed by the deformation of a small part, an adaptation of the models is required. The numerical results also confirm that better results can be obtained with a specific model. The parametric study utilizing the EBM also highlights that the natural frequencies and mode shapes can provide a rapid insight into a structure behavior. The natural frequencies and the mode shapes are dynamic properties that can be obtained easily experimentally. From the engineering point of view, the relation between the frequencies associated with the different models could represent a valuable guidance to identify the best model to be implemented quickly.

Although the EBM and the hybrid analysis retrieve the numerical results for the multiple frame structures treated in this work, it is necessary to analyze the influence of other elements present in common civil engineering infrastructures such as braces or filled areas (e.g., filled frames by masonry walls). In addition, there is the necessity to develop three-dimensional beam models to include the effects of torsion or to study asymmetric structures with coupling between the different directions.

Concerning the boundary conditions utilized for the Equivalent Beam Model, all the treated structures in this research were assumed clamped at the base and free at the top to represent the building conditions. Nevertheless, other boundary conditions should be investigated to confirm the accuracy of the EBM. For example, in civil engineering, buildings founded on soft soils should be modeled with base conditions less restrained to account for the flexibility of the foundation.

This study encourages the use of homogenized models such as the EBM in engineering applications to reduce the computational costs.

## Chapter 2

# Finite element formulation of the homogenized beam

*This chapter is part of a paper entitled «Finite element formulation of a homogenized beam for reticulated structure dynamics» submitted for publication in Computers&Structures*

**Abstract** The aim of this chapter is the development of an efficient finite element formulation to solve the weak form of the governing equations of the equivalent beam model presented in Chapter 1 that rule the global dynamic response of reticulated structures. We recall that the studied model is a 1D enriched form of the fourth-order Timoshenko beam equation and the motion is described by a sixth-order differential equation. The higher order of the differential equation is attributed to an additional kinematic mechanism that may appear under large stiffness contrasts between the cell elements. In this context, the construction of an original finite-element approximate solution is proposed. Weak formulations lead to generalized elementary stiffness and mass matrices. Through a representative example in the framework of linear elasticity, it is shown that this homogenized beam finite element (*HBFEM*) solution recovers the analytical results and is close to the finite element solution of the detailed structural model. This new formulation simplifies the implementation of the beam-like model in complex configurations, enables parametric studies, and could be easily used for a wide range of applications in the field of dynamics of solids and structures, other than free vibration analysis, at reduced computational costs.

### 2.1 EBM Weak formulation

The weak formulation permits the transfer of the exact or analytical solution of a problem to a numerical approximation. The EBM weak form is build from the strong form. This last is the result of the combination of the constitutive laws and equilibrium equations that are recalled here:

*Constitutive laws:*

$$\begin{aligned}
\text{Shear Force} \quad T(x, t) &= K_s \left( \frac{\partial u(x, t)}{\partial x} - \alpha(x, t) \right) \\
\text{Inner bending moment} \quad \mathcal{M}(x, t) &= \mathcal{K}_i \frac{\partial^2 u(x, t)}{\partial x^2} \\
\text{Global bending moment} \quad M(x, t) &= \mathcal{K}_g \frac{\partial \alpha(x, t)}{\partial x}
\end{aligned} \tag{2.1}$$

*Equilibrium equations:*

$$\forall x \in \Omega, \forall t \in [0, t_D], \left\{ \begin{aligned} \mathcal{T}(x, t) &= T(x, t) - \frac{\partial \mathcal{M}(x, t)}{\partial x} \\ \frac{\partial \mathcal{T}(x, t)}{\partial x} &= \Lambda \frac{\partial^2 u(x, t)}{\partial t^2} + f(x, t) \\ \frac{\partial \mathcal{M}(x, t)}{\partial x} &= -T(x, t) \end{aligned} \right. \tag{2.2}$$

We are interested in the displacement field  $u$  and the macroscopic rotation field  $\alpha$  as a function of the position  $x$  in the domain  $\Omega$ . The strong formulation of the system given in Equations (2.1) and (2.2) for each solution field is:

*Strong formulation:*

$$0 = \frac{\partial}{\partial x} \left[ K_s \left( \frac{\partial u}{\partial x} - \alpha \right) \right] - \frac{\partial^2}{\partial x^2} \left( \mathcal{K}_i \frac{\partial^2 u}{\partial x^2} \right) - f(x, t) - \Lambda \frac{\partial^2 u}{\partial t^2} \tag{2.3}$$

$$0 = \frac{\partial}{\partial x} \left( \mathcal{K}_g \frac{\partial \alpha}{\partial x} \right) + K_s \left( \frac{\partial u}{\partial x} - \alpha \right) \tag{2.4}$$

The procedure used in the development of the weak form involves three main steps as stated in [Reddy, 2004]. Let's consider the time independent arbitrary virtual fields  $u^*$  and  $\alpha^*$  kinematically admissible (KA) to zero (i.e.  $u^* = 0$ ,  $\partial u^*/\partial x = 0$  and  $\alpha^* = 0$  on  $\partial\Omega_u$ ), solution fields  $u$  and  $\alpha$  kinematically admissible (i.e.  $u = u_p$ ,  $\partial u/\partial x = u'_p$  and  $\alpha = \alpha_p$  on  $\partial\Omega_u$ ) and initial conditions for  $u$  (i.e.  $\partial^\ell u(x, 0)/\partial t^\ell = u^{(\ell)}$  for  $\ell = 0$  or  $1$ ).

Firstly, the strong formulation equations (Equations (2.3) and (2.4)) are multiplied by the virtual (or weighting) fields  $u^*$  and  $\alpha^*$  and integrated over the domain of interest. Herein, the numerical integration over the time domain is omitted on purpose.

$$0 = \int_0^H u^* \left\{ \frac{\partial}{\partial x} \left[ K_s \left( \frac{\partial u}{\partial x} - \alpha \right) \right] - \frac{\partial^2}{\partial x^2} \left( \mathcal{K}_i \frac{\partial^2 u}{\partial x^2} \right) - f(x, t) - \Lambda \frac{\partial^2 u}{\partial t^2} \right\} dx \tag{2.5}$$

$$0 = \int_0^H \alpha^* \left\{ \frac{\partial}{\partial x} \left( \mathcal{K}_g \frac{\partial \alpha}{\partial x} \right) + K_s \left( \frac{\partial u}{\partial x} - \alpha \right) \right\} dx \tag{2.6}$$

Secondly, it is required to distribute the differentiation by integrating the first term of both equations once by parts and the second term of the first equation twice. This procedure leads to:

$$0 = \int_0^H \left[ \frac{d^2 u^*}{dx^2} \left( \mathcal{K}_i \frac{\partial^2 u}{\partial x^2} \right) + \frac{du^*}{dx} \left( K_s \left( \frac{\partial u}{\partial x} - \alpha \right) \right) + u^* f(x, t) + u^* \Lambda \frac{\partial^2 u}{\partial t^2} \right] dx - \left[ u^* \left[ K_s \left( \frac{\partial u}{\partial x} - \alpha \right) - \frac{\partial}{\partial x} \left( \mathcal{K}_i \frac{\partial^2 u}{\partial x^2} \right) \right] \right]_0^H - \left[ \frac{du^*}{dx} \left( \mathcal{K}_i \frac{\partial^2 u}{\partial x^2} \right) \right]_0^H \quad (2.7)$$

$$0 = \int_0^H \left[ \frac{d\alpha^*}{dx} \left( \mathcal{K}_g \frac{\partial \alpha}{\partial x} \right) - \alpha^* K_s \left( \frac{\partial u}{\partial x} - \alpha \right) \right] dx - \left[ \alpha^* \left( \mathcal{K}_g \frac{\partial \alpha}{\partial x} \right) \right]_0^H \quad (2.8)$$

Thirdly, the actual boundary conditions are imposed. The coefficients of the weighting functions  $u^*$ ,  $\frac{du^*}{dx}$ , and  $\alpha^*$  in the boundary integrals correspond to the total shear force  $\mathcal{T}$ , the inner bending moment  $\mathcal{M}$ , and the global bending moment  $M$ , respectively.

$$\mathcal{T} \equiv K_s \left( \frac{\partial u}{\partial x} - \alpha \right) - \frac{\partial}{\partial x} \left( \mathcal{K}_i \frac{\partial^2 u}{\partial x^2} \right) \quad \mathcal{M} \equiv \mathcal{K}_i \frac{\partial^2 u}{\partial x^2} \quad M \equiv \mathcal{K}_g \frac{\partial \alpha}{\partial x} \quad (2.9)$$

The latter fields are the secondary variables of the weak form, while  $u$ ,  $\frac{du}{dx}$  and  $\alpha$  are called the primary variables. The boundary variables can be denoted at the end points of the domain as  $\mathcal{T}_0$ ,  $\mathcal{M}_0$ ,  $M_0$  at  $x = 0$  and  $\mathcal{T}_H$ ,  $\mathcal{M}_H$ ,  $M_H$  at  $x = H$ . The weak statements given in (2.7) and (2.8) can be expressed in the final form:

$$0 = \int_0^H \left[ \frac{d^2 u^*}{dx^2} \left( \mathcal{K}_i \frac{\partial^2 u}{\partial x^2} \right) + \frac{du^*}{dx} \left( K_s \left( \frac{\partial u}{\partial x} - \alpha \right) \right) + u^* f(x, t) + u^* \Lambda \frac{\partial^2 u}{\partial t^2} \right] dx + u^*(0) \mathcal{T}_0 - u^*(H) \mathcal{T}_H + \frac{du^*}{dx} \Big|_0 \mathcal{M}_0 - \frac{du^*}{dx} \Big|_H \mathcal{M}_H \quad (2.10)$$

$$0 = \int_0^H \left[ \frac{d\alpha^*}{dx} \left( \mathcal{K}_g \frac{\partial \alpha}{\partial x} \right) - \alpha^* K_s \left( \frac{\partial u}{\partial x} - \alpha \right) \right] dx + \alpha^*(0) M_0 - \alpha^*(H) M_H \quad (2.11)$$

The weak formulation can also be defined by Equation (2.12) as the sum of these two equations (Equations (2.10) and (2.11)).

$$\int_{\Omega} \left\{ \left( \frac{du^*}{dx} - \alpha^* \right) T + \frac{d^2 u^*}{dx^2} \mathcal{M} + \frac{d\alpha^*}{dx} M + u^* \Lambda \frac{\partial^2 u}{\partial t^2} \right\} dx = - \int_{\Omega} u^* f(x, t) dx + \int_{\partial\Omega_F} \left\{ u^* \mathcal{T} + \frac{du^*}{dx} \mathcal{M} + \alpha^* M \right\} dx \quad (2.12)$$

The classical variational equation associated with the weak formulation is retrieved (Equation (2.13)).

$$\forall (u^*, \alpha^*) \text{ KA to } 0, \forall (u, \alpha) \text{ KA and } \left[ \partial^\ell u(x, 0) / \partial t^\ell = u_0^{(\ell)} \text{ for } \ell = 0 \text{ or } 1 \right] \quad (2.13)$$

$$a((u, \alpha), (u^*, \alpha^*)) + \frac{\partial^2}{\partial t^2} b((u, \alpha), (u^*, \alpha^*)) = L(u^*, \alpha^*)$$



By introducing the constitutive laws defined in Equation (2.2), the following expressions are obtained for the linear form  $L$  and the bilinear forms  $a$  and  $b$  (Equation (2.14)).

$$\begin{aligned}
 a((u, \alpha), (u^*, \alpha^*)) &= \int_{\Omega} \left\{ \left( \frac{du^*}{dx} - \alpha^* \right) K_s \left( \frac{\partial u}{\partial x} - \alpha \right) + \frac{d^2 u^*}{dx^2} \mathcal{K}_i \frac{\partial^2 u}{\partial x^2} + \frac{d\alpha^*}{dx} \mathcal{K}_g \frac{\partial \alpha}{\partial x} \right\} dx \\
 b((u, \alpha), (u^*, \alpha^*)) &= \int_{\Omega} \{ u^* \Lambda u \} dx \\
 L(u^*, \alpha^*) &= - \int_{\Omega} u^* f(x, t) dx + \int_{\partial\Omega_F} \left\{ u^* \mathcal{T} + \frac{du^*}{dx} \mathcal{M} + \alpha^* M \right\} dx
 \end{aligned} \tag{2.14}$$

## 2.2 Enriched finite element formulation for reticulated structures

The weak form of the EBM enables the development of the homogenized beam finite element (HBFEM) formulation. This section details the construction of the finite element through the following steps:

- Formulation of the finite element model for an arbitrary degree of approximation.
- Choice of the approximation functions for the kinematic variables  $u$  and  $\alpha$  based on their differentiability requirements.
- Derivation of the approximation functions for  $u$  and  $\alpha$  over the element domain  $\Omega_e$ .
- Computation of the elementary matrices (stiffness and mass).

### 2.2.1 Finite element of the EBM

The 1D EBM is defined in  $\Omega = [0, H]$  and involves six degrees of freedom (DoF), three at each end, defined by  $u$ ,  $u'$ , and  $\alpha$ . In order to approximate the virtual fields  $u^*$  and  $\alpha^*$  and the solution fields  $u$  and  $\alpha$ , a 1D finite element beam is considered. The approximate fields are denoted by a '^'. The classical kinematic quantities  $\hat{u}$  (i.e. transverse displacement) and  $\hat{\alpha}$  (i.e. macroscopic rotation) are considered as well as  $\hat{u}'$  (i.e. derivative of  $\hat{u}$  with respect to  $x$ ). The latter term is introduced in order to manage the enrichment introduced by the consideration of inner bending in the structure.

Figure 2.1.(a) presents the physical problem and states the boundary conditions on the equivalent beam. Figure 2.1.b shows the discretized beam element and the notations associated with the HBFEM model.

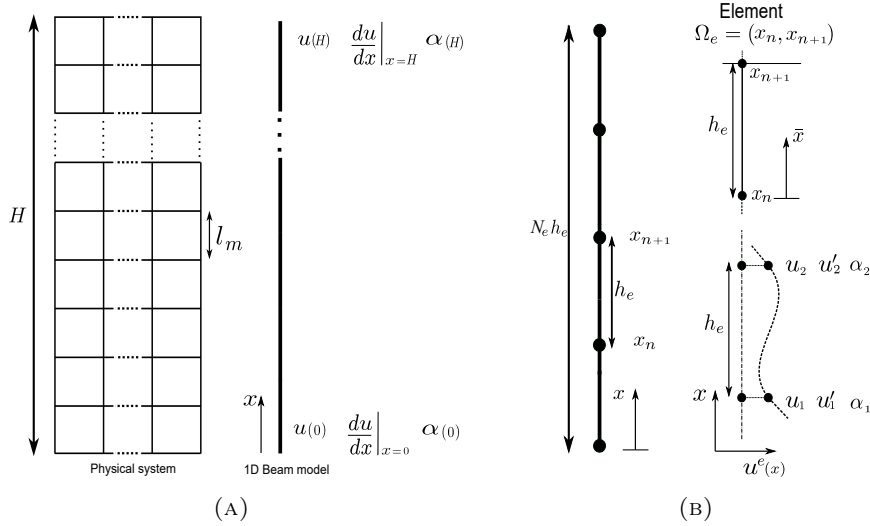


FIGURE 2.1: Finite element discretization for reticulated structures based on the EBM. (a) Physical problem, EBM, boundary conditions. (b) Definition of finite elements.

The approximation  $(\cdot)^e$  on element  $e$  of the solution fields  $u$  and  $\alpha$  as well as the virtual fields  $u^*$  and  $\alpha^*$  can be written as:

$$u^e(x, t) = \sum_{j=1}^m \hat{U}_j^e(t) \cdot \phi_j^{eU}(x) \quad ; \quad \alpha^e(x, t) = \sum_{j=1}^p \hat{\alpha}_j^e(t) \cdot \psi_j^{e\alpha}(x) \quad (2.15)$$

$$u^{*e}(x, t) = \sum_{j=1}^m \hat{U}_j^{*e}(t) \cdot \phi_j^{eU}(x) \quad ; \quad \alpha^{*e}(x, t) = \sum_{j=1}^p \hat{\alpha}_j^{*e}(t) \cdot \psi_j^{e\alpha}(x)$$

where  $\hat{U}^e$  and  $\hat{\alpha}^e$  are the values of the solution at the nodes of the finite element and  $m + p$  is to the number of DoF of the finite element.  $\phi_j^{eU}(x)$  and  $\psi_j^{e\alpha}(x)$  denote the interpolation functions associated with the DoF  $k$  (i.e.  $u, u', \alpha$ ) of degree  $m - 1$  and  $p - 1$ , respectively. For polynomial interpolation functions,  $m$  and  $p$  indicate the order of the polynomial. For the sake of conciseness, Equation (2.15) is rewritten in a vectorial form:

$$u^e(x, t) = \mathbf{D}_e^{uT}(x) \hat{\mathbf{u}}_e(t) + \mathbf{D}_e^{u'T}(x) \hat{\mathbf{u}}_e'(t) = \mathbf{D}_e^{uT}(x) \hat{\mathbf{U}}_e(t) \quad ; \quad \alpha^e(x, t) = \mathbf{D}_e^{\alpha T}(x) \hat{\boldsymbol{\alpha}}_e(t)$$

$$u^{*e}(x, t) = \mathbf{D}_e^{uT}(x) \hat{\mathbf{u}}_e^*(t) + \mathbf{D}_e^{u'T}(x) \hat{\mathbf{u}}_e'^*(t) = \mathbf{D}_e^{uT}(x) \hat{\mathbf{U}}_e^*(t) \quad ; \quad \alpha^{*e}(x, t) = \mathbf{D}_e^{\alpha T}(x) \hat{\boldsymbol{\alpha}}_e^*(t) \quad (2.16)$$

where  $\mathbf{D}_e^k$  is the vector containing the interpolation functions (shape functions) associated with the DoF  $k$  over the element,  $\hat{\mathbf{U}}_e$  is the vector of the element degrees of freedom associated with  $u$ , and  $\hat{\boldsymbol{\alpha}}_e$  is the vector of the element degrees of freedom associated with  $\alpha$ .

The vectorial form of the derivatives of the different fields is expressed as:

$$\begin{aligned} \frac{\partial u^e(x,t)}{\partial x} &= \mathbf{B}_e^{U^T}(x) \hat{\mathbf{U}}_e(t) \quad ; \quad \frac{\partial^2 u^e(x,t)}{\partial x^2} = \mathbf{B}'_e^{U^T}(x) \hat{\mathbf{U}}_e(t) \quad ; \quad \frac{\partial \alpha^e(x,t)}{\partial x} = \mathbf{B}_e^{\alpha^T}(x) \hat{\boldsymbol{\alpha}}_e(t) \\ \frac{\partial u^{*e}(x,t)}{\partial x} &= \mathbf{B}_e^{U^T}(x) \hat{\mathbf{U}}_e^*(t) \quad ; \quad \frac{\partial^2 u^{*e}(x,t)}{\partial x^2} = \mathbf{B}'_e^{U^T}(x) \hat{\mathbf{U}}_e^*(t) \quad ; \quad \frac{\partial \alpha^{*e}(x,t)}{\partial x} = \mathbf{B}_e^{\alpha^T}(x) \hat{\boldsymbol{\alpha}}_e^*(t) \end{aligned} \quad (2.17)$$

where  $\mathbf{B}_e^k$  and  $\mathbf{B}'_e^k$  are the vectors containing the first and second derivatives of the interpolation functions respectively. By considering the bilinear form  $a((u, \alpha), (u^*, \alpha^*))$  given in Equation (2.14) on the element domain  $\Omega_e$  and the interpolation given in Equations (2.16) and (2.17), the stiffness matrix  $\mathbf{K}_t$  can be derived by multiplying the solution and virtual fields (Equation (2.18)).

$$\mathbf{K}_t = \int_{\Omega_e} \left\{ \begin{bmatrix} \mathbf{B}_e^U \\ -\mathbf{D}_e^\alpha \end{bmatrix} \mathcal{K}_s \begin{bmatrix} \mathbf{B}_e^U \\ -\mathbf{D}_e^\alpha \end{bmatrix}^T + \begin{bmatrix} \mathbf{B}'_e^U \\ \mathbf{0} \end{bmatrix} \mathcal{K}_i \begin{bmatrix} \mathbf{B}'_e^U \\ \mathbf{0} \end{bmatrix}^T + \begin{bmatrix} \mathbf{0} \\ \mathbf{B}_e^\alpha \end{bmatrix} \mathcal{K}_g \begin{bmatrix} \mathbf{0} \\ \mathbf{B}_e^\alpha \end{bmatrix}^T \right\} dx \quad (2.18)$$

By considering the bilinear form  $b((u, \alpha), (u^*, \alpha^*))$  given in equation (2.14) for an element  $\Omega_e$  and the interpolation given in Equations (2.16), the elementary mass matrix  $\mathbf{M}_e$  can be derived (Equation (2.19)).

$$\mathbf{M}_e = \int_{\Omega_e} \begin{bmatrix} \mathbf{D}_e^U \\ \mathbf{0} \end{bmatrix} \Lambda \begin{bmatrix} \mathbf{D}_e^U \\ \mathbf{0} \end{bmatrix}^T dx \quad (2.19)$$

Note that the lines and columns associated with  $\alpha$  are empty because of the absence of the rotational inertia in the EBM.

## 2.2.2 Choice criterion of the interpolation functions

Two main criteria are taken into account to define the differentiability requirement of the approximation functions for the primary variables,  $u^e$  and  $\alpha^e$ :

$$u^e(x, t) = \sum_{j=1}^m \hat{\mathbf{U}}_j^e(t) \cdot \phi_j^e(x) \quad , \quad \alpha^e(x, t) = \sum_{j=1}^p \hat{\boldsymbol{\alpha}}_j^e(t) \cdot \psi_j^e(x) \quad (2.20)$$

- The essential boundary conditions of the element with end points  $n$  and  $n+1$  at time  $t$ :

$$u^e(x_n) = \hat{\mathbf{U}}_1^e, \quad u^e(x_n) = \hat{\mathbf{U}}_2^e, \quad u^e(x_{n+1}) = \hat{\mathbf{U}}_3^e, \quad u^e(x_{n+1}) = \hat{\mathbf{U}}_4^e \quad (2.21)$$

$$\alpha^e(x_n) = \hat{\boldsymbol{\alpha}}_1, \quad \alpha^e(x_{n+1}) = \hat{\boldsymbol{\alpha}}_2$$

- The degree of differentiation in the weak formulation, Equation (2.12). The approximation functions  $\phi_j^e$  and  $\psi_j^e$  should be continuous and differentiable as many times the weak formulation requires.

*Differentiability requirement.* On one side, the highest derivative involved in the weak formulation (Equation (2.12)) is the second derivative of  $u$  linked to the inner bending moment. It is therefore required to find a continuous approximation function for  $u^e$  with nonzero derivatives up to order two. On the other side, the term associated with the global bending moment shows that  $\alpha^e$  needs an approximation function derivable at least once with a nonzero derivative.

Inspired from the finite element formulations of the classical Euler-Bernoulli and Timoshenko beams, herein, polynomial functions are used to satisfy the approximation up to the highest relevant order. One reason for this choice is that the differentiation and the numerical integration of the algebraic polynomials are easy to handle. Since there are 6 conditions in an element, 6 polynomial terms are used, four of them for  $u^e$  (third degree polynomial) and two for  $\alpha^e$  (affine function):

$$u^e(x) = c_0 + c_1x + c_2x^2 + c_3x^3, \quad \alpha^e(x) = d_0 + d_1x \quad (2.22)$$

With such polynomial functions, the differentiability requirement is met. However, it should be noted that these functions have the minimum order required to satisfy the weak formulation of the boundary problem.

### 2.2.3 Derivation of the interpolation functions

*Element geometry associated with  $u^e$ .* As the third degree polynomial is defined by four parameters, four kinematic variables must be identified inside the element. To simultaneously define the geometry of the element, two of the nodal displacements are considered at the endpoints of the element. The other two are also set at the ends through their first derivatives. The first derivatives of  $u$ , involved in the boundary conditions, need to be included in the computation of the interpolation functions. The definition of the dependent variable  $u$  and its derivative at the nodes are thus ensured and no additional nodes are needed. Figure 2.2 displays the discrete element geometry and the nodal conditions for  $u$ . This continuity condition identifies the resulting functions as *Hermite interpolation functions*.

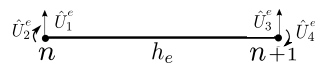


FIGURE 2.2: Nodal displacements and their derivatives in the discrete element with the notation defined in Equation (2.21).

Consequently, the approximate transverse displacement  $u^e$  in the element is as follows:

$$u^e(x) = \phi_1^e(x)\hat{U}_1^e + \phi_2^e(x)\hat{U}_2^e + \phi_3^e(x)\hat{U}_3^e + \phi_4^e(x)\hat{U}_4^e \quad (2.23)$$

For each independent Hermite function  $\phi_j^e$  (cubic polynomials), four parameters  $c_0^{(j)}, c_1^{(j)}, c_2^{(j)}$  and  $c_3^{(j)}$  are required with respect to the boundary conditions. The first function  $\phi_1^e$  is associated with the displacement of the node 1. Therefore, it needs to be equal to 1 at  $x_n$  and

0 at  $x_{n+1}$ , and its first derivative needs to be equal to 0 at both extremities. Likewise, the function  $\phi_3^e$  needs to be equal to 1 at  $x_{n+1}$  and 0 at  $x_n$  with zero derivatives at both ends. The second and fourth interpolation functions need to be 0 at both ends but their derivatives are set to 1 at  $x_n$  for  $\phi_2^e$  and at  $x_{n+1}$  for  $\phi_4^e$ .

The solution of the four systems of four equations leads to the interpolation functions  $\phi_j^e$  in terms of the local coordinate  $\bar{x}$  (Figure 2.1(b)):

$$\phi_1^e(\bar{x}) = 1 - 3 \left( \frac{\bar{x}}{h_e} \right)^2 + 2 \left( \frac{\bar{x}}{h_e} \right)^3, \quad \phi_2^e(\bar{x}) = \bar{x} \left( 1 - \frac{\bar{x}}{h_e} \right)^2 \quad (2.24)$$

$$\phi_3^e(\bar{x}) = 3 \left( \frac{\bar{x}}{h_e} \right)^2 - 2 \left( \frac{\bar{x}}{h_e} \right)^3, \quad \phi_4^e(\bar{x}) = \bar{x} \left[ \left( \frac{\bar{x}}{h_e} \right)^2 - \frac{\bar{x}}{h_e} \right]$$

Figure 2.3 depicts this set of Hermite interpolation functions and their derivatives.

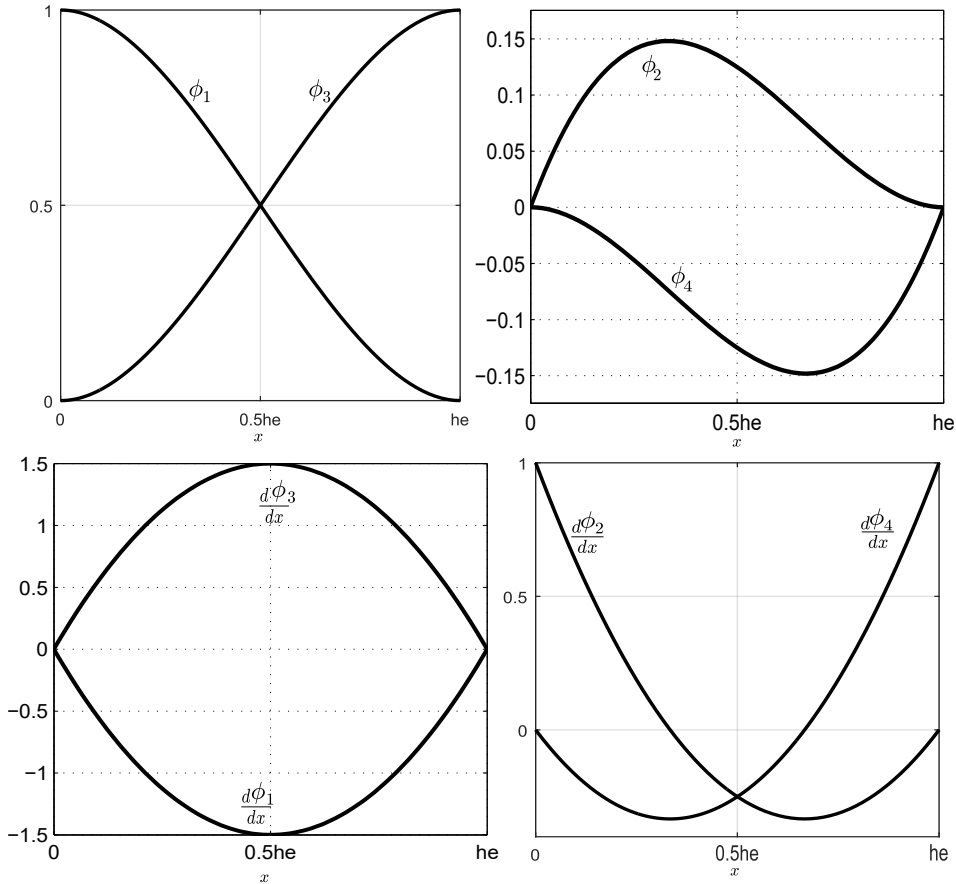


FIGURE 2.3: Hermite cubic interpolation functions (top) and their derivatives (bottom) for  $u^e$ .

*Element geometry associated with  $\alpha^e$ .* Since an affine polynomial approximation is described by two parameters only, two nodal variables are chosen at the end points of the element to describe its geometry properly. However, it is desired to increase the order of the interpolation functions of  $\alpha^e$  in order to improve the approximation to the solution field.

Thus, an internal node is defined inside the element (at  $\bar{x} = h_e/2$ ) following the strategy used in [Caillerie et al., 2015]. The order of the polynomial for  $\alpha^e$  given in Equation (2.22) is then increased by one (i.e., quadratic three-noded polynomial function):

$$\alpha^e(x) = d_0 + d_1x + d_2x^2 \quad (2.25)$$

Figure 2.4 shows the element geometry associated with the macroscopic rotation.

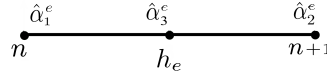


FIGURE 2.4: Nodal macroscopic rotation in the discrete element

Note that the order of the interpolation functions of both solution fields  $u$  and  $\alpha$  differs by one. It is then expected to have a consistent interpolation that allows avoiding the shear locking problem involved in classical Timoshenko beam models and plate models, commonly found when the shear stiffness is much bigger than the global bending stiffness [Reddy, 1997]. Thus, the approximation of the macroscopic rotation  $\alpha$  is as follows,

$$\alpha^e(x) = \psi_1^e(x)\hat{\alpha}_1 + \psi_2^e(x)\hat{\alpha}_2 + \psi_3^e(x)\hat{\alpha}_3 \quad (2.26)$$

more specifically,

$$\alpha^e(x) = \psi_1^e(x)\alpha^e(x_n) + \psi_2^e(x)\alpha^e(x_{n+1}) + \psi_3^e(x)\alpha^e\left(x_n + \frac{h_e}{2}\right) \quad (2.27)$$

The procedure used to determine the parameters of the cubic polynomials which approximate  $u^e$  is implemented again and the three systems of three equations are solved. The solution for the three parameters  $d_0^{(j)}$ ,  $d_1^{(j)}$ , and  $d_2^{(j)}$  for each interpolation function  $\psi_j^e$  yields the following *Lagrange family functions* (displayed in Figure 2.5):

$$\psi_1^e(\bar{x}) = \left(1 - \frac{\bar{x}}{h_e}\right) \left(1 - \frac{2\bar{x}}{h_e}\right), \quad \psi_2^e(\bar{x}) = -\frac{\bar{x}}{h_e} \left(1 - \frac{2\bar{x}}{h_e}\right), \quad \psi_3^e(\bar{x}) = 4\frac{\bar{x}}{h_e} \left(1 - \frac{\bar{x}}{h_e}\right) \quad (2.28)$$

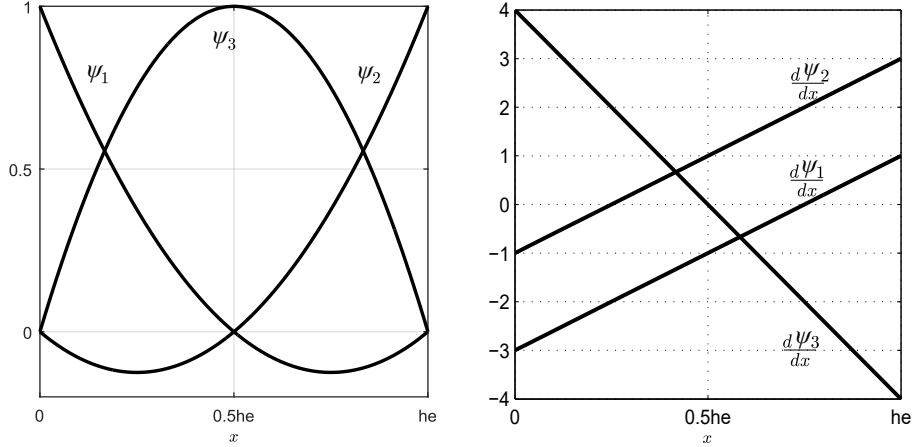


FIGURE 2.5: Lagrange quadratic interpolation functions (left) and their derivatives (right) for  $\alpha^e$ .

### 2.2.4 Elementary matrices

The seven algebraic equations of the finite element formulation are derived from the weak formulation (Equations (2.10) and (2.11)) in the following way. First, the solution fields  $u$  and  $\alpha$  are written as linear combinations of the interpolation functions (Equations (2.20)). Second, the virtual fields  $u^*$  and  $\alpha^*$  are successively chosen equal to each of the interpolation function. Thus, by taking  $u^* = \phi_k^e$  for  $k = 1, 2, 3$  or  $4$ , Equation (2.10) leads to the four following equations:

$$0 = \sum_{j=1}^4 \left( \int_{\Omega^e} \left[ \mathcal{K}_i \frac{d^2 \phi_k^e}{dx^2} \frac{d^2 \phi_j^e}{dx^2} + \mathcal{K}_s \frac{d\phi_k^e}{dx} \frac{d\phi_j^e}{dx} \right] dx \right) \hat{U}_j^e + \sum_{j=1}^4 \left( \int_{\Omega^e} \Lambda \phi_j^e \phi_k^e \right) \frac{\partial^2}{\partial t^2} \hat{U}_j^e - \sum_{j=1}^3 \left( \int_{\Omega^e} \mathcal{K}_s \frac{d\phi_k^e}{dx} \psi_j^e \right) \hat{\alpha}_j^e + \int_{\Omega^e} f \phi_k^e dx + Q_k^{e(1)} \quad (2.29)$$

and by taking  $\alpha^* = \psi_k^e$  for  $k = 1, 2$  or  $3$ , Equation (2.11) leads to the three following equations:

$$0 = \sum_{j=1}^3 \left( \int_{\Omega^e} \left[ \mathcal{K}_g \frac{d\psi_k^e}{dx} \frac{d\psi_j^e}{dx} + \mathcal{K}_s \psi_k^e \psi_j^e \right] dx \right) \hat{\alpha}_j^e - \sum_{j=1}^4 \left( \int_{\Omega^e} \mathcal{K}_s \psi_k^e \frac{d\phi_j^e}{dx} dx \right) \hat{U}_j^e + Q_k^{e(2)} \quad (2.30)$$

where

$$Q_k^{e(1)} = - \int_{\partial\Omega_f^e} \left( \phi_k^e \mathcal{T} + \frac{d\phi_k^e}{dx} \mathcal{M} \right) dx \quad ; \quad Q_k^{e(2)} = - \int_{\partial\Omega_f^e} \psi_k^e M dx$$

Therefore, it is possible to identify the components of the stiffness matrix  $K_t$ :

$$\mathbf{K}_t = \begin{bmatrix} \mathbf{K}^{e(11)} & \mathbf{K}^{e(12)} \\ \mathbf{K}^{e(21)} & \mathbf{K}^{e(22)} \end{bmatrix} \quad (2.31)$$

$$K_{kj}^{e(11)} = \int_{\Omega^e} \left( \mathcal{K}_i \frac{d^2 \phi_k^e}{dx^2} \frac{d^2 \phi_j^e}{dx^2} + K_s \frac{d \phi_k^e}{dx} \frac{d \phi_j^e}{dx} \right) dx \quad ; \quad K_{kj}^{e(12)} = - \int_{\Omega^e} \left( K_s \frac{d \phi_k^e}{dx} \psi_j^e \right) dx$$

$$K_{kj}^{e(12)} = K_{jk}^{e(21)} \quad ; \quad K_{kj}^{e(22)} = \int_{\Omega^e} \left( \mathcal{K}_g \frac{d \psi_k^e}{dx} \frac{d \psi_j^e}{dx} + K_s \psi_k^e \psi_j^e \right) dx$$

where  $\mathbf{K}^{e(11)}$  is the  $4 \times 4$  matrix related to the translational DoF,  $\mathbf{K}^{e(22)}$  is the  $3 \times 3$  matrix related to the rotational DoF,  $\mathbf{K}^{e(12)}$  and  $\mathbf{K}^{e(21)}$  are respectively  $4 \times 3$  and  $3 \times 4$  mixed matrices. The components of the mass matrix  $\mathbf{M}_e$  are given by:

$$M_{kj}^e = \int_{\Omega^e} \Lambda^e \phi_k^e \phi_j^e dx \quad (2.32)$$

The force vector of the beam element is defined by:

$$F_k^{e(1)} = \int_{\Omega^e} f \phi_k^e dx + Q_k^{e(1)} \quad ; \quad F_k^{e(2)} = Q_k^{e(2)} \quad (2.33)$$

The element degrees of freedom vector is:

$$\mathbf{E}_e = \left\{ u_1 \quad u_2 \quad u_3 \quad u_4 \quad \alpha_1 \quad \alpha_3 \quad \alpha_2 \right\}_e^T$$

where  $u_1$ ,  $u_2$  and  $\alpha_1$  are the degrees of freedom of the first node ( $x = x_n$ ),  $u_3$ ,  $u_4$  and  $\alpha_2$  are relative to the second node ( $x = x_{n+1}$ ) and  $\alpha_3$  is the internal degree of freedom located in the middle of the element. Superscript  $T$  represents the transposition operator.

Note that,  $u_1 = \hat{U}^e(x_n)$ ,  $u_2 = \left. \frac{d\hat{U}^e}{dx} \right|_{x=x_n}$ ,  $u_3 = \hat{U}^e(x_{n+1})$ , and  $u_4 = \left. \frac{d\hat{U}^e}{dx} \right|_{x=x_{n+1}}$ .

*Stiffness matrix*

Computing the integrals by using the interpolation functions (Equations (2.24) and (2.28)), the  $7 \times 7$  element stiffness matrix,  $\mathbf{K}_t$ , is:

$$\mathbf{K}_t = K_s \begin{bmatrix} \frac{6}{5h_e} + \frac{\mathcal{K}_i}{K_s} \frac{12}{h_e^3} & \frac{\mathcal{K}_i}{K_s} \frac{6}{h_e^2} + \frac{1}{10} & -\frac{6}{5h_e} - \frac{\mathcal{K}_i}{K_s} \frac{12}{h_e^3} & \frac{\mathcal{K}_i}{K_s} \frac{6}{h_e^2} + \frac{1}{10} & \frac{1}{10} & \frac{4}{5} & \frac{1}{10} \\ & \frac{2h_e}{15} + \frac{\mathcal{K}_i}{K_s} \frac{4}{h_e} & -\frac{\mathcal{K}_i}{K_s} \frac{6}{h_e^2} - \frac{1}{10} & \frac{\mathcal{K}_i}{K_s} \frac{2}{h_e} - \frac{h_e}{30} & -\frac{7h_e}{60} & \frac{h_e}{15} & \frac{h_e}{20} \\ & & \frac{6}{5h_e} + \frac{\mathcal{K}_i}{K_s} \frac{12}{h_e^3} & -\frac{\mathcal{K}_i}{K_s} \frac{6}{h_e^2} - \frac{1}{10} & -\frac{1}{10} & -\frac{4}{5} & -\frac{1}{10} \\ & & & \frac{2h_e}{15} + \frac{\mathcal{K}_i}{K_s} \frac{4}{h_e} & \frac{h_e}{20} & \frac{h_e}{15} & -\frac{7h_e}{60} \\ & \text{SYM} & & & \frac{2h_e}{15} + \frac{\mathcal{K}_g}{K_s} \frac{7}{3h_e} & \frac{h_e}{15} - \frac{\mathcal{K}_g}{K_s} \frac{8}{3h_e} & \frac{\mathcal{K}_g}{K_s} \frac{1}{3h_e} - \frac{h_e}{30} \\ & & & & & \frac{8h_e}{15} + \frac{\mathcal{K}_g}{K_s} \frac{16}{3h_e} & \frac{h_e}{15} - \frac{\mathcal{K}_g}{K_s} \frac{8}{3h_e} \\ & & & & & & \frac{2h_e}{15} + \frac{\mathcal{K}_g}{K_s} \frac{7}{3h_e} \end{bmatrix} \quad (2.34)$$



The matrix condensation technique is used to eliminate the interior degree of freedom  $\alpha_3$  and reduce the number of unknowns. The matrix  $\mathbf{K}_t$  is reorganized for  $\alpha_3$  (columns and rows are interchanged). The computation of the reduced matrix can be written as:

$$\mathbf{K}_e = \mathbf{K}_{aa} - \mathbf{K}_{ac}\mathbf{K}_{cc}^{-1}\mathbf{K}_{ca}$$

where  $a$  denotes the set of degrees of freedom retained for further analysis and  $c$  denotes the set of internal degrees of freedom to be condensed. Thus,  $\mathbf{K}_{aa} = \mathbf{K}_t(1 : 6, 1 : 6)$ ,  $\mathbf{K}_{ac} = \mathbf{K}_t(1 : 6, 7)$ ,  $\mathbf{K}_{ca} = \mathbf{K}_t(7, 1 : 6)$ , and  $\mathbf{K}_{cc} = \mathbf{K}_t(7, 7)$ . The reduced  $6 \times 6$  matrix  $\mathbf{K}_e$ , so-called consistent stiffness matrix, is presented in Equation 2.35. The difference between the matrices  $\mathbf{K}_t$  and  $\mathbf{K}_e$  is the addition of the coefficients  $a$ ,  $b$ ,  $c$ ,  $d$ , and  $e$  given in Equation 2.36.

$$\mathbf{K}_e = \mathbf{K}_s \begin{bmatrix} \frac{6}{5h_e} + \frac{\mathcal{K}_i}{K_s} \frac{12}{h_e^3} - a & \frac{\mathcal{K}_i}{K_s} \frac{6}{h_e^2} + \frac{1}{10} - b & -\frac{6}{5h_e} - \frac{\mathcal{K}_i}{K_s} \frac{12}{h_e^3} + a & \frac{\mathcal{K}_i}{K_s} \frac{6}{h_e^2} + \frac{1}{10} - b & \frac{1}{10} - c & \frac{1}{10} - c \\ \frac{2h_e}{15} + \frac{\mathcal{K}_i}{K_s} \frac{4}{h_e} - d & \frac{\mathcal{K}_i}{K_s} \frac{2}{h_e} - \frac{h_e}{30} - d & -\frac{\mathcal{K}_i}{K_s} \frac{6}{h_e^2} - \frac{1}{10} + b & \frac{\mathcal{K}_i}{K_s} \frac{2}{h_e} - \frac{h_e}{30} - d & -\frac{7h_e}{60} - \frac{h_e}{12} c & \frac{h_e}{20} - \frac{h_e}{12} c \\ \frac{6}{5h_e} + \frac{\mathcal{K}_i}{K_s} \frac{12}{h_e^3} - a & -\frac{\mathcal{K}_i}{K_s} \frac{6}{h_e^2} - \frac{1}{10} + b & \frac{6}{5h_e} + \frac{\mathcal{K}_i}{K_s} \frac{12}{h_e^3} - a & -\frac{\mathcal{K}_i}{K_s} \frac{6}{h_e^2} - \frac{1}{10} + b & -\frac{1}{10} + c & -\frac{1}{10} + c \\ \frac{2h_e}{15} + \frac{\mathcal{K}_i}{K_s} \frac{4}{h_e} - d & \frac{\mathcal{K}_i}{K_s} \frac{2}{h_e} - \frac{h_e}{30} - d & \frac{2h_e}{15} + \frac{\mathcal{K}_i}{K_s} \frac{4}{h_e} - d & \frac{\mathcal{K}_i}{K_s} \frac{2}{h_e} - \frac{h_e}{30} - d & \frac{h_e}{20} - \frac{h_e}{12} c & -\frac{7h_e}{60} - \frac{h_e}{12} c \\ \text{SYM} & & \text{SYM} & & \frac{2h_e}{15} + \frac{\mathcal{K}_g}{K_s} \frac{7}{3h_e} - e & \frac{\mathcal{K}_g}{K_s} \frac{1}{3h_e} - \frac{h_e}{30} - e \\ & & & & \frac{2h_e}{15} + \frac{\mathcal{K}_g}{K_s} \frac{7}{3h_e} - e & \frac{\mathcal{K}_g}{K_s} \frac{7}{3h_e} - e \end{bmatrix} \quad (2.35)$$

$$\begin{aligned}
 a &= \frac{16K_s}{25 \left( \frac{8h_e K_s}{15} + \frac{16\mathcal{K}_g}{3h_e} \right)} \\
 b &= \frac{4h_e K_s}{75 \left( \frac{8h_e K_s}{15} + \frac{16\mathcal{K}_g}{3h_e} \right)} \\
 c &= \frac{4 \left( \frac{h_e K_s}{15} - \frac{8\mathcal{K}_g}{3h_e} \right)}{5K_s \left( \frac{8h_e K_s}{15} + \frac{16\mathcal{K}_g}{3h_e} \right)} \\
 d &= \frac{h_e^2 K_s}{225 \left( \frac{8h_e K_s}{15} + \frac{16\mathcal{K}_g}{3h_e} \right)} \\
 e &= \frac{\left( \frac{h_e K_s}{15} - \frac{8\mathcal{K}_g}{3h_e} \right)^2}{K_s \left( \frac{8h_e K_s}{15} + \frac{16\mathcal{K}_g}{3h_e} \right)} \quad (2.36)
 \end{aligned}$$

*Mass matrix*

Computing the integrals by using the interpolation functions in Equation (2.24), the  $4 \times 4$  element mass matrix,  $\mathbf{M}_e$ , is:

$$\mathbf{M}_e = \frac{\Lambda h_e}{420} \begin{bmatrix} 156 & 22h_e & 54 & -13h_e & 0 & 0 \\ 22h_e & 4h_e^2 & 13h_e & -3h_e^2 & 0 & 0 \\ 54 & 13h_e & 156 & -22h_e & 0 & 0 \\ -13h_e & -3h_e^2 & -22h_e & 4h_e^2 & 0 & 0 \\ 0 & 0 & 0 & 0 & 0 & 0 \\ 0 & 0 & 0 & 0 & 0 & 0 \end{bmatrix} \quad (2.37)$$

Note that  $\mathbf{M}_e$  corresponds to the classical mass matrix of the Euler-Bernoulli beam model (massive beams) where the rotational inertia is not involved. As explained earlier, the HBFEM model describes the transverse dynamics of reticulated structures in the low frequency range. The participation of the rotational inertia is associated with much higher vibration modes, and such a situation is out of the scope of this work.

As observed, there is a difference in the size of the element stiffness matrix  $\mathbf{K}_e$  ( $6 \times 6$ ) and that of the element mass matrix  $\mathbf{M}_e$  ( $4 \times 4$ ). The latter then needs to be expanded to a ( $6 \times 6$ ) matrix with zeros to be consistent in the solution computation.

## 2.3 Validation of the homogenized finite beam element

### 2.3.1 A realistic steel structure

The ten-story four-bay planar frame shown in Figure 2.6 is used to illustrate the performance of the HBFEM model. A free vibration analysis is carried out to estimate the modal dynamic properties of the structure. The results of the modal analysis are compared with 1) the analytical solution of the EBM in order to evaluate the accuracy of the finite element approximation, 2) the results of a fully detailed numerical FEM model (realized with the finite element code [CEA, 2017]) and 3) an equivalent Timoshenko beam model to highlight the relevance of the proposed description of reticulated structures and the need of adding the inner bending mechanism.

The studied frame is made of steel and is inspired by a real building. Herein, the floors are not taken into account, and only one of the four planar frames shown in the direction of vibration is studied (see Figure 2.6). In addition, for the inner bending mechanism to

significantly contribute to the response of the structure, a high stiffness contrast between the vertical and the horizontal elements is introduced.

The cross sections of the structural members are chosen as wide flange beams (W-beams, I-shape), assigning much bigger sections to the columns than to the beams. The expected structural governing behavior is then characterized by the local bending of the horizontal beams and the bending at the structure scale of the columns. The sections and material properties of the structural members are listed in Table 2.1.

Property	Columns	Floor beams
Length (m)	3	5
Cross-sectional area $A$ (m <sup>2</sup> )	$5.246 \times 10^{-2}$	$7.923 \times 10^{-3}$
Moment of inertia $I$		
weak direction (m <sup>4</sup> )	$4.534 \times 10^{-4}$	$2.08 \times 10^{-5}$
strong direction (m <sup>4</sup> )	$9.65 \times 10^{-3}$	$1.45 \times 10^{-4}$
Young's modulus $E$ (GPa)	200	200
Density $\rho$ (kg/m <sup>3</sup> )	7860	7860
Damping ratio $\zeta$ (%)	2	2

TABLE 2.1: Geometric and material properties of the structural members

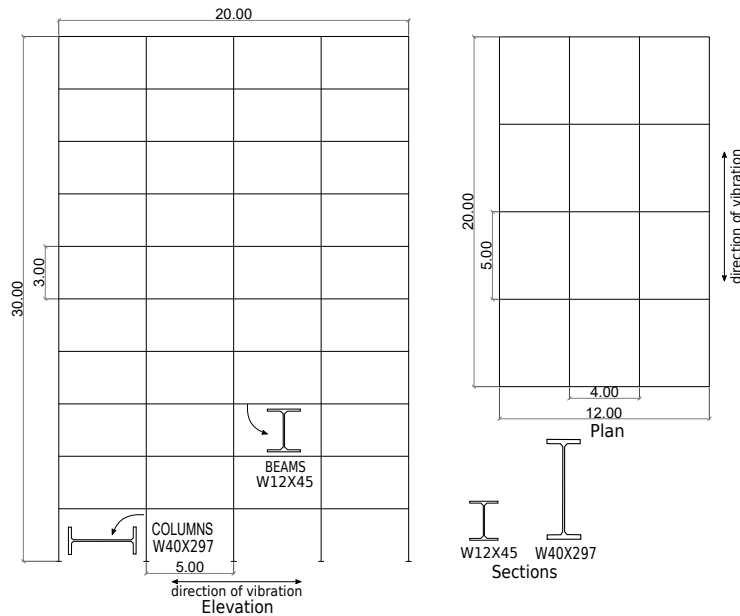


FIGURE 2.6: Elevation (left) and plan view (right) of the studied steel structure (all dimensions are in m).

The properties -or macroscopic parameters  $K_s$ ,  $\mathcal{K}_g$ ,  $\mathcal{K}_i$  and  $\Lambda$ - of the equivalent beam model are estimated through the static analysis of a unique story (unit cell). This procedure is widely explained in [Chesnais, 2010] for simple and double frame structures, in [Franco et al., 2019]

for multiple frame structures and in [Chesnais et al., 2011a] for buildings. The values for  $K_s$ ,  $\mathcal{K}_g$ ,  $\mathcal{K}_i$  and  $\Lambda$  of the studied structure are given in Table 2.2.

Macroscopic parameter	Description	Formula	Value
Linear mass, $\Lambda$	total mass of the unit cell divided by its size	$\rho/l_m(\sum A_i l_i)$	2.48 t/m
Global bending stiffness, $\mathcal{K}_g$	sum of the tension - compression stiffnesses of the vertical elements multiplied by the square of the lever arms	$\sum E_i A_i d_i^2$	$2.62 \times 10^6$ MN.m <sup>2</sup>
Inner bending stiffness, $\mathcal{K}_i$	sum of the bending stiffnesses of the vertical elements	$\sum E_i I_i$	$9.65 \times 10^3$ MN.m <sup>2</sup>
Shear stiffness, $K_s$	depends on the local bending stiffnesses of all the unit cell elements	Determined from a FEM model of the unit cell as presented in [Franco et al., 2019]	96.19 MN

TABLE 2.2: Macroscopic parameters of the studied structure

The HBFEM model results are also compared with those of the Timoshenko beam model, which is based on the classical theory for massive beams. The material and geometric properties of the Timoshenko beam model are determined from the macroscopic parameters of the frame structure: the linear mass of the unit cell  $\Lambda$ , the shear stiffness  $K_s$  and the global bending stiffness  $\mathcal{K}_g$ . In order to have the same shear stiffness in both models, an equivalent Poisson's ratio is determined through  $\nu_{eq} = \frac{A_s k_s E}{2(K_s)} - 1$  where  $k_s$  denotes the shear correction factor and  $A_s$  is the equivalent area of the section computed from  $\Lambda/\rho$ . Herein,  $k_s$  is taken equal to 1 because the transverse section shape is not defined. As Boutin et al. states in [Boutin et al., 2010], the shear deformability is much larger in the unit cell of reticulated structures than in the section of massive beams, then the equivalent Poisson's ratio  $\nu_{eq}$  calculated here may reach large values (much larger than 1). The global inertia is given by the ratio  $\mathcal{K}_g/E$ . Table 2.3 details the properties used to build the Timoshenko beam model.

Property	
Global Inertia $I_g$ (m <sup>4</sup> )	13.115
Equivalent section area $A_s$ (m <sup>2</sup> )	0.315
Young's modulus $E$ (GPa)	200
Density $\rho$ (kg/m <sup>3</sup> )	7860
Equivalent Poisson's ratio $\nu_{eq}$	326.5

TABLE 2.3: Geometric and material properties of the Timoshenko beam model

In the HBFEM and the Timoshenko beam models, the number of finite elements  $N_e$  used in the computations is the same as the number of stories  $N$  in the structure. The size of the finite element  $h_e = N l_m / N_e$  is thus equal to the size of the unit cell  $l_m$ . In Section 2.3.3, the accuracy of the HBFEM model is also investigated through a parametric study in which the finite element size  $h_e$  is varied with respect to the unit cell size  $l_m$  and it is shown that good results can also be obtained with  $N_e$  smaller than  $N$ .

### 2.3.2 Free vibration analysis

Modal analysis with the HBFEM model searches for the solution of the following eigenvalue problem:

$$\mathbf{K}\mathbf{E} - \omega^2\mathbf{M}\mathbf{E} = 0 \quad (2.38)$$

where  $\mathbf{K}$  and  $\mathbf{M}$  are the square stiffness and mass matrices of the whole homogenized beam. The vector  $\mathbf{E}$  contains all the nodal degrees of freedom. This equation can also be written as:

$$\begin{bmatrix} \mathbf{K}^{(11)} & \mathbf{K}^{(12)} \\ \mathbf{K}^{(21)} & \mathbf{K}^{(22)} \end{bmatrix} \begin{Bmatrix} \{\hat{u}\} \\ \{\hat{\alpha}\} \end{Bmatrix} - \omega^2 \begin{bmatrix} \mathbf{M}^{(11)} & 0 \\ 0 & \mathbf{M}^{(22)} \end{bmatrix} \begin{Bmatrix} \{\hat{u}\} \\ \{\hat{\alpha}\} \end{Bmatrix} = \{0\} \quad (2.39)$$

The HBFEM model is a 1D beam model discretized in  $N_e$  finite elements with 3 DoFs (degrees of freedom) at each node.

#### Eigenfrequencies and eigenmodes

The solution of the EBM equation of motion presented in Section 1.4.3 provides the eigenfrequencies and eigenmodes of the structure. For the HBFEM, the eigenvalue problem provided in 2.3.2 should be solved. The HBFEM model is then a 1D model discretized in 10 finite elements with 3 DoFs (degrees of freedom) at each node. As a result, the size of the global stiffness and mass matrices is  $33 \times 33$ . The boundary conditions are  $\hat{u}(0) = 0$ ,  $\hat{u}'(0) = 0$  and  $\hat{\alpha}(0) = 0$  at the bottom of the model, and  $\mathcal{T}(H) = 0$ ,  $\mathcal{M}(H) = 0$  and  $\mathcal{M}(H) = 0$  at the top. Table 2.4 presents the eigenfrequencies of the first three transverse modes obtained with the four models: the detailed FEM numerical model (subscript  $DFEM$ ), the analytical solution of the EBM (subscript  $EBM$ ), the homogenized beam finite element formulation (subscript  $HBFEM$ ) and the finite element solution of the Timoshenko beam model (subscript  $TFEM$ ). Table 2.5 presents the relative error  $\epsilon^{f_X}$  on the eigenfrequencies between each model  $f_X$  and the detailed numerical model  $f_{DFEM}$

$$\epsilon^{f_X} = 100 \times \frac{f_X - f_{DFEM}}{f_{DFEM}} \quad (2.40)$$

First of all, note that the HBFEM gives almost the same results as the analytical EBM which shows the good quality of the finite element approximation developed in this chapter. Moreover, only minor differences (smaller than 3 %) between the first three fundamental frequencies of the detailed numerical model and those of the EBM - HBFEM models are obtained. The frequency ratios, defined by  $f_{DFEM_i}/f_{DFEM_1}$ , are (1 ; 4.04 ; 9.70) and these values are different from the common values found in the literature for shear beams (1 ; 3 ; 5) or Euler-Bernoulli beams (1 ; 6.25 ; 17.36). The differences in the frequencies obtained with the Timoshenko beam model are larger than 30% evidencing that this model is not suitable for describing the dynamic behavior of this high stiffness contrast structure as it was expected.

Figure 2.7 compares the first three mode shapes evaluated with the four models. The dots on the curves indicate the nodes coinciding with the different stories of the structure. The

analytical EBM, the HBFEM and the Timoshenko beam models provide continuous displacements along the structure height. Conversely, the displacement values for the detailed FEM model are obtained only at each story location.

It is noted that the mode shapes of the analytical EBM and HBFEM models match those of the detailed numerical model. For the first three bending modes, all these models reproduce the eigenmodes correctly. The detailed FEM model and the HBFEM can hardly be distinguished. The opposite occurs with the Timoshenko beam model whose first mode shape describes a typical unrealistic shear response.

Mode	$f_{DFEM}$	$f_{EBM}$	$f_{HBFEM}$	$f_{TFEM}$
1	2.366	2.403	2.403	1.654
2	9.569	9.667	9.668	5.000
3	22.949	23.409	23.414	8.516

Mode	$\epsilon^{f_{EBM}}$	$\epsilon^{f_{HBFEM}}$	$\epsilon^{f_{TFEM}}$
1	1.564	1.564	-30.093
2	1.024	1.035	-47.748
3	2.004	2.026	-62.892

TABLE 2.4: Eigenfrequencies of the first three transverse vibration modes in Hz.

TABLE 2.5: Differences (%) between the eigenfrequencies of each of the analyzed models and those of the detailed numerical model according to Equation (3.12) and Table 2.4.

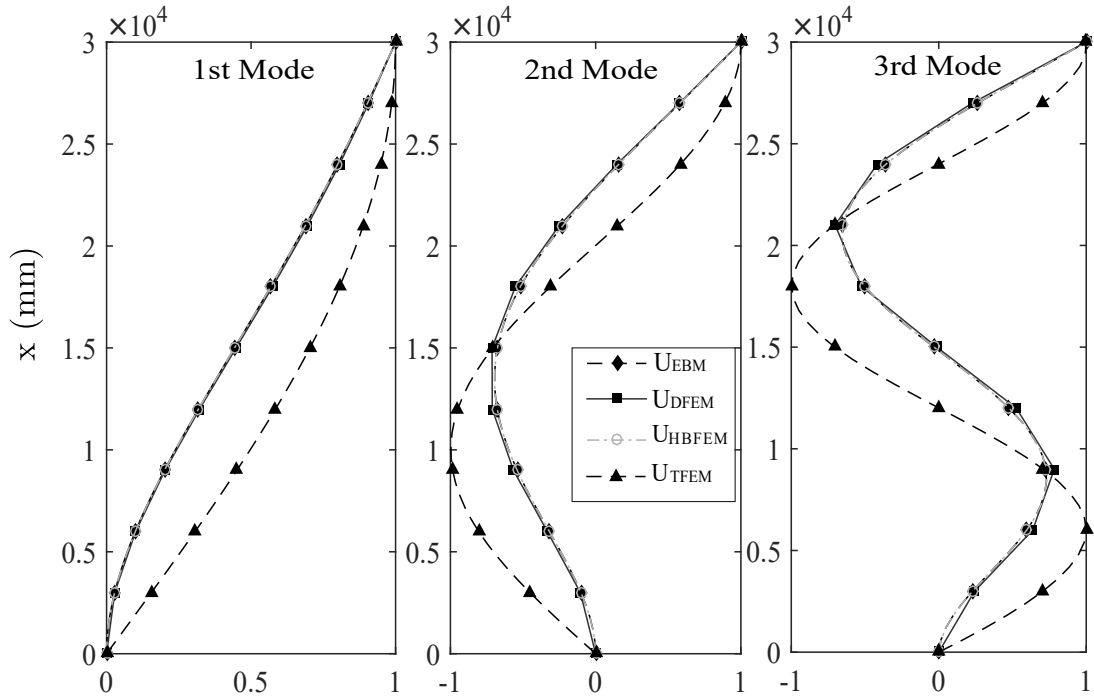


FIGURE 2.7: Comparison of the first three mode shapes of the structure shown in Figure 2.6. The diamond-dotted dashed black lines corresponds to the *EBM*. The square-dotted full black lines refer to the detailed FEM model (*DFEM*). The round-dotted dashed grey lines are associated with the *HBFEM* model. The triangle-dotted dashed black lines are for the Timoshenko beam model (*TFEM*).

### 2.3.3 A parametric study: principles of the analysis

In order to identify the accuracy of the HBFEM model with respect to the mesh size, a parametric study is conducted in the harmonic regime over one thousand two hundred different single frame structures with various  $N_e$ , the number of finite elements used in the HBFEM model.

Two main purposes of this parametric study are:

- To determine the domain of validity of the HBFEM model with respect to the number of finite elements  $N_e$ . It is needed to verify the existence of a range  $[N_e^{min}, N_e^{max}]$  where the HBFEM model results do not change with the mesh size. From a practical point of view, the value  $N_e^{min}$  is the most important. It is of interest to optimize the computational resources and therefore to investigate how close the HBFEM results are to the EBM results when the number of finite elements  $N_e$  is decreased.
- To identify the sources of error that may cause divergence of the results. For this, an in-depth analysis is performed for (1) structures with different governing response mechanisms and (2) different sizes of the finite elements  $h_e$  ( $h_e \rightarrow 0$  or  $N_e \rightarrow \infty$ ). Although testing very fine mesh is not conventional in convergence studies, once the convergence criterion is met, it may help to understand the HBFEM model performance.



Herein, the HBFEM model accuracy is assessed from a modal analysis with respect to the EBM. The accuracy of the EBM has been widely investigated for single frame structures in [Hans and Boutin, 2008], for multi-frame structures in [Franco et al., 2019] and for buildings in [Chesnais et al., 2011a].

### Description of the studied structures

We extend here the bunch of the analyzed structures in the parametric study of Chapter 1 and, in addition, we perform the analysis using the HBFEM model. Herein, one thousand two hundred single frame structures clamped at the base and free at the top are tested. All the structures are grouped into three sets of four hundred different structures with the number of cells  $N$  fixed at 10, 20, and 30. Each cell is a single frame composed of two vertical elements of length  $l_m = 3$  m and one horizontal element of length  $l_p = 3$  m. Their material properties are:  $E = 30$  GPa,  $\nu = 0.3$ ,  $\rho = 2300$  kg/m<sup>3</sup>. Only two parameters are varied from one structure to another: the thicknesses of the vertical and horizontal elements (from 50 mm to 1950 mm with a step of 100 mm). Each structure is analyzed with the HBFEM model using a number of finite elements  $N_e$  that varies from 1 to 100 with a step of 1.

The estimation of the macroscopic parameters  $\Lambda$ ,  $K_s$ ,  $\mathcal{K}_i$ , and  $\mathcal{K}_g$ , from the static analysis of a single unit cell, is performed according to the equations given in Section 1.5.2 on page 27. The governing mechanism of each of the structures is identified utilizing the identification criterion based on the macroscopic constants  $C$  and  $\gamma$  and represented in the domain graph in Figure 2.8. Each dot corresponds to a specific structure, and each color represents a set. See that with the chosen structure is possible to cover all the behavior regions in the domain graph.

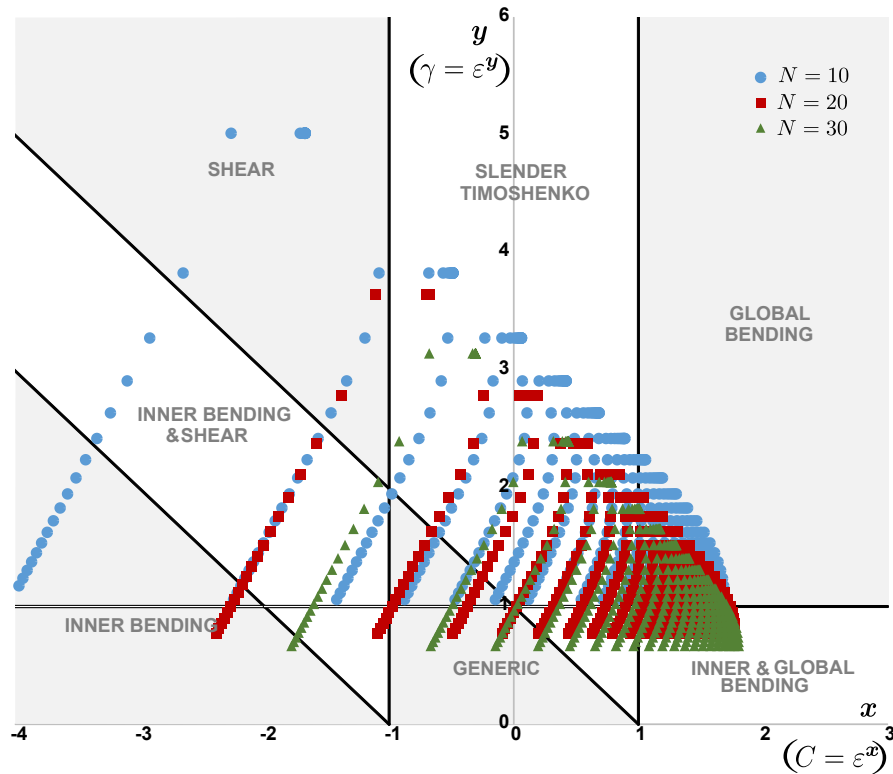


FIGURE 2.8: Domain behavior identification graph for the studied structures. Circle blue, square red, and triangle green dots correspond to the set of the four hundred structures with  $N = 10$ ,  $N = 20$  and  $N = 30$ , respectively.

### Eigenfrequency assessment

For the first set of structures ( $N = 10$ ), Figure 2.9 compares the first natural frequency estimated from the HBFEM model with different mesh sizes and the first natural frequency calculated with the analytical EBM. In Figure 2.9(a), the EBM being taken as the reference, the evolution of the relative error  $\epsilon^{f_{\text{HBFEM}}}$  is displayed with respect to  $N_e$ . It can be seen that the reduction of the mesh size stabilizes the errors (less than 1%) by  $N_e = 10$ . For  $N_e < 10$ ,  $\epsilon^{f_{\text{HBFEM}}}$  values are small (less than 10%). Only scattered results when  $N_e > 70$  show differences up to 16%. If a specific case (out of the four hundred cases) is taken apart (see Figure 2.9(b)), it is clear that the difference can increase not only when  $N_e$  tends to  $N_e^{\text{min}} = 1$  but also when it tends to  $N_e^{\text{max}} = 100$ . In theory, the smaller is  $h_e$  the higher is the accuracy of the finite element approximation and vice versa. However, the extreme refinement of the mesh of the HBFEM model does not necessarily increase the accuracy, and when  $h_e$  is very small, the HBFEM model may lead to higher discrepancies than those obtained with only one finite element for the whole 1-D beam. The reasons for such a situation are investigated in detail hereafter.

Moreover, these results indicate that the HBFEM model recovers very fast the EBM and can be used for a wide domain of mesh sizes to estimate the eigenfrequencies of a given structure. It is observed that three finite elements ( $N_e = 3$ ) are sufficient to find the first three

natural frequencies of structures with  $N = 10$ . A similar conclusion can be drawn for structures with  $N = 20$  and  $N = 30$  (see Figure 2.10). A single finite element ( $N_e = 1$ ) for the whole HBFEM model provides a rough estimate of the first natural frequency of the structure (up to 10 % difference with respect to the analytical solution). Notice that for the three set of structures ( $N = 10$ ,  $N = 20$  and  $N = 30$ ; Figures 2.9 and 2.10), there is a plateau with excellent accuracy between 10 and 70 finite elements. It indicates that the model accuracy does not depend on the ratio between the finite element size and the structure size but is related to the vibration wavelength. Thus, if very accurate results are desired, the number of finite elements should be chosen according to the considered mode and the wavelength. For example, ten finite elements already give very satisfying results (relative errors smaller than 0.5 %) to estimate the first vibration mode for all the set of structures ( $N = 10$ ,  $N = 20$  and  $N = 30$ ).

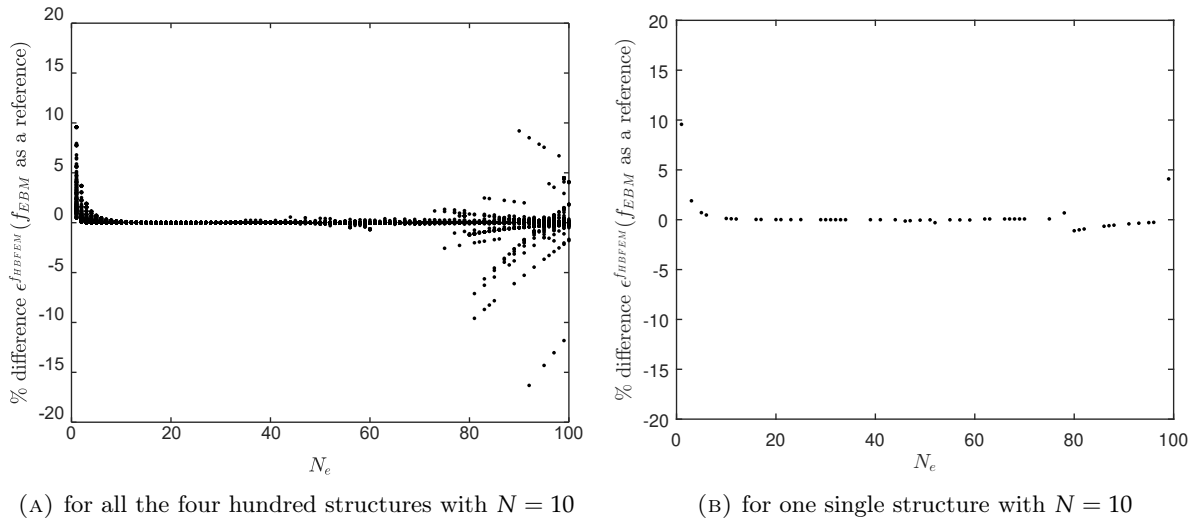


FIGURE 2.9: Variation of the relative error between the first natural frequency obtained with the HBFEM model and the first natural frequency obtained with the EBM as a function of the number of finite elements  $N_e$ . Each dot represents the result of a single structure evaluated with a fixed  $N_e$ . The 400 structures' properties are:  $E = 30\text{GPa}$ ,  $\nu = 0.3$ ,  $\rho = 2300 \text{ kg/m}^3$ ,  $N = 10$ , the unit cell is a single frame (two vertical elements and one horizontal of length 3000 mm), thicknesses vary from 50 mm to 1950 mm with a step of 100 mm, all the structures are clamped at the base and free at the top. For (b) the case corresponds to a structure with 50 mm thick vertical elements and a 250 mm thick horizontal element. The predominant mechanism is the shear of the cell generated by the local bending of the vertical elements.

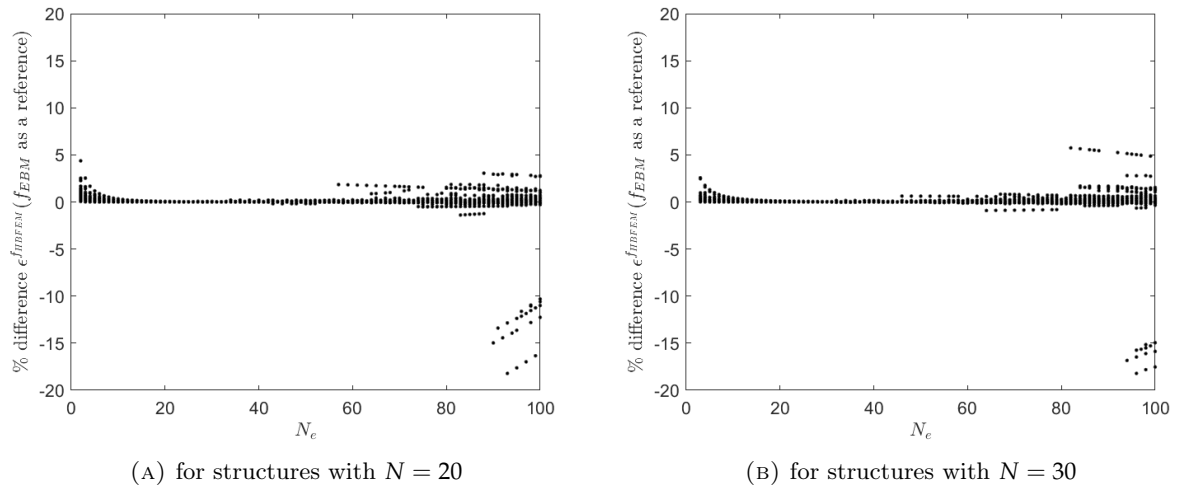


FIGURE 2.10: Variation of the relative error between the first natural frequency obtained with the HBFEM model and the first natural frequency obtained with the EBM as a function of the number of finite elements  $N_e$ . Each dot represents the result of a single structure evaluated with a fixed  $N_e$ . The structures' properties are:  $E = 30$  GPa,  $\nu = 0.3$ ,  $\rho = 2300$  kg/m<sup>3</sup>, a)  $N = 20$ , and b)  $N = 30$ , the unit cell is a single frame (two vertical elements and one horizontal), the thicknesses vary from 50 mm to 1950 mm with a step of 100 mm, all the structures are clamped at the base and free at the top.

Previous figures show only comparisons concerning the first fundamental frequency. Nevertheless, the same conclusions can be drawn for the second and third eigenfrequencies. The results for four different cases out of the four hundred of the first set ( $N = 10$ ) are presented in Figure 2.11, but for this time, the frequencies obtained with the HBFEM model are compared with the complete detailed numerical model. So, the error  $\epsilon^{f_{HBFEM}}$  is the one represented. The pattern remains the same. One finite element ( $N_e = 1$ ) gives the largest errors, but once  $N_e$  is increased, the HBFEM model quickly recovers the detailed numerical model solution, and at a certain point, the HBFEM solution diverges. The point of divergence depends on the structure typology. This analysis will be detailed in Section 2.3.3. As it is seen on the graphs, for a structure with 150 mm thick vertical elements and a 50 mm thick horizontal element ( $a_m = 150$  mm and  $a_p = 50$  mm) (Figure 2.11.a) the error divergence is reached first.

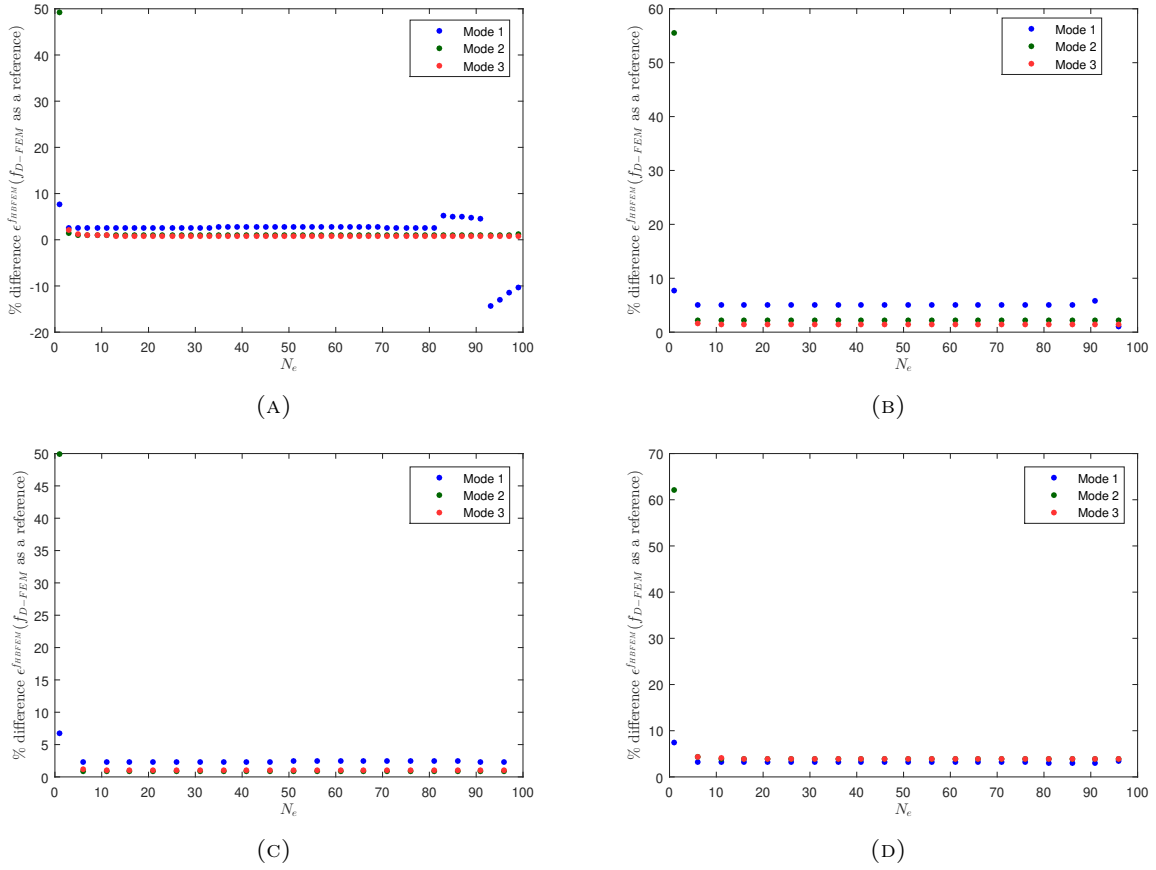


FIGURE 2.11: Variation of the relative error  $\epsilon^{HBFE}$  for the first three natural frequencies as a function of the number of finite elements  $N_e$ . Each dot represents the result of a single structure evaluated with a fixed  $N_e$ . The structures' properties are:  $E = 30$  GPa,  $\nu = 0.3$ ,  $\rho = 2300$  kg/m<sup>3</sup>,  $N = 10$ , a)  $a_m = 150$  mm and  $a_p = 50$  mm (shear behavior), b)  $a_m = 500$  mm and  $a_p = 100$  mm (inner bending behavior), c)  $a_m = 500$  mm and  $a_p = 150$  mm (shear behavior), and d)  $a_m = 500$  mm and  $a_p = 500$  mm (slender Timoshenko behavior). The unit cell is a single frame (two vertical elements and one horizontal). All the structures are clamped at the base and free at the top.

### Analysis of the divergence

Figures 2.9 and 2.10 show that there is a systematic evolution of the error with the analytical solution as  $N_e$  varies but very small finite elements ( $h_e < \frac{1}{70}H$  for the first mode) can cause the divergence of the solution. The explanation can be found by analyzing the components of the stiffness matrix  $\mathbf{K}_t$  presented in Section 2.2.4 (Equation (2.34)). The terms associated with the inner bending stiffness  $\mathcal{K}_i$  and the global bending stiffness  $\mathcal{K}_g$  are respectively divided by  $h_e^3$  and  $h_e$ . Therefore, they become very large when  $h_e$  tends to 0. Surprisingly, the first terms to diverge are those proportional to  $\frac{\mathcal{K}_g}{h_e}$ . It can be explained because  $\frac{\mathcal{K}_i}{h_e^3}$  depends on the local bending stiffness of the vertical elements proportional to the thickness term  $a_m^3$ , whereas  $\frac{\mathcal{K}_g}{h_e}$  depends on the tension-compression stiffness of the vertical elements and the length of the cell  $l_p^2$ .  $a_m$  being much smaller than  $l_p$ ,  $\frac{\mathcal{K}_g}{h_e}$  diverges first.

Since the response of all the studied structures is not controlled by the same mechanism or combination of mechanisms (i.e., shear, inner bending, global bending), large discrepancies appear for different values of  $h_e$  depending on the stiffness contrasts. Thus, to show the influence of the type of mechanism on the accuracy of the solution, the relative error is plotted with respect to the ratio of the global bending stiffness to shear stiffness  $C = \frac{\mathcal{K}_g}{\mathcal{K}_s L^2}$  ( $L$  refers to the characteristic length of vibration) in Figures 2.12(a) and (b) for each of the four hundred structures with  $N = 10$  cells. Figure 2.12(a) corresponds to the comparison between the EBM and the detailed numerical model and Figure 2.12(b) to the comparison between the HBFEM model with different values for  $N_e$  and the EBM (same relative errors as in Figure 2.9). In both figures, there is a range ( $1 < C < 200$ ) in which the error increases and reaches the highest values. The structures that fit in this range are those whose behavior is controlled by the shear mechanism ( $\mathcal{K}_g > \mathcal{K}_s$ ,  $\mathcal{K}_s > \mathcal{K}_i$  and  $\mathcal{K}_g \gg \mathcal{K}_i$ ) or by the global bending and shear mechanisms ( $\mathcal{K}_g$  and  $\mathcal{K}_s$  have the same importance and  $\mathcal{K}_g \gg \mathcal{K}_i$ ). These results suggest that the HBFEM model follows the EBM results and preserves the kinematics of the structure. Now, to exclude the variability of the relative error with respect to the mesh size (or  $N_e$ ), Figure 2.13(a) plots the relative error between the fundamental frequency obtained with the HBFEM model when  $N_e = 10$  and that of the EBM as a function of  $C$ . Notice that the relative errors are tiny (less than 0.5 %). In addition, Figure 2.13(b) presents the same discrepancies when the thickness contrast  $a_p/a_m$  between the horizontal and vertical elements varies. These graphs allow concluding that the differences between the results of the HBFEM model and those of the EBM are then attributed to the mesh size and are amplified when the local bending stiffness contrast between the horizontal and vertical elements is higher than 1 (structures that are controlled by the shear or global bending and shear mechanisms).

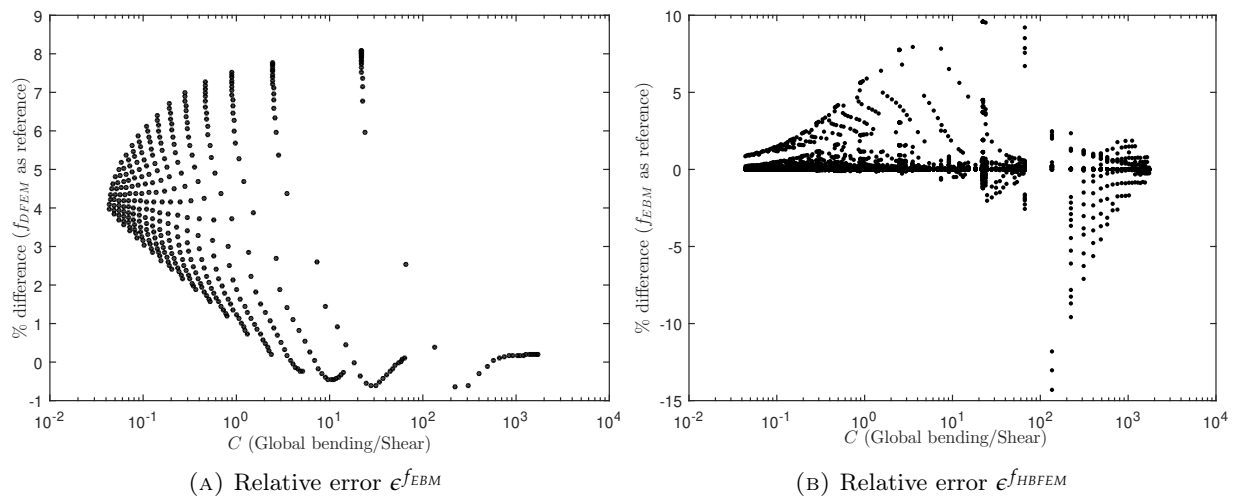


FIGURE 2.12: Relative error  $\epsilon^{f^X}$  as a function of the ratio  $C$  between the global bending stiffness and the shear stiffness for the set of four hundred structures with  $N = 10$ . (a) Assessment of the EBM with the detailed numerical model used as reference, (b) assessment of the HBFEM model (for  $N_e = 1 : 1 : 100$ ) with the EBM used as a reference.

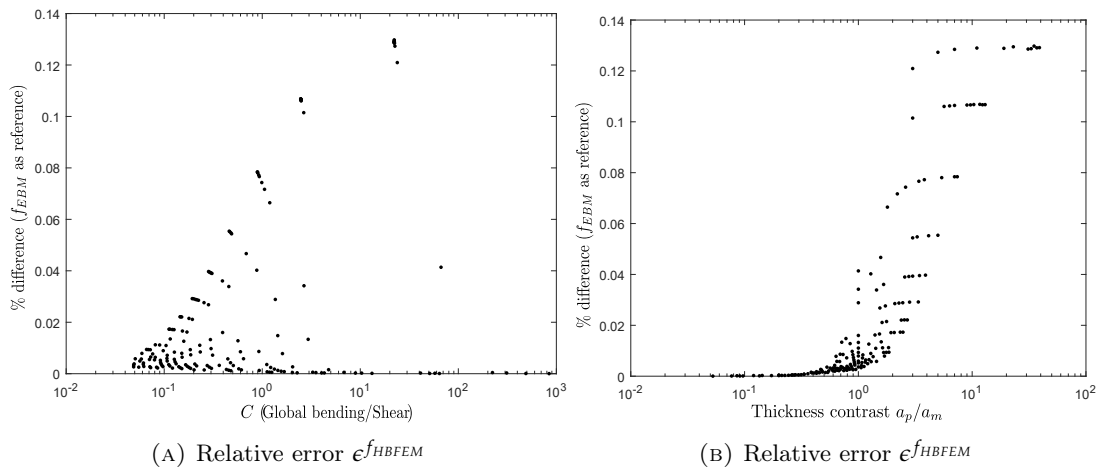


FIGURE 2.13: Relative error  $\epsilon^{f_{HBFEEM}}$  as (a) a function of  $C$  and as (b) a function of the thickness contrast between the horizontal elements (thickness  $a_p$ ) and the vertical elements (thickness  $a_m$ ) for the set of four hundred structures with  $N = 10$  when  $N_e = 10$ .

### Eigenmode assessment

After noticing that a small number of finite elements is sufficient to correctly estimate the eigenfrequencies, it is required to verify that this condition is also enough to evaluate the first three mode shapes. Thus, the mode shapes of the steel structure studied in Section 2.3.1 are recalled here to compare the modes obtained with the HBFEM model when  $h_e = Nl_m/3$ ,  $h_e = l_m$  and  $h_e = Nl_m/100$  with the EBM solution (See Figure 2.14). Notice that all the eigenmodes match well. The symbols on the curves indicate the transverse displacement values at the finite element nodes (e.g., for  $h_e = Nl_m/3$  only four nodes exist) and the interpolation functions are used to obtain the complete mode shapes. Table 2.6 summarizes the first three natural frequencies for each of the analyzed models. These results allow concluding that it is possible to accurately estimate the first three eigenmodes with a small number of finite elements ( $N_e = 3$ ). Note also that there is no divergence for a very fine mesh ( $N_e = 100$ ). Section 2.3.3 is devoted to searching for the origin of the divergence and the possible causes of error.

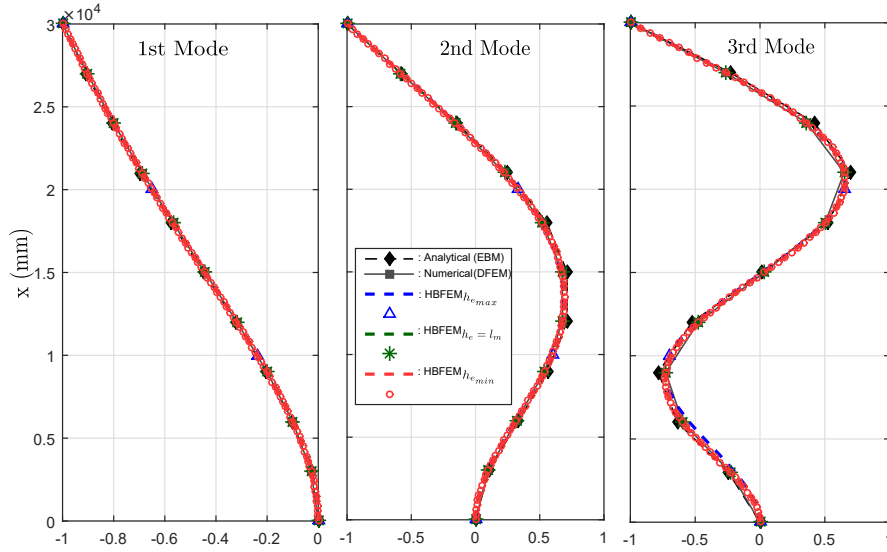


FIGURE 2.14: Comparison of the first three mode shapes provided by the HBFEM model with three different numbers of finite elements:  $N_e = 3$ ,  $N_e = N$  and  $N_e = 100$ . The diamond-dotted dashed black lines correspond to the EBM. The square-dotted full grey lines refer to the full FEM model. The triangle-dotted dashed blue lines are for the HBFEM model with  $h_e = Nl_m/3 > l_m$ . The star-dotted dashed green lines are for the HBFEM model with  $h_e = l_m$ . The round-dotted red lines are for the HBFEM model with  $h_e = Nl_m/100 < l_m$ .

Mode	$f_{DFEM}$	$f_{EBM}$	$f_{HBFEM}$		
			$N_e = 3$	$N_e = N$	$N_e = 100$
1	2.366	2.403	2.406	2.403	2.301
2	9.569	9.667	9.705	9.668	9.677
3	22.949	23.409	23.698	23.414	23.410

TABLE 2.6: Eigenfrequencies of the first three transverse vibration modes in Hz computed with the detailed numerical model (subscript DFEM), the EBM (subscript EBM), the HBFEM model with three different mesh sizes:  $N_e = 3$ ,  $N_e = N$  and  $N_e = 100$ .

## 2.4 Conclusion and perspectives

This chapter details the formulation of a new enriched beam finite element able to describe accurately the transverse dynamics of periodic reticulated structures. The proposed homogenized beam finite element (HBFEM) formulation is derived from an existing homogenized beam-like model, called equivalent beam model (EBM). In these models, the transverse dynamics of a structure at the macroscopic scale is described by two kinematic variables: the transverse displacement and the macroscopic rotation. The differentiability requirement for each kinematic variable is treated distinctly. Thus, Hermite cubic interpolation functions are used for the transverse displacement and Lagrange quadratic interpolation functions for the macroscopic rotation. The interpolation functions used to approximate the macroscopic



rotation field are kept one order lower than the one for the transverse displacement field to minimize the shear locking phenomenon. A six-by-six elementary stiffness matrix and a four-by-four elementary mass matrix are successfully derived.

The validation of the HBFEM model is performed for a realistic building structure. The HBFEM model is compared with the analytical solution of the EBM and the finite-element solution from a fully detailed structural model. The results show that the HBFEM model is efficient in representing the dynamic features and behavior of lattice structures. Besides, a mesh refinement test is conducted through a parametric study to determine the optimum number of finite elements to use in the HBFEM model. This study reveals that the finite element size is relevant to recover the exact solutions provided by the EBM (analytical form). The finite element size should be chosen according to the wavelength or the number of considered modes. It is shown that three finite elements are enough to fully describe the dynamic behavior up to the third transverse vibration mode. This last statement is convenient to reduce the number of degrees of freedom of the model and the computational time. The parametric study also evidences that the source of the differences between the HBFEM model and the EBM results is also linked to the governing response mechanism of the structure. It is noticed that the EBM and HBFEM model are a little less accurate when analyzing structures controlled by the shear mechanism or the combination of global bending and shear mechanisms. The order of the encountered differences on the fundamental frequency does not exceed 0.2% when ten finite elements are used. The implementation of the HBFEM model is encouraged to investigate the transverse response of, for example, small-scale lattice composites [Zheng et al., 2014, Fan et al., 2010] or, at a much larger scale, reticulated systems such as high-rise buildings [Rahgozar et al., 2010, Pan et al., 2020], for which robust and simplified models could be preferred. In addition, the HBFEM can be introduced in FEM based codes to perform large scale engineering studies (e.g., site-city interaction). In the next chapters, this work is dedicated to study more complex configurations (e.g., structures with several types of stories) and integration of the HBFEM model in non-linear response analyses.

## Chapter 3

# Application to real structures

The implementation of the beam models presented in Chapter 1 and the subsequent homogenized beam finite element (HBFEM) model developed in Chapter 2 correctly characterizes the transverse dynamics of real buildings if the structure fulfills specific requirements. Firstly, the analyzed structure must be vertically regular in mass, stiffness and strength to respect the periodicity condition required by the homogenization. Secondly, the building must be tall enough to respect the scale separation condition. Structures of at least five stories ( $\varepsilon \leq 0.3$ ) fulfill this condition. Finally, the dynamic characterization must be limited to the analysis of the vibration modes with a sufficiently long wavelength. For each vibration type, the maximum number of modes which can be modelled with this approach is approximately  $N/3$ , where  $N$  is the number of stories. This condition is typically valid in earthquake engineering studies where the lowest frequencies are of interest. In this framework, a lot of the existing reinforced concrete (RC) and steel buildings seem to easily fulfill the stated conditions.

The accuracy of the EBM (of Chapter 1) has been evaluated for fully periodic RC buildings in [Boutin et al., 2005, Chesnais, 2010, Chesnais et al., 2011a]. In compliance with *in-situ* ambient vibration tests, [Boutin et al., 2005] characterizes the dynamics of various RC buildings using Timoshenko beam models. Although, outstanding results are obtained, the mechanisms that govern the structural behavior are not fully discussed. Later, [Chesnais, 2010] focuses on understanding the mechanical functioning of shear wall buildings and proposes an analytical upgrading of the EBM to account for the contribution of the shear stiffness of the walls. [Chesnais et al., 2011a] verifies the accuracy of the proposed model by comparing the modal results for a 16-story RC shear wall building with those of a full finite element model. As a continuation of previous studies, in this chapter, we investigate the adaptability of the EBM and the HBFEM model in two important problems of earthquake engineering: (1) transient dynamic analyzes and (2) non-periodicity of buildings. Thus, we aim to *i*) take advantage of the multiscale analysis used in the construction of the continuous beam models to understand the dynamic behavior of a real structure *ii*), go out from the harmonic regime to perform transient analyses with real seismic signals (subject of Section 3.1) and *iii*) evaluate, with a free vibration analysis, the relevancy of the HBFEM model to study structures that are not fully periodic (subject of Section 3.2). Full finite element simulations are taken as references to verify the results obtained from the built continuous models.

### 3.1 Homogenized finite beam element model for a time history analysis using a real seismic record

This section aims to validate the HBFEM model in a time history linear analysis using a real seismic signal. For that, we introduce the numerical method used to perform the transient analysis and we evaluate the seismic response of the steel structure studied previously in Section 2.3.1.

#### 3.1.1 Newmark's method for linear systems

Time-history analysis is an effective dynamic analysis method to investigate the seismic performance of buildings. It can provide useful information for the earthquake-resistant design and the design of active and passive control devices to reduce structural vibrations. The approach is composed of a step-by-step direct integration, in which the time domain is discretized into a large number of small increments, and the equations of motion are solved for each time interval to obtain the structural responses in terms of accelerations, displacements, etc. In the context of a structure subjected to the ground motion by an earthquake excitation, the equation of motion cannot be solved in closed form, so, a numerical procedure is required. One of the most relevant papers about implicit methods was published by Newmark [Newmark, 1959]. He presented a family of step by step time integration methods for solving structural dynamic problems for seismic and blast loadings. Newmark's method looks for the physical approximation to the response through a numerical integration in the time domain. It operates directly on the equation of motion discretizing the solution in time steps. This method is applicable to linear and non-linear systems. Other schemes such as the  $\alpha$ -HHT method were also proposed in the 1980's [Hughes, 2012].

#### Equation of motion

In this section, we use Newmark's method to find the solution  $\mathbf{E}$  for the classical MDOF linear system:

$$\mathbf{M}\ddot{\mathbf{E}}(t) + \mathbf{C}\dot{\mathbf{E}}(t) + \mathbf{K}\mathbf{E}(t) = \mathbf{f}(t) \quad (3.1)$$

where  $\mathbf{E}$  is the vector of the  $d$  degrees of freedom (DOF),  $\mathbf{M}$  is the time-invariant mass matrix ( $d \times d$ ),  $\mathbf{C}$  is the damping matrix ( $d \times d$ ) and  $\mathbf{K}$  the stiffness matrix ( $d \times d$ ). The vector  $\mathbf{f}(t)$  is the time dependent excitation force of size  $d$  represented by the base acceleration converted into the applied inertia load  $-\mathbf{M}\mathbf{L}\ddot{\mathbf{u}}_{\mathbf{g}}(t)$  where  $\mathbf{L}$  is the influence vector and  $\ddot{\mathbf{u}}_{\mathbf{g}}$  the base acceleration. A dot over a quantity indicates a derivative with respect to time.

### Time discretization of the equation of motion

In Newmark's method, the solution  $\mathbf{E}$  is discretized in  $N_p$  time steps according to the following equations:

$$\dot{\mathbf{E}}_{i+1} = \dot{\mathbf{E}}_i + (\Delta t) [(1 - \gamma)\ddot{\mathbf{E}}_i + \gamma\ddot{\mathbf{E}}_{i+1}] \quad \mathbf{E}_{i+1} = \mathbf{E}_i + (\Delta t)\dot{\mathbf{E}}_i + \frac{(\Delta t)^2}{2} [(1 - 2\beta)\ddot{\mathbf{E}}_i + 2\beta\ddot{\mathbf{E}}_{i+1}] \quad (3.2)$$

where  $i \in \{1, 2, \dots, N_p - 1\}$  and the parameters  $\gamma$  and  $\beta$  are constant values associated to Newmark's method. The choice of these values is discussed afterward.

The equation of motion (3.1) is rewritten in the form of incremental acceleration  $\Delta\ddot{\mathbf{E}}$ , incremental velocity  $\Delta\dot{\mathbf{E}}$ , incremental displacement  $\Delta\mathbf{E}$  and incremental force  $\Delta\mathbf{f}$ . Thus, the discretized equation of motion at time step  $i$  is

$$\mathbf{M}\Delta\ddot{\mathbf{E}}_i + \mathbf{C}\Delta\dot{\mathbf{E}}_i + \mathbf{K}\Delta\mathbf{E}_i = \Delta\mathbf{f}_i \quad (3.3)$$

Now,

$$\Delta\mathbf{E}_i = \mathbf{E}_{i+1} - \mathbf{E}_i \quad \Delta\dot{\mathbf{E}}_i = \dot{\mathbf{E}}_{i+1} - \dot{\mathbf{E}}_i \quad \Delta\ddot{\mathbf{E}}_i = \ddot{\mathbf{E}}_{i+1} - \ddot{\mathbf{E}}_i \quad \Delta\mathbf{f}_i = \mathbf{f}_{i+1} - \mathbf{f}_i \quad (3.4)$$

Substituting Equations (3.2) in Equations (3.4),

$$\Delta\dot{\mathbf{E}}_i = (\Delta t)\ddot{\mathbf{E}}_i + \gamma(\Delta t)\Delta\ddot{\mathbf{E}}_i \quad \Delta\mathbf{E}_i = (\Delta t)\dot{\mathbf{E}}_i + \frac{(\Delta t)^2}{2}\ddot{\mathbf{E}}_i + \beta(\Delta t)^2\Delta\ddot{\mathbf{E}}_i \quad (3.5)$$

Equations (3.4) can be written according to the incremental displacement:

$$\Delta\dot{\mathbf{E}}_i = (\Delta t)\ddot{\mathbf{E}}_i + \frac{\gamma}{\beta(\Delta t)} \left( \Delta\mathbf{E}_i - (\Delta t)\dot{\mathbf{E}}_i - \frac{(\Delta t)^2}{2}\ddot{\mathbf{E}}_i \right) \quad \Delta\ddot{\mathbf{E}}_i = \frac{1}{\beta(\Delta t)^2} \left( \Delta\mathbf{E}_i - (\Delta t)\dot{\mathbf{E}}_i - \frac{(\Delta t)^2}{2}\ddot{\mathbf{E}}_i \right) \quad (3.6)$$

With Equations (3.6), Equation (3.3) can be rewritten as

$$\hat{\mathbf{K}}\Delta\mathbf{E}_i = \Delta\hat{\mathbf{f}}_i \quad (3.7)$$

where

$$\hat{\mathbf{K}} = \mathbf{K} + \frac{\gamma}{\beta(\Delta t)}\mathbf{C} + \frac{1}{\beta(\Delta t)^2}\mathbf{M} \quad (3.8)$$

$$\Delta\hat{\mathbf{f}}_i = \Delta\mathbf{f}_i + \left( \frac{1}{\beta(\Delta t)}\mathbf{M} + \frac{\gamma}{\beta}\mathbf{C} \right) \dot{\mathbf{E}}_i + \left[ \frac{1}{2\beta}\mathbf{M} + (\Delta t) \left( \frac{\gamma}{2\beta} - 1 \right) \mathbf{C} \right] \ddot{\mathbf{E}}_i \quad (3.9)$$

Remark:

- The time step  $\Delta t$  is kept constant for the duration of the analysis
- A discrete instant in time is given by  $t_i = i\Delta t$

### Step by step procedure

Based on the iteration procedure discussed in [Chopra et al., 2012], each step is explicitly described as follows:

1. Define  $\gamma$ ,  $\beta$  and  $\Delta t$
2. Calculate  $\ddot{\mathbf{E}}_0 = \mathbf{M}^{-1} (\mathbf{f}_0 - \mathbf{C}\dot{\mathbf{E}}_0 - \mathbf{K}\mathbf{E}_0)$
3. Compute  $\hat{\mathbf{K}}$  with Equation (3.8) (it does not vary in the numerical procedure for elastic cases)
4. Calculate the constant matrices  $\mathbf{a} = \frac{1}{\beta(\Delta t)}\mathbf{M} + \frac{\gamma}{\beta}\mathbf{C}$  and  $\mathbf{b} = \frac{1}{2\beta}\mathbf{M} + (\Delta t) \left( \frac{\gamma}{2\beta} - 1 \right) \mathbf{C}$  from the terms in Equation (3.9)
5. Calculate for each time step  $i$ 
  - $\Delta \hat{\mathbf{f}}_i = \Delta \mathbf{f}_i + \mathbf{a}\dot{\mathbf{E}}_i + \mathbf{b}\ddot{\mathbf{E}}_i$  (Equation (3.9))
  - $\Delta \mathbf{E}_i = \hat{\mathbf{K}}^{-1} \Delta \hat{\mathbf{f}}_i$  (Equation (3.7))
  - $\Delta \dot{\mathbf{E}}_i$  and  $\Delta \ddot{\mathbf{E}}_i$  (Equations (3.6))
  - $\mathbf{E}_{i+1} = \mathbf{E}_i + \Delta \mathbf{E}_i$  ;  $\dot{\mathbf{E}}_{i+1} = \dot{\mathbf{E}}_i + \Delta \dot{\mathbf{E}}_i$  ;  $\ddot{\mathbf{E}}_{i+1} = \ddot{\mathbf{E}}_i + \Delta \ddot{\mathbf{E}}_i$  (Equations (3.4))

### Stability and accuracy

The stability and the accuracy of the time stepping procedure depend on the parameters  $\gamma$ ,  $\beta$  and  $\Delta t$  which guarantee that  $\mathbf{E}_i \rightarrow \mathbf{E}(t_i)$  as  $\Delta t \rightarrow 0$ . The algorithm is consistent if the local truncation error  $\tau(t)$  at any step is such that:  $|\tau(t)| \leq e(\Delta t)^k$  with  $k > 0$  where  $k$  is the order of accuracy. Stability is guaranteed when the approximation error at time  $t$  does not add to the errors at subsequent time steps. An algorithm is defined unconditionally stable when it is stable irrespective of  $\Delta t$ .

In structural dynamics, especially when seismic loads are considered, only low frequency modal responses are of interest. Generally, the selection of the time step  $\Delta t$  depends on the sampling rate of the seismic signal, so, unconditionally stable algorithms are preferred. The use of this type of algorithms results in a substantial saving in terms of computational cost [Arruda and Castro, 2021a]. Two methods can degenerate from Equation 3.2 for two sets of values for  $\alpha$  and  $\beta$ : the linear acceleration method given by  $\beta = \frac{1}{6}$  and  $\alpha = \frac{1}{2}$ , and the constant average acceleration method given by  $\beta = \frac{1}{4}$  and  $\alpha = \frac{1}{2}$ . In this work, the latter is used to approximate the solution because of its unconditional stability.

### Selection of damping properties

The damping terms can describe complex dissipative phenomena such as bond-slip (friction between concrete and reinforcement), intrinsic damping properties of materials, opening and closing of microcracks in concrete, material hysteretic behavior, friction (e.g., in steel connections), contact/friction between structural and non-structural elements [Chopra et al., 2012]

thanks to equivalent approaches. The approximation of the viscous damping terms can have significant effects on the amplitude of the predicted dynamic response of the system. Various damping modeling techniques are available to account for such phenomena.

Widely used formulations for the viscous damping matrix  $\mathbf{C}$  are defined through linear relationships to the mass and stiffness matrices of the structure. The most common classical proportional damping models are the Caughey damping [Caughey, 1960] with especially its particular case, the Rayleigh damping [Rayleigh, 1945], and the Wilson-Penzien damping [Wilson and Penzien, 1972] (see Table 3.1). The Caughey damping is determined for the modal damping ratios  $\zeta$  of the structure through series of mass and stiffness proportional coefficients  $a_k$ . This formulation allows specifying the damping ratio  $\zeta$  of all the  $N_k$  modes. However, numerical deficiencies can be issued from the Caughey damping expressions (Equations (3.1.1a) and (3.1.1b)) because i) they build a fully populated matrix and ii) the algebraic equations are ill-conditioned. The latter issue, although solved by [Luco, 2008] through an explicit solution for the coefficients of Caughey series, has slowed down a widespread adoption of this model in numerical simulations. Therefore, for practical reasons, the banded matrix defined with the Rayleigh damping model is the most adopted model for the viscous damping in both linear and nonlinear time history analyses (Equations (3.1.2a) and (3.1.2b)). Nevertheless, recent works in modal analysis of instrumented buildings [Cruz and Miranda, 2017a, Cruz and Miranda, 2017b] show that the Rayleigh damping model overestimates the response of the structure, and that in seismic nonlinear response history analysis, the Rayleigh damping matrix can develop spurious (i.e. nonexistent) damping forces [Chopra and McKenna, 2016, Puthanpurayil et al., 2016] leading to inaccurate results. Thus, overall in the context of nonlinear response history analysis, [Chopra and McKenna, 2016] does not recommend the Rayleigh damping and demonstrates that the superposition of modal damping matrices (Equation (3.1.3)) eliminates the spurious damping forces. However, this last damping matrix is not popular in practical analyses because it is a fully populated matrix and its construction requires every frequency and mode. Despite the aforementioned studies, the modeling of the damping characteristics of a system is still an open discussion that converges into the need of choosing the damping model depending on the structural system and the specific loading conditions.

In this work, the viscous term given by the damping matrix  $\mathbf{C}$  is added through a classical Rayleigh damping approach. The matrix  $\mathbf{C}$  is thus a linear combination of the mass and stiffness matrices:  $\mathbf{C} = a_0\mathbf{M} + a_1\mathbf{K}$  where  $a_0$  and  $a_1$  are the mass proportional coefficient and the stiffness proportional coefficient, respectively. The damping coefficient  $\zeta$  is usually assumed equal to 5% of the critical damping in reinforced concrete structures [Petrini et al., 2008]. Recommended values for the damping ratio of steel structures are around 2%. In non-linear systems, the energy dissipation due to the material hysteretic behavior is modeled explicitly in the internal resisting force vector  $\mathbf{R}$  in the equation of motion.

---

<b>Caughey model</b>	$\mathbf{C} = \mathbf{M} \sum_{m=0}^{N_k-1} a_k (\mathbf{M}^{-1} \mathbf{K})^m$	(3.1.1a)
	$\tilde{\zeta}_i = \frac{1}{2} \sum_{m=0}^{N_k-1} a_k \omega_i^{2m-1}$	(3.1.1b)
<b>Rayleigh model</b>	$\mathbf{C} = a_0 \mathbf{M} + a_1 \mathbf{K}$	(3.1.2a)
	$\tilde{\zeta}_i = \frac{1}{2\omega_i} (a_0 + a_1 \omega_i^2),$	
	$a_0 = 2 \frac{(\tilde{\zeta}_a \omega_b - \tilde{\zeta}_b \omega_a) \omega_a \omega_b}{\omega_a^2 - \omega_b^2}, \quad a_1 = 2 \frac{\tilde{\zeta}_a \omega_a - \tilde{\zeta}_b \omega_b}{\omega_a^2 - \omega_b^2}$	(3.1.2b)
<b>Wilson-Penzien model</b>	$\mathbf{C} = \mathbf{M} \left( \sum_{m=1}^{N_k} \frac{2\tilde{\zeta}_k \omega_k}{M_k^*} \phi_k \phi_k^T \right) \mathbf{M}$	(3.1.3)

---

TABLE 3.1: Classical proportional damping models

### 3.1.2 A steel frame structure subjected to a moderate ground motion

From [Franco et al., 2022].

A transient dynamic analysis of the steel frame presented in Section 2.3.1 (Chapter 2) is now performed using Newmark's time integration scheme with the constant average acceleration assumption. The results of the HBFEM model are compared with those of the fully detailed FEM model.

In the following,  $d$  refers to the number of degrees of freedom and  $N_p$  to the number of data points of the dynamic force. We recall the governing equation of motion in matrix form:

$$\mathbf{M}\ddot{\mathbf{E}}(t) + \mathbf{C}\dot{\mathbf{E}}(t) + \mathbf{K}\mathbf{E}(t) = \mathbf{f}(t) \quad (3.10)$$

Herein, the viscous term  $\mathbf{C}$  corresponds to the Rayleigh damping matrix. The matrix  $\mathbf{C}$  is thus a linear combination of the mass and stiffness matrices where the proportional damping coefficients are  $a_0 = 0.4837$  and  $a_1 = 5.2742 \times 10^{-4}$  for this example. They represent 2% of the critical damping for the first two modes.

A low energy content seismic input is chosen in order to keep the results consistent with the elastic behavior of the models. The seismic input is the north-south component of the ground accelerogram of the earthquake event recorded on August 2, 2017 in Ibaraki, Japan. Its magnitude is 5.5 and the peak acceleration is 0.13 g with most of the energy content between 5 and 10 Hz as shown in Figure 3.1. A total duration of 120 s and a time step of 0.01 s are considered.

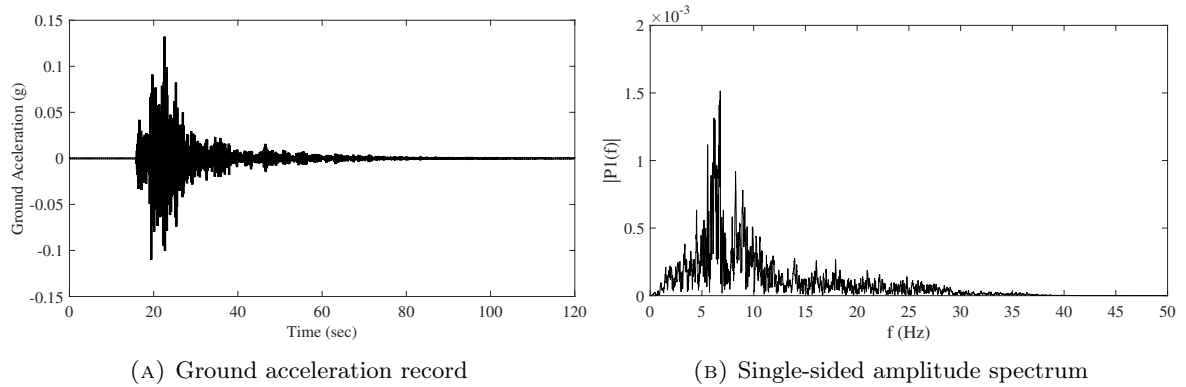


FIGURE 3.1: Ground acceleration record (a) and amplitude spectrum (b) of the north-south component of the earthquake event recorded on August 2, 2017 in Ibaraki, Japan. The magnitude is 5.5 and the peak acceleration is 0.13 g.

Figure 3.2 displays two simulations of the top roof displacement of the structure with respect to time and its amplitude Fourier spectrum. They were obtained with the detailed finite element model and the HBFEM model, i.e. the finite element approximation of the EBM. Figure 3.2(a) shows the time window (between 0 and 40 s) where the maximum top roof displacement of the structure is reached. The results show a satisfactory agreement in terms of both time and spectral amplitudes in the lower frequency range. Nonetheless, the HBFEM model provides a maximum displacement value slightly higher (5.14% more) than the one obtained with the detailed FEM model.

On the spectra of Figure 3.2(b) the peaks of the fundamental frequency (around 2.4 Hz) are well pronounced and their amplitudes agree for both models. Although the second vibration mode is much more excited with the HBFEM model, the peak for the natural frequency (around 9.6 Hz) is well identified. These results are encouraging and show that the HBFEM model provides very good estimations of the structural response at lower computational costs. Once the geometry is defined in MatLab for the HBFEM model and in Cast3M for the detailed FEM model, the computation time of the dynamic analysis with the same resources could easily be four times longer for the detailed FEM model. It is needed to recall that the HBFEM model of the studied structure considers four times fewer DoFs than the detailed finite element model. Additionally, this example highlights the contribution of the HBFEM model to the EBM description: solving this type of problem could be mathematically expensive with an entirely analytical model.



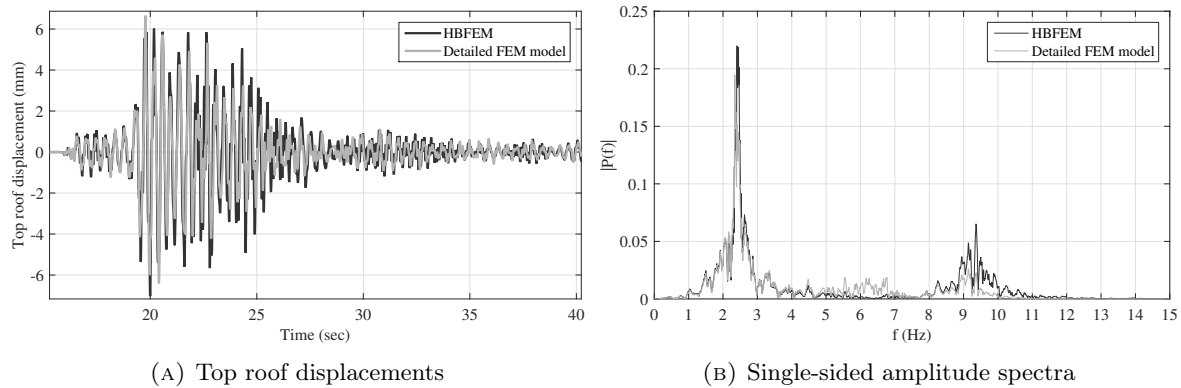


FIGURE 3.2: Top roof displacements (a) and their amplitude spectra (b) obtained with the detailed finite element model (grey) and the HBFEM model (black)

## 3.2 Homogenized beam models of structures with various typical stories

Mid-rise and high-rise buildings are usually designed based on a typical story distribution replicated all along the height of the structure. Commonly, the cross-sections of the structural elements are reduced from a specific floor without changing the geometrical arrangement, aiming to reduce the material weight and costs.

The dynamic analysis of structures with such a vertical irregularity implies a loss of periodicity, which disfavors the essential condition required to implement the homogenization techniques and other simplified 1-D models (e.g., [Su et al., 2016]). Thus, the EBM results, where the elastostatic properties of a unique story are taken into account, could not be realistic enough. Hence, our hypothesis is that the use of the HBFEM formulation proposed in Chapter 2 makes it possible to build a 1D model by assembling the EBM corresponding to the  $t$ -number substructures which respect a condition of local periodicity (or the  $t$ -number groups of stories with the same properties). In other words, if each of the typical stories represents at least five stories in the structure, the periodicity condition can still be valid for such a building. Thus, in this section, the dynamic characteristics of a structure with two different typical stories are evaluated by using the HBFEM model. Our objective is to demonstrate that the HBFEM model facilitates the numerical implementation of the EBM in the analysis of complex structures. Also, we will see that the HBFEM results are very close to the ones provided by fully detailed numerical models, but they require much fewer computational resources.

### 3.2.1 Integration of different unit cell properties in the HBFEM model

Lets consider a structure of  $N$  stories with  $s$ —number of periodic substructures (or  $s$ —number of typical stories). Thus, the construction of the beam model based on the HBFEM formulation starts with the definition of the mass and stiffness matrices of the system as well as the boundary and loading conditions. The construction of the global mass matrix  $\mathbf{M}$  and the global stiffness matrix  $\mathbf{K}$  are based on the assembly of the mass matrices  $\mathbf{M}^{S_i}$  and stiffness

matrices  $\mathbf{K}^{s_i}$  of the  $s$ -number of periodic substructures. Thus, the individual  $\mathbf{M}^{s_i}$  and  $\mathbf{K}^{s_i}$  are defined from the unique unit cell properties, or macroscopic parameters, of the typical story  $s_i$ . Now, we consider a structure with two periodic substructures ( $s = 2$ ) as displayed in Figure 3.3. The construction of the HBFEM model is then based on the elastostatic properties of the two substructure unit cells of size  $l_{m_1}$  and  $l_{m_2}$  each one.

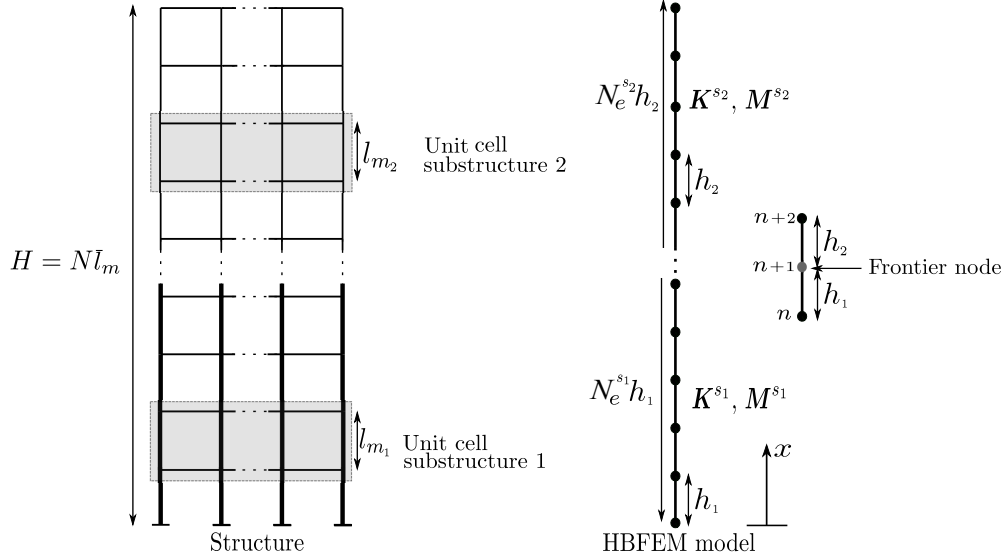


FIGURE 3.3: Structure composed of two periodic substructures (Left). HBFEM model parameters and nodal definition at the boundary between the two substructures (Right)

The macroscopic kinematic variables  $\hat{U}$  and  $\hat{a}$  defined at the boundary  $n + 1$  of both periodic substructures  $s_1$  and  $s_2$  in the 1-D model are represented in Figure 3.4.

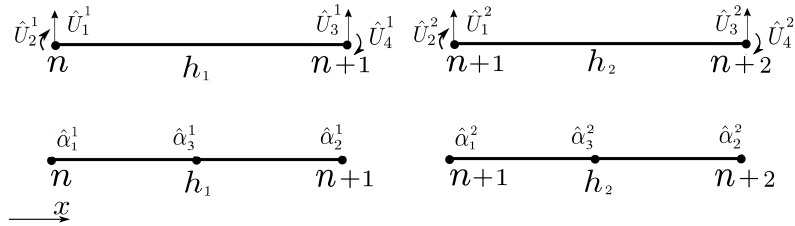


FIGURE 3.4: Nodal kinematic variables of the finite beam elements located at the boundary node  $n + 1$  between the two substructures

The assembly of the individual stiffness matrices  $\mathbf{K}^{s_1}$  and  $\mathbf{K}^{s_2}$  of both substructures is performed in the same manner as each elementary matrix  $\mathbf{K}_t$  is assembled for two finite

elements ( $N_e = 2$ ). Then, the global matrix of the structural system  $\mathbf{K}$  is given by:

$$\mathbf{K} = \begin{bmatrix} \left[ \begin{array}{c} \mathbf{K}^{s_1} \\ \mathbf{K}^{s_2} \end{array} \right] \end{bmatrix}$$

where  $\mathbf{K}^{s_i}$  is a  $d_{s_i} \times d_{s_i}$  matrix. The parameter  $d_{s_i}$  denotes the number of DoF of the periodic substructure  $s_i$  and is equal to the number of nodes  $N_e^{s_i} + 1$  of the finite elements of the substructure times the number of degrees of freedom per node  $d_n = 3$ , therefore  $d_{s_i} = 3(N_e^{s_i} + 1)$ . Then, the number of nodes of the whole structure is  $(\sum_{i=1}^s N_e^{s_i}) + 1$  and the total number of DoF is  $d = 3 [(\sum_{i=1}^s N_e^{s_i}) + 1]$ . The global stiffness matrix  $\mathbf{K}$  is a  $d \times d$  matrix. The stiffness matrices of the substructures  $\mathbf{K}^{s_1}$  and  $\mathbf{K}^{s_2}$  can then be defined as:

$$\mathbf{K}^{s_1} = \begin{bmatrix} K_{11}^{s_1} & K_{12}^{s_1} & \cdots & K_{1(d_{s_1}-2)}^{s_1} & K_{1(d_{s_1}-1)}^{s_1} & K_{1d_{s_1}}^{s_1} \\ K_{21}^{s_1} & K_{22}^{s_1} & \cdots & K_{2(d_{s_1}-2)}^{s_1} & K_{2(d_{s_1}-1)}^{s_1} & K_{2d_{s_1}}^{s_1} \\ \vdots & \vdots & \ddots & \vdots & \vdots & \vdots \\ K_{(d_{s_1}-2)1}^{s_1} & K_{(d_{s_1}-2)2}^{s_1} & \cdots & K_{(d_{s_1}-2)(d_{s_1}-2)}^{s_1} & K_{(d_{s_1}-2)(d_{s_1}-1)}^{s_1} & K_{(d_{s_1}-2)d_{s_1}}^{s_1} \\ K_{(d_{s_1}-1)1}^{s_1} & K_{(d_{s_1}-1)2}^{s_1} & \cdots & K_{(d_{s_1}-1)(d_{s_1}-2)}^{s_1} & K_{(d_{s_1}-1)(d_{s_1}-1)}^{s_1} & K_{(d_{s_1}-1)d_{s_1}}^{s_1} \\ K_{d_{s_1}1}^{s_1} & K_{d_{s_1}2}^{s_1} & \cdots & K_{d_{s_1}(d_{s_1}-2)}^{s_1} & K_{d_{s_1}(d_{s_1}-1)}^{s_1} & K_{d_{s_1}d_{s_1}}^{s_1} \end{bmatrix}$$

$$\mathbf{K}^{s_2} = \begin{bmatrix} K_{11}^{s_2} & K_{12}^{s_2} & K_{13}^{s_2} & \cdots & K_{1(d_{s_2}-1)}^{s_2} & K_{1d_{s_2}}^{s_2} \\ K_{21}^{s_2} & K_{22}^{s_2} & K_{23}^{s_2} & \cdots & K_{2(d_{s_2}-1)}^{s_2} & K_{2d_{s_2}}^{s_2} \\ K_{31}^{s_2} & K_{32}^{s_2} & K_{33}^{s_2} & \cdots & K_{3(d_{s_2}-1)}^{s_2} & K_{3d_{s_2}}^{s_2} \\ \vdots & \vdots & \vdots & \ddots & \vdots & \vdots \\ K_{d_{s_2}1}^{s_2} & K_{d_{s_2}2}^{s_2} & K_{d_{s_2}3}^{s_2} & \cdots & K_{d_{s_2}(d_{s_2}-1)}^{s_2} & K_{d_{s_2}d_{s_2}}^{s_2} \end{bmatrix}$$

and the main assembly of the global matrix  $\mathbf{K}$  occurs at the node  $n + 1$  where the DoF  $\hat{U}_3^{s_1}$  and  $\hat{U}_1^{s_2}$ ,  $\hat{U}_4^{s_1}$  and  $\hat{U}_2^{s_2}$ ,  $\hat{\alpha}_2^{s_1}$  and  $\hat{\alpha}_1^{s_2}$  need to be coupled as follows:

$$\mathbf{K} = \begin{bmatrix} \begin{bmatrix} K_{11}^{s_1} & K_{12}^{s_1} & \cdots & K_{1(d_1-2)}^{s_1} & K_{1(d_1-1)}^{s_1} & K_{1d_1}^{s_1} \\ K_{21}^{s_1} & K_{22}^{s_1} & \cdots & K_{2(d_1-2)}^{s_1} & K_{2(d_1-1)}^{s_1} & K_{2d_1}^{s_1} \\ \vdots & \vdots & \ddots & \vdots & \vdots & \vdots \end{bmatrix} & \begin{bmatrix} K_{(d_1-2)1}^{s_1} & K_{(d_1-2)2}^{s_1} & \cdots & K_{(d_1-2)(d_1-2)}^{s_1} + K_{11}^{s_2} & K_{(d_1-2)(d_1-1)}^{s_1} + K_{12}^{s_2} & K_{(d_1-2)d_1}^{s_1} + K_{13}^{s_2} & \cdots & K_{1d_2}^{s_2} \\ K_{(d_1-1)1}^{s_1} & K_{(d_1-1)2}^{s_1} & \cdots & K_{(d_1-1)(d_1-2)}^{s_1} + K_{21}^{s_2} & K_{(d_1-1)(d_1-1)}^{s_1} + K_{22}^{s_2} & K_{(d_1-1)d_1}^{s_1} + K_{23}^{s_2} & \cdots & K_{2d_2}^{s_2} \\ K_{d_1 1}^{s_1} & K_{d_1 2}^{s_1} & \cdots & K_{d_1(d_1-2)}^{s_1} + K_{31}^{s_2} & K_{d_1(d_1-1)}^{s_1} + K_{32}^{s_2} & K_{d_1 d_1}^{s_1} + K_{33}^{s_2} & \cdots & K_{3d_2}^{s_2} \\ \vdots & \vdots & \ddots & \vdots & \vdots & \vdots & \ddots & \vdots \end{bmatrix} \\ \begin{bmatrix} K_{d_2 1}^{s_2} & & & & & & & \\ & K_{d_2 2}^{s_2} & & & & & & \\ & & K_{d_2 3}^{s_2} & & & & & \\ & & & \cdots & & & & \\ & & & & & & & K_{d_2 d_2}^{s_2} \end{bmatrix} & \end{bmatrix}$$

The assembly of the global mass matrix  $\mathbf{M}$  is performed in the same manner as the one of  $\mathbf{K}$  using the individual mass matrices  $\mathbf{M}^{s_1}$  and  $\mathbf{M}^{s_2}$ .

$$\mathbf{M} = \begin{bmatrix} \begin{bmatrix} \mathbf{M}^{s_1} \end{bmatrix} \\ \begin{bmatrix} \mathbf{M}^{s_2} \end{bmatrix} \end{bmatrix}$$

### 3.2.2 Case study: the Grenoble City Hall (GCH)

#### Description of the structure

The Grenoble City Hall (GCH) is a reinforced concrete structure with a square patio of two stories crowned with a tower at one side, which is the object of this study. The tower has 11 stories above the patio building which corresponds to 13 stories from ground to top. This building was completed in 1967 and is currently in use, operating as the town hall of Grenoble, France. The tower is 52 m high from ground to top, 43 m long and 13 m wide (Figure 3.5). The structural components are columns, 4 pillars (containing the staircases and elevator shafts) and beams. The main hall, located at the ground story, is a floor with double height (6.4 m) where the only vertical members are the four pillars. They support a prestressed transfer slab on which the tower is built. The cross-section of the pillars decreases after the transfer slab. The inter-story height is 3.2 m for the typical stories of the tower. Every column starts in the prestressed transfer slab. The ten stories above the transfer slab have an identical structural distribution. However, the column sections slightly decrease from

the 6th story above the transfer slab. In the last story (11th from the transfer slab or 13th from the ground), this distribution changes and the structural components are basically shear walls. The building has also two basements with the same column distribution as the typical stories of the tower. The foundations rely on deep piles anchored in a stiff layer of sand and gravel [Michel et al., 2010b].

### Previous works

The GCH building was the first building instrumented in France and has been monitored since 2004 by the French Accelerometric Network (RAP). The determination of its modal parameters has been done by ambient vibration measurements in order to calibrate simplified lumped-mass models and full 3D numerical models [Michel and Gueguen, 2006, Michel et al., 2010b] to perform seismic analyses with moderate and strong motions. A modal identification carried out by [Michel et al., 2010b] finds the first three vibration modes:

- the first flexural mode in the longitudinal direction at 1.15 Hz,
- the first flexural mode in the transverse direction at 1.22 Hz,
- the first torsional mode at 1.44 Hz.

In each direction (i.e., longitudinal and transverse), the identification of the beam-type behavior of the building is based on the computation of the ratios between the second frequency and the first frequency  $f_2/f_1$  and the mode shapes. In [Michel and Gueguen, 2006], the GCH building fundamental mode is said to look like a mode of a bending beam and the frequency ratios for the longitudinal and transverse directions are 3.9 and 4.7 respectively. These ratio values are associated, in the Timoshenko beam model [Boutin et al., 2005], with an intermediate behavior (i.e., neither pure shear nor pure bending). In this work, we aim to verify the structural behavior of the GCH building by analyzing the macroscopic parameters provided by the elastostatic analysis of the unit cell (a unique story) and the identification criterion proposed by [Hans and Boutin, 2008]. This building has also been the subject of vulnerability studies by [Desprez, 2010], who validated a 3D numerical model to analyze retrofitting techniques in the pillars using fiber reinforced polymer. The [Desprez, 2010] numerical model found again the first five modes measured in-situ [Michel, 2007]. This full numerical model is used in this work as a reference model to verify the performance of the HBFEM model in the framework of linear elastic analyses.

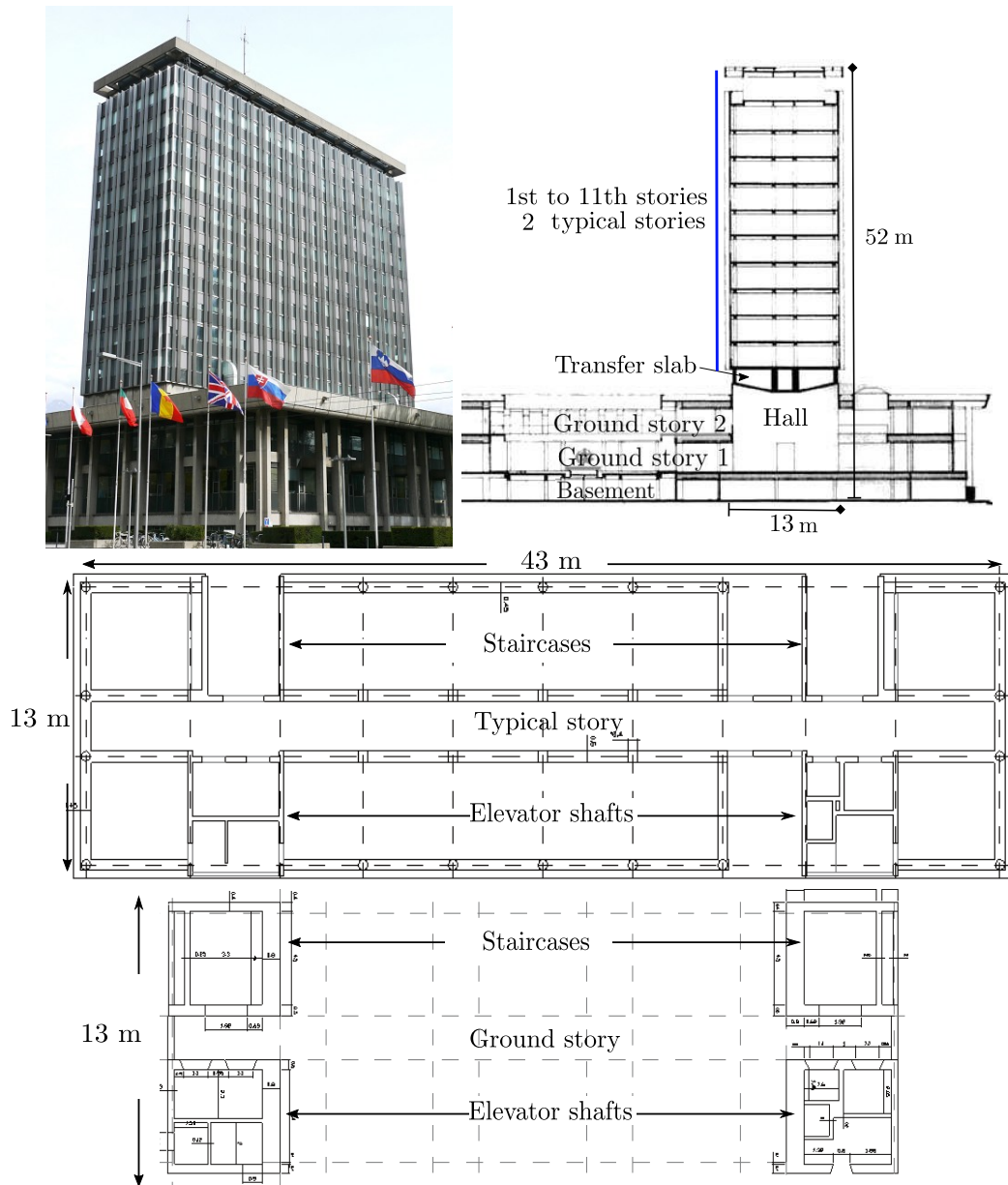


FIGURE 3.5: The Grenoble City Hall tower block. Top left: General view [Jacques Mossot, 2007]. Top right: Front side view of the tower block [Michel et al., 2010b]. Bottom: typical story and ground story plan views

### Scope of this study

The EBM and the HBFEM model are well suited to fully periodic or vertically regular buildings based on only frame-form (i.e., beams and columns) or tunnel-form (i.e., only shear walls and slabs) structural systems and they can significantly reduce the needed computational resources. The vertical irregularity of the GCH building (i.e., it is not fully periodic) and its various structural components (i.e., shear walls, columns, beams and slabs) complexify the construction of the equivalent beam models a little. Thus, our objective with the Grenoble City Hall building study is to highlight that we can build a one-dimensional model of a complex building structure by understanding its mechanical functioning from the homogenization

analytical basis. In this section, we focus our analysis on the **linear elastic framework**. We estimate the natural frequencies and mode shapes of the GCH building through equivalent beam models and compare the results with those of full detailed numerical models. The construction of the continuous models follows the **hybrid** strategy up to now presented and summarized through the flow diagram in Figure 3.6. The first step is the static analysis of a unique story of the building to find the macroscopic parameters of the continuous models. Once the continuous beam models are completed, the dynamic analysis can be performed (i.e., free vibration analysis).

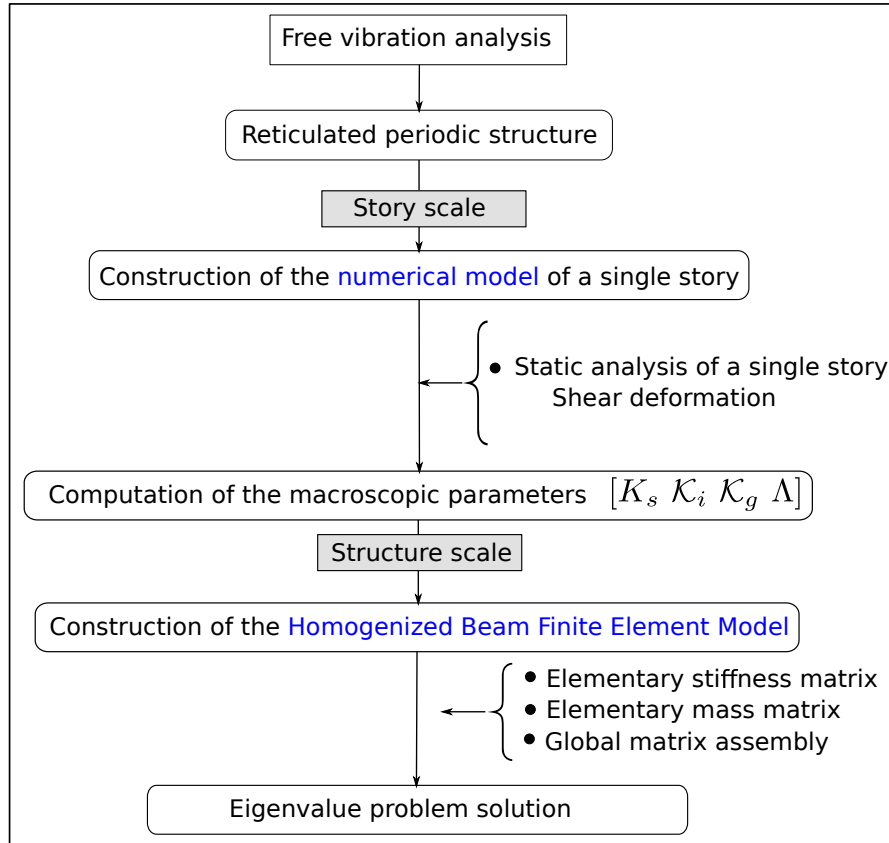


FIGURE 3.6: Hybrid strategy for free vibration analysis with the HBFEM model

This section is composed of three main parts. First of all, the full detailed numerical model [Desprez, 2010] is introduced together with the obtained dynamic properties. As a matter of information, in-situ findings [Michel, 2007] are also presented. Secondly, the construction of the continuous model of the GCH building is explained. Two different schemes are implemented to analyze the influence of the vertical irregularity of the building on the results. For the first scheme, the EBM and the HBFEM model are constructed based on only the quasi-periodic section of the GCH tower. For the second scheme, the full 13-story GCH tower block is analyzed. Thus, the properties of the two typical stories, ground story and basement are all included in the HBFEM model. Figure 3.7 illustrates the considered sections on the GCH tower block. Note that the stories are numbered from the transfer slab.

The HBFEM models are compared with numerical simulations. Finally, we discuss the GCH building dynamic behavior, the implemented strategy and the results.

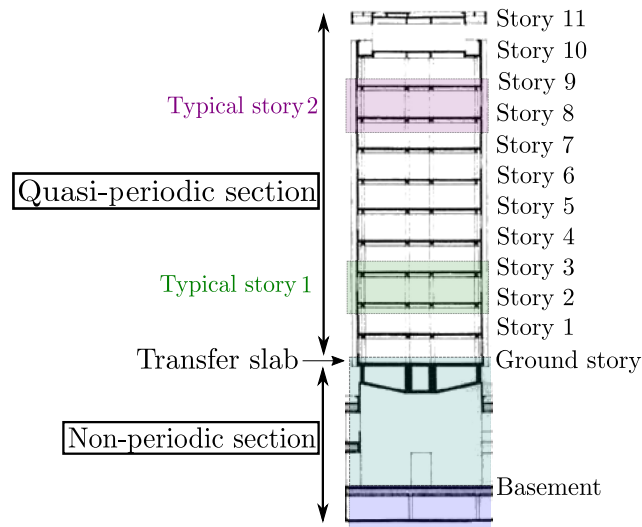


FIGURE 3.7: Quasi-periodic and non-periodic sections of the GCH tower block.

### Numerical model of the GCH building

[Michel et al., 2010a, Desprez, 2010] present a detailed finite element model of the 13-story tower (see Figure 3.9). The structure is modeled using multifiber beam elements in the finite element code Cast3M [CEA, 2017]. The columns, beams and shear walls of the four pillars are modeled as Timoshenko beam elements, whereas the slabs and last story walls are modeled as shell elements. The model has a total of 12275 nodes and 73650 degrees of freedom. The plan view and dimensions of the structural member cross-sections considered in the geometry definition of the numerical model are shown in Figure 3.8 and Table 3.2. The main geometrical features and the material properties are summarized:

$$\begin{aligned} \text{Building height } H &= 52 \text{ m,} \\ \text{Basement heights } l_{b_1} &= 3.47 \text{ m and } l_{b_2} = 4.68 \text{ m, hall height } l_h = 7.7 \text{ m,} \\ \text{Inter-story height } l_m &= 3.2 \text{ m} \end{aligned}$$

$$\begin{aligned} \text{Concrete properties: } E_c &= 32 \text{ GPa, } \nu_c = 0.2, \rho_c = 2400 \text{ kg/m}^3 \\ \text{Steel properties: } E_s &= 200 \text{ GPa, } \nu_s = 0.3, \rho_s = 7800 \text{ kg/m}^3 \end{aligned}$$

The construction of the numerical model is based on the following assumptions:

- The connections between the structural elements are perfectly-rigid.
- A weak soil-structure interaction is considered. Then, the structure model is clamped at the base.
- The frame elements (columns and beams) are modeled as Timoshenko beams. The pillars are also modeled as frame elements with U-shape cross sections.



- The bending stiffness of the floors is taken into account. They are modeled as Love-Kirchhoff shell elements (DKT elements)
- The walls at the last story are modeled as shell elements.

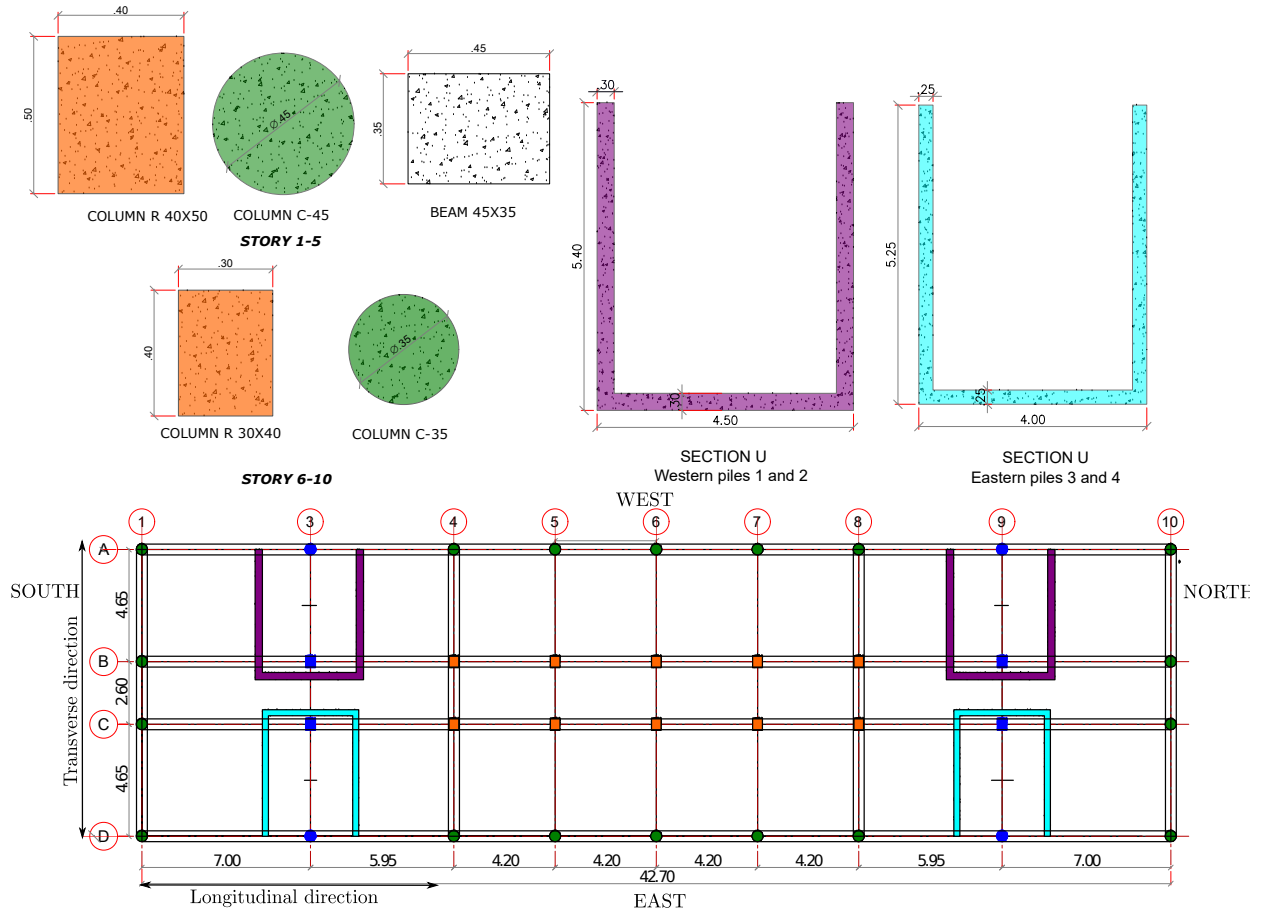


FIGURE 3.8: Sections considered in the numerical model (the stories are numbered from the transfer slab). Top left: column and beam sections for the two typical stories. The cross-section of the columns slightly decrease from the 6th story. Top right: pillar sections. Bottom: plan view of the distribution considered in the numerical model

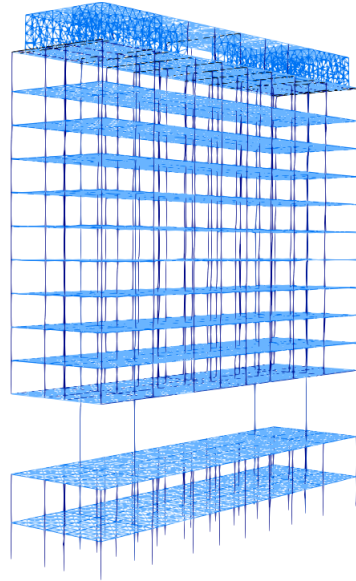


FIGURE 3.9: Full detailed numerical model (12275 nodes and 21278 elements) of the Grenoble City Hall tower block [Desprez, 2010].

Property	Basement	Ground story	Typical story 1	Typical story 2
Number of stories	2	1	5	5
Story height, $l_m$ (m)	4.08 <sup>a</sup>	7.7	3.2	3.2
Slab thickness (m)	0.14	0.16	0.14	0.14
Beam sections (cm)	45×35	300 × 65 <sup>b</sup> - 200 × 115 <sup>c</sup>	45×35	45×35
Column sections (cm)	40×50	—————	40×50	30×40
Pillar sections	R-shape	R-shape	U-shape	U-shape

TABLE 3.2: Geometrical properties extracted from the detailed numerical model. (a) Average of the two basement story heights =  $0.5 \times (3.47 + 4.68)$  m. (b) 4 beams in the longitudinal direction. (c) 3 beams in the transverse direction.

The first six vibration modes are shown in Table 3.3. These frequencies are compared with the frequencies obtained from in-situ measurements in Table 3.4. A very good correlation is found for five vibration modes. The 2nd transverse mode (4.997 Hz) exhibited in the numerical model was not identified in the in-situ measurements. The in-situ results are shown for general information. The reference values to verify the EBM and the HBFEM model results are those of the detailed numerical model.

The frequency ratios  $f_i/f_1$  for each direction are the following:

Longitudinal modes 1 ; 4.29

Transverse modes 1 ; 4.22

Torsional modes 1 ; 3.91

These frequency ratios are different from the common values found in the literature for shear beams (1 ; 3 ; 5) or Euler-Bernoulli beams (1 ; 6.25 ; 17.36). A hasty judgment of the structure behavior based on the mode shapes can be limited to say that the structure behaves globally in bending and that no rotation of the floors is observed in the first longitudinal mode. However, the first transverse mode exhibits some rotation of the floors with respect to the horizontal. Note that the in-situ measurements and the numerical model show that the longitudinal and transverse vibrations are uncoupled. Thus, in this work, both directions are studied independently.

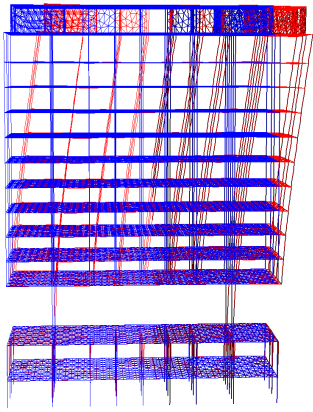
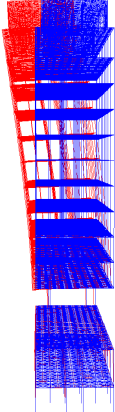
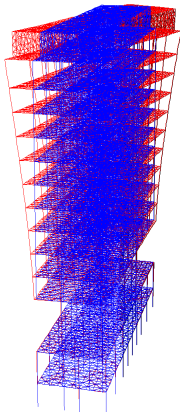
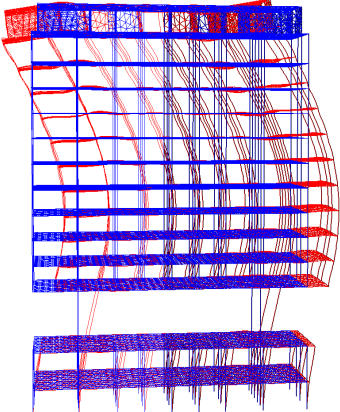
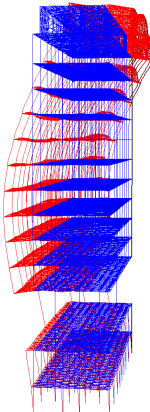
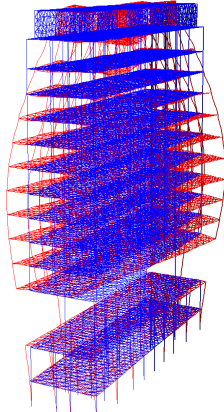
Mode 1 1st flexural longitudinal 1.096 Hz	Mode 2 1st flexural transverse 1.185 Hz	Mode 3 1st torsional 1.431 Hz
		
Mode 4 2nd flexural longitudinal 4.703 Hz	Mode 5 2nd flexural transverse 4.997 Hz	Mode 6 2nd torsional 5.598 Hz
		

TABLE 3.3: First vibration modes of the Grenoble City Hall from the full detailed numerical model [Desprez, 2010]

Modal frequencies [Hz]			
In-situ [Michel, 2007]	Numerical model [Desprez, 2010]	Mode	error [%]
1.16	1.10	1st flexural longitudinal	5.17
1.22	1.19	1st flexural transverse	2.46
1.45	1.43	1st torsional	1.38
4.50	4.70	2nd flexural longitudinal	4.44
—	5.00	2nd flexural transverse	—
5.70	5.60	2nd torsional	1.75

TABLE 3.4: Comparison of the first modal frequencies of the Grenoble City Hall building obtained with the ambient vibrations and the numerical model.

### Construction of 1D models for the GCH building

One considers the GCH tower block as a structure with a quasi-periodic section above the transfer slab (i.e., from 1st to 11th stories) and a non-periodic section beneath the transfer slab (i.e., the ground and basement stories) (see Figure 3.7). Simultaneously, and according to the definitions stated in Section 3.2.1 on page 82), the quasi-periodic section is composed of two periodic substructures with a slight difference on the cross-section of the columns. The first substructure has the geometric properties of the typical story from the 1st to the 5th stories, and the second one has the properties from the 6th to the 11th stories. On the other hand, the non-periodic section, under the transfer slab, has no periodic substructures as it does not respect any of the homogenization conditions (e. g., more than five repeated stories, same story height). Additionally, the 11th story is totally different from the rest of stories. Herein, we only considered its mass and no stiffness contribution is added.

This particular configuration of the GCH tower block is suitable to test the performance and detect the limits of the HBFEM model and the EBM. Therefore, the continuous models of the GCH tower block are obtained under two different schemes to verify the influence on the results of considering the periodic and non-periodic sections:

- A first scheme analyzes only the quasi-periodic section of the GCH tower (with the two periodic substructures) assuming two consecutive homogenized parts; the first one for the stories 1 to 5 above the transfer slab and the second one for the stories 6 to 11. Thus, an HBFEM model, named HBFEM-1, is created following the procedure in Section 3.2.1. Additionally, two different EBMs are built based on the characteristics of the two groups of typical stories. It is of interest to quantify the effects of the slight absence of periodicity on the structure by using the EBMs. Each EBM corresponds to a tower with eleven identical stories. The model EB-1 has the properties of the lower stories (from the 1st to the 5th story) and the model EB-2 has the properties of the upper stories (from the 6th to the 10th story). The results from HBFEM-1 and the EBMs are compared to those of a new detailed numerical model, called DFEM-1, where only the quasi-periodic section (from the 1st to the 11th stories) of the detailed numerical model presented previously (Figure 3.9) is analyzed as shown in Figure 3.10. The relevant geometrical properties for all three types of model, the HBFEM, EBMs and the detailed numerical model, are:

$$N = 11, H = 35.2 \text{ m}, l_m = 3.2 \text{ m}$$

- A second scheme searches the response of the whole structure, with both quasi-periodic and non-periodic sections. The non-periodic part represents a third of the entire GCH tower block, which makes its study relevant. It comprises the ground and basement stories that substantially differ from the typical stories by their inter-story height, shear wall dimensions and slab thickness. In this scheme, each story is considered as an independent unit cell with its own macroscopic parameters. It implies that the HBFEM model of the second scheme has three additional stories at the base with different elementary matrices. Herein, only the HBFEM model is compared with the detailed numerical model of the GCH tower block shown in Figure 3.9. The main features of the two models are:

$$N = 14, H = 51.05 \text{ m}, l_{b_1} = 3.47 \text{ m}, l_{b_2} = 4.68 \text{ m}, l_h = 7.7 \text{ m}, l_m = 3.2 \text{ m}$$

*Analyzed models* For all the models, the following assumptions apply: the connections between the structural elements are perfectly rigid, the structure is clamped at the base and free at the top end.

Table 3.5 summarizes the analyzed models.

Scheme	Unit cell properties	EBM	HBFEM model	Detailed numerical model
<b>1: Quasi-Periodic section</b>	Typical story 1	EB-1	HBFEM-1	DFEM-1
	Typical story 2	EB-2		
<b>2: Non-periodic section</b>	Basements	—	HBFEM-2	DFEM-2
+	+ ground story			
<b>quasi-periodic section</b>	+ typical stories 1, 2			

TABLE 3.5: Analyzed models in the schemes 1 and 2

### Scheme 1: Analysis of the GCH building quasi-periodic section

**Numerical model: DFEM-1** Figure 3.10 displays the complete finite element mesh for the 11th-story quasi-periodic section of the GCH tower block (above the transfer slab). The geometrical distribution of the elements in the story is kept identical to the original numerical model. The same material properties are used.

$$N = 11, H = 35.2 \text{ m}, l_m = 3.2 \text{ m}$$

$$\text{Concrete properties: } E_c = 32 \text{ GPa}, \nu_c = 0.2, \rho_c = 2400 \text{ kg/m}^3$$

$$\text{Steel properties: } E_s = 200 \text{ GPa}, \nu_s = 0.3, \rho_s = 7800 \text{ kg/m}^3$$

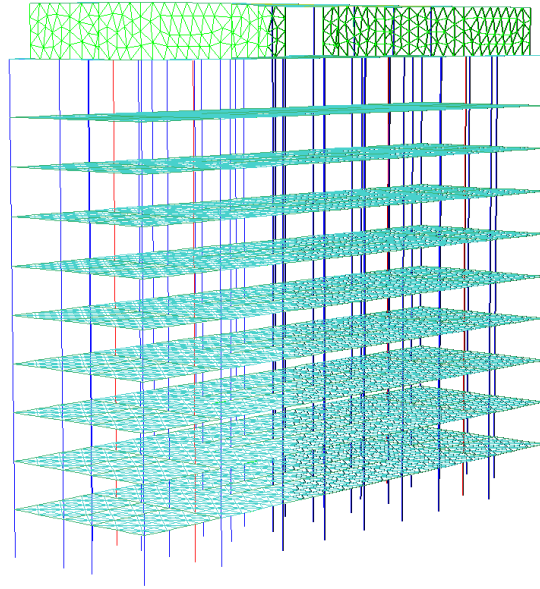


FIGURE 3.10: Full detailed numerical model DFEM-1 of the 11th-story quasi-periodic section of the Grenoble City Hall tower block. (9864 nodes and 17080 elements.)

Table 3.6 shows the first six computed mode shapes for the quasi-periodic section of the GCH tower block. For the flexural modes, the colors refer to the vertical displacement ( $UZ$ ). The red regions go upwards and the blue regions go downwards. For the torsional modes, it is the transverse displacement ( $UY$ ) that is represented. The first three frequencies are 1.537 Hz, 1.551 Hz and 1.79 Hz for the 1st transverse, longitudinal and torsional modes. The 2nd transverse, longitudinal and torsional modes appear at 7.755 Hz, 8.068 Hz and 8.702 Hz. The frequency ratios  $f_i/f_1$  in each direction are:

Longitudinal modes 1 ; 5.20

Transverse modes 1 ; 5.05

Torsional modes 1 ; 4.85

If compared with the original numerical model, the frequency ratios are still different from shear or Euler-Bernoulli beams. Now, the transverse modes appear at a lower frequency than the longitudinal modes but the global shape remains the same for both directions. The global bending of the tower generated by the tension-compression of the vertical elements is still observed as well as the rotation of the floors in the first transverse mode.

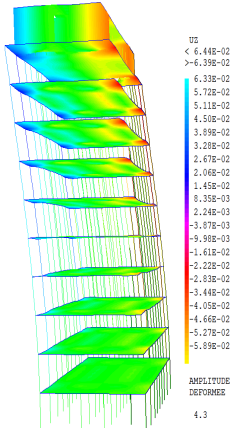
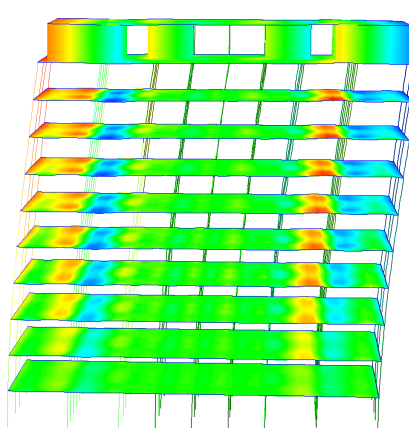
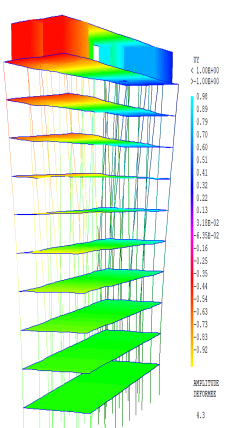
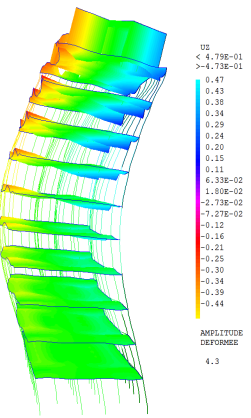
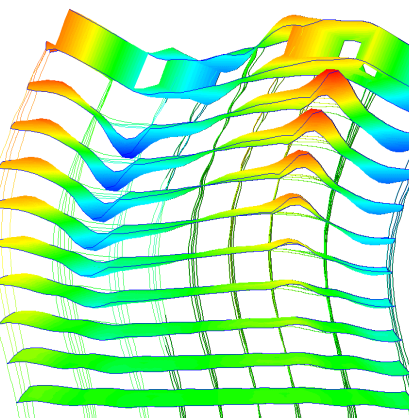
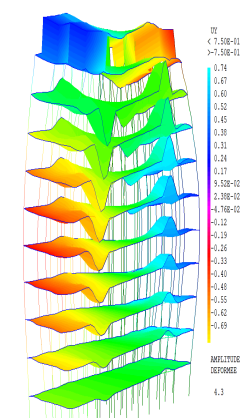
<p>Mode 1 1st flexural (transverse) 1.537 Hz</p>	<p>Mode 2 2nd flexural (longitudinal) 1.551 Hz</p>	<p>Mode 3 1st torsional 1.795 Hz</p>
		
<p>Mode 4 3rd flexural (transverse) 7.755 Hz</p>	<p>Mode 5 4th flexural (longitudinal) 8.068 Hz</p>	<p>Mode 6 2nd torsional 8.702 Hz</p>
		

TABLE 3.6: First vibration modes of the upper tower section of the Grenoble City Hall building (full detailed numerical model DFEM-1)

### Properties of the continuous models EB-1, EB-2 and HBFEM-1

**Macroscopic parameters** The macroscopic parameters, or unit cell properties, are defined by the linear mass of the story  $\Lambda$ , the shear stiffness  $K_s$ , the global bending stiffness  $\mathcal{K}_g$  and the inner bending stiffness  $\mathcal{K}_i$ . The linear mass  $\Lambda$  is the mass of a story divided by the story height. The estimation of  $\mathcal{K}_g$  and  $\mathcal{K}_i$  is realized in EXCEL. A table of the element's cross-sections and the concrete properties (Elastic modulus  $E_c$  and mass density  $\rho_c$ ) is created to compute the global bending inertia  $I_g = A_i d_i^2$  and the inner bending inertia  $I_i$ . Then,  $\mathcal{K}_g = \sum E_c A_i d_i^2$  and  $\mathcal{K}_i = \sum E_c I_i$  are quickly evaluated. The inertia of the reinforcing bars are taken into account by means of the equivalent concrete area.



The computation of  $K_s$  requires the numerical model of a single story to impose a shear deformation of the cell and obtain  $K_s$  based on  $K_s = |\sum T|l_m/\Delta U$ , where  $T$  is the shear force in each vertical element (columns and pillars) generated by a differential horizontal displacement  $\Delta U$  between the bottom and the top of the story.

### Story model for the computation of the shear stiffness $K_s$

To assess  $K_s$ , we need to impose the macroscopic shear deformation on a finite element model of a single story with periodic boundary conditions. We perform this analysis using two different FEM-based pieces of software, Cast3M and ETABS, with a double objective: to verify the values for  $K_s$  and the periodic conditions identified by the homogenization, and to provide two different modeling strategies, which are conditioned by the software environment, to capture the shear deformation of the story's FE model. On the one hand, the unit cell in Cast3M can be modeled as a common story with the floor at the top level supported by the vertical elements (see Figure 3.11), and the periodic boundary conditions can be assigned to the rotations of the top and bottom nodes of every vertical element. Note that a multifiber beam model which includes the steel reinforcement is used for this study. On the other hand, ETABS does not allow us to impose periodic conditions, so we opted for modeling the point with a bending moment equal to zero which is located at the mid-height of the vertical elements when the rotations are periodic. In this model, the floor is at mid-level with half of the vertical elements underneath and above the floor. Thus, in ETABS, we capture the shear deformation of the story by imposing the differential horizontal displacement  $\Delta U$  with free nodal rotations at the ends of the half vertical elements (Figure 3.13).

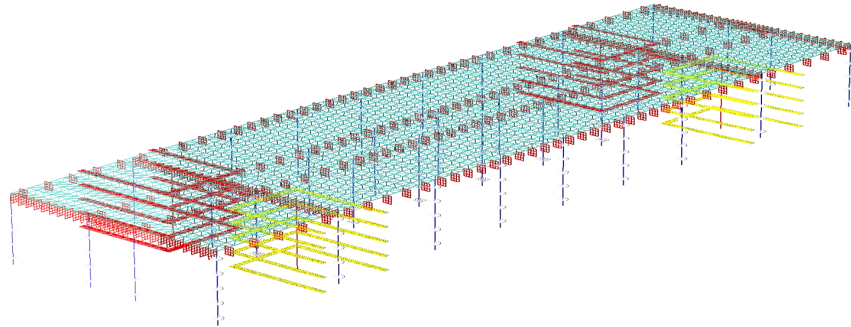


FIGURE 3.11: Full detailed multifiber beam model of a single story in Cast3M

To generate the shear deformation of the story model in Cast3M, the boundary conditions (as presented in Section 1.5.2) consist of (Figure 3.12):

- All the nodes are left free to rotate but the rotations must be equal at both ends of every vertical element ( $\theta_{i_{n_+}} = \theta_{i_{n_-}}$ ).
- The vertical displacements of all the nodes are restrained ( $v_{n_+} = v_{n_-} = 0$ ).
- The horizontal displacements  $u$  at the level  $n_-$  are set to zero ( $u_{n_-} = 0$ ).



- For all the nodes at the level  $n_+$ , the horizontal displacements  $u$  are set equal to the differential displacement  $\Delta U$  (as the model is linear, this value does not influence the result and we chose  $\Delta U = 3.2$  m (the height of the story) for convenience).

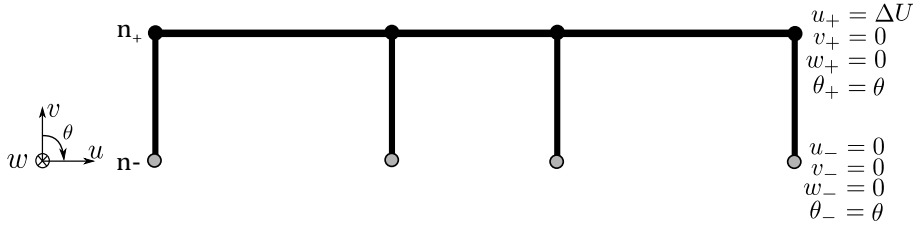


FIGURE 3.12: Boundary conditions in the Cast3M story model (Transverse direction)

For the ETABS story model, all the listed conditions are applicable but the periodic condition  $\theta_{i_{n_+}} = \theta_{i_{n_-}}$ . The end nodes of the model, which correspond to the middle of the vertical elements, are simply set free to rotate (Figure 3.13).

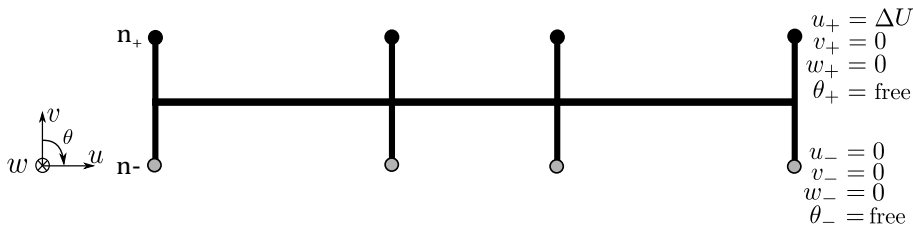


FIGURE 3.13: Boundary conditions in the ETABS story model (Transverse direction)

Figures 3.15-3.14 present the unit cell's shear deformation in the longitudinal and transverse directions for the Cast3M and ETABS story models. The colors represent the vertical displacements. Table 3.7 shows the estimated values of  $K_s$  for both story models. The difference between the models is small in both directions ( $< 14.4\%$ ). This comparison, although used only for the verification process, ensured the quality of the Cast3M results which are used herein for the rest of the computations. The possible reasons for the difference can be the assumed boundary conditions, the modeling environment itself, the fact that the vertical elements are discretized with multifiber beams in Cast3M, or the mesh refinement of the shell elements used to model the floor etc... For example, Table 3.7 compares the  $K_s$  values for different mesh densities for the floor (0.20, 0.30, 0.50, 0.70 and 0.95). Notice the mesh refinement variation influences the  $K_s$  values (up to 14.5% difference with respect to the mean). In the detailed numerical model (Figure 3.10), we set the mesh density to 0.95. Thus, as a matter of coherence, we stick to the results provided by a density of 0.95 in the story model. Moreover, the values provided for the mesh size 0.95 are close to the calculated mean of  $K_s$  for both typical story groups and directions.

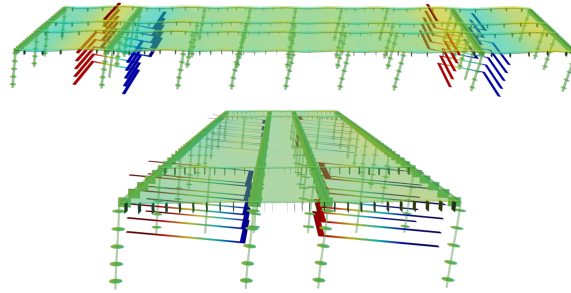


FIGURE 3.14: Shear deformation of the unit cell in Cast3M. Top: Longitudinal direction. Bottom: Transverse direction. The colors represent the vertical displacements

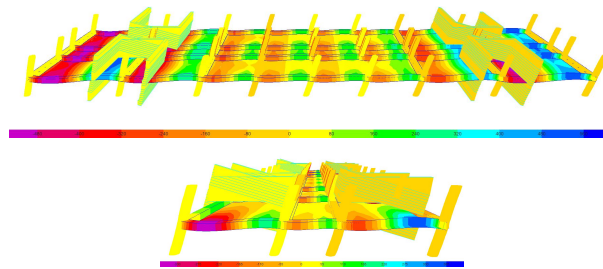


FIGURE 3.15: Shear deformation of the unit cell in ETABS. Top: Longitudinal direction. Bottom: Transverse direction. The colors represent the vertical displacements.

Typical story	Direction	$K_s$ (Cast3M)[MN]	$K_s$ (ETABS)[MN]	% difference
1	Longitudinal	1086.92	1024.33	5.76
	Transverse	1276.47	1459.93	14.37
2	Longitudinal	705.48	657.83	6.75
	Transverse	979.37	1043.19	6.52

TABLE 3.7: Comparison of the shear stiffness  $K_s$  obtained with the story model in Cast3M and in ETABS (897 nodes and 1320 elements).

		$K_s$ (Cast3M) [MN]					
		0.20	0.30	0.50	0.70	0.95	Mean (% var)
Number of nodes		13937	6287	2655	1463	897	
1	Longitudinal	1186.63	1044.11	1079.19	1243.06	1086.92	1127.98 (7.4)
	Transverse	1164.86	1165.15	1620.41	1257.64	1276.47	1296.91 (14.5)
2	Longitudinal	749.91	682.66	706.70	776.42	705.48	724.23 (5.24)
	Transverse	899.59	891.04	1231.39	959.98	979.37	992.27 (14.00)

TABLE 3.8: Variation of the shear stiffness with respect to the mesh density used to model the floor in Cast3M.

Table 3.9 summarizes the macroscopic parameters of the typical stories 1 and 2 to build the EB-1, EB-2 and HBFEM-1 models.

Macroscopic parameters	Typical story 1		Typical story 2	
	L	T	L	T
$\Lambda$ , linear mass (ton/m)	164		158	
$K_s$ , shear stiffness (MN)	1086.92	1276.47	705.48	979.37
$\mathcal{K}_i$ , inner bending stiffness (MN m <sup>2</sup> )	$1.66 \times 10^6$	$1.51 \times 10^6$	$1.66 \times 10^6$	$1.51 \times 10^6$
$\mathcal{K}_g$ , global bending stiffness (MN m <sup>2</sup> )	$1.36 \times 10^8$	$1.01 \times 10^7$	$1.24 \times 10^8$	$8.74 \times 10^6$

TABLE 3.9: Macroscopic parameters for the typical stories 1 and 2 in the longitudinal (L) and transverse (T) directions.

### The GCH building dynamic behavior

Once all the macroscopic parameters are estimated from the static analysis of a single story, the macroscopic constants  $C$  and  $\gamma$  can be evaluated and the mechanism or the combination of mechanisms (i.e., shear, inner bending and global bending) that govern the dynamic behavior of the GCH building for the first vibration modes can be identified. The macroscopic constants' expressions are recalled here:

$$C = \frac{\mathcal{K}_g}{K_s L^2} \quad L_k = \frac{2H}{\pi(2k-1)} \quad \gamma = \frac{\mathcal{K}_i}{\mathcal{K}_g} \quad (3.11)$$

The scale ratio  $\varepsilon_k = \frac{l_m}{L_k} = \frac{\pi(2k-1)}{2N}$  with the mode number  $k=1$  and the number of stories  $N = 11$  is 0.14. Then, the macroscopic constants for the typical story 1 are  $C = 249.76 = \varepsilon^{(\mathbf{x}=-2.84)}$  and  $\gamma = 0.012 = \varepsilon^{(\mathbf{y}=2.24)}$  in the longitudinal direction, which settle a point in the *inner bending and shear* beam domain of the graph of Figure 1.7. The same model is obtained for the typical story 2 (Table 3.10).

Unit cell properties	$N$	$C$	$\gamma$	Behavior
Typical story 1	11	249.76	0.012	Inner bending and shear
Typical story 2	11	350.02	0.013	Inner bending and shear

TABLE 3.10: Identified behaviors in the longitudinal direction.

In the transverse direction, the governing behavior is also described by an *inner bending and shear* beam model ( $C = 15.76 = \varepsilon^{(\mathbf{x}=-1.42)}$  and  $\gamma = 0.15 = \varepsilon^{(\mathbf{y}=0.97)}$  for the typical story 1)

Unit cell properties	$N$	$C$	$\gamma$	Behavior
Typical story 1	11	15.76	0.15	Inner bending and shear
Typical story 2	11	17.77	0.17	Inner bending and shear

TABLE 3.11: Identified behaviors in the transverse direction.

The frequency ratios  $f_k/f_1$  of the first modes given by the numerical model D-FEM1 (e.g., 1 ; 5.20 in the longitudinal direction) agree well with the identified inner bending and shear

beam model. There is a large interaction between the shear deformation of the unit cell and the inner bending of the vertical elements that would not be possible to capture with a Timoshenko beam model. As shown in Figure 1.19, the large ratio  $C > 1$  would provide a point in the shear beam model and a frequency ratio much closer to 3 which does not correspond with the identified behavior.

**Natural frequencies and mode shapes** After the computation of the macroscopic parameters, the dynamics of the EBMs, EB-1 and EB-2, and the HBFEM-1 model can be solved. The solution of the equation of motion Eq.(1.8) (Section 1.4.3) provides the results for EB-1 and EB-2. The results of the HBFEM model are obtained from the solution of the eigenproblem presented in Section 2.3.2 and the assembly procedure described in Section 3.2.1.

Tables 3.12 and 3.13 summarize the first two eigenfrequencies  $f_i = \omega_i/2\pi$  obtained for the EBMs and the HBFEM model in the longitudinal and transverse directions of the GCH tower block. The relative difference  $\epsilon^{f_{HBFEM}}$  on the eigenfrequencies between the HBFEM model and the detailed numerical model is computed with:

$$\epsilon^{f_{HBFEM}} = 100 \times \frac{f_{HBFEM} - f_{DFEM}}{f_{DFEM}} \quad (3.12)$$

**Correlation between the mode shapes** The mode shapes obtained with every model are presented in Figure 3.16. The vertical axe corresponds to the normalized height and the horizontal axe refers to the normalized displacement with respect to the maximum. In order to verify the correlation between the corresponding mode shapes the modal assurance criterion (MAC) defined in [Allemang, 1982] is adopted:

$$\text{MAC}(\phi_i^A \phi_i^B) = \frac{[(\phi_i^A)^T \phi_i^B]^2}{[(\phi_i^A)^T \phi_i^A][(\phi_i^B)^T \phi_i^B]} \quad (3.13)$$

where  $\phi_i^A$  corresponds to the mode shape vector obtained with the continuous model and  $\phi_i^B$  is the mode shape vector obtained from the detailed numerical model for the same natural frequency. As long as a high MAC value is found (i.e., larger than 80%), we consider that the continuous model mode shape agrees well to the numerical mode shape. Even though the second fundamental frequency differs from the DFEM-1 model in 15%, the MAC correlation values are above 98% in both directions.

Mode	EB-1	EB-2	HBFEM-1	$\epsilon^{f_{HBFEM-1}}$	Ratio	DFEM-1	Ratio
1	1.63	1.59	1.60	3.23%	1	1.55	1
2	9.24	9.32	9.29	15.12%	5.77	8.07	5.21

TABLE 3.12: Comparison of the first two modal frequencies in Hz for the **longitudinal** direction with the quasi-periodic section numerical model (Figure 3.10).

Mode	EB-1	EB-2	HBFEM-1	$\epsilon^{f_{HBFEM-1}}$	Ratio	DFEM-1	Ratio
1	1.60	1.59	1.56	1.29%	1	1.54	1
2	8.87	8.99	8.82	13.65%	5.65	7.76	5.04

TABLE 3.13: Comparison of the first two modal frequencies in Hz for the **transverse** direction with the quasi-periodic section numerical model (Figure 3.10).

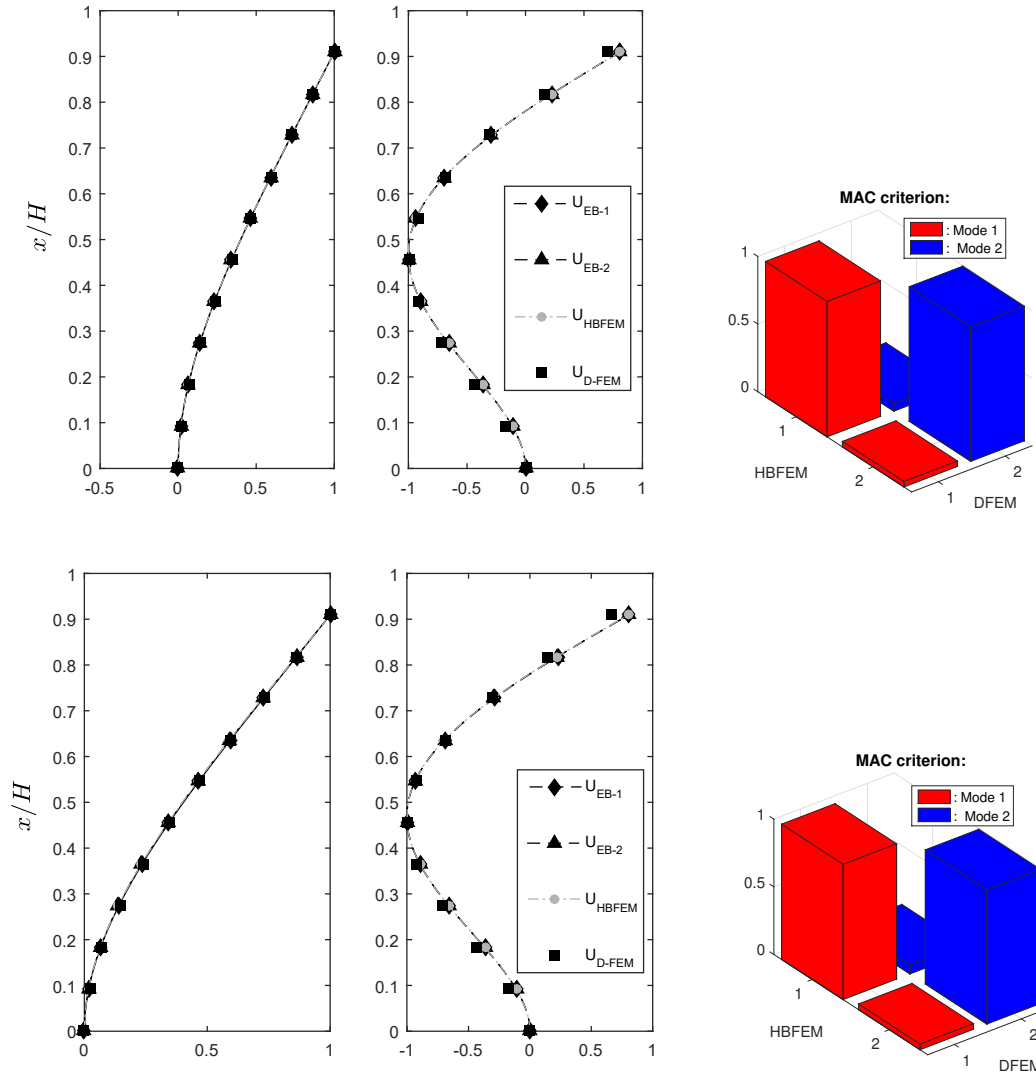


FIGURE 3.16: On the left, comparison between the mode shapes obtained using the EB-1 (diamonds), EB-2 (triangles), HBFEM-1 model with the two unit cell properties (gray circles) and the detailed numerical model DFEM-1 of Figure 3.10 (squares) for the longitudinal (top) and transverse (bottom) directions. The mode shapes are normalized with respect to the maximum displacement. On the right, correlation (MAC values) for the first vibration mode (red) and the second vibration mode (blue).

**Comments on the results for scheme 1** Notice that the EBM results, for EB-1 and EB-2, are quite similar despite the difference in the column cross-sections for both typical stories. This similarity is not surprising, because the identified behavior from both typical stories corresponds to the inner bending and shear beam model. The values of  $\mathcal{K}_i$  are controlled by the shear walls whose geometry and material properties remain the same in the two typical stories. The study of the upper part of the GCH tower block (above the transfer slab) validates the proposed strategy for analyzing a structure with different typical stories through the substructure assembly procedure and widens the application domain of the HBFEM model. Moreover, the modal frequencies obtained with the HBFEM model are near the results of the EB-1 and EB-2. For the first modes, the EB-2, which is the softer model, gives the lower frequencies but, surprisingly, this is not the case for the higher modes.

The comparison with the detailed numerical model DFEM-1 shows that the HBFEM-1 model retrieves the first vibration modes in the longitudinal and transverse directions as well as for the eigenfrequencies (less than 5 % of difference) as for the mode shapes. However, the differences for the second vibration modes are much larger (around 15 %). Two main reasons can explain these discrepancies. Firstly, the accuracy of the EBMs and the HBFEM model directly depends on the value of the scale ratio  $\varepsilon$ . The larger  $\varepsilon$  is, the less accurate the EBMs and the HBFEM are. The macroscopic length  $L$ , which is related to the vibration wavelength, becomes smaller as the number of the analyzed mode increases and, as a consequence, the scale ratio  $\varepsilon$  increases. If the third vibration mode is estimated, it is normal to obtain even higher differences between the full detailed numerical model and the HBFEM model. Secondly, other mechanisms such as the shear acting on very thick vertical elements may emerge at the leading order, which could be the case for the walls of the staircases and elevator shafts of the GCH building. Let us focus on this last reason to investigate how we can improve the results.

It is required to recall that one of the EBM hypotheses is that the structural elements behave as Euler-Bernoulli beams, so the internal shear stiffness (i.e.,  $GA_s$ ) of the elements is supposed much larger than their bending stiffness. This hypothesis is not relevant while modeling very thick elements because their shear deformation can become significant during bending at the story and structure scales, especially for the higher modes which have a shorter wavelength. For the local scale, the effect of the shear in the elements experiencing bending are automatically taken into account by the method used for the calculation of the EBM shear stiffness  $K_s$  from a finite element model of one story. For the global scale, [Chesnais, 2010] proposes a modification of the EBM that accounts for the shear stiffness of the vertical elements. A description of the upgraded EBM was already presented in Chapter 1.

The GCH building is a frame building with four pillars of shear walls. The largest shear wall thickness<sup>1</sup> in the longitudinal direction is 4.50 m. For the first vibration mode, the thickness order is  $a_m/l_m = O(\varepsilon_1^{-0.18})$  for  $N = 11$ . In the transverse direction, the largest thickness is 5.40 m which corresponds to an order of magnitude of  $a_m/l_m = O(\varepsilon_1^{-0.27})$ . According to the listed conditions in Section 1.4.5, the shear of the walls must be considered at the story

<sup>1</sup>Thickness refers to the element length in the direction of the analysis.

scale in both directions, but it does not emerge at the structure scale. In other words, the EBMs are still valid at the structure scale but, at the story scale, the shear of the walls must be included in the calculation of  $K_s$ . In the detailed numerical model, the pillars, columns and beams are modeled as Timoshenko beam elements. Hence, the computation of  $K_s$ , with the imposed boundary conditions in the story model (see Figure 3.12 on page 98), takes into account the shear of the walls and columns at the story scale. It seems that we modeled it correctly, and the condition at the story scale is fulfilled. For the second vibration mode,  $\varepsilon$  is bigger and the orders of magnitude become:

- in the longitudinal direction:  $a_m/l_m = O(\varepsilon_2^{-0.40})$ ,  $C = O(\varepsilon_2^{-9.10})$  and  $\gamma = O(\varepsilon_2^{5.22})$
- in the transverse direction:  $a_m/l_m = O(\varepsilon_2^{-0.62})$ ,  $C = O(\varepsilon_2^{-5.84})$  and  $\gamma = O(\varepsilon_2^{2.24})$

These values are obtained from the parameters of the typical story 1 but both typical stories have the same behavior. For both directions, the influence of the shear of the walls increases and the representative point on the domain graph moves in the inner bending zone. We now assume that we need to take into account the shear of the walls at the structure scale. For that, we have two options: 1) we utilize the upgraded EBM by [Chesnais, 2010] or 2) as the shear of the cells can be neglected for the higher modes, we utilize what Chesnais names the inner Timoshenko model. [Chesnais, 2010] demonstrates that the upgraded EBM is a generalized continuous model that improves the results for shear wall structures. The implementation of this model is out of the scope of this work, and we limit the analysis to the specific description of the inner Timoshenko model (Equation(1.15)) in order to understand the mechanical functioning of the structure and to complement the analysis performed with the HBFEM model.

The macroscopic parameters of the inner Timoshenko model are the linear mass, the inner bending stiffness  $\mathcal{K}_i$  and the shear of the walls stiffness  $\mathcal{K}_m$ . The values to be used for the GCH tower block are summarized in Table 3.14. As  $\mathcal{K}_i$  and  $\mathcal{K}_m$  depend mainly on the properties of the four pillars, they have the same values for both typical stories. The ratios  $C^m = \mathcal{K}_i / (\mathcal{K}_m L^2)$ , which measure the contrast between the stiffnesses of the inner bending and the shear of the walls, are also calculated for the first two vibration modes. For example, for  $k = 1$  in the longitudinal direction, the order of  $C^m = O(\varepsilon_1^{3.19}) < O(\varepsilon_1)$  confirms that the shear of the walls is negligible at the structure scale. The difference between the orders of  $C^m$  in each direction also reveals that the participation of the shear of the walls at the structure scale is much more important in the transverse direction.

Direction	$\mathcal{K}_i$	$\mathcal{K}_m$	L		$C^m$	
			k=1	k=2	k=1	k=2
Longitudinal	1662201.61	1658006.11	22.41	7.47	$0.002=O(\varepsilon_1^{3.19})$	$0.018=O(\varepsilon_2^{4.74})$
Transverse	1514147.01	164724.74	22.41	7.47	$0.018=O(\varepsilon_1^{2.06})$	$0.165=O(\varepsilon_2^{2.13})$

TABLE 3.14: Macroscopic parameters for the inner Timoshenko model with  $N = 11$  stories.

The results obtained with the HBFEM-1 model for the first vibration mode and with the inner Timoshenko model (subscript ITIMO) with the macroscopic parameters given in Table 3.14 for the second mode is presented in Tables 3.15 and 3.16. Notice that the errors are highly reduced and now lower than 1% in both longitudinal and transverse directions for the second vibration mode.

#### Computation of the 2nd mode with the ITIMO model ( $K_m$ )

Mode	HBFEM-1 & ITIMO	Ratio	DFEM-1	Ratio	$\varepsilon^{fx}$
1	1.60	1	1.55	1	3.87%
2	<b>8.01</b>	<b>5.04</b>	8.07	5.21	<b>-0.74%</b>

TABLE 3.15: Comparison of the first two modal frequencies in Hz for the **longitudinal** direction obtained with the HBFEM-1 model (mode 1), the inner Timoshenko model (mode 2) and with the quasi-periodic section numerical model (Figure 3.10).

Mode	HBFEM-1 & ITIMO	Ratio	DFEM-1	Ratio	$\varepsilon^{fx}$
1	1.56	1	1.54	1	1.29%
2	<b>7.71</b>	<b>4.94</b>	7.76	5.04	<b>-0.64%</b>

TABLE 3.16: Comparison of the first two modal frequencies in Hz for the **transverse** direction obtained with the HBFEM-1 model (mode 1), the inner Timoshenko model (mode 2) and with the quasi-periodic section numerical model (Figure 3.10).

**Alternative for scheme 1** We have seen that, in order to obtain the dynamic properties (i.e., eigenfrequencies and mode shapes) of the GCH tower quasi-periodic section, two different models were used for the first and second vibration modes in each direction : the HBFEM model and the inner Timoshenko model, respectively. However, since the HBFEM model is a generalization of the Timoshenko beam model, we can still use it for both vibration modes if the appropriate macroscopic parameters are included. Let us represent the structural behavior in terms of the macroscopic constants  $C$  and  $\gamma$ . For the first vibration mode, the *inner bending and the shear of the cell* govern the dynamic behavior with  $C > O(\varepsilon^{-1})$  and



$\gamma < O(\varepsilon)$  (in agreement with the values in Tables 3.10 and 3.11). The shear of the walls  $K_m$  does not participate at the structure scale. Therefore, the values for the macroscopic parameters  $K_s$ ,  $\mathcal{K}_i$  and  $\mathcal{K}_g$  are the same as in Table 3.9. For the second mode, the shear of the walls emerges at the structure scale, but the shear of the cell becomes negligible compared to the inner bending. The HBFEM model needs to degenerate into the inner Timoshenko model with  $C^m > O(\varepsilon)$  and  $\gamma < O(\varepsilon)$ . To do so, new values of the macroscopic parameters  $K_s'$ ,  $\mathcal{K}_i'$  and  $\mathcal{K}_g'$  are introduced :  $K_s' = K_m$  of Table 3.14 and  $\mathcal{K}_g' = \mathcal{K}_i$  of Table 3.9. The new value  $\mathcal{K}_i'$  must respect  $\gamma < O(\varepsilon)$ , so  $\mathcal{K}_i' = \gamma \mathcal{K}_g' = \gamma \mathcal{K}_i$ . The modified HBFEM model using this change in the macroscopic parameters encounters the numerical solution with errors less than 1% for the second vibration mode in both directions. Tables 3.17 and 3.18 summarize these final results. The frequency values, 1.87 Hz and 1.85 Hz in each direction (L and T), for the first vibration mode using the modified HBFEM model are not presented in these tables. We recall that the modified HBFEM model does not represent the *inner bending and shear of the cell* mechanisms associated with the first vibration mode but the *inner bending and shear of the walls* mechanisms which appear from the second vibration mode.

#### Computation of the 2nd mode with the modified HBFEM model ( $K_m$ )

Mode	modified HBFEM-1	Ratio	DFEM-1	Ratio	$\epsilon^{f_{\text{HBFEM-1}}}$
1	1.59	1	1.55	1	3.87%
2	<b>8.09</b>	<b>5.09</b>	8.07	5.21	<b>0.25%</b>

TABLE 3.17: Comparison of the first two modal frequencies in Hz for the **longitudinal** direction obtained with the HBFEM-1 model (mode 1), the modified HBFEM model (mode 2) and with the quasi-periodic section numerical model (Figure 3.10).

Mode	modified HBFEM-1	Ratio	DFEM-1	Ratio	$\epsilon^{f_{\text{HBFEM-1}}}$
1	1.56	1	1.54	1	1.29%
2	<b>7.78</b>	<b>4.99</b>	7.76	5.04	<b>0.26%</b>

TABLE 3.18: Comparison of the first two modal frequencies in Hz for the **transverse** direction obtained with the HBFEM-1 model (mode 1), the modified HBFEM model (mode 2) and with the quasi-periodic section numerical model (Figure 3.10).

As stated earlier, the construction of a continuous model for the dynamic analysis of buildings where the shear of the walls does not emerge at the structure scale does not require to change the macroscopic parameter values in the HBFEM model, neither to use the upgraded EBM by [Chesnais, 2010]. Nevertheless, the selection of the continuous model must be the result of an in-depth analysis of the building mechanical functioning based on the identification criteria. It is always recommended to identify the structural governing mechanism(s) for the desired

vibration mode to choose a continuous model representing its global behavior correctly. On the one hand, we have seen that the use of specific models can lead to slightly better results than the generalized ones with less calculations. On the other hand, a more generalized model as the EBM or its upgraded version could for the analysis of every vibration mode. The validation of the EBM and the HBFEM model here presented fulfills the required steps towards the improvement of the HBFEM model based on the upgraded EBM.

### Scheme 2: Analysis of the entire GCH building (non-periodic + quasi-periodic sections)

In the first scheme, the modal response of the quasi-periodic section is well reproduced, and the mechanical functioning of the GCH structure is understood through the elastostatic analysis of a single story. The implemented strategy is satisfactory, and the overall results agree well with those of the detailed numerical model. Moreover, the structure quasi-periodic section analysis allowed verifying that the EBM and the HBFEM model limits are not related to the slight absence of periodicity because of the two different typical stories but to the role of the shear walls on the structure behavior. Hence, it is still an open question to know the limits of the HBFEM model concerning the non-respect of periodicity. Thus, hereafter, the entire GCH tower block is analyzed. A new HBFEM model is built with the macroscopic properties of all the existing stories (HBFEM-2) and compared with the complete detailed model presented in Figure 3.9 (DFEM-2).

### Properties of the HBFEM-2 model

**Macroscopic parameters** The static analysis of the ground story and the basement provides the macroscopic parameters given in Table 3.19. In addition to these properties, the macroscopic parameters of the typical stories 1 and 2 (Table 3.9) are needed to build the HBFEM-2 model.

Macroscopic parameters	Ground story		Basement	
	L	T	L	T
$\Lambda$ , linear mass (ton/m)	263.37		197.64	
$K_s$ , shear stiffness (MN)	3482.47	34001.66	1391.36	1731.45
$\mathcal{K}_i$ , inner bending stiffness (MN m <sup>2</sup> )	$5.26 \times 10^6$	$4.71 \times 10^6$	$5.26 \times 10^6$	$4.71 \times 10^6$
$\mathcal{K}_g$ , global bending stiffness (MN m <sup>2</sup> )	$2.62 \times 10^8$	$1.68 \times 10^7$	$2.94 \times 10^8$	$2.02 \times 10^7$

TABLE 3.19: Ground and basement story macroscopic parameters in the longitudinal (L) and transverse directions (T).

Note that while the inner bending and global bending stiffnesses keep the same order of magnitude for both ground and basement stories, the shear stiffness  $K_s$  differs significantly in both directions. The difference comes from the large bending stiffness of the transfer slab

at the ground story, which controls the story shear deformation. Assuming that the whole structure is made by the repetition of the ground story, the macroscopic constants  $C$  and  $\gamma$  for the ground story are 68.34 and 0.02 in the longitudinal direction, and 0.45 and 0.28 in the transverse direction, respectively. Based on these values, the behavior of the structure in the longitudinal direction combines the inner bending and shear mechanisms, which agrees with the identified behavior of the typical stories, whereas, in the transverse direction, the behavior is governed by all the three mechanisms  $K_s$ ,  $\mathcal{K}_i$ , and  $\mathcal{K}_g$ .

**Natural frequencies and mode shapes** The solution of the eigenvalue problem provides the first natural frequencies in each direction as presented in Tables 3.20 and 3.21. Interestingly, the results are much better than expected. The errors with respect to the detailed numerical model DFEM-2 keep the same order of magnitude as the errors obtained for the GCH quasi-periodic section (see Tables 3.12-3.13). As analyzed earlier, the high errors of the second mode are associated with the inner shear mechanism of the shear walls that emerges at the structure scale which is not included in the HBFEM-2 model. This errors are smaller in th HBFEM-2 than in the HBFEM-1 because the addition of the ground and basement stories increases the slenderness of the building that descreases the influence of the inner shear mechanism of the walls. The initial question to find the limits of the model concerning periodicity is still open. Even when both sections, quasi-periodic and non-periodic, are introduced in the HBFEM model, the overall results are satisfactory with differences no higher than 6% for the first vibration mode and slightly higher than 10% for the second vibration mode. Figure 3.17 displays the first two mode shapes in the longitudinal and transverse directions. Although a difference between the natural frequencies is observed, the mode shapes of the HBFEM-2 and DFEM-2 are in pretty good agreement as shown by the MAC correlation (larger than 98%) for both directions.

Mode	HBFEM-2	Ratio	DFEM-2	Ratio	$\epsilon^{f_{HBFEM-2}}$
1	1.16	1	1.10	1	5.45 %
2	5.31	4.58	4.71	4.23	12.74%

TABLE 3.20: Comparison of the first two modal frequencies in Hz for the **longitudinal** direction with the detailed numerical model (Figure 3.9).

Mode	HBFEM-2	Ratio	DFEM-2	Ratio	$\epsilon^{f_{HBFEM-2}}$
1	1.22	1	1.19	1	2.52%
2	5.47	4.48	5.00	4.21	9.40%

TABLE 3.21: Comparison of the first two modal frequencies in Hz for the **transverse** direction with the detailed numerical model (Figure 3.9).

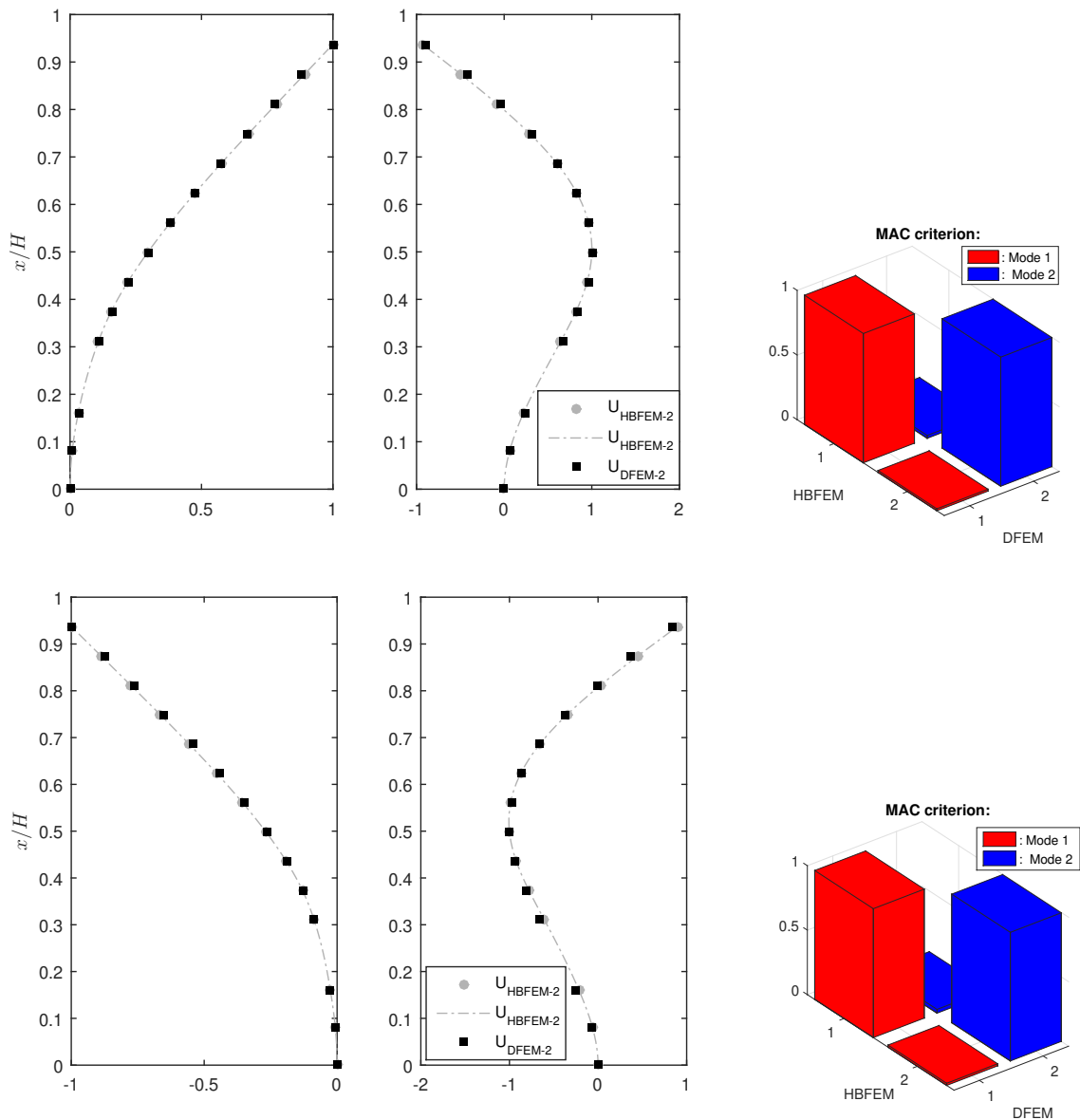


FIGURE 3.17: On the left, comparison of the first two mode shapes obtained with the HBFEM-2 model with the four unit cell properties (gray circles) and the detailed numerical model DFEM-2 of Figure 3.9 (squares) for the longitudinal (top) and transverse (bottom) directions. The mode shapes are normalized with respect to the maximum displacement. On the right, correlation (MAC value) for the first vibration mode (red) and the second vibration mode (blue).

### 3.2.3 Discussion about the results and the implemented methodology

The multiscale procedure for constructing the continuous models presented in this section allows understanding the GCH tower block's mechanical functioning. The contribution of each mechanism (i.e., shear of the cell, inner bending and global bending) is taken into account in each of the used continuous models and identified from the static analysis of a single story of the quasi-periodic section. The identification criterion evidences that the inner bending and shear mechanisms control the GCH behavior. This result agrees with the mode shapes

and the frequency ratios (1 ; 4.29 for the longitudinal direction and 1 ; 4.22 for the transverse direction) obtained from the full detailed numerical model. The numerical model clearly shows the bending deformation of the floors associated with the shear of the cell and the bending of the vertical elements at the structure scale.

We evaluated the performance of the continuous models (i.e., the EB-1, EB-2 (or EBMs) and the HBFEM model) to analyze non fully periodic structures. However, when only the quasi-periodic part is evaluated, the EBMs and HBFEM results get closer to the numerical ones (less than 4 % difference in the longitudinal direction for the 11-story model of scheme 1). The slight variation in the frequencies and mode shapes between the EBMs and the HBFEM model shows that the cross-section reduction of the columns at the mid-height of the structure does not influence the structure behavior. This could be explained because the global bending of the pillars and the bending of the floors associated with the shear of the cell control the dynamics of the structure. The first vibration mode shapes are well recovered for the two studied schemes. The HBFEM model retrieves the EBM results with additional versatility for advanced numerical implementations. The HBFEM model can take into account the various typical stories of a building which can be a significant advantage for analyzing high-rise buildings. The HBFEM model highly reduces the computational cost compared to the detailed numerical model. Although one part of the continuous model's construction requires the static analysis of a single story numerical model, it still represents a significant saving of computational resources. The single-story model of the GCH comprises 897 nodes (5382 DoFs) instead of the 9864 nodes (59184 DoFs) of the full numerical model with 11 stories.

### 3.3 Conclusion and perspectives

#### 3.3.1 Main results

The objective of this chapter is to validate the Homogenized beam finite element (HBFEM) model for the transverse dynamic analysis of real structures in the elastic range.

We start by performing a transient analysis using the HBFEM model. We present the numerical time-stepping procedure used and we perform the dynamic analysis of a realistic steel frame structure using real recorded ground motions. The seismic responses computed with the HBFEM and the detailed FEM models coincide very well.

The second part of this chapter introduces the methodology for the analysis of structures with vertical irregularity. The Grenoble City Hall (GCH) building is used as a case study. The full detailed numerical model calibrated with in-situ measurements by [Desprez, 2010] is used as a reference. This model is also slightly modified to include only the quasi-periodic section of the GCH tower block. The analysis of the 1-D model based on the HBFEM formulation aims at verifying, in the harmonic regime, the vibration frequencies and mode shapes of the structure. The construction of the HBFEM model for the GCH building, adopting the analytical EBM principles, requires the computation of the macroscopic parameters: the linear mass  $\Lambda$ , the shear stiffness of the cell  $K_s$ , the global bending stiffness  $\mathcal{K}_g$ , and the

inner bending stiffness  $\mathcal{K}_i$ . We then perform the static analysis of each typical story. The computation of the shear stiffness of the cell  $K_s$  is very delicate and requires the construction of a numerical model of a single story of the periodic structure.

This numerical model is built using two different pieces of software, ETABS and Cast3M, to validate the numerical results for  $K_s$ . The modeling method in each code requires different strategies to impose on the story model the boundary conditions identified by the homogenization method. As ETABS does not allow to set periodic boundary conditions, we model the story with the floor at the mid-height with half of the vertical elements beneath the floor and the other half over the floor. In Cast3M, the story can be modelled with the slab at the top level. Although we use different unit cell models in each code, the obtained values for  $K_s$  in ETABS and Cast3M are very close and allow us to validate the proposed procedures. The  $K_s$  obtained with Cast3M is taken to perform further computations.

Once all the macroscopic parameters are determined, the mechanisms that govern the dynamic behavior are obtained based on the identification criterion proposed by [Hans and Boutin, 2008]. The leading mechanisms for the GCH structure correspond to a combination of the inner bending and the shear of the cell in both longitudinal and transverse directions. The eigenfrequencies and mode shapes are estimated with the HBFEM model and compared with the results of the full detailed numerical model. A good agreement between both models is obtained up to the second flexural mode in each direction even when the non-periodic part of the structure is included in the analysis.

The performed mesh refinement test over the GCH single story numerical model shows that the deformation of the floors highly influences the shear stiffness values. Thus, to allow comparisons, the same mesh density was used in both the story model and the complete model of the structure.

Although, the EBMs are built for single frame structures where the elements behave as Euler-Bernoulli beams and their thickness is neglected, the numerical models presented consider the real geometry. Thus, the shear contribution of the walls is taken into account in both the complete numerical models and in the calculation of  $K_s$  with the single story models.

### 3.3.2 Limitations and future works

#### Soil-structure interaction

The full numerical model of the GCH building assumes totally fixed boundary conditions at the base of the structure. The good correlation encountered between the frequencies and mode shapes of the numerical model and of the in-situ measurements supports this assumption for the GCH building. However, buildings founded on soft soils may exhibit other mechanisms such as rocking which are totally neglected with the fixed end condition assumptions. In such a case, it could be necessary to take into account the soil properties in the HBFEM model and replace the fixed condition by a FEM-based description of the soil.

**Maximum stiffness contrast between two periodic substructures**

Considering high ratios between the stiffnesses of two consecutive periodic substructures may lead to a loss of accuracy of the HBFEM model. The order of this ratio could be identified to estimate the validity domain of the HBFEM model.

**Encountered types of behavior in regular concrete structures**

The existence of various structural elements such as walls and columns in current RC structures changes the stiffness distribution along the story of the structure generating high contrasts between vertical and horizontal elements. Thus, the combination of new mechanisms such as the inner bending may control the structural behavior. In such a case, the structure response cannot be described by the Timoshenko beam model.

## Chapter 4

# Towards a new damage indicator using the Equivalent Beam Model and multifiber beam elements

In the previous chapters, our analyses are focused on the description of the structural behavior at the global scale considering a 1-D model: dynamic properties such as eigenfrequencies and eigenmodes have been determined as well as story displacements and rotations through time history analyses in the elastic framework. These are the first steps of earthquake engineering to estimate damage on buildings subjected to seismic excitation. Besides, the assessment of the effects of the forces acting on the structural elements is crucial. Hence, in this chapter, our interest lies in describing the response at the element (or intermediate) and material (or local) scales. Our first objective is to relate the structural dynamic behavior to the mechanical functioning in order to compute the strains (nodal rotation, deformation) and the internal forces (shear forces, bending moments) of each element.

Thus, in the first part of this chapter, we start by describing the process to go from the structure description, given by the driving kinematic variables - the displacement  $u$  and the story rotation  $\alpha$ -, to the element description, finding the hidden kinematic variables - mainly the nodal rotations - needed for the element dynamics. To do that, we introduce the second part of the *hybrid analysis*, the first part of which was presented in Chapter 1. We keep focusing on the elasto-static analysis of a single story and the identification criterion of the structural dynamic behavior. Once the element boundary conditions are known, the estimation of the internal forces is performed by solving the classical equilibrium equations of the Euler Bernoulli beam. The study cases are single-frame and multiple-frame structures. Finally, the analytical results are compared with the results obtained from analyzing a fully detailed numerical model of the whole structure. The second part presents the strategy to capture the non-linear effects. The numerical model used for a single story is upgraded by introducing non-linear constitutive laws to the structural materials. The finite element method based on multifiber beam elements is used to capture the non-linear behavior of the structural elements. The evolution of the story macro deformation due to each of the main structural mechanisms (shear, inner bending, and global bending) is estimated and integrated into the



analysis of the Equivalent Beam Model (EBM) for single frame structures. Herein, a non-linear transient analysis is performed to validate the implemented procedure by comparing the results with fully numerical simulations. So, the coupling between the HBFEM and the multifiber beam elements (MFEM) integrated into the story analysis is used to describe the structural behavior at both global and local scales and to identify the governing mechanism(s).

The last part of this work focuses on how the proposed modeling approach could be used to develop a wide range of damage indicators. Several studies have been performed to define damage indices for building structures, and there are various methods for computing those indices. However, most of the indices depend on the material (masonry, reinforced concrete...) and geometric features ("low-rise", "high-rise", "slender") of the structure. For some cases, these indices fail to take into account the variation of the behavior from one structure to the other even in the same "category" and the influence of the type of deformation (e.g., shear, bending, the combination of both...) on the failure mechanism. So the applicability of these indices is reduced to the specific typologies that serve on their construction. This limitation has not been straightforwardly solved yet, and therefore, it is currently the subject of discussion in the last part of this research. The analysis that we perform at the end of this chapter provides some insights on the formulation of a robust damage indicator based on the usual global indicators such as ductility, top roof displacement, inter-story drift. It could even be adapted to cyclic loading-based or energy-based indicators. With this approach, the damage is directly related to the structural behavior and not only to the general material or geometry presented by current seismic design codes. In this context, the last part of this chapter is dedicated to proposing a new form for a damage indicator based on the identification criterion presented in Chapter 1. An exhaustive parametric study identifies that the relevancy of the widely used global indices such as the top roof displacement and inter-story drift can be directly associated with the governing mechanism(s).

## 4.1 Continuation of the hybrid analysis: story and element scales

Once, the global response of the structure is determined in terms of the macro kinematic variables  $u$  and  $\alpha$ , it is possible to apply the macroscopic deformation on a story model in order to compute the internal forces of the structural elements.

The studies presented in Chapter 1 conclude that the homogenized models and the identification criterion can be generalized to a large number of periodic structures (multiframe structures or buildings). Nevertheless, the implementation of the HPDM method on more complex structures quickly becomes a tedious task. We therefore propose here the extension of the procedure which substitutes a part of the analytical expressions describing the internal kinematics of the unit cell for an entirely numerical analysis which makes it possible to: 1) construct the equivalent beam model describing the global behavior, called here analysis at the global (or building or structure) scale (denoted  $\mathbf{G}$ ), and 2) return to the intermediate (or story scale) in order to calculate the deformations and the forces of the structural elements

(denoted **I**). This procedure will henceforth be called *Hybrid intermediate analysis*. To reconstruct the parameters that depend on the geometry of the structure, this procedure is based on a finite element model of the typical story on which static calculations are performed. This type of modeling is valid for every structure which respects the homogenization assumptions: the conditions of periodicity, separation of scales and "overall deformation". In this section, the procedure for implementing the different static analyzes of the story is detailed using the diagram in Figure 4.1. The analysis at the global scale was presented in Chapter 1. The objective is to determine the response of each element in terms of internal efforts (axial force **N**, shear force **T** and bending moment **M**) as a function of the deformation at the structure scale (or global scale).

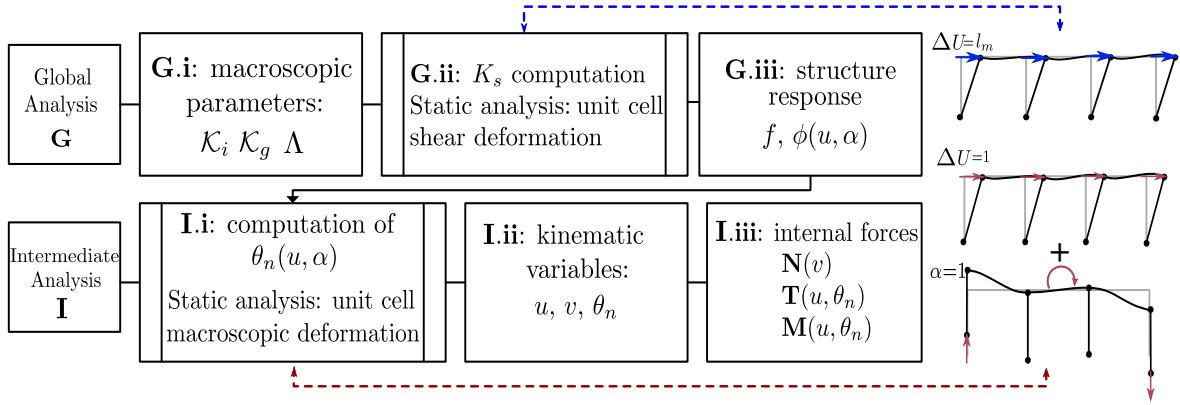


FIGURE 4.1: Stages of the proposed hybrid analysis

#### 4.1.1 Computation of the nodal rotation

The estimation of the internal forces and deformations are led by the structural deformation obtained from the global scale analysis. That means that the global kinematic variables  $u$  and  $\alpha$  are known at this point and the hidden kinematic variables need to be estimated to find the element description. For example, the internal kinematics within the unit cell of single frame structures is driven by the nodal rotation  $\theta$  which can be calculated from the transverse displacement  $u$  and the macroscopic rotation  $\alpha$  using the internal equilibrium equation given by the HPDM (Equation (4.1)). This equation depends on the static bending stiffnesses  $k_p$  and  $k_m$  of the horizontal and vertical elements defined in Chapter 1 on page 14.

$$k_p(\alpha - \theta) + k_m(u' - \theta) = 0 \quad \Rightarrow \quad \theta = K_s \left( \frac{\alpha}{k_m} + \frac{u'}{k_p} \right) \quad (4.1)$$

(primes stands for the differentiation with respect to  $x$ )

#### 4.1.2 Hybrid analysis : Part II

For single frame structures, the nodal rotation  $\theta$  can be determined from Equation (4.1). However, the number of hidden kinematic variables increases for multiple frame structures

with complex analytical expressions. For these structures, we propose to perform a static analysis of the story FE model subjected to the macroscopic deformation (I.i) (Figure 4.1) to compute the cell element deformation. The macroscopic deformation superposes effects from two different origins: the variation of the transverse displacement  $u$  between the bottom and the top of the story and the story rotation  $\alpha$ . Therefore two loading conditions are applied to the story model. The first condition imposes a unit differential transverse displacement  $\Delta U=1$  between the bottom and top of the story. Vertical displacements are blocked, and the nodal rotation is periodic at both ends, as presented in Chapter 1 for condition B (page 1.10). The second condition imposes a unit macroscopic rotation  $\alpha=1$ , which corresponds to the vertical displacement difference  $\Delta V$  between walls on the opposite sides. Here, the ends of the other vertical elements are left free for the vertical displacements and the periodicity of the nodal rotation between the bottom and the top of each vertical element is again ensured (See Figure 4.2).

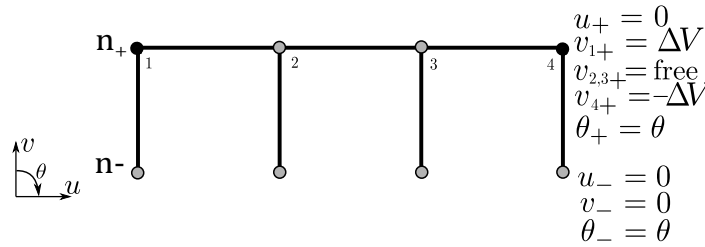


FIGURE 4.2: Boundary conditions associated with global bending deformation of the story model

The rotations at each node  $\theta_n$  are recovered for both conditions. They are later multiplied by the values of  $l_m u'$  and  $\alpha$  given by the analysis at the global scale and summed up (I. ii). The local kinematics and the boundary conditions of the elements being identified, the efforts (i.e. axial force, shear force and bending moment) in the elements are directly estimated from the constitutive and balance equations of the classical Euler-Bernoulli beam formulation in the longitudinal and transverse directions (I. iii).

Herein, the nodal displacement  $u$  is assumed to be equal to the average displacement  $U$  at the level  $n$  as we consider that the relative displacement between the different nodes at the same level is very small.

### 4.1.3 Computation of the internal forces

Let's now focus on the computation of the shear forces and bending moments of the elements. Figure 4.3 represents the notation for the deformation of an element  $b$  in the structure. The variables  $u_{O(b)}$ ,  $u_{E(b)}$  denote the transverse displacements,  $v_{O(b)}$ ,  $v_{E(b)}$  the longitudinal displacements and  $\theta_{O(b)}$ ,  $\theta_{E(b)}$  the rotations. The variables  $\mathbf{N}$ ,  $\mathbf{T}$  and  $\mathbf{M}$  represent the axial force, shear force and bending moment, respectively. The subscript  $O$  and  $E$  state for Origin and End, respectively.

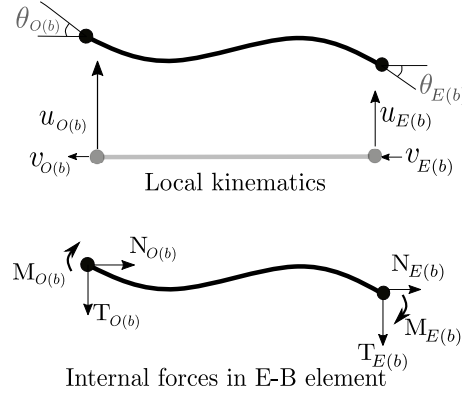


FIGURE 4.3: Notation at the element scale: nodal description of the kinematics and the internal forces: axial force  $\mathbf{N}$ , shear force  $\mathbf{T}$  and bending moment  $\mathbf{M}$ .

The forces at the endpoints of an element are deduced from the Euler-Bernoulli beam constitutive laws and local balance equations at the location  $s$  for the longitudinal and transverse vibrations:

*Element constitutive laws and balance equations:*

$$\text{Longitudinal} \quad \mathbf{N}(s) = EA \frac{dv(s)}{ds} \quad \mathbf{N}'(s) = -\rho A \omega^2 v(s) \quad (4.2)$$

$$\text{Transverse} \quad \mathbf{T}'(s) = -\rho A \omega^2 u(s) \quad \mathbf{M}(s) = EI_b \frac{d^2 u(s)}{ds^2} \quad \mathbf{M}'(s) = -\mathbf{T}(s) \quad (4.3)$$

where  $E$  is the material elastic modulus,  $\rho$  is the material mass density,  $A$  is the element cross-section area,  $I_b$  the element second moment of area and  $\omega$  is the vibration angular frequency. The nodal forces and bending moments for the element  $b$  are obtained through the integration of the constitutive and balance equations (4.2) and (4.3) using the nodal kinematic variables  $u_i$ ,  $v_i$  and  $\theta_i$  at the endpoints ( $i = O(b), E(b)$ ) as boundary conditions.

*Nodal forces and bending moment at  $O(b)$ :*

$$\text{for vibrations} \left\{ \begin{array}{l} \mathbf{N}(v_O, v_E) = \frac{EA}{l_L} \frac{v_E - v_O \cos(l/l_L)}{\sin(l/l_L)} \\ \mathbf{T}(u_O, u_E, \theta_O, \theta_E) = \frac{EI_b}{l_T^3} \frac{u_O (\cosh(l/l_T) \sin(l/l_T) + \sinh(l/l_T) \cos(l/l_T))}{\cos(l/l_T) \cosh(l/l_T) - 1} \\ \quad - \frac{EI_b}{l_T^3} \frac{u_E (\sin(l/l_T) + \sinh(l/l_T))}{\cos(l/l_T) \cosh(l/l_T) - 1} \\ \quad + \frac{EI_b}{l_T^2} \frac{\theta_O \sin(l/l_T) \sinh(l/l_T) - \theta_E (\cos(l/l_T) - \cosh(l/l_T))}{\cos(l/l_T) \cosh(l/l_T) - 1} \\ \mathbf{M}(u_O, u_E, \theta_O, \theta_E) = \frac{-EI_b}{l_T^2} \frac{u_O \sin(l/l_T) \sinh(l/l_T) + u_E (\cos(l/l_T) - \cosh(l/l_T))}{1 - \cos(l/l_T) \cosh(l/l_T)} \\ \quad - \frac{EI_b}{l_T} \frac{\theta_O (\cosh(l/l_T) \sin(l/l_T) - \sinh(l/l_T) \cos(l/l_T))}{1 - \cos(l/l_T) \cosh(l/l_T)} \\ \quad + \frac{EI_b}{l_T} \frac{\theta_E (\sin(l/l_T) - \sinh(l/l_T))}{1 - \cos(l/l_T) \cosh(l/l_T)} \end{array} \right. \quad (4.4)$$

where  $l$  is the element length,  $l_L = (E/(\rho\omega^2))^{0.5}$  is the characteristic length associated with the longitudinal vibrations, and  $l_T = (EI_b/(\rho A\omega^2))^{0.25}$  is the characteristic length associated with the transverse vibrations. The compression wavelength and the bending wavelength are given by  $2\pi l_L$  and  $2\pi l_T$  respectively.

Thanks to the separation of scales, the vibration of the overall structure is associated with a quasi-static behavior at the local scale:  $l \ll l_L$  and  $l \ll l_T$  for the considered frequency. Thus, the solution at the element scale can be deduced from a static analysis. So, when  $l/l_T$  tends to zero in Equation 4.4,

the nodal forces and bending moment on the element are:

*Nodal forces and bending moment at  $O(b)$ :*

$$\text{for quasi-static} \begin{cases} \mathbf{N}(v_O, v_E) &= \frac{EA}{l}(v_E - v_O) \\ \mathbf{T}(u_O, u_E, \theta_O, \theta_E) &= \frac{12EI_b}{l^3}(u_O - u_E) + \frac{6EI_b}{l^2}(\theta_O + \theta_E) \\ \mathbf{M}(u_O, u_E, \theta_O, \theta_E) &= \frac{6EI_b}{l^2}(u_E - u_O) - \frac{2EI_b}{l}(2\theta_O + \theta_E) \end{cases} \quad (4.5)$$

#### 4.1.4 Verification of the hybrid procedure

In order to investigate the efficiency of the proposed hybrid procedure for the computation of the internal forces, single and triple frame structures made of interconnected beams are taken as examples to present the results at both the structure and element scales. Thus, this section reports the results obtained from the free transverse vibration analysis using the HBFEM (i.e., the finite element formulation including all three mechanisms: shear, global bending and inner bending).

All the treated structures have  $N = 10$  stories and the material properties are given by an elastic modulus  $E = 30$  GPa, Poisson's ratio  $\nu = 0.2$ , and mass density  $\rho = 2300$  kg/m<sup>3</sup>, representative of concrete. The structure spans and walls lengths are identical  $l_m = l_p = 3000$  mm. As it has been done up to now, the verification consists in comparing the element forces ( $\mathbf{N}$ ,  $\mathbf{T}$  and  $\mathbf{M}$ ) obtained from two different methods: 1) the complete *hybrid analysis*: the HBFEM is used to study the dynamic behavior of the structure at the global scale and the macroscopic properties are obtained thanks to a static numerical model of a single story, and 2) a full numerical analysis with a FEM model of the entire structure. This numerical model is built in Cast3M [CEA, 2017] and consists of a 2D model, where the structural elements are Euler-Bernoulli beams discretized with a fine mesh density. The nodes at the base of the structures are fixed and the nodes at the top end are free. In addition, the verification of the quasi static regime of elements is done by comparing the shear force and bending moments computed with the E-B dynamic and quasi-static equations (Equations (4.4) and (4.5), respectively).

Table 4.1 lists the treated structures. Only the thickness of the elements  $a_m$  and  $a_p$  changes from one case to another. The first seven correspond to structures made of single frames (two walls and one floor per story,  $n_w = 2$ ). The next seven are made of three frames (four

walls and three floors per story,  $n_w = 4$ ) with identical walls that have the same geometrical properties as the single frame structures. For the last five structures, the thicknesses of the external and internal walls differ but the floor thickness is kept constant. Although, the chosen thicknesses for these structures are not realistic, we can generate the different types of governing mechanisms: shear, inner bending, and global bending.

Case	$a_{me}$	$a_{mi}$	$a_p$	$n_w$
0	50	50	50	2
1	74.02	74.02	74.02	2
2	50	50	200	2
3	500	500	500	2
4	500	500	150	2
5	471	471	74	2
6	500	500	20	2
7	50	50	50	4
8	74.02	74.02	74.02	4
9	50	50	200	4
10	500	500	500	4
11	500	500	150	4
12	471	471	74	4
13	500	500	20	4
14	74.02	200	74.02	4
15	50	200	200	4
16	500	200	500	4
17	500	200	150	4
18	471	200	74	4

TABLE 4.1: List of the studied cases with different thicknesses for external and internal walls  $a_{me}$  and  $a_{mi}$ , respectively.  $n_w$  are the number of walls, and  $a_p$  the thickness of the floors.  $a_p$  and  $a_m$  are given in mm

The equivalent beam properties (macroscopic parameters): shear stiffness, inner bending stiffness and global bending stiffness are computed from the static analysis of one story, and reported on Table 4.3. The numerical model of a single story is built in order to find the shear stiffness value and the nodal rotations. This procedure is done for both the single and triple frame structures. Figures 4.4 and 4.5 show the computed shear force and the bending moment at the bottom end of the elements with respect to the structure height for the first two modes of a single frame (Case 0) and a triple frame structure (Case 12), respectively. For this analysis we compute the following variables for comparing the analytical and numerical results:

$u_a$	Transverse displacement from the HBFEM model (Normalized-unitless)
$u_n$	Transverse displacement from the detailed FEM model (Normalized-unitless)
$\alpha_a$	Macroscopic rotation from the HBFEM model
$\alpha_n$	Macroscopic rotation from the detailed FEM model
$\theta_a$	Nodal rotation at the story scale from the HBFEM model and the hybrid procedure
$\theta_n$	Nodal rotation at the story scale from the detailed FEM model
$\mathbf{T}_{a_d}$	Shear force in the walls modelled as Euler-Bernoulli beams for vibrations (Equation 4.4) with the boundary conditions $\theta_a$ and $u_a$
$\mathbf{T}_{a_s}$	Shear force in the walls modelled as Euler-Bernoulli beams for quasi-static states (Equation 4.5) with the boundary conditions $\theta_a$ and $u_a$
$\mathbf{T}_{a+n}$	Shear force in the walls modelled as Euler-Bernoulli beams with the boundary conditions $\theta_n$ and $u_n$
$\mathbf{T}_n$	Shear force from the detailed FEM model
$\mathbf{M}_{a_d}$	Bending moment at the bottom of the walls modelled as Euler-Bernoulli beams for vibrations (Equation 4.4) with the boundary conditions $\theta_a$ and $u_a$
$\mathbf{M}_{a_s}$	Bending moment at the bottom of the walls modelled as Euler-Bernoulli beams for quasi-static states (Equation 4.5) with the boundary conditions $\theta_a$ and $u_a$
$\mathbf{M}_n$	Bending moment at the bottom of the walls from the detailed FEM model

TABLE 4.2: List of the computed kinematic variables mm-rad, shear forces in KN, and bending moment in KN mm

Table 4.4 compares analytical and numerical results for the fundamental frequency, the displacement at the first level ( $x = 3\text{m}$ ), and internal forces of the external vertical elements at the base. The overall observation of this analysis is that for most of the treated cases, the analytical results agree well with the numerical results. The errors on the fundamental frequency do not exceed 10% for most of the cases. Only when there is a high stiffness contrast between the walls and floors large errors are obtained (Cases 6,13, and 16). Deformed shapes are also in good agreement for most cases, although significant differences (more than 20 %) can be observed for the first story displacement value (of Table 4.4). Internal forces values are then affected by the displacement discrepancies on the elements at the base of the structure. This is a classical problem of the homogenized models where the periodicity is not assured. It could be remarked that the accuracy of the analytical results is highly dependent on the type of mechanism that governs the dynamic behavior of the structure (i.e., shear beam, inner bending beam, global bending beam). Thus, excluding very contrasted structures, small error values are encountered for inner bending beam structures, while for structures where the shear mechanism governs, the errors are more significant.

Case	Governing mechanism(s)	$K_s$ MN	$K_i$ MN mm <sup>2</sup>	$K_g$ MN mm <sup>2</sup>	$\Lambda$ ton mm <sup>-1</sup>	C	$\gamma$	x	y
0	Shear	0.28	6.25E+05	6.75E+09	3.45E-10	66.6765	0.0001	-2.27	5.02
1	Shear	0.90	2.03E+06	9.99E+09	5.11E-10	30.4173	0.0002	-1.85	4.59
2	Shear	0.81	6.25E+05	6.75E+09	6.90E-10	22.9101	0.0001	-1.69	5.02
3	Global bending and shear	278.78	6.25E+08	6.75E+10	3.45E-09	0.6638	0.0093	0.22	2.53
4	Inner bending and shear	12.19	6.25E+08	6.75E+10	2.65E-09	15.1778	0.0093	-1.47	2.53
5	Inner bending and shear	1.26	5.22E+08	6.36E+10	2.34E-09	138.8288	0.0082	-2.67	2.59
6	Inner bending and shear	2.57	6.25E+08	6.75E+10	2.35E-09	71.9718	0.0093	-2.31	2.53
7	Shear	0.69	1.25E+06	6.75E+10	8.05E-10	268.528	0.001	-3.02	5.89
8	Shear	2.24	4.06E+06	9.99E+10	1.19E-09	122.4909	0.001	-2.60	5.46
10	Global bending and shear	691.60	1.25E+09	6.75E+11	8.05E-09	2.6758	0.0019	-0.53	3.40
11	Shear	35.15	1.25E+09	6.75E+11	5.64E-09	52.64	0.0019	-2.14	3.40
12	Inner bending and shear	3.79	1.04E+09	6.36E+11	4.84E-09	459.4333	0.0016	-3.31	3.46
13	Inner bending and shear	5.14	1.25E+09	6.75E+11	4.74E-09	360.3763	0.0019	-3.18	3.40
14	Shear	3.42	4.20E+07	1.17E+11	1.77E-09	93.7583	0.0004	-2.45	4.28
16	Shear	259.13	6.65E+08	6.35E+11	6.67E-09	6.7129	0.001	-1.03	3.71
17	Shear	27.68	6.65E+08	6.35E+11	4.26E-09	62.8361	0.001	-2.24	3.71
18	Inner bending and shear	3.81	5.62E+08	5.99E+11	3.60E-09	430.9448	0.0009	-3.28	3.77

TABLE 4.3: Macroscopic properties and identified mechanism(s) of the studied structures. Case 9 and 15 are not reported.



Case	$f_n$ Hz	$f_a$ Hz	r. error %	$u_n$	$u_a$	r. error %	$T_{ad}$ KN	$T_{as}$ KN	$T_{a+n}$ KN	$T_n$ KN	r. error %	$M_{ad}$ KN mm	$M_{as}$ KN mm	$M_n$ KN mm	r. error %
0	0.24	0.25	-2.52	0.10	0.09	7.13	7.27	7.28	7.29	7.29	0.26	11254.88	11257.13	11254.62	-0.02
1	0.36	0.37	-2.52	0.10	0.09	7.21	23.28	23.28	23.35	23.35	0.29	36068.88	36060.16	36064.54	0.01
2	0.27	0.29	-6.44	0.15	0.11	22.71	20.44	20.44	19.37	19.37	-5.54	30692.32	30692.47	29075.53	-5.56
3	1.82	1.88	-3.17	0.05	0.05	5.73	3372.32	3373.08	3364.40	3364.33	-0.26	5737607.88	5738665.98	5709987.00	-0.50
4	0.71	0.74	-3.49	0.03	0.03	-0.59	386.57	387.53	385.65	385.70	-0.48	1894943.27	1896459.58	1908568.28	0.63
5	0.40	0.39	2.13	0.02	0.02	2.43	87.04	86.66	91.97	91.98	5.79	1015478.26	1015066.30	1040000.44	2.40
6	0.32	0.48	-49.71	0.02	0.02	-31.55	111.25	111.93	56.56	56.57	-97.87	1279887.46	1280892.60	1055681.08	-21.33
7	0.25	0.26	-3.31	0.11	0.10	9.27	7.48	7.48	6.72	6.72	-11.21	11470.96	11470.99	10203.19	-12.43
8	0.37	0.38	-3.36	0.11	0.10	9.21	24.11	24.10	21.70	21.70	-11.10	37006.43	37006.05	32947.28	-12.32
10	2.25	2.35	-4.35	0.09	0.08	7.55	4580.62	4580.64	4986.11	4986.13	8.13	7471150.52	7471185.67	7824180.06	4.51
11	0.80	0.83	-3.19	0.04	0.04	-0.51	466.65	466.62	464.00	463.97	-0.57	2073520.98	2073405.28	2084931.13	0.55
12	0.43	0.42	2.04	0.02	0.02	3.14	100.80	100.79	107.48	107.47	6.22	1069637.83	1069555.09	1101163.74	2.87
13	0.32	0.48	-49.61	0.02	0.02	-30.77	112.51	112.50	56.89	56.88	-97.78	1283398.04	1283334.78	1057206.07	-21.39
14	0.41	0.42	-1.60	0.06	0.06	0.87	18.62	18.62	22.04	22.04	15.54	30872.49	30872.60	36031.90	14.32
16	1.49	1.68	-12.41	0.08	0.08	-7.13	6322.71	6322.78	3839.84	3839.89	-64.66	1000869.26	1000876.72	6360858.58	-57.35
17	0.79	0.81	-3.15	0.05	0.05	-0.67	517.02	517.00	516.50	516.48	-0.10	2168730.16	2168645.65	2167501.96	-0.05
18	0.43	0.43	0.90	0.03	0.03	2.33	132.53	132.55	139.06	139.08	4.70	1185803.24	1185984.93	1217825.23	2.61

TABLE 4.4: Comparison of the results obtained with the full finite element model and the HBFEM. Case 9 and 15 are not reported.

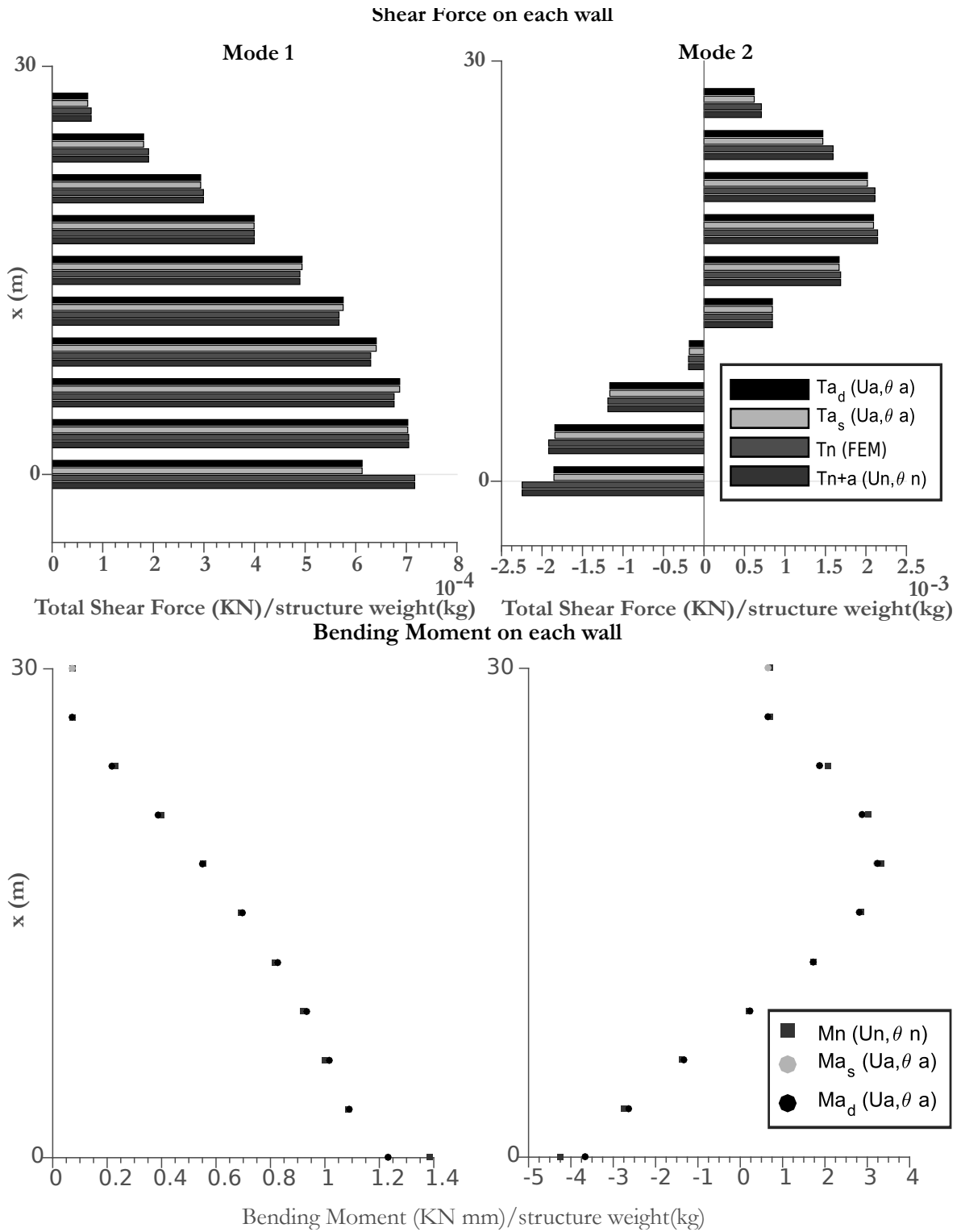


FIGURE 4.4: Shear force (top) and bending moment (bottom) of the walls for the first two eigenmodes. Single frame structure (Case 0).

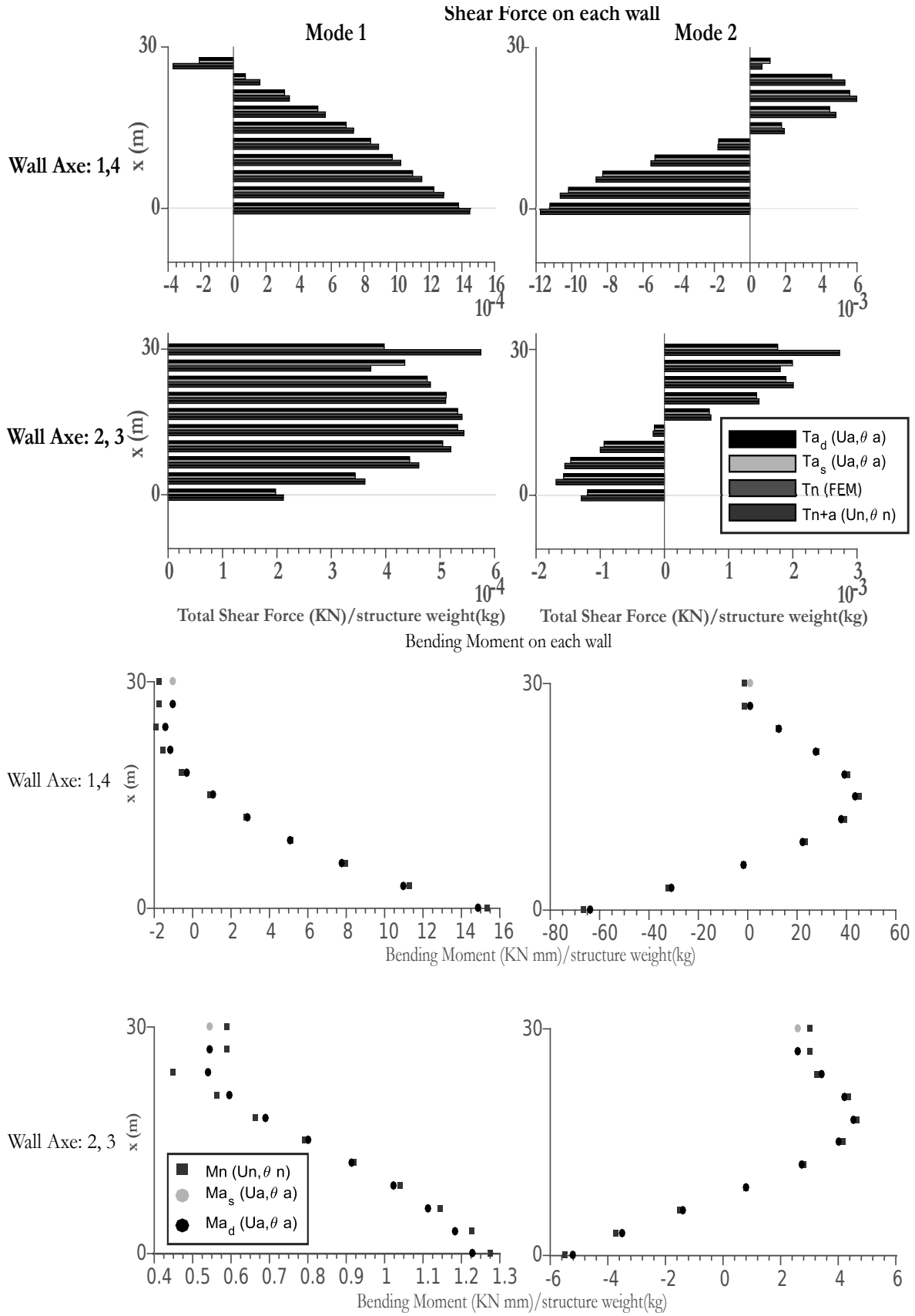


FIGURE 4.5: Shear force (top) and bending moment (bottom) of the external and internal walls for the first two eigenmodes. Triple frame structure (Case 12).

**Observations for each governing mechanism(s)**

- Shear and global bending beam-like structures (slender Timoshenko) show outstanding results at the three different scales. Only minor differences in the displacement values of the first story are present. Smaller values are obtained if compared with numerical results. We attribute this error to border effects.
- For inner bending and shear beam-like structures, modes frequency ratios are set in (1, 4, 10). Macroscopic rotation does not meet the numerical results leading to high errors in the global bending moment values. The maximum shear force is obtained for elements at the base of the structure. For the internal ones, the shear force graph describes an asymmetrical vertical bell-shaped distribution where the highest shear force is concentrated near the mid-height and decreases slowly for upper stories and more rapidly for lower stories. Thus, the elements at the base have the minimum shear force. The bending moment at the bottom of the external elements follows an exponential trending line with a negative slope. As a result, bending moment values decrease markedly, and it stabilizes for the last stories. For internal walls, the decrease of bending moment values is less significant than for external walls.
- For shear beam-like structures, modes frequency ratios are set in (1, 3, 5). The macroscopic rotation does not meet the numerical results, leading to high global bending moment values errors. Nodal rotation values for the first vibration mode are larger before the structure mid-height and decrease for higher stories. Lower values are then found around the top of the structure. In shear beam-like multiple frame structures of identical walls, both external and internal walls have different shear force magnitudes. Internal walls withstand higher shear forces with lower nodal rotation values than external ones (See cases 7, 8, and 9). This difference decreases as the slab thickness increases. The same conclusions are obtained for the magnitude of bending moments.
- The results for structures with thicker internal walls than external ones barely meet the numerical results (See cases 14 and 15). Nodal rotation values are close to numerical results only for the internal walls when the slab is thicker than the external walls (Case 15). Conversely, when the slab has the same thickness as the external walls (Case 14), nodal rotation values are close to numerical results for both internal and external walls. Internal walls in this type of structure withstand higher shear forces and bending moments. Analytical results show that shear forces and bending moments are broadly underestimated and overestimated for external and internal walls, respectively. However, modal shapes in displacement and macroscopic rotation do not seem to have significant errors (max. 9%). Moreover, frequency ratios show clearly a shear-type behavior (i.e.,  $f_i/f_1 = 1, 3-3.3, 5-6.3$ ) with relative errors below 6% in the three first modes. The macroscopic rotation shows significant differences with numerical results, so global bending moments do not follow numerical values.

#### 4.1.5 Conclusions of the return to the element scale

The proposed procedure called here *hybrid analysis part II* verifies that it is possible to return to the element scale description once the macro-deformation of a multiple-frame structure is determined. From the static analysis of a single story, the solution of the internal equilibrium was found. The hidden kinematic variable at the global scale  $\theta$  was estimated and allowed the estimation of the internal forces of the structural members.

Comparing the results issued from the hybrid analysis and those from the fully detailed numerical model show a good agreement. However, the relative error between the shear forces and bending moments values given by the analytical forms and the detailed numerical model is more significant for the elements at the bottom and top of the structure. The analytical results seem to be disturbed by the boundary effects at the first and last stories (edge effects). We have verified whether the origin of such differences is related to the procedure of the hybrid analysis (Part II) or the kinematic variable values  $u$  and  $\alpha$  by substituting directly the analytical by the numerical kinematic variables within the hybrid analysis to obtain the internal forces (i.e., variables with the subscript  $n + a$ ). It means that both analytical and numerical values for  $u$  and  $\alpha$  were used to estimate the shear force and bending moment from the solution of the E-B element equations. The results show that numerical values of  $u$  and  $\alpha$  using the theoretical solution of E-B beams can reproduce the same results as those obtained with the detailed numerical model. Besides, these results indicate that the discrepancies between analytical and numerical results have their origin neither in the element formulation (E-B equations) nor in the hybrid analysis procedure. Thus, the source of the error can be mainly attributed to the analytical values for  $u$  and  $\alpha$ . Besides, we observe that when the macroscopic rotation  $\alpha$  is less relevant (minimal values), as it occurs in shear and inner bending type structures, we found less agreement between the analytical and the fully detailed numerical model. However, when  $\alpha$  recovers its importance in global bending type structures, the accuracy increases. Thus, a way to overpass this problem could be to neglect the value of  $\alpha$  when computing the forces in the element for the structures governed by the inner bending and shear mechanism(s).

Even though some slight differences are encountered between the HBFEM results and those of the fully detailed numerical model (less than 10% relative errors), the proposed hybrid procedure offers two major advantages: (a) with the static analysis of a single story, few numerical resources are needed if compared with fully detailed finite element models, and, (b) the passage between the description at the structure scale and the element scale is performed using mainly analytical equations. Moreover, in the element quasi-static state, thanks to the scale separation, the Euler-Bernoulli static beam equations are enough to compute the members' internal forces.

## 4.2 Introducing non-linear behavior into the Equivalent Beam Model

Beyond the elasticity range, the expressions of the shear stiffness  $K_s$ , the inner bending stiffness  $\mathcal{K}_i$ , and the global bending stiffness  $\mathcal{K}_g$  given in Section 1.4.2 are not valid. We recall that, in the elastic range, these stiffnesses can be computed from the elasto-static properties of a single story. However, in the inelastic range, their values are conditioned by their evolution as a function of the global deformation as stated by the constitutive laws specified in Section 1.4.3. The evolution of each stiffness is then governed by two main aspects: the non-linear constitutive laws of the materials and the story deformation governed by the three macro mechanisms (i.e., shear, inner bending, and global bending). For this, three different FEM models of a single story are required. The cross section of the finite elements in the story are discretized with four-node quadrilateral elements. Then, a constitutive law for each material is defined.

In the first part of this section, we give a brief introduction to the multifiber beam element, and we present the material constitutive models for structural members used as case study. These uni-axial stress-strain relationships are based on theoretical and empirical models already available in the literature. In the second part, we focus our analyses at the intermediate scale (story scale). We deal with the macro deformation of the story for the three mechanisms. Herein, the challenge is to define the most appropriate boundary conditions used in each of the three numerical models (FEM-MFEM based). In the last part, we rebuild the 1D model -HBFEM model- based on the information from the local and intermediate scales and we perform a non-linear analysis of a structure. The nonlinear solution of a structure through the HBFEM model is found taking into account that:

- The stiffness matrix  $\mathbf{K}$  varies because the macroscopic parameters, -initially defined for the elastic range-  $\mathcal{K}_i$ ,  $\mathcal{K}_g$ , and  $K_s$  are now time dependent and space dependent variables. The time-varying factor comes directly from the time variation of the dynamic load demand and the space variability comes from the fact that each unit cell deforms differently.
- The solution of the global equilibrium yields the displacement of the structural degrees of freedom.

Non-local elasticity: According to this theory, the stress at a reference point  $\mathbf{x}$  in the body depends not only on the strains at  $\mathbf{x}$  but also on strains at all other points of the body.

### 4.2.1 Coupling of the HBFEM and multifiber beam element method (MFEM)

#### Multifiber beam element principles

Composite and heterogeneous structures and materials may require multiple modeling strategies to capture effects at different scales. Heterogeneity and mechanical complexity are critical

features of reinforced concrete structures that make multiscale analysis necessary. It is clear that there is an extended variety of numerical and computational tools available that allow full 3D modeling of buildings. However, these sophisticated models require high computational costs due to a large number of degrees of freedom and limit large scale analysis. Thus, a simplified multiscale analysis will be performed based on the coupling of the HBFEM model and a Multifiber Finite Element Model (MFEM).

MFEM has been reported as a proper tool for studies on degradation of reinforced concrete (RC) structures (i.e. material level), showing high agreement between numerical and experimental analysis with a reasonable computational cost. This formalism allows the introduction of fine nonlinear mechanisms (e.g. crack induced damage, plasticity, unilateral effect, ...) in a simple way. Thus, MFEM is proposed as a practical tool to evaluate progressive damages at local scale.

Multifiber beam elements have been developed since more than three decades ago [chan1982; Scordelis, 1984; Spacone et al., 1996]. They are based on the cross-section discretization in a series of longitudinal layers (for a 2-D beam) or fibers (for a 3-D beam). Figure 4.6 summarizes the principles of this method. Working at section level with simple uniaxial constitutive models (e.g., strain-stress relationships), the 3-D behavior under axial and bending forces is obtained through integration of fiber response over the cross-section.

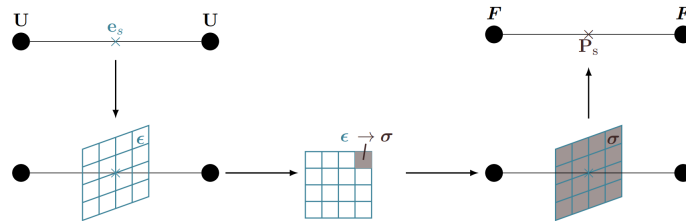


FIGURE 4.6: Principle of the multifiber beam element [CAPDEVIELLE, 2016]

#### 4.2.2 Local scale: Constitutive laws for concrete and reinforcing steel

Reinforced concrete structures subjected to seismic loads may respond in the nonlinear range causing various phenomena in the constituent materials such as cracking in concrete or plasticity of rebars. Multiple non-linear models for both concrete and steel can be found in the literature that account for such phenomena and can be integrated during the analysis.

##### Concrete behavior: La Borderie's model

The model proposed by La Borderie [La Borderie, 1991] is used in this study to describe the nonlinear behavior of concrete. This model has been widely used for the analysis of reinforced concrete structures under cyclic and dynamic loads (e.g. [Desprez, 2010], [Arruda and Castro, 2021b]).

The main effects taken into account by this concrete constitutive law are the asymmetry between the softening behaviours in tension and in compression, the permanent strains and the so-called unilateral effect which is crucial when dealing with cyclic loadings.

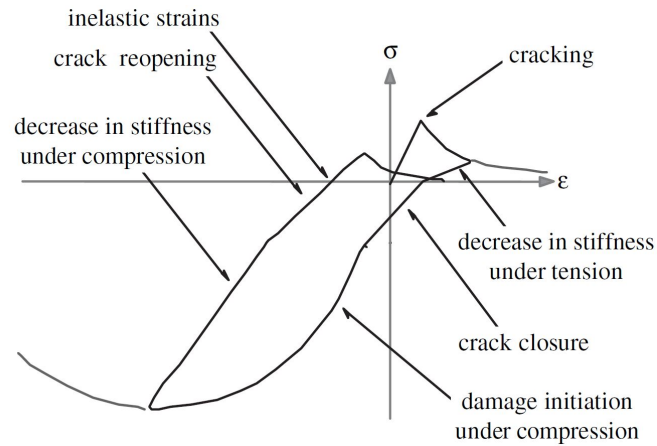


FIGURE 4.7: Stress-strain relationship for concrete- La Borderie damage model [Ile et al., 2008]

**Parameters description** Constitutive parameters  $\beta_1$  and  $\beta_2$  control the permanent strains associated with tension and compression, respectively.  $A_1$ ,  $B_1$  are the parameters that define the behavior in traction, and  $A_2$ ,  $B_2$  in compression.  $Y_{01}$  and  $Y_{02}$  determine the energy released in tension and compression, respectively.

The parameters used for the damage model are similar to the ones presented in [Desprez, 2010] and are listed in Table 4.5.

Parameter	Description	Common appropriate values
$E_0$	initial Young modulus	32 000 MPa
$\nu$	Poisson coefficient	0.2
$A_1$	curvature control	6000 MPa <sup>-1</sup>
$A_2$		5 MPa <sup>-1</sup>
$B_1$		1
$B_2$		1.6
$\beta_1$	material constant in tension	1 MPa
$\beta_2$	material constant in compression	-40 MPa
$Y_{01}$	initial elastic threshold in tension	$2.7 \times 10^{-4}$ MPa
$Y_{02}$	initial elastic threshold in compression	$2.5 \times 10^{-2}$ MPa
$\sigma_f$	crack closure stress	-3 MPa

TABLE 4.5: R/C elements: material parameters for concrete



### Reinforcing steel behavior: modified Giuffrè-Menegotto-Pinto

The reinforcing steel stress-strain relationship is described by the modified model Giuffrè-Menegotto-Pinto [Giuffrè, 1970, Menegotto and Pinto, 1977] widely used in nonlinear modeling of reinforced concrete elements [Grange et al., 2009, Desprez, 2010, Almeida et al., 2017]. This modified model describes a one-dimensional constitutive law that takes into account the kinematic hardening (Bauschinger effect), and the post-elastic buckling rules proposed by [Monti and Nuti, 1992]. The effects of the isotropic hardening can also be included in this model following the rules proposed by [Filippou et al., 1983]. Nevertheless, this latter aspect is not considered in the model used in this study. This model is characterized by a good balance between simplicity and accuracy proved by experimental results of cyclic tests on steel bars.

**Parameters description** The adopted model then consists of four controlling curves that describe the elastic, post-yield, hardening behaviour and the buckling of the steel as represented in 4.8. The buckling effect is integrated by means of the slenderness of the reinforcing bar  $L/D$  given by the ratio between the spacing of the stirrups  $L$  and the bar diameter  $D$ .

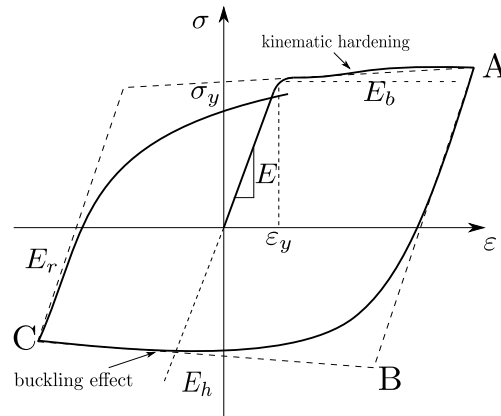


FIGURE 4.8: Stress-strain relationship for steel- Giuffrè-Menegotto-Pinto including buckling stiffness softening

As presented in [Fragiadakis et al., 2008], The curved segments are defined by the following equations:

$$\sigma^* = b\varepsilon^* + \frac{(1-b)\varepsilon^*}{(1+\varepsilon^{*R})^{1/R}} \quad (4.6)$$

where the normalised strain and stress are obtained by:

$$\varepsilon^* = \frac{\varepsilon - \varepsilon_r}{\varepsilon_0 - \varepsilon_r} \quad (4.7)$$

$$\sigma^* = \frac{\sigma - \sigma_r}{\sigma_0 - \sigma_r} \quad (4.8)$$

and

$$R = R_0 - \frac{A_1 \zeta}{A_2 + \zeta}, \quad \zeta = \varepsilon_r - \varepsilon_y \quad (4.9)$$

The hardening ratio for post-yield softening segments in compression is defined as:

$$b_h = 0.003((L/D)^* - L/D) \quad (4.10)$$

This steel model is characterized by the following six (time-invariant) parameters:

Parameter	Description	Common values
$R_0$	initial value of the cyclic curvature parameter	20
$A_1$	curvature control	18.5
$A_2$	curvature control	0.15
$A$		0.006
$A_6$	to update elastic modulus when reversal from compression	620-1000
$(L/D)^*$	ratio to account for the buckling effect	5

TABLE 4.6: R/C elements: material parameters for steel

This model can be integrated in the Cast3M software [CEA, 2017] with the option: *ACIER\_UNI*.

### 4.2.3 Intermediate scale: Prescribing the macrodeformation to a single story

The non-linearity is expressed in terms of stiffness degradation. The evolution of the three macroscopic parameters  $\mathcal{K}_i$ ,  $\mathcal{K}_g$ , and  $K_s$  is estimated numerically by prescribing the macrodeformation related to each mechanism to a single story of the structure. The macrodeformation is guided by the kinematic variables appearing at the global scale  $u$  and  $\alpha$  and the EBM constitutive laws in Equations 2.1 (§Section 1.4.3 on page 13). In this section, we compute the force - deformation relationships for each mechanism (shear, inner bending, global bending) based on a single frame story in order to represent the secant stiffness degradation.

#### Shear stiffness evolution

As aforementioned, one method to impose the shear distortion of the unit cell FE model is by applying a differential displacement  $\Delta U$  between the top and the bottom nodes. It is also possible by imposing a force  $T$  at the top nodes. However, the expected shear deformation is only obtained under specific boundary conditions. Thus, the shear stiffness can be estimated with the following equation:

$$\sum_{j=1}^{n_w} T_j = -K \frac{\Delta U}{l_m} \quad (4.11)$$

As performed in Chapter 1, we impose boundary conditions at the nodes according to the condition B (see page 29) which is recalled in Figure 4.9. For each vertical element:

- the rotations of the top and bottom ends are set to be equal,
- the vertical displacements are blocked,
- the differential horizontal displacement  $\Delta U$  is imposed between the bottom and top of each vertical element.

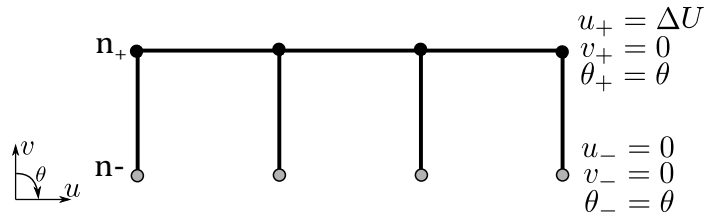
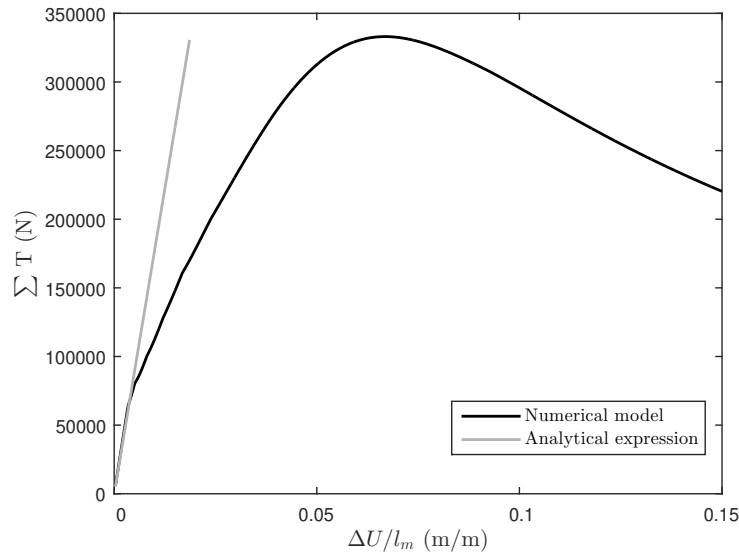


FIGURE 4.9: Boundary conditions associated with shear deformed model

The non-linear evolution of the shear deformation is displayed in Figure 4.13. In the elastic range, we compare the stiffness computed from the analytical formula given in Equation(1.2) (clear gray slope) to verify the coherence with the numerical model. The displacements at the iteration  $j$  are plotted on the structure in Figure 4.11.

FIGURE 4.10: Comparison of shear stiffness evolution obtained with the numerical model and the analytical equation for  $K_s$  (Equation(1.2))

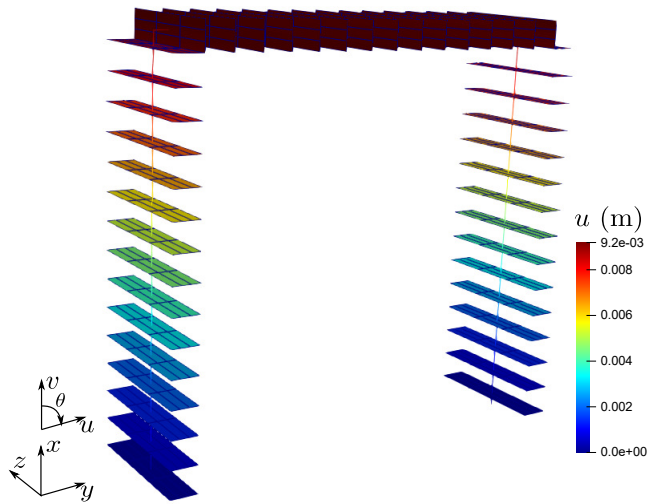


FIGURE 4.11: Shear deformation on a single frame story using boundary conditions of Figure 4.9

### Inner bending stiffness evolution

Now, we are interested in estimating the evolution of the inner bending stiffness  $\mathcal{K}_i$  as a function of the cell deformation. We know that the inner bending mechanism is controlled by the bending of the vertical elements which are synchronized by the horizontal ones. As the local bending stiffness of the vertical elements acts in the inner bending deformation, the bending stiffness of the horizontal elements should be neglected. Then, the macroscopic deformation associated with the inner bending mechanism can be modelled in the cell by imposing a differential rotation  $\Delta\theta$  and the associated boundary conditions on the internal kinematic variables. The sum of the bending moments on the vertical elements is proportional the inner bending stiffness and the differential rotation. Thus,  $\mathcal{K}_i$  can be found from the following equation:

$$\sum_{j=1}^{n_w} M_j = -\mathcal{K}_i \frac{\Delta\theta}{l_m}, \quad \mathcal{K}_i = \sum_{j=1}^{n_w} k_{ij} \quad (4.12)$$

In order to impose the inner bending deformation in the cell, we need to apply a nodal rotation difference on the vertical elements and capture the resulting bending moment. At this condition, the internal bending moment is constant all along each vertical element. Figure 4.12 illustrates the required boundary conditions.

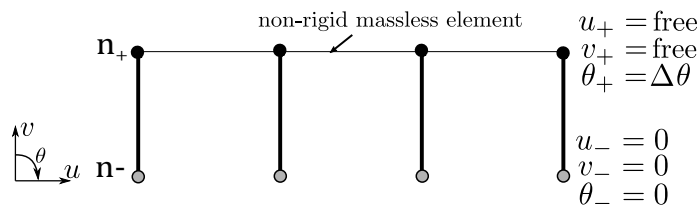


FIGURE 4.12: Boundary conditions associated with inner bending deformed model

The non-linear evolution of the shear deformation is represented in Figure 4.13. As performed for  $K_s$ , we compare the stiffness computed from the analytical formula for  $\mathcal{K}_i$  given in Equation(1.2) (clear gray slope) to verify the coherence with the numerical model for an elastic response. A refinement of the fibers section is required to obtain the complete curve of the evolution of the total bending moment on the vertical elements with respect to the nodal rotation difference applied at the top node of the vertical elements.

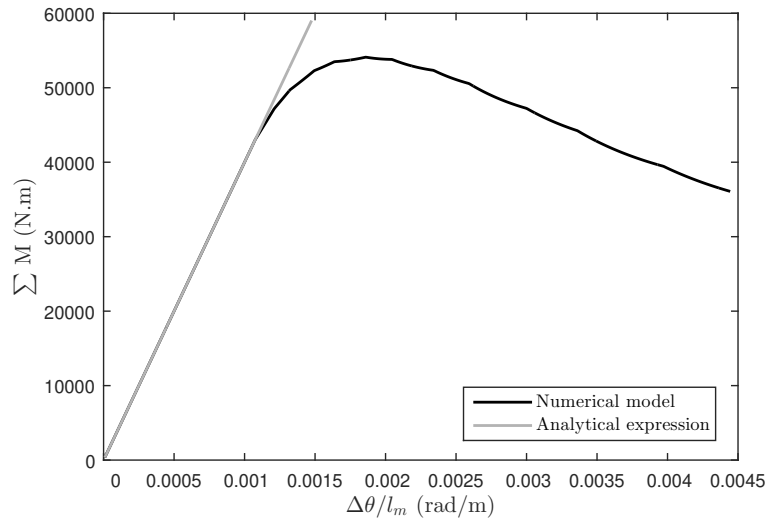


FIGURE 4.13: Total bending moment of the vertical elements as a function of the imposed nodal rotation difference

The kinematics at the iteration  $j$  are plotted on the structure in Figure 4.14.

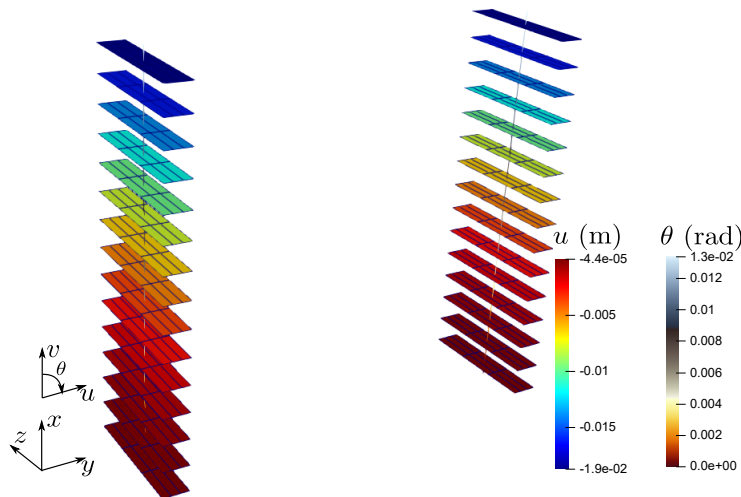


FIGURE 4.14: Inner bending deformation on a single frame story using boundary conditions of Figure 4.12

### Global bending stiffness evolution

At the structure scale, the traction-compression on vertical elements occurs when the global bending mechanism governs. The global bending stiffness depends on the macroscopic rotation  $\alpha$ . The rotation of the story around the symmetry axis involves the differential vertical displacement  $\Delta V$  at the left and right side of the structure. The coupled axial force  $N$  acting on the vertical elements originates from this rotation  $\alpha$ . The constitutive law for the global bending moment  $M = \mathcal{K}_g \frac{d\alpha}{dx}$  at a location  $n$  can also be expressed as a function of the geometrical features and the axial force  $N$  as follows:

$$\sum_{j=1}^{n_w} N_j d_j = -\mathcal{K}_g \frac{\Delta V}{l_m 0.5 l_{pt}}, \quad M = \sum_{j=1}^{n_w} N_j d_j, \quad \Delta \alpha = \frac{\Delta V}{0.5 l_{pt}} \quad (4.13)$$

For the boundary conditions to impose to the single story model, we consider that:

- the rotations of the top and bottom ends are set to be equal,
- the horizontal displacements are blocked,
- the differential vertical displacement  $\Delta V$  is imposed between the external vertical elements.

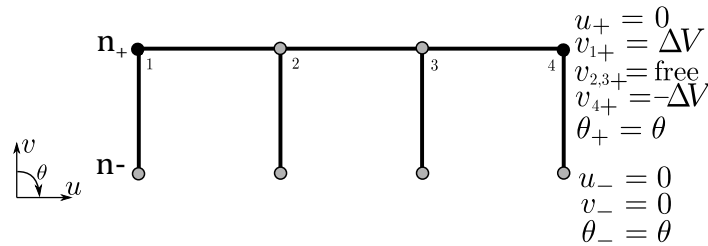


FIGURE 4.15: Boundary conditions associated with global bending deformed model

Figures 4.16 and 4.17 present the global bending moment - macroscopic rotation distortion relationship and the global bending deformation on a single frame story using boundary conditions of Figure 4.15, respectively.

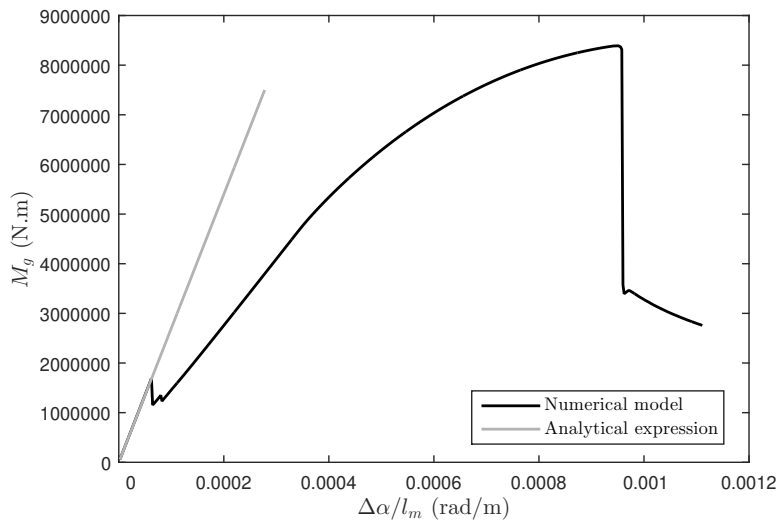


FIGURE 4.16: Global bending moment - macroscopic rotation distortion relationship

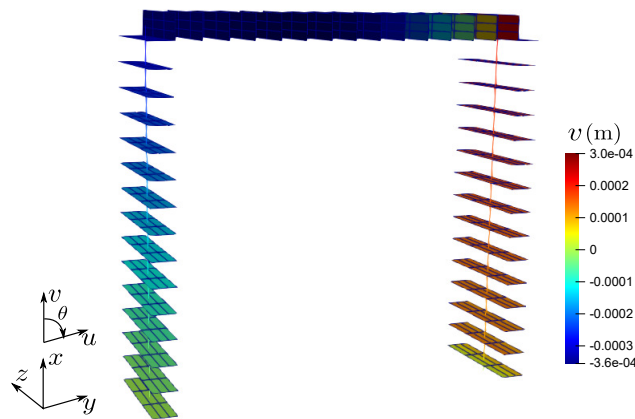


FIGURE 4.17: Global bending deformation on a single frame story using boundary conditions of Figure 4.15

#### 4.2.4 Global scale: Implementation of the Newmark method for non-linear analysis

*"Any nonlinear model can be represented as a linear model with time-varying characteristics"* (Young, 1984).

The time-stepping procedure to obtain the solution of the linear elastic HBFEM model is presented in Chapter 3 via the Newmark method. In order to find the solution of the non-linear system, the step-by-step integration includes an iterative procedure to account for the variation of the stiffness matrix  $\mathbf{K}$  at each time step. The procedure converges to a state that satisfies the material constitutive relations within the specified tolerance.

Herein, it is required to find the solution  $\mathbf{E}$  for:

$$\mathbf{M}\ddot{\mathbf{E}}(t) + \mathbf{C}\dot{\mathbf{E}}(t) + \mathbf{R}(\mathbf{E}(t)) = \mathbf{f}(t) \quad (4.14)$$

where  $\mathbf{M}$  is the time-invariant mass matrix ( $d \times d$ ),  $\mathbf{C}$  is the damping matrix ( $d \times d$ ), and  $\mathbf{R}$  is the resisting forces at time  $t$  that can be written as  $\mathbf{R} = \mathbf{K}(t)\mathbf{E}(t)$  where the stiffness matrix  $\mathbf{K}(t)$  varies with time. As in the linear scheme,  $\mathbf{f}(t)$  is the time dependent excitation force of size  $d$  represented by the base acceleration converted into the applied inertia load  $-\mathbf{M}\mathbf{L}\ddot{\mathbf{u}}_g(t)$  ( $d \times N_p$ ) where  $\mathbf{L}$  is the influence vector and  $\ddot{\mathbf{u}}_g$  the base acceleration.  $d$  refers to the number of degrees of freedom, and  $N_p$  to the length of data points of the dynamic force.

In this work, the construction of the damping matrix is based on the following hypotheses:

- A constant-damping assumption. That means that  $\mathbf{C}$  is a constant in the term  $\mathbf{C}\dot{\mathbf{E}}$ .
- A Rayleigh damping model with invariant coefficients  $a_k$  ( $k = 1, 2$ ) and invariant damping ratio  $\zeta$ .



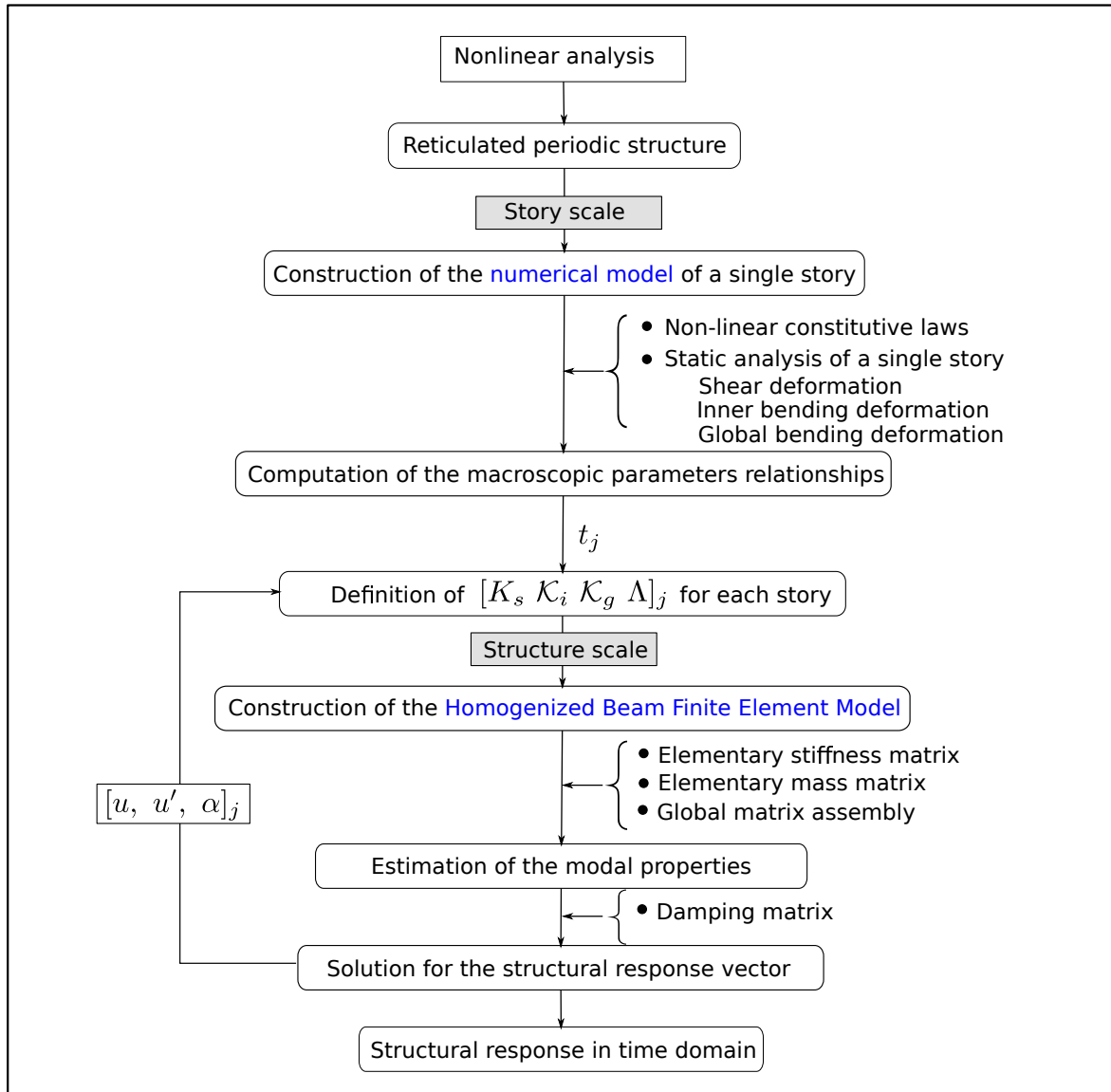


FIGURE 4.18: Non-linear analysis procedure

We corroborate the ability of the HBFEM model in reproducing the structure behavior by the comparison of the top-roof displacement time-histories of a 10-story frame reinforced concrete structure. The material and geometrical properties are given in Table 4.7 and Figure 4.19. The material non-linearity follows the constitutive laws of concrete and steel previously described.

Property	Columns	Floor beams
Length (m)	3	5
Cross-sectional area $A$ (m <sup>2</sup> )	$0.70 \times 0.70$	$0.70 \times 0.50$
Young's modulus $E$ (GPa)	30	30
Density $\rho$ (kg/m <sup>3</sup> )	2300	2300
Damping ratio $\zeta$ (%)	5	5

TABLE 4.7: Geometry and material properties of the 10-story reinforced concrete structure taken as case study.

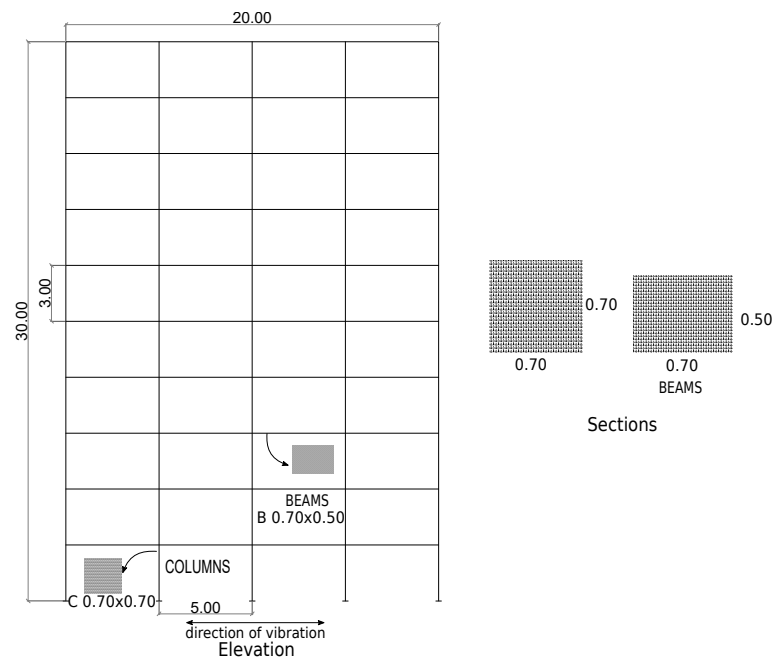


FIGURE 4.19: Elevation of the studied RC frame structure (all dimensions are in m).

The response of the structure is now obtained by using the non-linear numerical solution of the HBFEM model. The response to a moderate intensity solicitation of 0.4 g (Figure 4.20) is obtained. The results show that there is a coherence between the top roof displacement histories of the HBFEM model and the detailed numerical model. Although, the maximum displacement difference is about 15%, the results are encouraging and evidence the ability of the proposed strategy to reproduce the structure behavior.

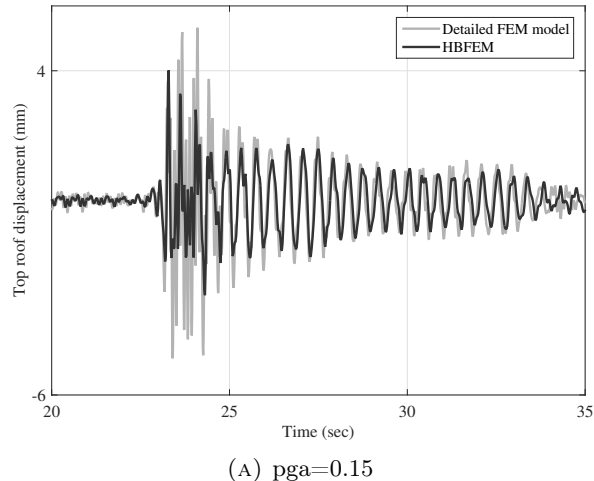


FIGURE 4.20: HBFEM model validation, roof displacement time-history.

Indeed, in the non-linear range, the periodicity on the structure is almost lost because each unit cell enters to a different damage state. However, if the analyses are limited at low intensity dynamic forces, that is, with light incursion into the non-linear range, we should be able to capture the global non-linear response of the structure. The developments here presented are primary steps to the integration of non-linearity on the HBFEM model by the non-linear static analysis of a single unit cell. Further developments on this approach will be explored in future studies.

### 4.3 About the need for a new damage indicator

Earthquake engineers are often confronted with evaluating the state of damage of structures subjected to earthquake events or even, during the design stage, to assign a level of the expected damage in new structures for a given earthquake. Civil infrastructure is likely to experience damage because of different reasons. On the one hand, most of the structures were designed and built before the appearance of the actual knowledge in earthquake engineering and most recent earthquake codes, which have evolved substantially in the last two decades, and on the other hand, because civil infrastructures degrade naturally over time (aging effects). Seismic vulnerability assessment makes it possible to decide whether a structure needs to be reinforced or not and reduces the probability that potential and irreparable damages occur in future earthquake events. This probability of damage is one of the keys to decision-making and requires the definition of damage indicators. These damage indices are then useful tools for quantitatively expressing the level of damage in civil structures. Kinematic parameters such as story drift ratio, top roof displacement have been adopted as engineering demand parameters (EDP) to quantify the level of demand, performance or damage of civil engineering structures. In this work, we search to quantify the damage state of a structure or its structural components with respect to the ultimate resistance based on easy-readable . [Desprez, 2010] vulnerability studies have confirmed that the comparison between global and local indicators could lead to discrepancies and hinders the consistency of the evaluation especially for retrofitted buildings.

Reinforcement of a structure can modify its dynamic behavior and causes it to no longer stick to the original typology, without however finding a place in a new typology. Therefore, a proposal for the construction of a robust damage indicator able to evolve according to the structural behavior is presented in this part.

### 4.3.1 Main characteristics of damage indicators

Numerous damage measures have already been proposed in the literature [Mihai, 2013]. These damage indices can generally be classified into the following main categories:

- Local damage indices – define the damage state of an element within the structure.
- Global damage indices – take into account the damage state of the whole structure by combining local damage indices.

Other general categories classify damage indices into modal based and non-modal approaches. On the one hand, modal-based damage indexes are those parameters obtained from free vibration analysis or frequency domain experimental data such as period, frequency, mode shapes, or modal damping. This type of damage index offers practicality because it can be obtained from quick analysis. On the other hand, non-modal parameters based on damage indices are defined using a damage parameter such as ductility, which can be expressed in terms of curvature, rotation or displacement, inter-story drift, and energy, or a combination of a few of those parameters. The ductility and the inter-story drift are the most commonly used non-modal damage parameters. Damage indices can also have a non-cumulative or cumulative nature. For example, inter-story drift, top roof displacement, strain, and modal frequency are non-cumulative indices, whereas mainly energy-based parameters can have cumulative characteristics. Whether the index is cumulative or not, it can be formed by combining global or local indicators such as drift (FEMA 356 (ASCE,2000)), displacement, rotation, curvature, stiffness, frequency, or energy.

**Global damage indicators** Global damage indices are calculated by weighting the local indices or by comparing the modal properties of the structure before and after the seismic action [Mihai, 2013]. We list here the main non-cumulative most common damage indices: *Drift*: In a discrete model, it is the ratio of displacement difference between consecutive levels, divided by floor height; in a continuous system can be approximated by the spatial derivative of displacement along height.

**Local damage indicators** These indicators can have a cumulative nature if the loads are cyclic and depend on the motion and the number of loading–unloading cycles, but can also be of non-cumulative nature if no cyclic loading occurs [Mihai, 2013]. Commonly used local damage indices are strain or stress values to quantify damage in concrete and yielding of the steel bars.

The development of the ductility concept led to the development of the first damage models. Newmark and Rosenblueth, proposed in 1971 the ductility factor as a mean to assess damage. The factor can be expressed either as the rate between the maximum value (subscript  $m$ ) and the yielding value (subscript  $y$ ) of curvature –  $\Phi$ , rotation –  $\theta$  or displacement –  $u$ . From then, various damage indices have been proposed based on the ductility of kinematic variables change rates such as the well-known drift index as summarized in Table 4.8. The main vulnerability assessment methodologies like Hazus (ATC40, 1996) and Risk-UE LM2 (Risk-UE, 2003) are based on the inter-story drift and the top displacement, respectively, which are global non-cumulative damage indicators.

Ductility ratio (Newmark and Rosenblueth (1971))	$\mu_r(\Phi) = \frac{\Phi_m}{\Phi_y}$	(4.8.1a)
	$\mu_r(\theta) = \frac{\theta_m}{\theta_y}$	(4.8.1b)
	$\mu_r(u) = \frac{u_m}{u_y}$	(4.8.1c)
Damage index (stiffness) (Lybas (1977)) (Roufail (1981))	$I_D = \frac{k_0}{k_m}$	(4.8.2)
Flexural damage stiffness (Banon et al. (1981))	$FDR = \frac{M_u \Phi_m}{M_m \Phi_u}$	(4.8.3)
Damage index (Bracci et al. (1989))	$I_D = \frac{\Phi_m - M_u/k_m}{\Phi_u - M_u/k_u}$	(4.8.4)
Drift (FEMA 356 (ASCE,2000))	$s = \frac{\Delta u}{l_m} = \frac{u_{n+1} - u_n}{l_m}$	(4.8.5)

TABLE 4.8: Non-cumulative damage indices

### 4.3.2 Discrepancies between damage indicators

#### Example of the Grenoble City Hall

The retrofitting study performed by [Desprez, 2010, Desprez et al., 2015] on the City Hall Building of Grenoble (GCH), France reveals high discrepancies between global and local damage indicators. Although regions at the base and after the transfer slab were reinforced with fiber-reinforced polymers, results show a significant increment of the top roof displacement and the inter-story drift despite reducing damage on steel bars. The initial and the final (reinforced) state of the structure are compared in terms of drift, displacement, and strain along the structure height as presented in Figure 4.21. It is observed that the plastification zone moves to the immediate higher stories of the reinforced region. In this example, moving the initial plastic hinge location change the vibratory behavior of the structure. The lower

contribution of second bending mode and higher contribution of the first one lead to increase top displacement and reducing curvature, that is directly linked to strains.

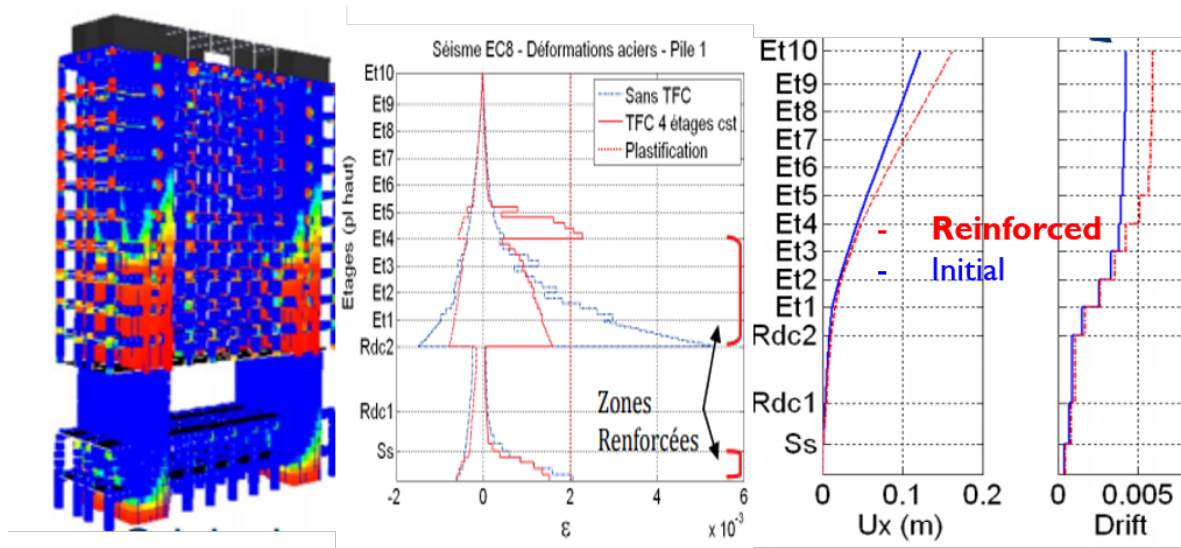


FIGURE 4.21: Numerical simulation results before and after the proposed reinforcement strategy of the Grenoble City Hall building [Desprez, 2010].

### 4.3.3 Strategy for the definition of a new damage indicator

Up to now, we have designed and verified all the required tools that we need to capture the effects at both global and local scales by performing the coupling between two robust methodologies: the homogenized finite element (HBFEM) model as a result of the HPDM and, the multifiber beam elements. The lecture of information at both scales allows us to carry out a large study to find the correlation between the different damages indicators associated with each type of governing mechanism(s). Thus, from now, we are interested in evaluating the non-linear response of structures by recovering simultaneously:

- the main dynamic description parameters (i.e., displacement, first derivative of displacement (drift), second derivative of displacement (curvature) and frequencies).
- the internal forces, moments and strain on the elements.

The new indicator should be typology independent, have great adaptability, and be based on the nature of the structure. For this purpose, we propose estimating the damage states in terms of the primary kinematic variables: displacement, drift, and curvature. The capacity curve of the structure and the correlation between the kinematics and damage levels for each governing mechanism provide critical points for identifying the most suitable indicator.

#### Form of the Behavior Response based Damage Indicator (BRDI)

The proposed damage indicator depends on two types of functions:

- the *adaptive functions*  $f_{w_x}$ : determined by the stiffness ratios  $C$  and  $\gamma$ , they adapt as a function of the governing type mechanism(s) and the analyzed vibration mode. The adaptive functions are multipliers of the ductility function.
- *ductility function*  $g$ . It establishes the relationship between the kinematic variable displacement  $U$ , drift  $\delta U$ , and curvature  $\phi$  and their yielding threshold, respectively.

$$DI = f_{w_i}(C, \gamma)g(U, U_y) + f_{w_j}(C, \gamma)g(\delta U, \delta U_y) + f_{w_k}(C, \gamma)g(\phi U, \phi U_y) \quad (4.15)$$

## 4.4 Conclusions and perspectives

In the first part of this chapter, we extended the hybrid analysis procedure proposed in Chapter 1, called here *hybrid analysis part II*, which verifies that it is possible to return to the element scale description once the macro-deformation of a multiple-frame structure is determined. From the static analysis of a single story, the solution of the internal equilibrium was found. The hidden kinematic variable at the global scale  $\theta$  was estimated and allowed the estimation of the internal forces of the structural members. The comparisons of the results issued from the hybrid analysis and those from the fully detailed numerical model show a good agreement. However, some discrepancies were encountered on the elements located at the bottom and top of the structure. These errors could be associated with the discrepancy between the real boundary conditions at the first and last stories and the periodicity assumptions (edge effects). We have verified whether the origin of the encountered differences was related to the procedure of the hybrid analysis (Part II) or the kinematic variable values  $u$  and  $\alpha$  by substituting directly the analytical by the numerical kinematic variables within the hybrid analysis to obtain the internal forces. However, the results obtained retrieve the exact values provided by the fully detailed numerical model, so the errors are mostly linked to the values of the transverse displacement,  $u$  and the macroscopic rotation  $\alpha$  at first and last stories.

The validation of the homogenized beam finite element (HBFEM) model in linear and nonlinear dynamic analyses for reticulated symmetric structures and the understanding of the structure mechanical functioning thanks to the developed procedure could provide an alternative and sophisticated tool for performing extensive numerical simulations in earthquake engineering studies with a low computational cost.

The analyses that we perform at the end of this chapter provides some insights on the formulation of a robust damage indicator based on the usual global indicators such as ductility, top roof displacement, inter-story drift. It could even be adapted to cyclic loading-based or energy-based indicators. With this approach, the damage could be directly related to the structural behavior and not only to the general material or geometry presented by current seismic design codes. We propose a new form for a damage indicator based on the identification criterion presented in Chapter 1. An exhaustive parametric study could identify the relevancy of the widely used global indices such as the top roof displacement and inter-story drift on the governing mechanism(s).

# General conclusions

Chapter 1 introduces the beam models issued from the homogenization method of periodic discrete media (HPDM) implemented on frame structures. First, we start describing the generic beam model of [Boutin and Hans, 2003, Hans and Boutin, 2008] and here called the Equivalent Beam Model (EBM) that forms the basis of this study. Then, we provide a numerical procedure named *hybrid analysis* that enables the application of the EBM to complex reticulated structures. The idea is to numerically solve the unit cell's kinematics by realizing a static analysis with appropriate boundary conditions. Once the macroscopic parameters are calculated, the dynamic analysis can be performed with the EBM.

We implement this strategy on several fictitious structures and reproduce the results given in the literature. These previous results are restricted to very simple cases: single and double frame structures. In this work, the EBM is applied to a great variety of multiple frame structures. The comparisons with numerical models built in the Cast3M FEM software concludes that the analytical results are encouraging, and more complex structures could be modeled. Only for some highly contrasted structures, whose behavior is governed by the deformation of a small part, an adaptation of the models is required. The numerical results also showed that a specific model including only the governing mechanism(s) could give better results than the general EBM.

We propose a strategy called Hybrid analysis to study multi-frame structures. We see that the type of boundary conditions used in the one-story model can strongly influence the accuracy of the results. It is verified that the adopted boundary conditions (Condition B: macroscopic shear deformation, periodic nodal rotations, and restriction of the vertical displacement of every vertical element) in the numerical model of the story give very close results between the numerical calculations and the analytical formula for both shear of the cell stiffness and frequencies.

The performed parametric study also highlights that the natural frequencies and mode shapes can provide rapid insight into a structure functioning. The natural frequencies and the mode shapes are dynamic properties that can be obtained easily experimentally. From the engineering point of view, the relation between the frequencies is a feature of the different models, which could represent valuable guidance for the quick identification of the best model to implement.

In Chapter 2, we detail the formulation of a new enriched beam finite element that accurately describes the transverse dynamics of periodic reticulated structures. The proposed homogenized beam finite element (HBFEM) formulation is derived from the Equivalent Beam Model. Elementary stiffness and mass matrices are derived from virtual power formulation



principles. Interpolation functions are used to approximate the kinematic variables that describe the transverse dynamics of the structure. Particular attention is paid to the validation of the HBFEM model by means of an extensive parametric study. The results show that the proposed 1D FEM model retrieves the EBM solutions for modal analysis. A detailed analysis is also conducted to define the finite element size. It is observed that the finite element size should be chosen according to the wavelength or the number of considered modes. It is shown that three finite elements are enough to fully describe the dynamic behavior up to the third transverse vibration mode. This last statement is convenient to reduce the number of degrees of freedom of the model and the computational time. The parametric study also evidences that the source of the differences between the HBFEM model and the EBM results is also linked to the governing response mechanism of the structure. It is noticed that the EBM and HBFEM model are a little less accurate when analyzing structures controlled by the shear mechanism or the combination of global bending and shear mechanisms.

In Chapter 3, we validate the homogenized beam finite element model (HBFEM) for the transient analysis of the transverse dynamics of real structures in the elastic range. We introduce the used numerical time-stepping procedure, and we perform the dynamic analysis on a realistic steel frame structure using natural recorded ground motions. The seismic responses computed with the HBFEM and the detailed FEM model agree well.

We introduce the methodology for the analysis of structures with vertical irregularity. The Grenoble City Hall (GCH) building is used as a case study. The full detailed numerical model calibrated with in-situ measurements by [Desprez, 2010] was used as a reference. This model is also slightly modified to include only the quasi-periodic section of the GCH tower block. The construction of the 1D model based on the HBFEM formulation aimed at retrieving, in the harmonic regime, the vibration frequencies and modes of the structure. The HBFEM model for the GCH building, adopting the hybrid analysis principles, required the computation of the macroscopic parameters: the linear mass  $\Lambda$ , the shear of the cell stiffness  $K_s$ , the global bending stiffness  $\mathcal{K}_g$ , and the inner bending stiffness  $\mathcal{K}_i$ . We perform the static analysis for each of the typical stories. The computation of the shear stiffness  $K_s$ , being very delicate, requires the construction of a numerical model of a single story of the periodic structure.

We identify that the leading mechanism for the GCH structure corresponds to a combination of the inner bending and the shear of the story in both longitudinal and transverse directions. Such a mechanism, integrated into the HBFEM model, is not included in usual beam models that may not be capable of reproducing the GCH building dynamic response.

In summary, the HBFEM model is an enriched but simplified and fast-performance model to study the transverse dynamics within the low-frequency range of all the reticulated frame structures that respect the conditions given by the homogenization. The HBFEM model includes three functioning mechanisms: shear, inner bending, and global bending. The model is validated for modal analyses and time history analyses in the linear elastic range of real structures. A strategy to extend its applicability to the nonlinear framework is proposed.

In Chapter 4, we aim to assess the vulnerability of structures by studying also the structural elements at the local scale.

Each of the three mechanisms: shear, local bending, and global bending are linked to the unit cell description by an internal kinematics that explicitly gives access to the forces acting on the elements. Thus, while the structure remains in the elastic domain, at each level and each instant, the deformation of the structure being known by integration of the EBM, the contributions of each of the three mechanisms are also found, which solves the internal kinematics and allows obtaining the local forces. This strategy is tested on twenty single or triple-frame structures and validated by comparison with detailed numerical models. The variations that appear mainly at the ends of the structure are due to loss of periodicity at the edges, currently not considered in the EBM model.

The second part of Chapter 4 aims to build new damage indicators. The literature already offers a large number of them, but they are often used interchangeably regardless of the mechanism(s) that govern the behavior of the structure, which limits their relevance.

In the same idea of reducing the computational cost, the homogenization principles used to build the EBM model are assumed. The numerical model of a single cell is built using multi-fiber beam elements and nonlinear constitutive laws for the materials (i.e., concrete and steel). Assuming that the kinematics in the nonlinear regime remains controlled by all three mechanisms, the nonlinear evolution of the macroscopic parameters is determined by a nonlinear static analysis at the cell level. The nonlinear evolution of the macroscopic parameters is then used in a temporal calculation performed at the structure scale: at each time step, the evolution of the local kinematics leads to reevaluating the macroscopic parameters. Therefore the structure model allows determining the force and strain increments to move to the next time step. A first numerical example shows very encouraging results in using this approach.

The analyses that we perform at the end of this chapter provide some insights on the formulation of a robust damage indicator based on the usual global indicators such as ductility, top roof displacement, inter-story drift. It could even be adapted to cyclic loading-based or energy-based indicators. With this approach, the damage could be directly related to the structural behavior and not only to the general material or geometry presented by current seismic design codes. We propose a new form for a damage indicator based on the identification criterion presented in Chapter 1. An exhaustive parametric study could identify the relevancy of the widely used global indices such as the top roof displacement and inter-story drift on the governing mechanism(s).

The procedure proposed in this work for the seismic response evaluation of buildings has shown promising results. A new enriched finite element formulation for buildings was successfully developed and validated. This 1D model enlarges the capabilities for assessing existing structures, designing new structures, and performing parametric studies for the research. However, we recognize that we leave many questions still open, which can be solved in future works.

For the perspectives of this study, we can list the following:

Although the EBM and the hybrid analysis retrieve the numerical results for the multiple frame structures treated in this work, it is necessary to analyze the influence of other elements in the cell of common civil engineering infrastructures such as braces or filled areas (e.g., frames filled with masonry walls). In addition, there is the necessity to study asymmetric structures where new kinematic variables, and indeed new mechanisms, can appear due to torsion.

The full numerical model of the GCH building is assumed totally fixed boundary conditions at the base of the structure. The excellent correlation encountered between the numerical model's frequencies and mode shapes and the in-situ measurements supports this assumption for the GCH building and the performed analyses in this work. However, buildings founded on soft soils may exhibit other mechanisms such as rocking, which are neglected with fixed end condition assumptions. In such a case, it could be necessary to take into account the soil properties in the HBFEM model and replace the fixed condition with a FEM-based description of the soil.

Considering high ratios between the stiffness of two consecutive periodic substructures may lead to a loss of accuracy of the HBFEM model. The order of this ratio could be identified to estimate the validity domain of the HBFEM model implementation.

The following aspects of modeling buildings remain challenging; plane-unsymmetrical buildings, the effect of torsion, contribution of stiffness of braced elements or non-structural elements, secondary effects such as P-delta, and modeling of damping.

Concerning the definition of a new damage indicator, the integration of energy-based damage indicators could be appropriated to correlate the seismic demand with the damage level. Parametric studies with more strategical approaches based on machine learning techniques can help light up the correlation between the damage level and the structure governing mechanism(s).

# Bibliography

- [Abdoul-Anziz and Seppecher, 2018] Abdoul-Anziz, H. and Seppecher, P. (2018). Strain gradient and generalized continua obtained by homogenizing frame lattices. *Mathematics and mechanics of complex systems*, 6(3):213–250.
- [Abrate and Sun, 1983] Abrate, S. and Sun, C. (1983). Dynamic analysis of geometrically nonlinear truss structures. *Computers & Structures*, 17(4):491 – 497.
- [Allaire et al., 2016] Allaire, G., Briane, M., and Vanninathan, M. (2016). A comparison between two-scale asymptotic expansions and bloch wave expansions for the homogenization of periodic structures. *SEMA journal*, 73(3):237–259.
- [Allemang, 1982] Allemang, R. J. (1982). A correlation coefficient for modal vector analysis. In *Proc. 1st Int. Modal Analysis Conference*, pages 110–116.
- [Almeida et al., 2017] Almeida, A., Ferreira, R., Proença, J. M., and Gago, A. S. (2017). Seismic retrofit of rc building structures with buckling restrained braces. *Engineering Structures*, 130:14–22.
- [Aoubiza et al., 1996] Aoubiza, B., Crolet, J. M., and Meunier, A. (1996). On the mechanical characterization of compact bone structure using the homogenization theory. *Journal of Biomechanics*, 29(12):1539–1547.
- [Arruda and Castro, 2021a] Arruda, M. and Castro, L. (2021a). Non-linear dynamic analysis of reinforced concrete structures with hybrid mixed stress finite elements. *Advances in Engineering Software*, 153:102965.
- [Arruda and Castro, 2021b] Arruda, M. and Castro, L. (2021b). Non-linear dynamic analysis of reinforced concrete structures with hybrid mixed stress finite elements. *Advances in Engineering Software*, 153:102965.
- [Battista et al., 2018] Battista, A., Della Corte, A., dell’Isola, F., and Seppecher, P. (2018). Large deformations of 1D microstructured systems modeled as generalized Timoshenko beams. *Zeitschrift für angewandte Mathematik und Physik*, 69(3):1–22.
- [Bennet et al., 1986] Bennet, W., Kwatny, H., Blankenship, G., and Barkakati, N. (1986). Continuum modeling of lattice structures with application to vibration control. In *24th Aerospace Sciences Meeting*, page 173.
- [Bensoussan et al., 1978] Bensoussan, A., Lions, J., and Papanicolaou, G. (1978). Asymptotic analysis for periodic structures. *Studies in Mathematics and its Applications*.

- [Boutin et al., 2014] Boutin, C., Antoine, R., and Hans, S. (2014). Large scale modulation of high frequency waves in periodic elastic composites. *Journal of the Mechanics and Physics of Solids*, 70.
- [Boutin et al., 2017] Boutin, C., Giorgio, I., Placidi, L., et al. (2017). Linear pantographic sheets: asymptotic micro-macro models identification. *Mathematics and Mechanics of Complex Systems*, 5(2):127–162.
- [Boutin and Hans, 2003] Boutin, C. and Hans, S. (2003). Homogenisation of periodic discrete medium: Application to dynamics of framed structures. *Computers and Geotechnics*, 30(4):303–320.
- [Boutin et al., 2010] Boutin, C., Hans, S., and Chesnais, C. (2010). *Generalized Beams and Continua. Dynamics of Reticulated Structures*, pages 131–141. Springer New York, New York, NY.
- [Boutin et al., 2005] Boutin, C., Hans, S., Ibraim, E., and Roussillon, P. (2005). In situ experiments and seismic analysis of existing buildings. Part II: Seismic integrity threshold. *Earthquake Engineering & Structural Dynamics*, 34(12):1531–1546.
- [Boutin and Viverge, 2016] Boutin, C. and Viverge, K. (2016). Generalized plate model for highly contrasted laminates. *European Journal of Mechanics - A/Solids*, 55:149 – 166.
- [Caillerie et al., 2015] Caillerie, D., Kotronis, P., and Cybulski, R. (2015). A Timoshenko finite element straight beam with internal degrees of freedom. *International Journal for Numerical and Analytical Methods in Geomechanics*, 39(16):1753–1773.
- [Caillerie et al., 1989] Caillerie, D., Trompette, P., and P., V. (1989). Homogenisation of periodic trusses. pages 303–320.
- [CAPDEVIELLE, 2016] CAPDEVIELLE, S. (2016). *Introduction du gauchissement dans les éléments finis multifibres pour la modélisation non linéaire des structures en béton armé*. Theses, Université Grenoble Alpes.
- [Caughey, 1960] Caughey, T. (1960). Classical normal modes in damped linear dynamic systems.
- [CEA, 2017] CEA (2017). Cast3M v. 17. <http://www-cast3m.cea.fr/>.
- [Chesnais, 2010] Chesnais, C. (2010). *Dynamique de milieux réticulés non contreventés : application aux bâtiments*. Thesis, Ecole Centrale de Lyon.
- [Chesnais et al., 2011a] Chesnais, C., Boutin, C., and Hans, S. (2011a). *Structural Dynamics and Generalized Continua*, pages 57–76. Springer Berlin Heidelberg, Berlin, Heidelberg.
- [Chesnais et al., 2011b] Chesnais, C., Hans, S., and Boutin, C. (2011b). Dynamics of reticulated structures: Evidence of atypical gyration modes. *International Journal for Multiscale Computational Engineering*, 9(5):515–528.

- [Chopra et al., 2012] Chopra, A. K. et al. (2012). *Dynamics of structures*. Pearson Education Upper Saddle River, NJ.
- [Chopra and McKenna, 2016] Chopra, A. K. and McKenna, F. (2016). Modeling viscous damping in nonlinear response history analysis of buildings for earthquake excitation. *Earthquake Engineering & Structural Dynamics*, 45(2):193–211.
- [Cioranescu and Paulin, 1999] Cioranescu, D. and Paulin, J. S. J. ((1999)). *Homogenization in perforated media*, pages 1–70. Springer, New York, NY.
- [Cruz and Miranda, 2017a] Cruz, C. and Miranda, E. (2017a). Evaluation of damping ratios for the seismic analysis of tall buildings. *Journal of Structural Engineering*, 143(1):04016144.
- [Cruz and Miranda, 2017b] Cruz, C. and Miranda, E. (2017b). Evaluation of the rayleigh damping model for buildings. *Engineering Structures*, 138:324–336.
- [Desprez, 2010] Desprez, C. (2010). *Analyse et Réduction de la Vulnérabilité Sismique des Structures Existantes : Renforcement par Collage de Tissus de Fibres de Carbone (TFC)*. Thesis, Institut National Polytechnique de Grenoble - INPG.
- [Desprez et al., 2015] Desprez, C., Kotronis, P., and Mazars, J. (2015). Seismic vulnerability assessment of a RC structure before and after FRP retrofitting. *Bulletin of Earthquake Engineering*, 13(2):539–564.
- [Dos Reis and Ganghoffer, 2012] Dos Reis, F. and Ganghoffer, J. (2012). Construction of micropolar continua from the asymptotic homogenization of beam lattices. *Computers & Structures*, 112-113:354 – 363.
- [Fan et al., 2010] Fan, H.-L., Zeng, T., Fang, D.-N., and Yang, W. (2010). Mechanics of advanced fiber reinforced lattice composites. *Acta Mechanica Sinica*, 26(6):825–835.
- [Filippou et al., 1983] Filippou, F. C., Popov, E. P., and Bertero, V. V. (1983). Effects of bond deterioration on hysteretic behavior of reinforced concrete joints.
- [Forest et al., 2001] Forest, S., Pradel, F., and Sab, K. (2001). Asymptotic analysis of heterogeneous Cosserat media. *International Journal of Solids and Structures*, 38(26-27):4585–4608.
- [Fragiadakis et al., 2008] Fragiadakis, M., Pinho, R., and Antoniou, S. (2008). Modelling inelastic buckling of reinforcing bars under earthquake loading. *Computational Structural Dynamics and Earthquake Engineering: Structures and Infrastructures Book Series*, 2:347.
- [Franco et al., 2019] Franco, C., Chesnais, C., Semblat, J.-F., Desprez, C., and Giry, C. (2019). Une technique d’homogénéisation appliquée aux bâtiments périodiques multiporiques. In *10ème colloque national de l’AFPS - AFPS’19*, Strasbourg, France.

- [Franco et al., 2022] Franco, C., Chesnais, C., Semblat, J.-F., Giry, C., and Desprez, C. (2022). Finite element formulation of a homogenized beam for reticulated structure dynamics. *Computers Structures*, 261-262:106729.
- [Germain, 1973] Germain, P. (1973). The method of virtual power in continuum mechanics. Part 2: Microstructure. *SIAM Journal on Applied Mathematics*, 25(3):556–575.
- [Giuffrè, 1970] Giuffrè, A. (1970). Il comportamento del cemento armato per sollecitazioni cicliche di forte intensità. *Giornale del Genio Civile*.
- [Grange et al., 2009] Grange, S., Kotronis, P., and Mazars, J. (2009). Numerical modelling of the seismic behaviour of a 7-story building: NEES benchmark. *Materials and Structures*, 42(10):1433–1442.
- [Hans, 2002] Hans, S. (2002). *Auscultation dynamique de bâtiments et modélisation par homogénéisation : contribution à l'analyse de la vulnérabilité sismique*. Thesis, INSA Lyon.
- [Hans and Boutin, 2008] Hans, S. and Boutin, C. (2008). Dynamics of discrete framed structures: a unified homogenized description. *Journal of Mechanics of Materials and Structures*, 3(9):1709–1739.
- [Hans et al., 2000] Hans, S., Ibraim, E., Pernot, S., Boutin, C., and Lamarque, C.-H. (2000). Damping identification in multi-degree-of-freedom system via a wavelet-logarithmic decrement— Part 2: study of a civil engineering building. *Journal of Sound and Vibration*, 235(3):375–403.
- [Heki, 1968] Heki, K. (1968). On the effective rigidities of lattice plates. *Recent Researches of Structural Mechanics*, pages 31–46.
- [Heki, 1972] Heki, K. (1972). Stress analysis of lattice plates as anisotropic continuum plates. *Proc. of 1971 IASS Pacific symposium Part II on TENSION STRUCTURES and SPACE FRAMES, AIJ, Tokyo*.
- [Hughes, 2012] Hughes, T. J. (2012). *The finite element method: linear static and dynamic finite element analysis*. Courier Corporation.
- [Ile et al., 2008] Ile, N., Nguyen, X.-H., Kotronis, P., Mazars, J., and Reynouard, J. M. (2008). Shaking table tests of lightly rc walls: Numerical simulations. *Journal of Earthquake Engineering*, 12(6):849–878.
- [Jacques Mossot, 2007] Jacques Mossot (2007). Grenoble-hoteldeville. image-id. 95460. [Online; accessed March 06, 2020].
- [Kerr and Accorsi, 1985] Kerr, A. D. and Accorsi, M. L. (1985). Generalization of the equations for frame-type structures; a variational approach. *Acta mechanica*, 56(1-2):55–73.

- [La Borderie, 1991] La Borderie, C. (1991). *Phénomènes unilatéraux dans un matériau endommageable: Modélisation et application à l'analyse de structures en béton*. PhD thesis, Paris 6.
- [Luco, 2008] Luco, J. E. (2008). A note on classical damping matrices. *Earthquake Engineering & Structural Dynamics*, 37(4):615–626.
- [MATLAB, 2015] MATLAB (2015). *version 8.5.0 (R2015a)*. The MathWorks Inc., Natick, Massachusetts.
- [McCallen and Romstad, 1988] McCallen, D. and Romstad, K. (1988). A continuum model for the nonlinear analysis of beam-like lattice structures. *Computers & Structures*, 29(2):177 – 197.
- [Menegotto and Pinto, 1977] Menegotto, M. and Pinto, P. E. (1977). Slender rc compressed members in biaxial bending. *Journal of the Structural Division*, 103(3):587–605.
- [Meza Fajardo and Papageorgiou, 2019] Meza Fajardo, K. C. and Papageorgiou, A. S. (2019). Ductility demands of tall buildings subjected to base rocking induced by rayleigh waves. *Earthquake Engineering & Structural Dynamics*, 48(10):1174–1194.
- [Michel, 2007] Michel, C. (2007). *Vulnérabilité Sismique de l'échelle du bâtiment à celle de la ville - Apport des techniques expérimentales in situ - Application à Grenoble*. Theses, Université Joseph-Fourier - Grenoble I.
- [Michel and Gueguen, 2006] Michel, C. and Gueguen, P. (2006). Dynamic behaviour of the first instrumented building in france: The grenoble town hall. first european conference on earthquake engineering and seismology.
- [Michel et al., 2010a] Michel, C., Guéguen, P., El Arem, S., Mazars, J., and Kotronis, P. (2010a). Full Scale Dynamic Response of a RC Building under Weak Seismic Motions Using Earthquake Recordings, Ambient Vibrations and Modelling. *Earthquake Engineering and Structural Dynamics*, 39(4):419–441.
- [Michel et al., 2010b] Michel, C., Guéguen, P., El Arem, S., Mazars, J., and Kotronis, P. (2010b). Full-scale dynamic response of an rc building under weak seismic motions using earthquake recordings, ambient vibrations and modelling. *Earthquake Engineering & Structural Dynamics*, 39(4):419–441.
- [Mihai, 2013] Mihai, M. (2013). A theoretical review of the damage indices used to model the dynamic nonlinear behavior of reinforced concrete structures. *Buletinul Institutului Politehnic din Iasi. Sectia Constructii, Arhitectura*, 59(2):109.
- [Monti and Nuti, 1992] Monti, G. and Nuti, C. (1992). Nonlinear cyclic behavior of reinforcing bars including buckling. *Journal of Structural Engineering*, 118(12):3268–3284.



- [Moreau and Caillerie, 1998] Moreau, G. and Caillerie, D. (1998). Continuum modeling of lattice structures in large displacement applications to buckling analysis. *Computers & structures*, 68(1-3):181–189.
- [Newmark, 1959] Newmark, N. M. (1959). A method of computation for structural dynamics. *Journal of the engineering mechanics division*, 85(3):67–94.
- [Noor, 1988] Noor, A. K. (1988). Continuum Modeling for Repetitive Lattice Structures. *Applied Mechanics Reviews*, 41(7):285–296.
- [Noor and Mikulas, 1988] Noor, A. K. and Mikulas, M. M. (1988). Continuum modeling of large lattice structures: Status and projections. In *Large Space Structures: Dynamics and Control*, pages 1–34. Springer.
- [Pan et al., 2020] Pan, Y., Ventura, C. E., Xiong, H., and Zhang, F.-L. (2020). Model updating and seismic response of a super tall building in shanghai. *Computers & Structures*, 239:106285.
- [Petrini et al., 2008] Petrini, L., Maggi, C., Priestley, M. J. N., and Calvi, G. M. (2008). Experimental verification of viscous damping modeling for inelastic time history analyzes. *Journal of Earthquake Engineering*, 12(sup1):125–145.
- [Pradel and Sab, 1998] Pradel, F. and Sab, K. (1998). Cosserat modelling of elastic periodic lattice structures. *Comptes Rendus de l'Académie des Sciences-Series IIB-Mechanics-Physics-Astronomy*, 326(11):699–704.
- [Puthanpurayil et al., 2016] Puthanpurayil, A. M., Lavan, O., Carr, A. J., and Dhakal, R. P. (2016). Elemental damping formulation: an alternative modelling of inherent damping in nonlinear dynamic analysis. *Bulletin of Earthquake Engineering*, 14(8):2405–2434.
- [Rahgozar et al., 2010] Rahgozar, R., Ahmadi, A. R., and Sharifi, Y. (2010). A simple mathematical model for approximate analysis of tall buildings. *Applied Mathematical Modelling*, 34(9):2437 – 2451.
- [Rallu et al., 2018] Rallu, A., Hans, S., and Boutin, C. (2018). Asymptotic analysis of high-frequency modulation in periodic systems. analytical study of discrete and continuous structures. *Journal of the Mechanics and Physics of Solids*, 117:123–156.
- [Rayleigh, 1945] Rayleigh, L. (1945). *Theory of Sound*. Dover: New York, NY, 1.
- [Reddy, 1997] Reddy, J. (1997). On locking-free shear deformable beam finite elements. *Computer Methods in Applied Mechanics and Engineering*, 149(1):113 – 132.
- [Reddy, 2004] Reddy, J. (2004). *An introduction to the finite element method*, volume 1221. McGraw-Hill New York.
- [Sanchez-Palencia, 1983] Sanchez-Palencia, E. (1983). Homogenization method for the study of composite media. In *Asymptotic Analysis II*—, pages 192–214. Springer.

- [Su et al., 2016] Su, R., Tang, T., and Liu, K. (2016). Simplified seismic assessment of buildings using non-uniform timoshenko beam model in low-to-moderate seismicity regions. *Engineering Structures*, 120:116–132.
- [Tollenaere and Caillerie, 1998] Tollenaere, H. and Caillerie, D. (1998). Continuous modeling of lattice structures by homogenization. *Advances in Engineering Software*, 29(7):699 – 705.
- [Viverge et al., 2016] Viverge, K., Boutin, C., and Sallet, F. (2016). Model of highly contrasted plates versus experiments on laminated glass. *International Journal of Solids and Structures*, 102-103:238 – 258.
- [Wilson and Penzien, 1972] Wilson, E. L. and Penzien, J. (1972). Evaluation of orthogonal damping matrices. *International Journal for Numerical Methods in Engineering*, 4(1):5–10.
- [Yi et al., 2015] Yi, S., Xu, L., Cheng, G., and Cai, Y. (2015). FEM formulation of homogenization method for effective properties of periodic heterogeneous beam and size effect of basic cell in thickness direction. *Computers & Structures*, 156:1 – 11.
- [Zheng et al., 2014] Zheng, Q., Ju, S., and Jiang, D. (2014). Anisotropic mechanical properties of diamond lattice composites structures. *Composite Structures*, 109:23–30.